

# **Propane Dehydrogenation on Metal and Metal Oxide Catalysts**

*Propaan Dehydrogenatie op Metaal en Metaal Oxide Katalysatoren*

*(met een samenvatting in het Nederlands)*

## **Proefschrift**

ter verkrijging van de graad van doctor aan de Universiteit Utrecht op gezag van de rector magnificus, prof. dr. G. J. van der Zwaan, ingevolge het besluit van het college voor promoties in het openbaar te verdedigen om woensdag 12 november 2014 des middags te 4.15 uur

door

**Jesper Johannes Hendrik Bernardus Sattler**

geboren op 10 maart 1986, te Veenendaal

Promotor: Prof. dr. ir. B. M. Weckhuysen

This PhD thesis is completed with financial support from the National Research School Combination-Catalysis (NRSC-C) and ACTS-ASPECT (project number 053.62.007).

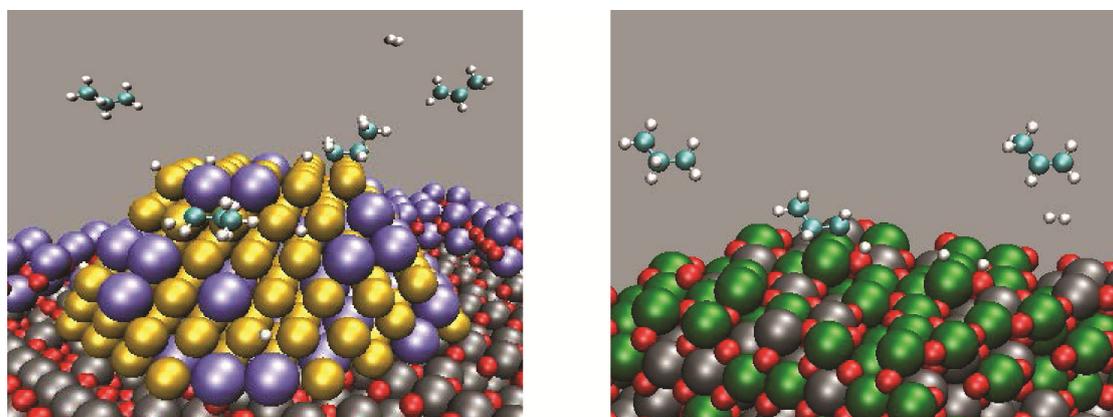
## Table of Contents

<b>Chapter 1</b>	-	General Introduction: Catalytic Dehydrogenation of Light Alkanes	5
Part 1			
<b>Chapter 2</b>	-	Operando Raman Spectroscopy during the Deactivation of Pt and Pt-Sn/Al <sub>2</sub> O <sub>3</sub> Propane Dehydrogenation Catalysts in a Lab-Scale Setup	79
<b>Chapter 3</b>	-	Nano-Scale Chemical Imaging of Individual Catalyst Particles for Studying the Coke Formed During Propane Dehydrogenation	105
<b>Chapter 4</b>	-	Pt-Ga/Al <sub>2</sub> O <sub>3</sub> as a Highly Active, Selective and Stable Catalyst for the Dehydrogenation of Propane	133
Part 2			
<b>Chapter 5</b>	-	Operando UV-Vis Spectroscopy of a CrO <sub>x</sub> /Al <sub>2</sub> O <sub>3</sub> Propane Dehydrogenation Catalyst in a Pilot-Scale Reactor	161
<b>Chapter 6</b>	-	Real-Time Quantitative Operando Raman Spectroscopy on a CrO <sub>x</sub> /Al <sub>2</sub> O <sub>3</sub> Propane Dehydrogenation Catalyst in a Pilot-Scale Reactor	175
Part 3			
<b>Chapter 7</b>	-	Summary, Concluding Remarks and Future Prospects	197
<b>Appendices</b>			215
<b>List of Abbreviations</b>			225
<b>List of Publications</b>			227
<b>Acknowledgements</b>			229
<b>About the Author</b>			231



## Chapter 1

# General Introduction: Catalytic Dehydrogenation of Light Alkanes



An introduction on the catalytic dehydrogenation of light alkanes, more specifically propane, will be given. The relevance of this reaction, as well as the current industrial processes will be discussed. Emphasis is put on critically assessing the catalytic performance of Pt, CrO<sub>x</sub> and GaO<sub>x</sub> catalyst formulations, which have been extensively studied in literature. The Chapter ends with an outline of the research performed in this PhD Thesis.

This Chapter is based on a shortened version of the manuscript: J.J.H.B. Sattler, J. Ruiz-Martinez, E. Santillan-Jimenez, B.M. Weckhuysen, Catalytic Dehydrogenation of Light Alkanes on Metals and Metal Oxides, *Chem. Rev.* (2014) DOI: 10.1021/cr50002436

## 1.1 Setting the Scene

Catalysts are materials able to increase the rate of a chemical reaction, without being consumed in the process. They are used in the production process of virtually every product, from plastics and electronics to drugs and food. Probably the most well-known example are the catalytic converters used in cars to convert environmentally harmful gasses, such as CO and NO<sub>x</sub>, to harmless compounds. Another area where catalysis is very important is the petrochemical industry. Large amounts of catalysts are used for converting the large hydrocarbons of crude oil into smaller, more valuable molecules, such as gasoline and light olefins. Light olefins, such as ethylene or propylene, are of high importance to the chemical industry, as these compounds are extensively used as building blocks. For example, they are used to produce polymers (e.g., polyethylene and polypropylene), oxides (e.g., ethylene glycol, acetaldehyde, acetone and epoxypropylene) and important chemical intermediates (e.g., ethylbenzene and propionaldehyde).<sup>1-4</sup> The demand of these building blocks has increased steadily over the last years.<sup>5</sup> In Figure 1.1, the uses as well as the recent and (predicted) future growth of the olefin supply and demand are shown. Fluid catalytic cracking (FCC) and steam cracking of naphtha, light diesel and other oil products are the most common methods for obtaining these light olefins, accounting for 97% of the propylene production in 2007.<sup>6,7</sup>

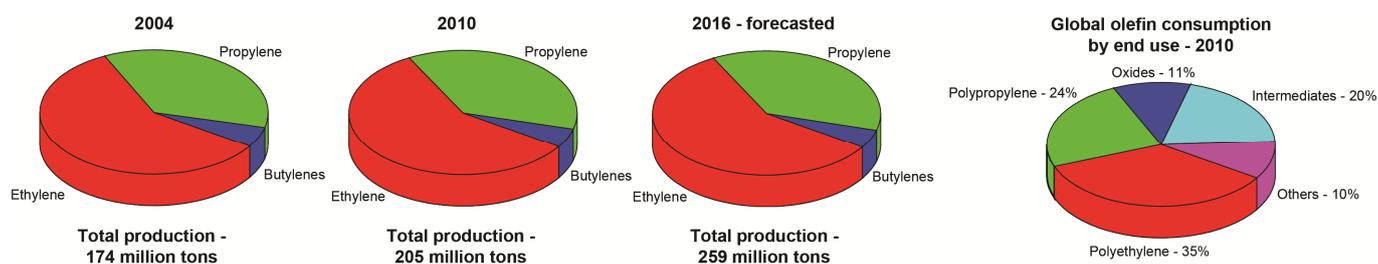


**Figure 1.1.** Consumption of ethylene, propylene and butylenes in 2004, 2010 and 2016 (predicted). In addition, the products made by these olefins are shown in the graph to the right.<sup>7</sup>

A number of factors including the high-energy demands of these processes, their low selectivity towards the production of particular olefins, dwindling petroleum reserves,

and rising oil prices are the driving force to search for a more economical feedstock and more efficient conversion technologies. In recent years, hydraulic fracturing or “fracking” technologies have improved to the point where large volumes of shale gas can be extracted in a cost-effective manner. In fact, the United States already obtains one-quarter of their natural gas production from shale gas deposits and this is expected to increase in the coming years due to the emphasis that is being given to the attainment of energy independence.<sup>8,9</sup> This increased supply of natural gas has resulted in a drop of gas costs of about 75% relative to 2005 prices, making natural gas very attractive both as an energy source and as feedstock for the production of transportation fuels or chemicals. This includes light olefins, which can be obtained by first converting natural gas into synthesis gas and by subsequently converting the latter either directly through the Fischer-Tropsch-to-Olefins (FTO) process or indirectly through the Methanol-To-Olefins (MTO) route with an intermediate methanol synthesis step.

**Table 1.1.** Gas composition of 6 different shale gas deposits in the United States. Larger hydrocarbons, hydrogen and oxygen are present in trace amounts and are not given.<sup>10</sup>

Shale deposit	Methane (%)	Ethane (%)	Propane (%)	Carbon oxides (%)	Nitrogen (%)
Barnett Shale (avg. of 4 wells)	86.8	6.7	2.0	1.7	2.9
Marcellus Shale (avg. 4 wells)	85.2	11.3	2.9	0.4	0.3
Fayetteville Shale (1 well)	97.3	1.0	0.0	1.0	0.7
New Albany Shale (avg. 4 wells, N <sub>2</sub> not reported)	89.9	1.1	1.1	7.9	-
Antrim Shale (avg. 4 wells)	62.0	4.2	1.1	3.8	29.0
Haynesville Shale (1 well)	95.0	0.1	0	4.8	0.1

As is shown in Table 1.1, in addition to methane, shale gas deposits contain considerable amounts of natural gas liquids (NGL), such as ethane, propane and larger hydrocarbons, which are easily separated from the main component methane.<sup>11</sup>

The relative high price for naphtha and other oil based feedstocks as compared to natural gas liquids, such as ethane, has caused a shift in the production of light olefins in the United States, with ethane crackers being constructed and naphtha crackers being either dismantled or converted. Given that, relative to naphtha cracking, the steam cracking of ethane produces a negligible amount of olefins other than ethylene, the supply of propylene has dropped and its price has risen sharply, creating opportunities for on-purpose catalytic technologies, such the catalytic dehydrogenation of light paraffins into the corresponding olefins.<sup>12</sup> Indeed, the profitability of propane dehydrogenation is determined to a large extent by the price difference between propane and propylene, which is large at the current market conditions. An additional advantage of dehydrogenation technologies is that dehydrogenation is an on-purpose technique, which yields exclusively a particular olefin instead of a mixture of products. In fact, the industrial dehydrogenation processes are currently optimized in such a way, that they can produce olefins of polymer-quality purity. As of this writing, ca. 5 million tons of propylene are produced annually by propane dehydrogenation (PDH).<sup>13,14</sup> However, this number is expected to increase significantly in the upcoming years as dozens of new PDH installations have been announced worldwide, with many of these installations already being under construction.<sup>15-18</sup> Notably, there is a similarly advantageous market situation for the dehydrogenation of butanes, although the impact of this compound on the chemical industry as a whole is less significant than for example ethylene and propylene.

## **1.2 Commercial Alkane Dehydrogenation Processes**

To date, five industrial processes for the dehydrogenation of light alkanes have been patented, two of which are currently in use.<sup>19-22</sup> As of April 2012, 5 million tons of propylene were being produced by the 14 propane dehydrogenation plants around the globe.<sup>13,14</sup> The global demand of propylene was 103 million tons that year and is expected to increase by 4-5% on a yearly basis.<sup>23,24</sup> Literally dozens of new dehydrogenation installations have been planned or are already under construction, amounting to an additional 14 million tons of propylene to be produced annually by

2018.<sup>13,14,25</sup> Additionally, six isobutane dehydrogenation installations are currently in operation, with three other plants planned.<sup>24</sup> The majority of these new facilities will be built in China or the United States and will use either the Catofin<sup>®</sup> (Lummus) or Oleflex<sup>™</sup> (UOP) technologies. A compilation of all existing and planned propane dehydrogenation installations is shown in Figure 1.2. Furthermore, in Table 1.2, a comparison is made between the Catofin<sup>®</sup> and Oleflex<sup>™</sup> processes. The STAR (UHDE) process will be applied for the first time in two installations in the Middle

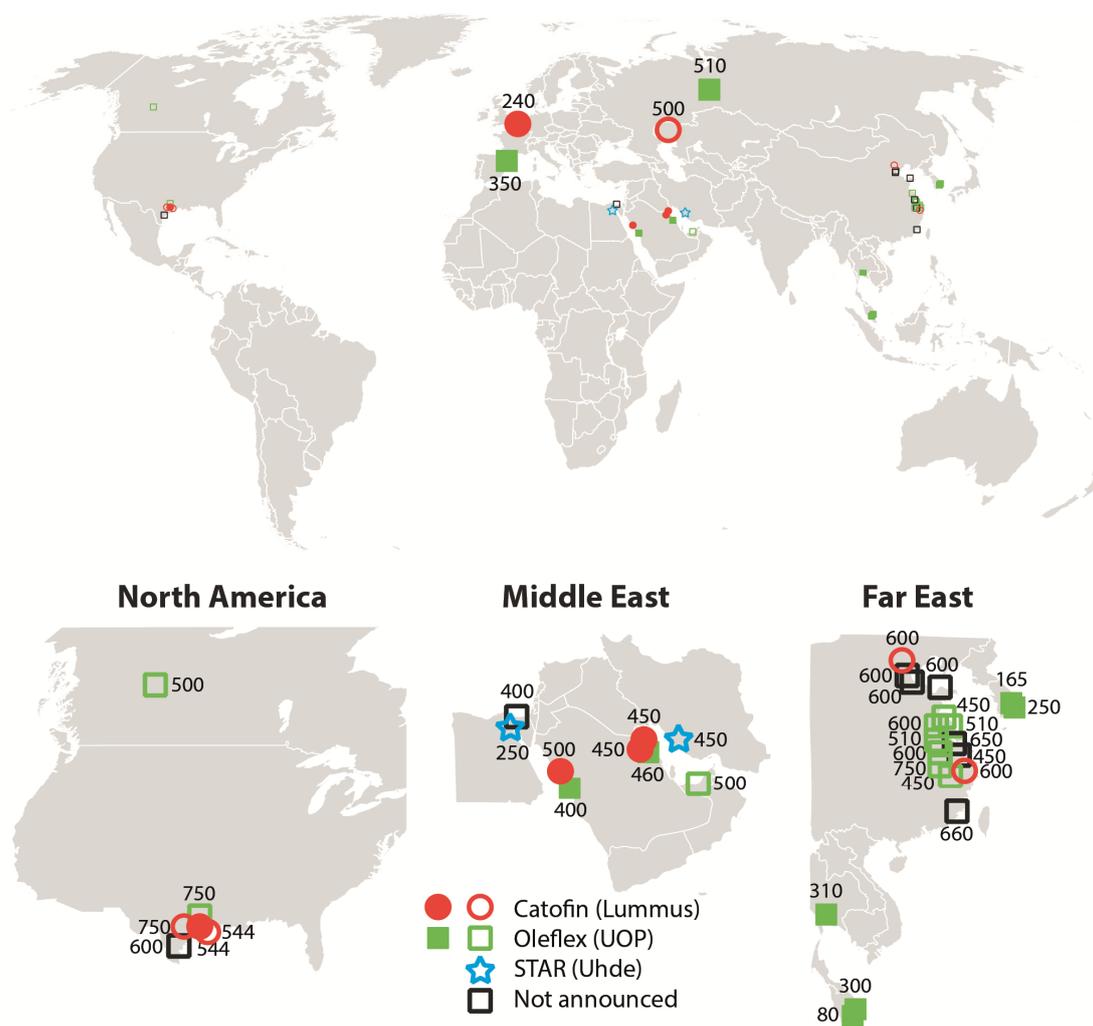


**Figure 1.2.** An overview of propane dehydrogenation installations currently in operation (filled squares) and installations that have been announced and are expected to start up before 2018 (unfilled squares). The number shows the maximum production of each plant (×1,000 tons per year). The locations of the facilities are approximations.<sup>13,14,25,26</sup> For some of the newly announced PDH installations (unfilled black squares), the industrial process to be used remains to be announced.

East that are currently under construction. The other two processes, fluidized bed dehydrogenation (FBD) process (Snamprogetti and Yarsintez) and Linde-BASF PDH, have not yet been commercially applied.

### 1.2.1 Catofin<sup>®</sup> Process

The Catofin<sup>®</sup> process, by CB&I Lummus, is based on the Houdry Catadiene<sup>®</sup> process, which originally was exclusively used for the dehydrogenation of isobutane to isobutylene. In turn, isobutylene was employed for the production of methyl tertiary butyl ether (MTBE), a fuel additive used to raise the octane number of gasoline. For environmental reasons the use of MTBE has decreased in recent years, causing a shift in the use of Catofin<sup>®</sup> installations to alternative purposes, such as propane dehydrogenation. A Catofin<sup>®</sup> installation generally consists of 5-8 parallel adiabatic fixed bed reactors containing a chromia-alumina catalyst. The reaction is run at temperatures of approximately 575 °C and pressures between 0.2 and 0.5 bar.<sup>27</sup> Each reactor alternates between dehydrogenation, regeneration and purge steps, each lasting a few minutes (15-30 min being needed for one complete cycle). Each individual reactor is made to run continuously so there are always some reactors performing dehydrogenation reactions while other reactors are being regenerated or purged, which results in a constant flow of reaction products.<sup>28</sup> A schematic of a

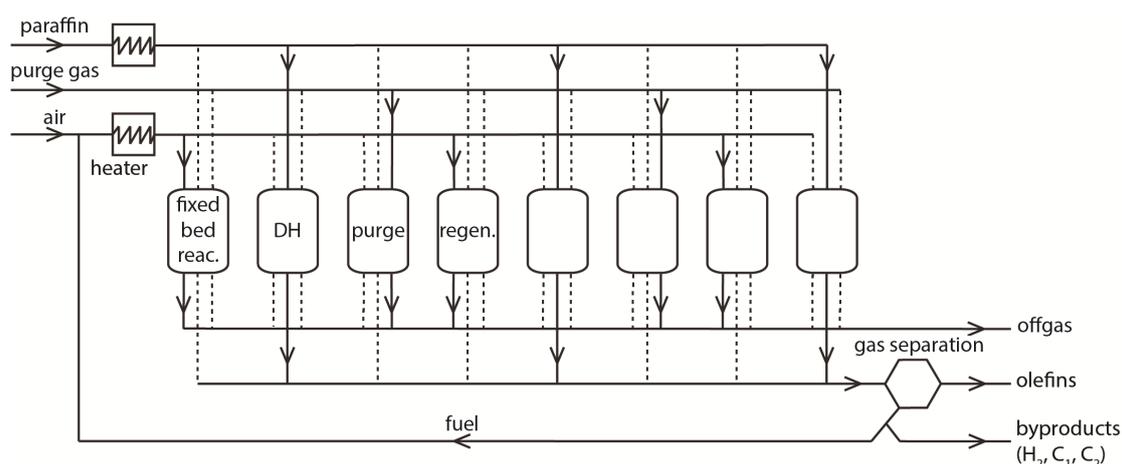


**Figure 1.3.** Schematic representation of a Catofin<sup>®</sup> dehydrogenation unit. Eight parallel reactors alternate between dehydrogenation (DH), purge and regeneration (regen.). Olefins produced are separated from side products that are subsequently mixed with oxygen and combusted to heat the reactors during the regeneration step.

Catofin® dehydrogenation installation is shown in Figure 1.3. The duration of the dehydrogenation step depends on the heat content of the catalyst bed, which decreases rapidly due to the endothermic nature of the reaction. Part of the heat required for the reaction is introduced to the reactors by preheating the reaction feed, with additional heat being provided by adjacent reactors that are regenerating the coked catalysts. Moreover, fuel gas is added to the reactor during the regeneration step in order to generate supplementary heat,<sup>29</sup> and inert material is added to the catalyst bed to increase its heat storage capacity.<sup>30</sup> The catalyst remains in use for 2-3 years and the progressive loss in activity with time-on-stream is being counteracted by gradual increases in temperature in order to afford a constant dehydrogenation activity throughout the entire catalyst life span.<sup>31,32</sup>

### 1.2.2 Oleflex™ Process

The Oleflex™ process by UOP uses a very different reactor design comprising a series of fluidized bed reactors, a catalyst regeneration unit and a product recovery section. A schematic representation is shown in Figure 1.4.<sup>33</sup> The reaction is run using a Pt-Sn-based catalyst at pressures between 1 and 3 bar and temperatures ranging from 525 to 705 °C. Three or four adiabatic radial flow reactors containing the

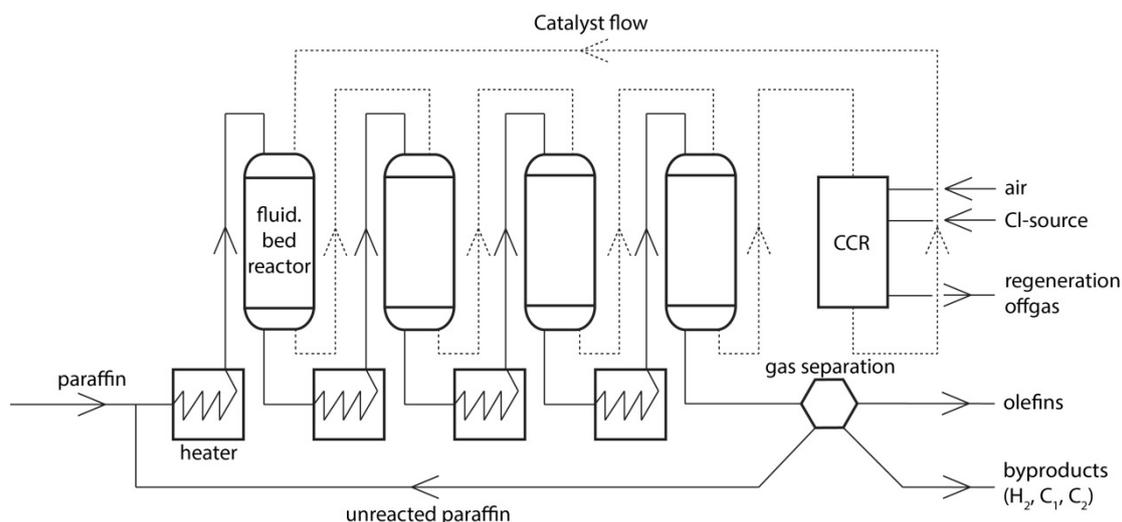


**Figure 1.4.** Schematic representation of an Oleflex™ dehydrogenation unit. A simplified version of the gas separation unit used to separate paraffins, cracking products and hydrogen from olefins is shown.

catalyst, are connected in series with preheaters in between. These preheaters heat the gas flow and represent the main source of heat in the reactor system. The catalyst flows through the system, the last reactor being connected to a continuous catalyst regeneration unit (CCR) that regenerates the catalyst by burning of any carbon deposits and re-dispersing the Pt on the support material by means of treating the catalyst with a chlorine-air mixture. The entire system is designed to operate continuously in order to obtain an uninterrupted stream of reaction products. The regenerated catalyst is then reintroduced to the first reactor, completing an entire cycle every 5 to 10 days. Product recovery is done by cooling, compressing and drying the reactor effluent, hydrogen being cryogenically separated from the hydrocarbons. The latter are led through a selective hydrogenation unit to remove di-olefins and acetylenes. Polymer-quality propylene is obtained after flowing the hydrocarbons through a de-ethanizer and a propane-propylene splitter. More detailed information on the Catofin® and Oleflex™ processes is presented in Table 1.2.

**Table 1.2.** Specifics of the Catofin® and Oleflex™ commercial dehydrogenation processes.<sup>24,25,28,33–38</sup>

	Catofin®	Oleflex™
Catalyst formulation	18-20 wt% CrO <sub>x</sub> on an alumina support, promoted by 1-2 wt% Na or K.	<1 wt% Pt and 1-2 wt% Sn on an alumina support, promoted by 0-1 wt% Na or K.
Process license holder	CB&I Lummus	UOP (Honeywell)
Used for	Dehydrogenation of propane, isobutane and isopentanes.	Dehydrogenation of propane and isobutane.
Operating conditions	575 °C at 0.2-0.5 bar.	525-705 °C at 1-3 bar.
Reactor type	Multiple parallel fixed bed reactors.	A fluidized bed reactor consisting of three separate parts: several reactors in series, a product recovery section and

		catalyst regeneration section.
Main source of heat	Heating of the catalyst material during regeneration by burning off coke and the addition of fuel gas.	Preheating of the gas flow before each reactor.
Reaction program	Typically 12 min of dehydrogenation, 3 min of purge, 12 min of regeneration and 3 min of purge.	The separate parts of the reactor run continuously as the fluidized catalyst bed moves from one section to the next.
Deactivation	Twofold: deposition of coke due to side reactions, and thermal sintering of the alumina support leading to a loss of surface area.	Twofold: deposition of coke and sintering of the Pt nanoparticles. In addition, catalyst particle attrition is an issue due to the fluidized bed.
Regeneration	Combustion of the coke deposits.	Combustion of the coke deposits, additionally chlorine is added to assist with Pt re-dispersion.
Catalyst lifetime	1-2 years before the reactor is shut down and the catalyst is replaced. Catalyst lifetime is prolonged by increasing the temperature to maintain high propylene yield, at the cost of lower selectivity.	1-3 years, new catalyst being continuously added to the reactor system and dusts formed due to catalyst attrition being continually removed.

### 1.2.3 Other Patented Alkane Dehydrogenation Processes

The Steam Active Reforming (STAR) process<sup>®</sup> developed by Uhde utilizes a very different reactor setup. The reaction is run at 6-9 bar and temperatures between 500-600 °C, steam being added to the feed to reduce paraffin partial pressure and coke formation. Since the catalyst has to be stable in the presence of steam, Pt-Sn supported on a (basic) zinc-aluminate is used with calcium/magnesium-aluminate as a

binder. Very little coke is deposited on the catalyst surface and thus, dehydrogenation cycles may be as long as 7 h before regeneration becomes necessary.

A fixed bed reactor system, consisting of two separate reactors placed in a series, is used.<sup>39,40</sup> The first is a top-fired tubular reformer-type reactor, which is externally heated by an oven. Most of the heat is provided at the top of the reactor, where the dehydrogenation activity is highest. The gas mixture exiting the first reactor is cooled prior to being introduced into the second so-called oxy-reactor, where an oxygen-steam mixture is used to selectively combust part of the hydrogen formed, shifting the equilibrium towards higher olefin yields. In addition, the combustion of hydrogen provides the heat required for the additional conversion of propane. The olefins in the resulting gas mixture are separated from any residual hydrogen and other side products, which are combusted to heat the dehydrogenation reactor oven. A schematic representation of this reactor setup is shown in Figure 1.5. Currently, two dehydrogenation installations using the Uhde STAR process<sup>®</sup> are being constructed in Egypt and Iran.

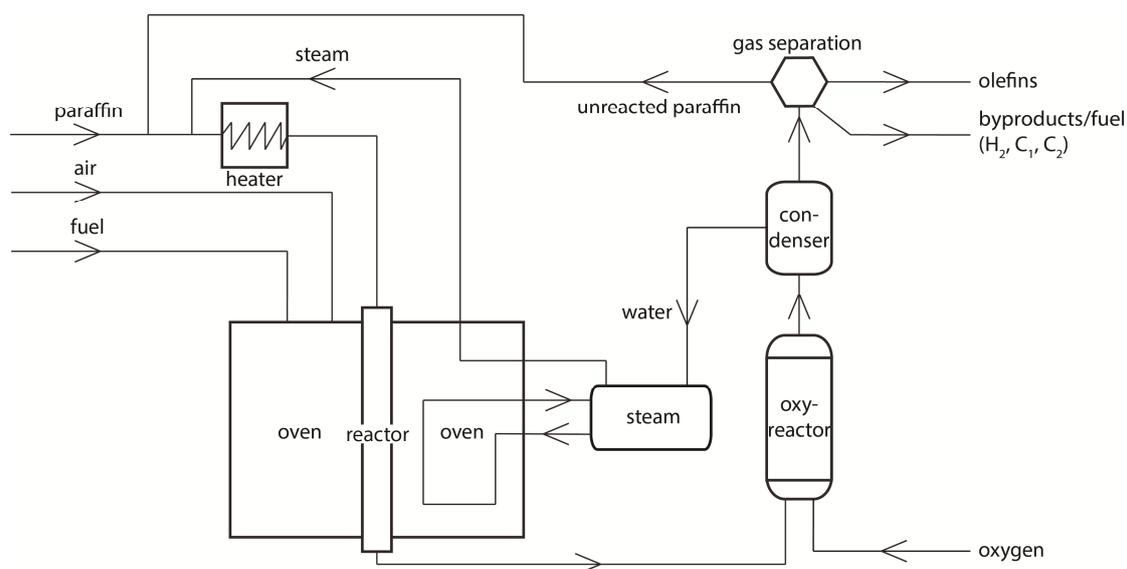


**Figure 1.5.** Schematic representation of a Steam Active Reforming (STAR) dehydrogenation unit. The system comprises two fixed bed reactors, one located in the oven and an oxy-reactor where hydrogen is combusted. A simplified version of the gas separation unit used to separate the olefins from paraffins, cracking products and residual hydrogen is shown.

Figure 1.6 shows a schematic representation of the Fluidized Bed Dehydrogenation (FBD) process, licensed by Snamprogetti and Yarsintez, in which a fluid catalytic

cracking-like (FCC) reactor system is used for the dehydrogenation of propane. An alkane is flowed through a staged fluidized bed at pressures between 1.1 and 1.5 bar and temperatures between 550 and 600 °C. A  $\text{CrO}_x/\text{Al}_2\text{O}_3$  catalyst, promoted with an alkali metal is used. The catalyst deactivates over time and is therefore continuously transported to a regenerator connected to the reactor to combust the carbon deposits. The heat required for the dehydrogenation reaction is provided by heating the catalyst material to temperatures above 700 °C in the regenerator. A fuel gas is routinely added during regeneration as the combustion of the carbon deposits alone does not provide enough heat to achieve these temperatures. Upon its return to the reactor the catalyst cools again to temperatures below 560 °C. Finally, a system comprising a jet scrubber and cyclones in the head of the reactor is used to remove any dust formed by catalyst attrition.<sup>30</sup>

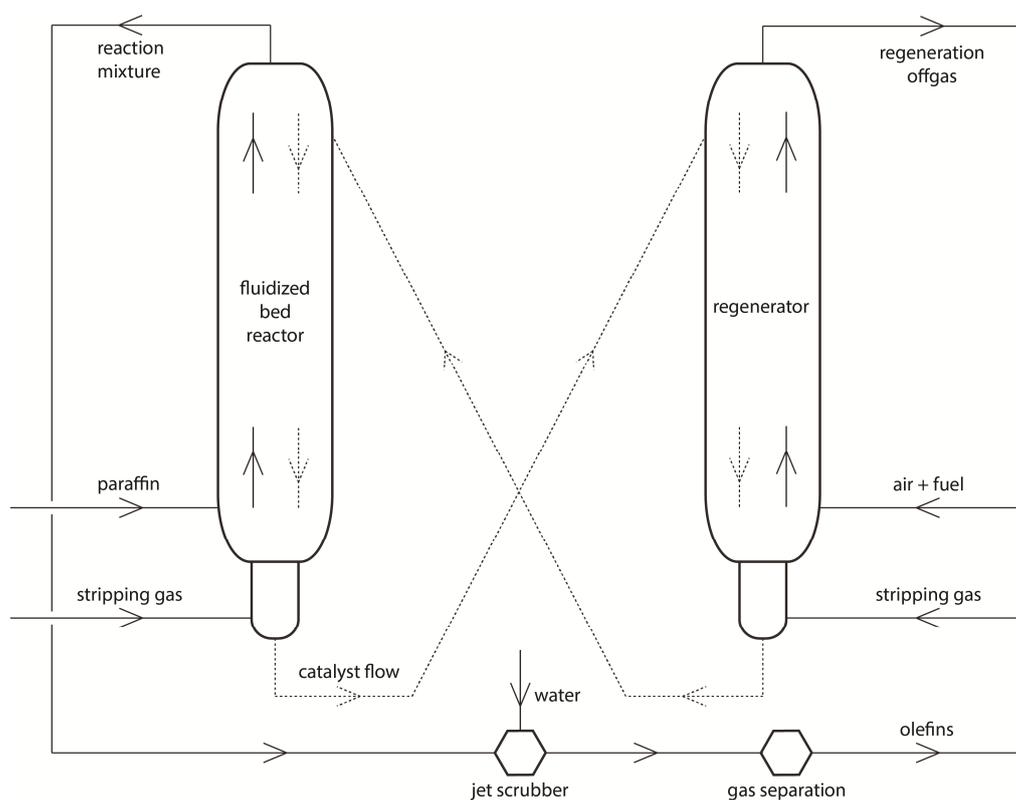


**Figure 1.6.** Schematic representation of the Fluidized Bed Dehydrogenation (FBD) reactor system. A simplified version of the gas separation section is shown.

The Linde-BASF PDH process, of which a schematic representation is shown in Figure 1.7, uses a Pt-Sn catalyst supported on  $\text{ZrO}_2$  for dehydrogenating light paraffins isothermally at a temperature of 590 °C. The process shows various

similarities with the STAR process<sup>®</sup>, as the reaction feed is diluted with steam and an externally heated fixed bed reactor is used. Three of these reactors operate in parallel, with two in dehydrogenation and one in regeneration mode, ensuring a continuous flow of reaction products. A mixture of air and steam is used to regenerate the catalyst and the reactor is purged before and after the regeneration step.<sup>39</sup>

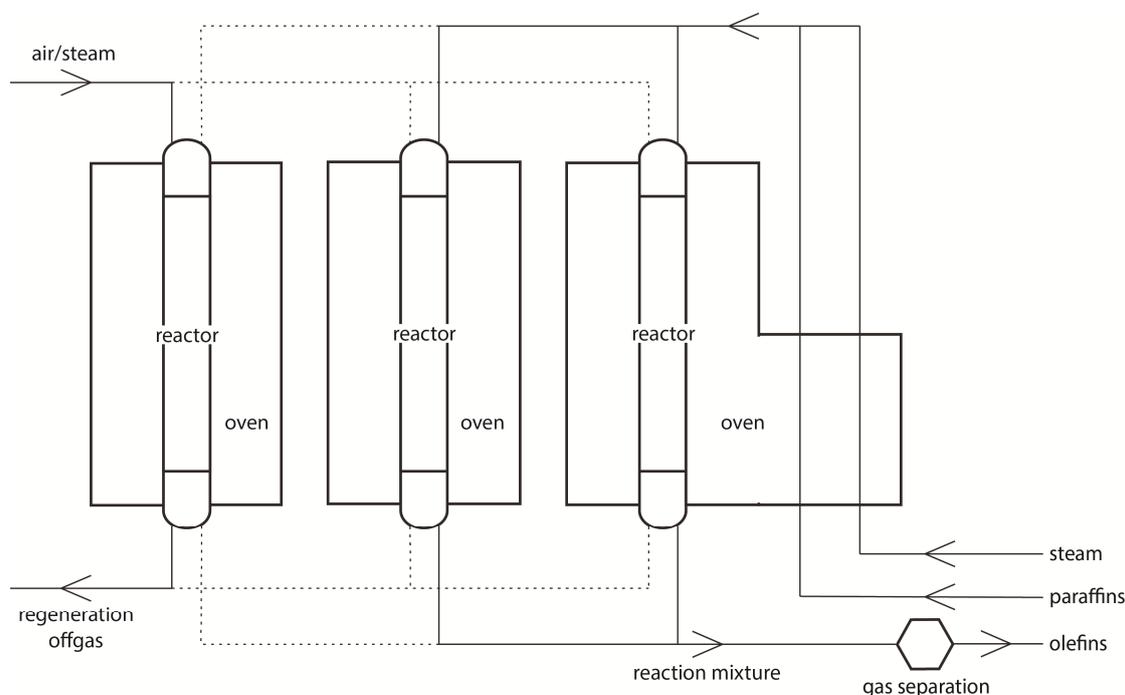


**Figure 1.7.** Schematic representation of the Linde-BASF PDH process. A simplified version of the gas separation section is shown.

### 1.3 Thermodynamics of Alkane Dehydrogenation

From the chemical perspective, dehydrogenation is a one-step reaction through which light paraffins can be converted into the corresponding olefins and hydrogen, as illustrated below for the dehydrogenation of propane:



However, the reaction is thermodynamically limited and highly endothermic, which according to Le Chatelier's principle, implies that higher reaction temperature and/or lower paraffin partial pressure are needed to achieve high conversions. Indeed,

temperatures of 550-750 °C are typically required in the dehydrogenation of C<sub>2</sub>-C<sub>4</sub> paraffins to obtain alkane conversions  $\geq 50\%$  at 1 bar, as is shown in Figure 1.8. Moreover, given that the enthalpy required to dehydrogenate alkanes decreases as the chain becomes longer ( $\Delta H_{298}^0 = 137 \text{ kJ mol}^{-1}$  for ethane, 124.3 kJ mol<sup>-1</sup> for propane and 117.6 kJ mol<sup>-1</sup> for isobutane dehydrogenation), a considerably larger amount of energy is required to dehydrogenate light paraffins on a mass basis. The pressure dependence is also shown in Figure 1.8, lower pressures clearly resulting in higher olefin yields at a given temperature.

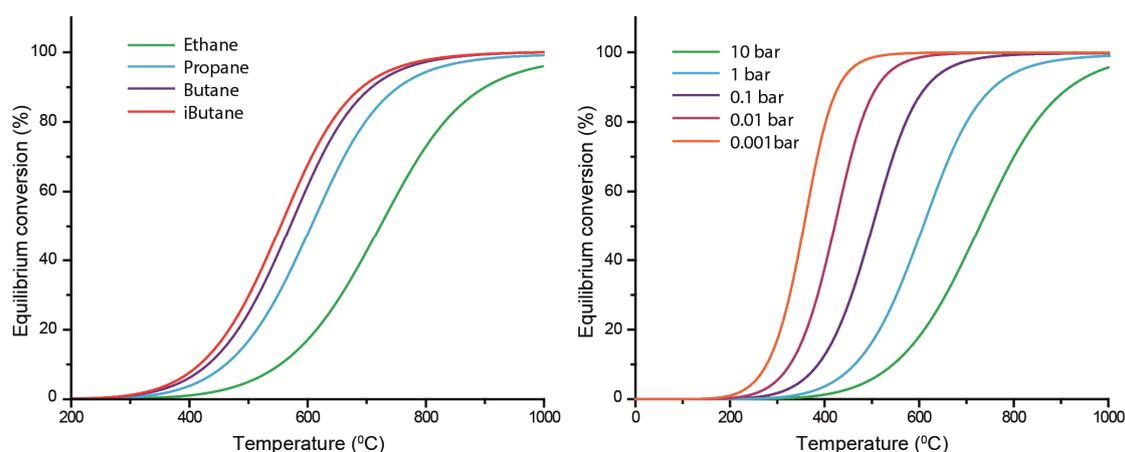


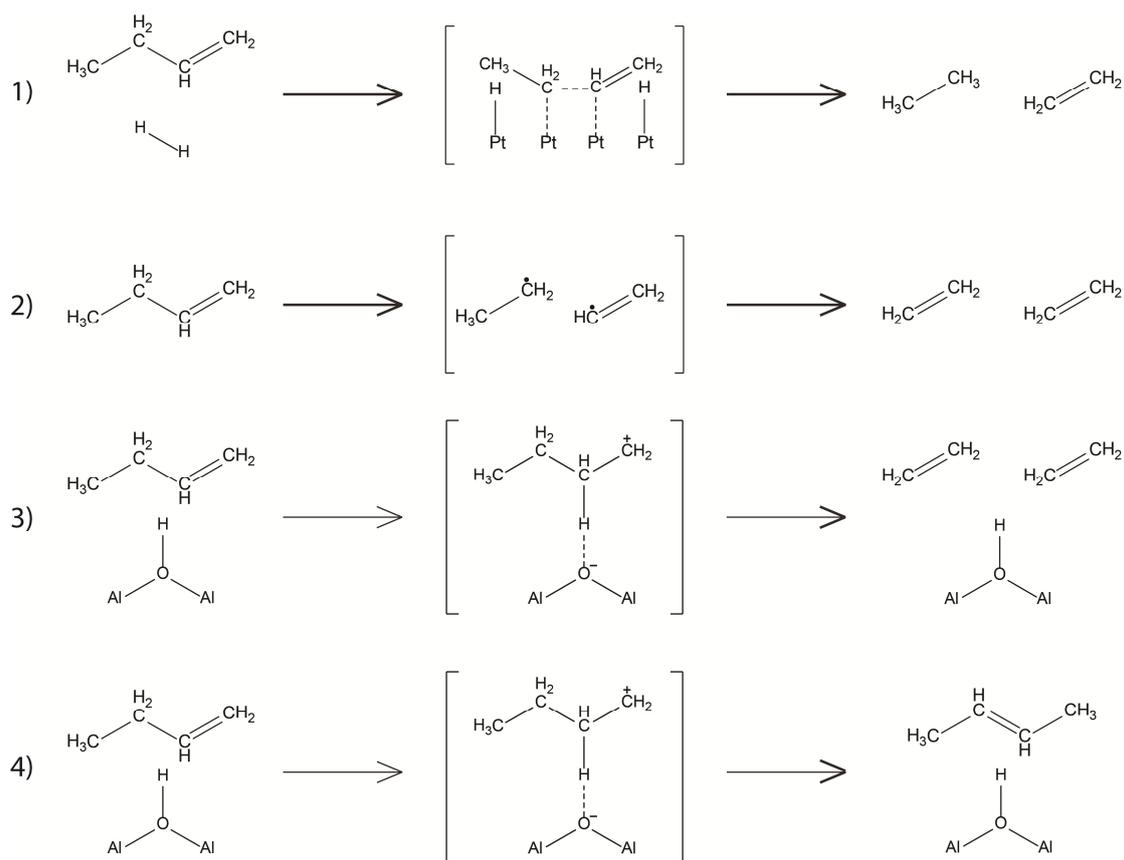
**Figure 1.8.** Equilibrium conversion of C<sub>2</sub>-C<sub>4</sub> paraffins to olefins as a function of temperature at 1 bar (left) and pressure dependence of the dehydrogenation of propane as a function of temperature (right).

The C-H bonds of paraffins and olefins have considerably higher dissociation energies than their C-C bonds, meaning that catalysts that favor C-H over C-C bond cleavage are required in order to avoid side reactions. An additional complicating factor is that olefins are considerably more reactive than their paraffinic counterparts, which can further lead to unwanted side and secondary reactions. Three types of side reactions can occur, namely hydrogenolysis, cracking and isomerization. In hydrogenolysis, the addition of hydrogen into a C-C bond within a paraffin results in the formation of two smaller alkanes. Since hydrogen adatoms and/or C<sub>x</sub>H<sub>y</sub> adspecies are required for alkane hydrogenolysis to occur, this reaction is believed to be catalyzed by Pt sites.<sup>41,42</sup> Cracking also results in the cleavage of a paraffin to form two smaller hydrocarbons, although in this instance no hydrogen is required. Thermal cracking hardly occurs at dehydrogenation reaction conditions, as it requires temperatures of

450-750 °C and pressures of 5-70 bar. This reaction proceeds via the formation of radical intermediates, which rearrange into an alkane and an alkene. Catalytic cracking is different as it requires a catalyst with Brønsted and/or Lewis acidity and proceeds via the formation of a carbocation intermediate, albeit it also results in the formation of an alkenes and an alkane.<sup>43-45</sup> Isomerization is the rearrangement of atoms within a molecule. For example, during the dehydrogenation of isobutylene to isobutylene, the former may transform to 1- or 2-butylene, which may dehydrogenate further to 1-3-butadiene. The rearrangement can take place via a carbocation intermediate formed on a Brønsted acid site, or through an adsorbed species on the active phase of the catalyst.<sup>46-48</sup> By increasing the temperature, the rates of both C-H and C-C cleavage reactions are increased, and therefore, temperature and pressure must be carefully controlled to achieve an optimal olefin yield. In short, the balance between dehydrogenation and these side reactions is very complex.

Fortunately, dehydrogenation appears to be catalyzed by different active sites than the side reactions, which means high olefin yields can be obtained by careful catalyst design. For instance, cracking reactions are efficiently catalyzed by Brønsted acid sites, while large Pt ensembles also display activity for hydrogenolysis, cracking and isomerization reactions. Scheme 1.1 shows an overview of the reactions that may be catalyzed by Brønsted acid and Pt sites on a typical Pt-based dehydrogenation catalyst.<sup>27</sup>

An additional problem is that the low pressures and high temperatures required to obtain high olefin yields are also optimal conditions for the formation of coke deposits. Consequently, the performance of dehydrogenation catalysts progressively deteriorates with time-on-stream, making it necessary to regenerate the catalysts frequently in order to preserve sufficient activity. This is particularly important when the process operates at high alkane conversions, due to the fact that polymerized olefins are believed to be coke precursors (see Scheme 1.1). Hence, during the selection of the operational conditions in any industrial dehydrogenation process, a compromise must be struck between olefin selectivity and paraffin conversion.



**Scheme 1.1.** Examples of the side reactions that may occur when 1-butylene is exposed to a Pt/Al<sub>2</sub>O<sub>3</sub> catalyst: 1) hydrogenolysis, 2) thermal cracking, 3) catalytic cracking and 4) isomerization.

Notably, the reaction equilibrium can be shifted to higher paraffin conversions by reducing the partial pressure of the paraffin or by withdrawing the hydrogen produced. As was discussed before, two strategies have been adopted in industry to lower paraffin partial pressure, namely reducing the pressure below atmospheric (Catofin<sup>®</sup>) or diluting the paraffin feed with steam (STAR process<sup>®</sup>).<sup>27,49</sup> Hydrogen can be removed from the reaction medium by selective hydrogen combustion (SHC), which involves the addition of an oxidant to the reaction feed in order to burn off the hydrogen formed during dehydrogenation. Relatively mild oxidants, e.g. CO<sub>2</sub> are preferred, as the use of strong oxidants, like O<sub>2</sub>, risk also combusting the hydrocarbon reactants and products. Through this approach, a considerable amount of heat is generated, which promotes the endothermic dehydrogenation reaction. A solid oxygen carrier, such as ceria, can also be employed for this purpose.<sup>50</sup> Another strategy is to

use a membrane permeable for hydrogen to withdraw the latter from the system, thereby shifting the equilibrium towards higher olefin yields.<sup>51-53</sup>

The oxidative dehydrogenation (ODH) of paraffins is related to SHC by the fact that an oxidant is also added to the feed, although in ODH the latter is done to directly oxidize the paraffin to the respective olefin. ODH has some advantages that make it a very attractive alternative to non-oxidative dehydrogenation, including the facts that the reaction is exothermic (propane ODH:  $\Delta H_{298}^0 = -117 \text{ kJ mol}^{-1}$ ) and not equilibrium limited. However, to control side reactions, such as cracking and the excessive oxidation of reaction products, is very challenging.

## 1.4 Alkane Dehydrogenation Catalysts

Two types of formulations are typically used for the non-oxidative dehydrogenation of light olefins: noble metal-based and metal oxide-based catalysts. Although Pt represents the only precious metal that has been extensively studied, various metal oxides have been successfully tested, with  $\text{CrO}_x$  being the most prominent example due to its industrial use. Furthermore, promising results were obtained by using gallium, indium, vanadium, iron and molybdenum oxides. In the specific case of propane dehydrogenation, only Pt,  $\text{CrO}_x$  and  $\text{GaO}_x$  catalysts are able to effectively activate the C-H bond. In this section, the active sites, deactivation and support and promoter effects of these three compounds will be discussed.

### 1.4.1 Platinum-based Catalysts

In the 1960s, new technologies were developed for the synthesis of the long-chain linear olefins used in the production of biodegradable detergents.<sup>27</sup> This new approach was inspired by the well-known bifunctional metal supported catalysts utilized in catalytic reforming, where a noble metal catalyzes hydrogenation and dehydrogenation reactions, while the acid support provides the active sites needed for isomerization, cyclization and hydrocracking reactions. In contrast dehydrogenation catalysts are monofunctional, as the acidic function must be minimized in order to avoid side reactions.

Albeit all the noble metals of Group VIII B are active in the catalytic dehydrogenation of alkanes, Pt is the only noble metal utilized in commercial applications. The first industrial alkane dehydrogenation technology, namely the Pacol™ process (UOP), was first commercialized in 1968. Based on an alumina-supported platinum catalyst, the process greatly contributed to the widespread use of linear olefins in the detergent industry. In the early 1970s UOP developed the Oleflex™ process, which was initially applied for the production of butadiene and later extended to propylene.

#### 1.4.1.1 *Nature of the active sites*

Noble metals are active for dehydrogenation in the metallic state and in some cases a reduction step is necessary prior to reaction. The dehydrogenation reaction of light alkanes is insensitive to the structure of the platinum particles, i.e., dehydrogenation activity is independent of the platinum particle size or crystallographic plane exposed. As only the amount of active sites is relevant, small particles are preferred. However, undesired side reactions that occur during alkane dehydrogenation, such as hydrogenolysis, isomerization and coke formation, are sensitive to the structure of the platinum particles, although there is no general consensus regarding the effect of the dispersion on the rate of these reactions. Some studies stress the markedly inverse relationship between particle size and the rate of hydrogenolysis (see Figure 1.9), the latter reaction being one of the main causes of coke formation.<sup>54–57</sup> Contrarily, others believe that for hydrogenolysis to take place, carbon deposits need to be in the vicinity of adsorbed hydrogen, which is more likely to occur on large ensembles of Pt than on small particles.<sup>39,58,59</sup>

DFT calculations have been employed to calculate the energy barrier of propane dehydrogenation on flat (111) and stepped (211) Pt crystal planes by Yang et al.<sup>57</sup> Indeed, it was found that step sites are more reactive, as the energy barrier to form propylene is much lower on step sites (24–34 kJ/mol) than on the flat surface (63–72 kJ/mol). Nevertheless, propane adsorbs more strongly on the latter, forming propylidyne intermediates believed to serve as precursors for both hydrogenolysis and coke formation.<sup>57,60</sup>

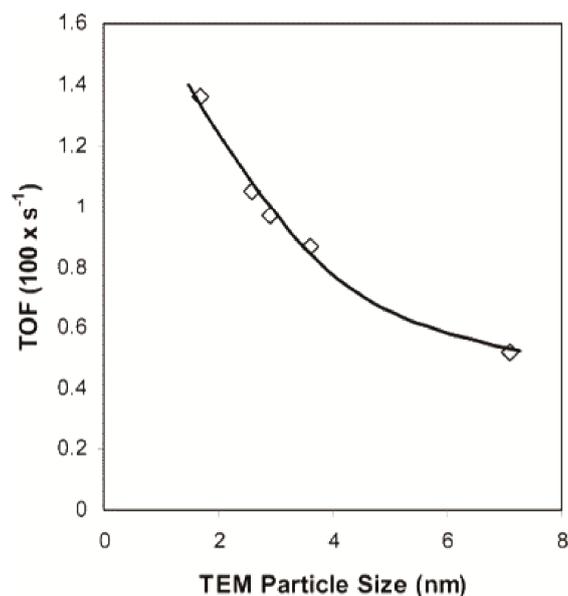


**Figure 1.9.** Structure sensitivity of ethane hydrogenolysis on 1% Pt/SBA-15 with Pt particle sized ranging from 1.7 to 7.1 nm. Reprinted with permission from ref. 54, copyright 2005, American Chemical Society.

#### 1.4.1.2 Catalyst deactivation

Two main processes cause the deactivation of Pt-based dehydrogenation catalysts. First and foremost, the side reactions that form carbon deposits on the catalyst surface lead to the coverage of the active sites with coke, which results in a drop in activity. As it is not possible to completely prevent coke deposition, the catalyst needs to be regenerated frequently by combusting the coke deposits. However, the high temperature of both the regeneration process and the dehydrogenation reaction, triggers the agglomeration, or sintering, of the platinum nanoparticles, the concomitant loss in active sites also resulting in catalyst deactivation. In addition to temperature, the composition of the reaction mixture has a profound influence on the sintering behavior of Pt supported catalysts. As early as 1977, Fiedorow et al. showed that Pt/Al<sub>2</sub>O<sub>3</sub> catalysts more readily sinter in an oxygen-containing atmosphere than in a hydrogen containing atmosphere at temperatures above 600 °C.<sup>61,62</sup> A third important factor determining catalyst sintering is the interaction between Pt and the catalyst support. Nagai et al. reported that Pt on Al<sub>2</sub>O<sub>3</sub> readily sinters after treatment in air at 800 °C, while Pt on CeO<sub>2</sub> remains stable due to the strong Pt-O-Ce bond. The authors proposed that the strength of the Pt-support interaction depend on the electron density of the oxide used as support.<sup>63</sup>

However, Pt can be re-dispersed on the catalyst by the addition of low amounts of oxygen and chlorine in the feed at temperatures around 500 °C, although this process can only occur when the interaction between the support and the  $\text{PtO}_x$  and  $\text{PtO}_x\text{Cl}_y$  species formed is such that mobile surface complexes are produced.<sup>61,64–69</sup>

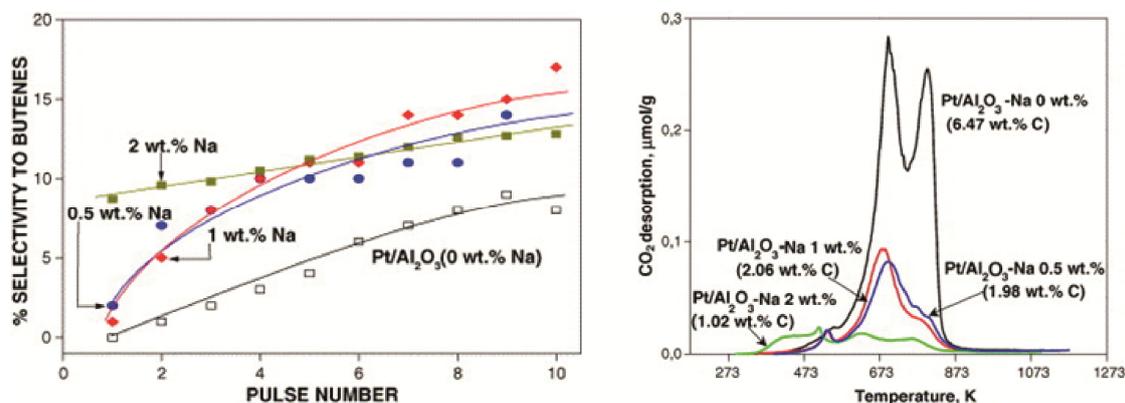


**Figure 1.10.** Selectivity to butylenes as a function of the number of butane pulses on a Pt/Al<sub>2</sub>O<sub>3</sub> catalyst doped with different amounts of Na (left) and TPO profiles of the spent catalysts (right) showing that Na has a positive effect on the selectivity and that the presence of Na decreases the coke deposition, respectively. Reprinted from ref. 69, copyright 2006, with permission from Elsevier.

#### 1.4.1.3 Role of the support

Good supports for alkane dehydrogenation catalysts have to be thermally stable, especially under the harsh hydrothermal conditions that the material experiences during the regeneration step. In addition, limited support acidity is needed in order to avoid undesirable side reactions, such as coke formation and alkane isomerization. Finally, for an optimal distribution of the metallic particles, a relatively large surface area and uniform pore size distribution is preferred.<sup>70</sup>

High surface area alumina is the classical support employed in platinum-based dehydrogenation catalysts due to its high thermal stability, mechanical strength and its exceptional ability of maintaining the platinum nanoparticles dispersed, which is crucial to attain stable catalyst performance. However, most alumina supports are acidic and therefore, promoters are used to curb support acidity. The addition of alkaline metals, such as Li, Na and K, poisons these acid sites, suppressing the formation of coke on the support as is shown in Figure 1.10.<sup>69,71–74</sup> Additionally, these

promoters can modify the properties of the platinum and suppress side reaction, such as hydrogenolysis and isomerization, reportedly due to a reduction in the effective size of platinum clusters.<sup>54-57</sup> Zn and Mg have also been used to dope the support, since the resulting spinel phase is less acidic and more thermally stable. These spinels also curtail the sintering of platinum due to a strong metal-support interaction.<sup>75-78</sup>

Yet another strategy is to use more stable polymorphs of alumina, such as  $\theta$ - or  $\alpha$ -alumina, since the latter have considerably less Brønsted acid sites relative to  $\gamma$ -alumina, albeit they also tend to have considerably lower surface areas. It is also important to mention that in order to reach a high dispersion of Pt on the support, Lewis acid sites and amphoteric OH groups are required, which limits the use of  $\text{SiO}_2$  and basic supports such as MgO or ZnO. Indeed, by hydrothermally treating  $\gamma\text{-Al}_2\text{O}_3$  prior to impregnation, the formation of additional hydroxyl groups results in a better Pt dispersion after impregnation and calcination.<sup>79</sup>

Zeolites are a commonly used alternative as a support for dehydrogenation catalysts. Dumesic and coworkers reported Pt-Sn supported on zeolite K-L to be a highly active, selective and stable catalyst in the selective dehydrogenation of isobutane.<sup>80-83</sup> The authors suggest that in the presence of K, zeolite L can stabilize small Pt-Sn particles in the micropores of the support. In addition, this catalyst shows a high tolerance to coke deposition. This is particularly important as the strong acid sites of zeolites make them very susceptible to coking.<sup>70</sup> Further modifications of the catalyst involving the neutralization of the residual acid sites with Cs after Pt reduction, improved the selectivity of the catalyst in the dehydrogenation of n-pentane and n-heptane.<sup>84</sup> On the other hand, mesoporous silica was found to be an unsuitable support, as the Pt-Sn nanoparticles readily sinter due to the weak metal-support interaction.<sup>70</sup>

#### 1.4.1.4 *Role of the promoters*

In spite of the fact that platinum-based catalysts display very high activity in dehydrogenation reactions, their intrinsic selectivity to alkenes, as well as the catalyst stability are not entirely satisfactory. Consequently, the addition of promoters, which are able to modify the catalytic properties of platinum, is necessary to obtain an optimal catalyst. Tin is by far the most studied promoter and all the platinum-based catalyst formulations that are industrially applied include this post-transition metal. The addition of tin modifies both the platinum active phase and the support. Essentially, this promoter suppresses hydrogenolysis and isomerization reactions,

minimizes metal sintering, neutralizes the acidity of the support and facilitates the diffusion of the coke species from the metal surface to the support. Although these beneficial effects of tin promotion are well known and have been amply described in the literature, the working principles of the platinum-tin system are still under debate. Indeed, both geometric and electronic effects have been invoked to explain the mechanisms through which tin influences the catalytic properties of platinum. However, it is clear that SnO<sub>2</sub> species present on the catalyst are reduced by either the hydrocarbon feed or during a pre-reduction step, yielding a Pt-Sn alloy. The reducibility of SnO<sub>2</sub> depends largely on the interaction with the support (strong interaction makes the reduction more difficult), and the proximity to the Pt (which assists with the reduction of the Sn).<sup>70</sup>

From the geometric point of view, it has been suggested that isomerization, hydrogenolysis and the formation of coke precursors can all be suppressed by reducing the size of platinum nanoparticles.<sup>82,83,85,86</sup> Notably, the formation of a platinum-tin alloy and/or the partial covering of the platinum particles by tin species results in the creation of smaller platinum ensembles. Olsbye et al. have suggested that tin selectively covers low coordination platinum sites (such as steps, corners, edges and defects), which they believe are responsible for the hydrogenolysis reaction.<sup>87,88</sup> Furthermore, the so-called ensemble effect can be employed to explain the geometric advantages of Sn addition to Pt-based catalysts. Dehydrogenation is believed to be a structure-insensitive reaction, meaning that very small groups or even single Pt atoms can catalyze the reaction. On the other hand, side reactions, such as coking, are structure-sensitive, and require relatively large ensembles of Pt. Pt-Sn alloy formation effectively reduces the amount of neighboring Pt atoms within the ensembles, curbing these structure-sensitive reactions. Moreover, it has been suggested that the sintering of Pt nanoparticles is retarded with the addition of Sn.<sup>88</sup> Additionally, coke precursors prefer to adsorb on large Pt ensembles and thus, the addition of Sn facilitates the migration of these precursors from the Pt-Sn surface to the support, effectively reducing the detrimental effects of coke deposition.<sup>85,89</sup>

A secondary effect of Sn addition is the modification of the electronic properties of platinum. Alloyed metallic Sn or Sn<sup>2+</sup> species in close contact with platinum are able to transfer electrons to the 5d band of platinum atoms, which alters the adsorptive and catalytic properties of the metal. The interaction of promoters with platinum can be assessed by measuring the heat of adsorption of distinct probe molecules through

microcalorimetric methods.<sup>90-95</sup> Dumesic et al. performed a thorough adsorption microcalorimetry study and observed that the heat of ethylene and isobutylene adsorption decreases with the addition of tin.<sup>96-98</sup> Infrared spectroscopy revealed that during the adsorption of ethylene, tin suppresses the formation of ethylidyne species and weakens the molecular adsorption of ethylene on the platinum surface. Additional DFT calculations explained these experimental results by revealing an increase in the electron density of platinum, which weakens the adsorption of ethylidyne on platinum atoms in close contact with tin. As mentioned in the previous section, ethylidyne is suspected to be an important precursor of coke and hydrogenolysis. Furthermore, DFT calculations described in the Chapter 1.5 reveal that Sn promotion significantly reduces the dehydrogenation reaction rate of platinum catalysts, as the energy barrier of the dissociative adsorption of propane is increased. On the other hand, the selectivity is increased as the energy barrier for the desorption of propylene drops, making deep dehydrogenation and cracking reactions less likely.<sup>95,99,100</sup> The balance between these two effects results in an optimum ratio of Pt and Sn, which these calculations suggest is Pt<sub>3</sub>Sn.

Based on X-ray Photoelectron Spectroscopy (XPS) observations, Siri et al. reported an increase of the electron density of platinum when tin was incorporated to silica and  $\gamma$ -alumina-supported catalysts.<sup>101</sup> DFT calculations have shown that the addition of Sn also reduces the heat of adsorption of hydrogen on the Pt-Sn (111) surface, which suggests that the diffusion of hydrogen atoms is more facile on the latter than on a Pt (111) surface.<sup>58,102</sup> Figure 1.11 illustrates the important role that the electronic modification of Pt by Sn is believed to play in inhibiting coke formation. The left part of the Figure shows high energy resolution fluorescence detection X-ray absorption near edge structure (HERFD-XANES) intensity contour maps of the Pt L<sub>3</sub>-edge of catalysts comprising alumina-supported Pt (top) and Pt-Sn (bottom). The right part of the Figure shows a graphical interpretation of the XANES spectra, which illustrates the size of the metallic nanoparticles in both catalysts increasing during the regeneration step, an effect that is more severe for Pt/Al<sub>2</sub>O<sub>3</sub>. A shift to higher energies in the XANES spectra during the reduction step reveals that Pt becomes more electronegative, which is attributed to the formation of the Pt-Sn alloy. This phenomenon, which is triggered by the partial reduction of the SnO<sub>2</sub> present on the support, is reversed during the oxidation step.<sup>103</sup> Sn-enrichment of the Pt nanoparticles

may be a problem, as the Pt<sub>3</sub>Sn alloy is believed to be significantly more active for the dehydrogenation reaction than the PtSn alloy.<sup>95,104</sup>

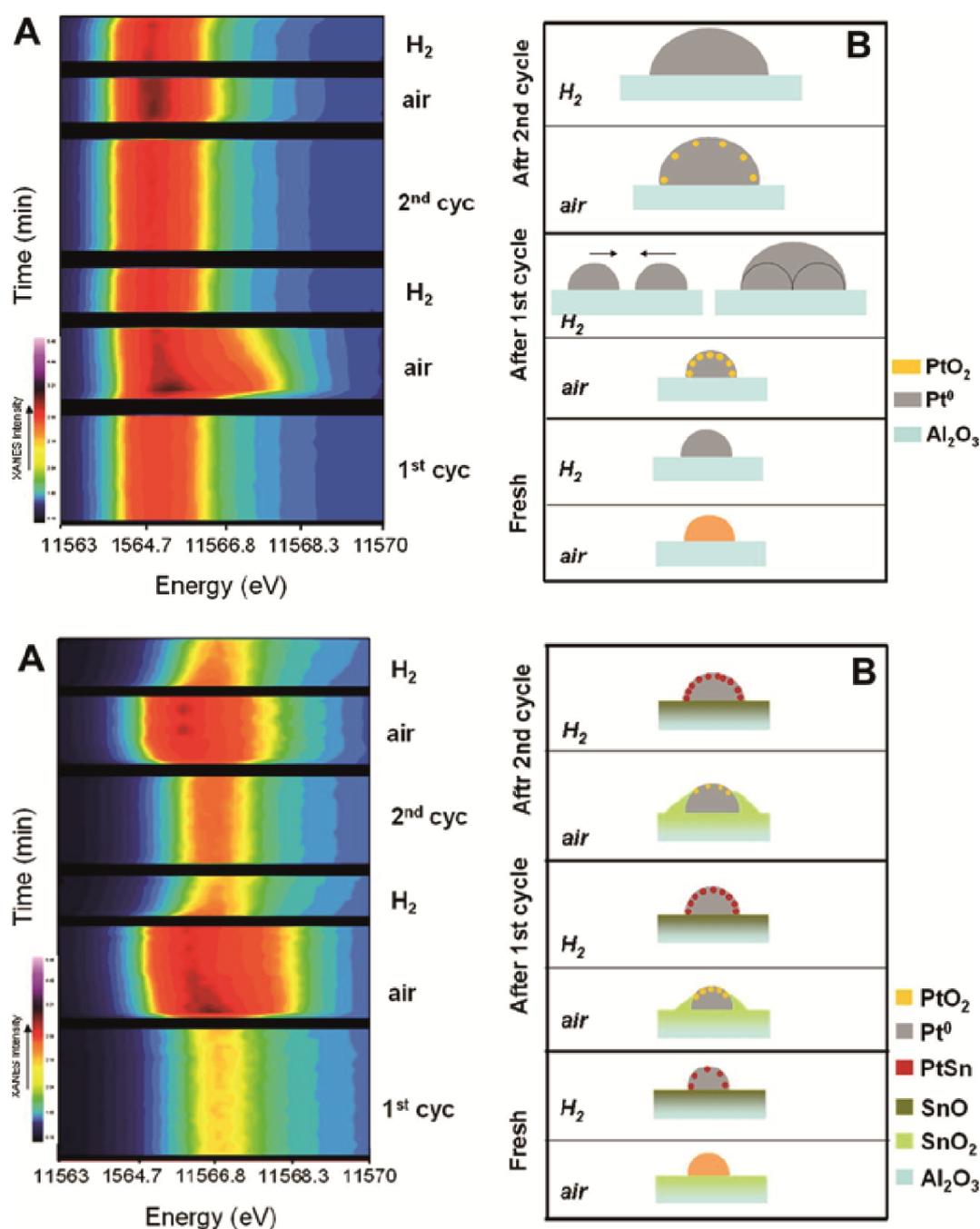


**Figure 1.11.** In the Figures to the left, HERFD-XANES intensity contour maps (Pt-L<sub>3</sub> edge) of Pt/Al<sub>2</sub>O<sub>3</sub> (top) and Pt-Sn/Al<sub>2</sub>O<sub>3</sub> (bottom) catalysts are shown at different stages of a dehydrogenation experiment. The Figures to the right depict the interpretation of Iglesia-Juez et al. for these spectra in terms of changes to the Pt nanoparticles. Reprinted from ref. 103, copyright 2010, with permission from Elsevier.

To summarize the discussion above, Figure 1.12 shows an artist impression of a Pt-Sn nanoparticle on alumina.

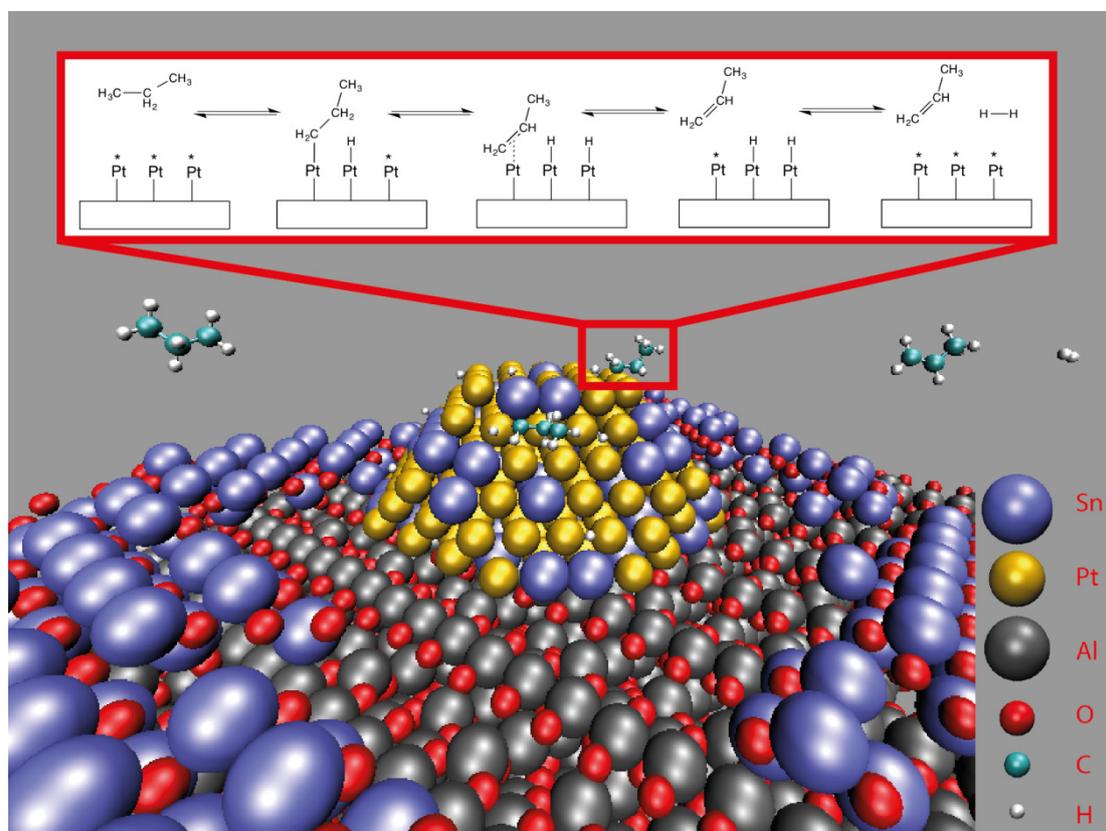


**Figure 1.12.** An artist's impression of a Pt-Sn nanoparticle within a Pt-Sn/Al<sub>2</sub>O<sub>3</sub> catalyst. The surface of the alumina is covered with SnO<sub>2</sub>, which gets reduced when in close proximity to Pt and incorporated into a bimetallic Pt-Sn nanoparticle. Surface Pt atoms catalyze the dehydrogenation reaction according to the mechanism shown in the inset.

Other metals have been studied as promoters of the activity of platinum in the catalytic dehydrogenation of alkanes. Most notably, zinc prevents undesired side reactions, such as coke formation and isomerization, in a similar fashion to tin.<sup>105–110</sup> GaO<sub>x</sub> and InO<sub>x</sub> dopants are used to hinder side reactions by the poisoning of surface Brønsted acid sites, while the formation of Pt-Ga and Pt-In alloys have both a geometric and electronic effect on the Pt nanoparticles, decreasing coke deposition further.<sup>111–114</sup> Another alloy that has been investigated is Pt-Ge, which is believed to function in a way analogous to Pt-Sn, although the electronic effect is believed to be

weaker.<sup>115</sup> Table S1.1 provides an overview of the different CrO<sub>x</sub> catalysts discussed in this section, which are used for the dehydrogenation of light paraffins.

#### 1.4.2 Chromium Oxide-based Catalysts

Chromium oxide-based catalysts have been one of the most actively investigated formulations since Frey and Huppke first reported the dehydrogenation activity of Cr<sub>2</sub>O<sub>3</sub> in 1933.<sup>116</sup> During the 1940's, catalysts comprising chromia supported on alumina were used by UOP to industrially dehydrogenate butane, and has been applied to several processes for the dehydrogenation of light olefins henceforth.<sup>27</sup> Given the industrial relevance of formulations comprising chromium oxide, their structure under different reaction conditions, the nature of the active sites, the role of the support, the effect of alkali metals promoters, and the mechanism of the dehydrogenation reaction over these catalysts have all been intensively studied.

##### 1.4.2.1 *Nature of the active sites*

Since the adsorption of paraffin molecules takes place on Cr-O sites, understanding the exact nature of these species under dehydrogenation reaction conditions is critically important.<sup>117</sup> On freshly prepared catalysts a number of surface species, including Cr<sup>6+</sup>, Cr<sup>5+</sup>, Cr<sup>3+</sup> and Cr<sup>2+</sup>, have been identified. Furthermore, chromates, polychromates, crystalline  $\alpha$ -chromia and amorphous chromia have been identified through a variety of techniques.<sup>118-121</sup> The relative concentration of these species seems to be dependent on a number of factors, such as chromium loading (relative to the surface area of the support), the calcination treatment used during catalyst preparation, and the type of support employed. This is illustrated in Figure 1.13, where chromium species deposited on a mesoporous silica and alumina support are compared by UV-Raman spectroscopy. Different species are observed depending on the Cr loading: at low loadings isolated CrO<sub>4</sub><sup>2-</sup> species predominate, while at higher concentrations Cr-O-Cr species become prevalent due to the formation of Cr<sub>2</sub>O<sub>3</sub> crystallites. These crystallites are more readily formed on the mesoporous silica support than on the alumina, as the interaction between chromium oxide and the mesoporous silica is relatively weak.

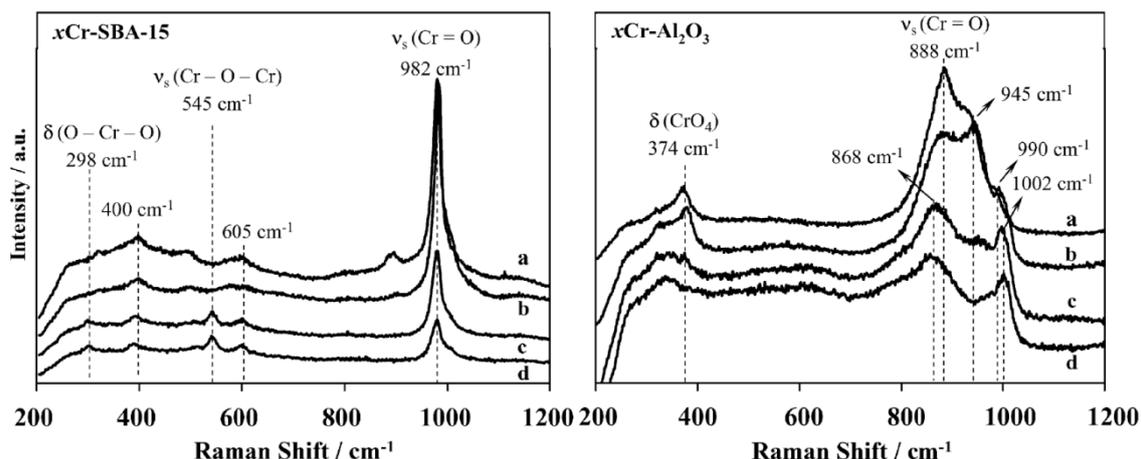


**Figure 1.13.** The graphs represent UV-Raman spectra of  $x$  wt%  $\text{CrO}_x/\text{SBA-15}$  (mesoporous silica) and  $\text{CrO}_x/\text{Al}_2\text{O}_3$  catalysts ( $x$ : a=0.5, b=1, c=5, d=10). Bands corresponding with  $\text{CrO}_4^{2-}$  and Cr-O-Cr species are observed at different loadings and correspond with isolated Cr atoms and crystalline  $\text{Cr}_2\text{O}_3$ . Reprinted from ref. 122, copyright 2009, with permission from Elsevier.

Prior to the 1990's, the study of the structure of chromium oxide-based dehydrogenation catalysts had been restricted to conditions far removed from those found under real operation. For this catalytic system, this represented a great limitation, as the reaction mixtures are believed to reduce chromium oxide species. The development of in-situ spectroscopic techniques made it possible to probe these catalysts under reaction conditions. As is shown in Figure 1.14 with XANES and Figure 1.15 with UV-Vis spectroscopy, it was observed that surface  $\text{Cr}^{3+}$  species are produced at the expense of  $\text{Cr}^{6+}$  species during the initial stages of the dehydrogenation reaction and that polychromate is more easily reduced than monochromate.<sup>122–125</sup> Consequently,  $\text{Cr}^{3+}$ ,  $\text{Cr}^{2+}$ , as well as a mixture of both have been proposed as the active species.<sup>126–129</sup>  $\text{Cr}^{6+}$  or  $\text{Cr}^{5+}$  have not been observed to be active for the dehydrogenation reaction, albeit  $\text{Cr}^{6+}/\text{Cr}^{5+}$  species do appear to be the precursor of the active sites. This has been attributed to the fact that reduction of  $\text{Cr}^{5+}$  species leads to the formation of monomeric  $\text{Cr}^{3+}$  active sites. Indeed, it has been observed that  $\text{Cr}^{5+}$  species, that are not reduced in a hydrogen atmosphere, can be reduced by alkanes.<sup>130–134</sup>

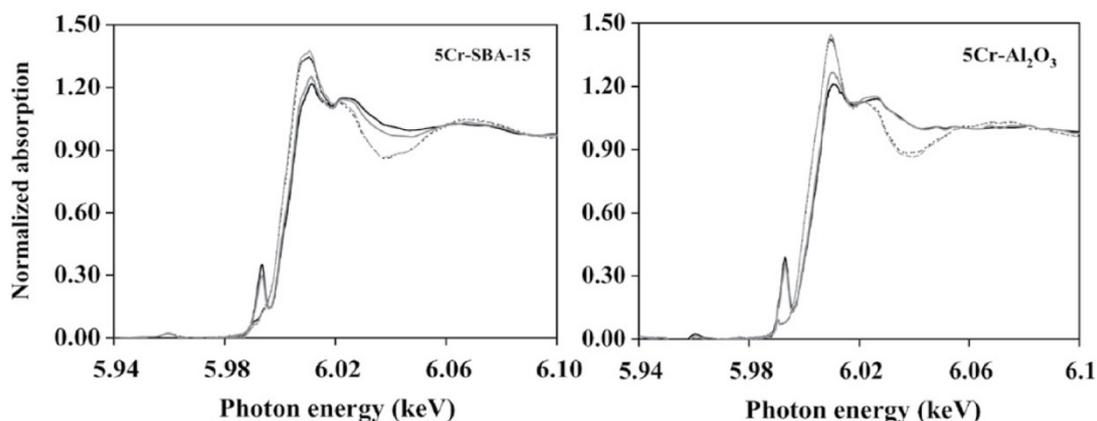


**Figure 1.14.** In-situ XANES spectra of the Cr K-edge of the 5 wt% catalysts after oxidative pre-treatment (black solid line), after 90 s of dehydrogenation (black broken line), after 15 min of PDH (grey broken line) and after regeneration (grey full line). Notably, the  $\text{Cr}^{6+}$  species present on the catalyst are reduced to  $\text{Cr}^{3+}$  species in the first 90 s of the reaction. Reprinted from ref. 122, copyright 2009, with permission from Elsevier.

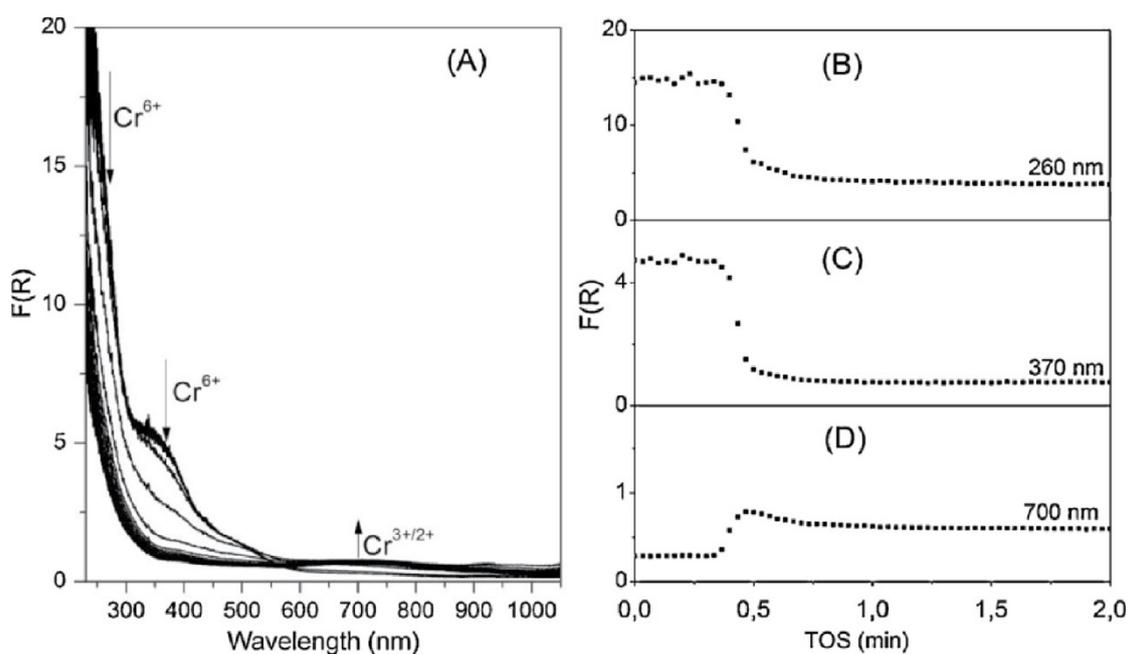


**Figure 1.15.** The graph to the left shows in-situ diffuse reflectance spectra obtained during the dehydrogenation of propane on a  $\text{CrO}_x/\text{SBA-15}$  catalyst. In the bottom right graph, the relative change of bands (B-D), corresponding to  $\text{Cr}^{3+}$  and  $\text{Cr}^{6+}$  is shown. Both graphs illustrate that  $\text{Cr}^{3+}$  (band at 700 nm) is formed at the expense of  $\text{Cr}^{6+}$  (bands at 260 and 370 nm) during PDH. Reprinted from ref. 133, copyright 2011, with permission from Elsevier.

With respect to coordination, it appears that  $\text{Cr}^{3+}$  sites need to be coordinatively unsaturated in order to show catalytic activity.<sup>135</sup> Indeed, a semi-quantitative relationship has been found between the amount of pseudo-octahedral  $\text{Cr}^{3+}$  formed during reduction and the dehydrogenation activity shown by the catalyst.<sup>124,125</sup> Furthermore, it has been observed that isolated  $\text{Cr}^{3+}$  species with two coordinative vacancies are formed on  $\text{CrO}_x/\text{Al}_2\text{O}_3$  catalysts in the presence of an alkane. Thus, it appears that these catalysts contain coordinatively unsaturated  $\text{Cr}^{3+}$  under reaction conditions. Experiments performed with Cr loadings above monolayer coverage, which have been shown to include crystalline chromia clusters, suggest that bulk  $\text{Cr}^{3+}$  ions in a perfect octahedral environment are inactive towards alkane dehydrogenation. Admittedly, these fully coordinated  $\text{Cr}^{3+}$  species are highly stable, whereas coordinatively unsaturated  $\text{Cr}^{3+}$  species would try to attain the stability of bulk  $\text{Cr}^{3+}$  ions by adsorbing alkane molecules from the gas phase.

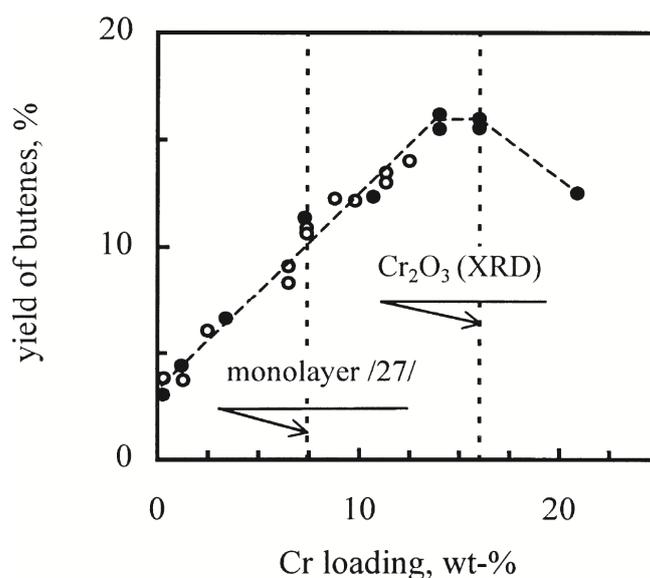


**Figure 1.16.** Yield of butylenes at 540 °C over a chromia-alumina catalyst as a function of Cr loading. Activity increases linearly with concentration, even above monolayer concentration. However, the yield drops once  $\text{Cr}_2\text{O}_3$  crystallites start being detected via XRD. Reprinted from ref. 136, copyright 2000, with permission from Elsevier.

With respect to nuclearity, the need for a highly dispersed active phase is highlighted by the fact that while activity first rises with increasing chromium loading, a drop in activity is observed when the loading is such that crystalline  $\text{Cr}_2\text{O}_3$  starts forming, as

illustrated in Figure 1.16.<sup>136–138</sup> The fact that activity and Cr loading hold an almost linear relationship below monolayer coverage suggests that both isolated and clustered  $\text{Cr}^{3+}$  centers are catalytically active. Actually, three different types of  $\text{Cr}^{3+}$  ions have been detected by spectroscopic techniques at these loadings: 1)  $\text{Cr}^{3+}$  species formed by reduction of surface  $\text{Cr}^{6+}/\text{Cr}^{5+}$  ions; 2) isolated centers of  $\text{Cr}^{3+}$  ions stabilized by the alumina surface; and 3) small amorphous (and thus XRD invisible)  $\text{Cr}^{3+}$  clusters.<sup>31,32</sup> Determining the individual contributions of these species to catalytic performance has proven to be extremely challenging. Some studies correlating dehydrogenation activity with Cr-speciation suggested that a vast majority of catalytic activity can be ascribed to the dispersed  $\text{Cr}^{3+}$  phase, the role of the other phases being the replenishment of the depleted  $\text{Cr}^{3+}$  surface phase during long runs.<sup>124,125,139</sup> More detailed studies involving the calculation of turn-over frequencies (TOF) have led some workers to propose that multinuclear  $\text{Cr}^{3+}$  sites are more active than isolated  $\text{Cr}^{3+}$  ions, a proposition which finds both support and dissent in literature.<sup>120,132,136,140–142</sup> Kumar et al. observed that when  $\gamma$ -alumina was employed as the catalyst support, oligomeric chromium oxide species would display the highest activity and selectivity. However, when mesoporous silica was used as the carrier, isolated chromia species with a coordination number larger than 4 showed the highest activity.<sup>122</sup> It is clear that the optimal nuclearity of active  $\text{Cr}^{3+}$  sites remains a topic still under debate.

Albeit selectivity has been found to be insensitive to chromium loading, it does alter as a function of time-on-stream.<sup>143</sup> At first, the selectivity towards alkenes is fairly low and the catalyst produces mainly carbon oxides. This is attributed to the fact that during this induction period, highly oxidized and thus catalytically inactive, chromium species are being reduced to active chromium species with lower oxidation states.

To summarize, in recent years dehydrogenation activity has been mostly assigned to  $\text{Cr}^{3+}$  species that are both dispersed and coordinately unsaturated. Thus, it seems that active sites need to fulfill oxidation state, coordination and nuclearity requirements. In fact, these and other factors, such as the origin of  $\text{Cr}^{3+}$  species, have been used by some workers to classify the catalytically active sites.<sup>144–146</sup>

It should also be mentioned that many other factors could also influence the activity of Cr-based dehydrogenation catalysts. For example, the addition of  $\text{CO}_2$  as a weak oxidant is known to improve the activity of the chromium dehydrogenation catalyst by removing the evolved hydrogen through the reverse water gas shift reaction, which

effectively shifts the equilibrium towards product formation.<sup>147-149</sup> At the same time, CO<sub>2</sub> is ineffective at oxidizing the Cr<sup>3+</sup> species, the active in dehydrogenation, to catalytically inactive Cr<sup>6+</sup> species.<sup>133,150,151</sup>

In order to obtain high activity the operating conditions need to be considered as well, since activity is directly proportional to both the reaction temperature and the partial pressure of the alkane. Propane conversion and propylene selectivity are inversely proportional and directly proportional to space velocity, respectively. In studies performed on CrO<sub>x</sub>/Al<sub>2</sub>O<sub>3</sub> catalysts used in the non-oxidative dehydrogenation of ethane it was found that decreasing the gas hourly space velocity (GHSV) from 3600 h<sup>-1</sup> to 600 h<sup>-1</sup>, resulted in an increase in ethane conversion from 27.6 to 31.4 %, while selectivity to ethylene decreased from 91.7 to 64.9 %.<sup>152</sup> This effect has been attributed to the fact that lower gas hourly space velocities favor ethane activation as well as methane and coke formation. In conclusion, it is possible to achieve high activity and selectivity over Cr-based hydrogenation catalysts by adjusting the composition of the catalysts and/or the operating conditions.

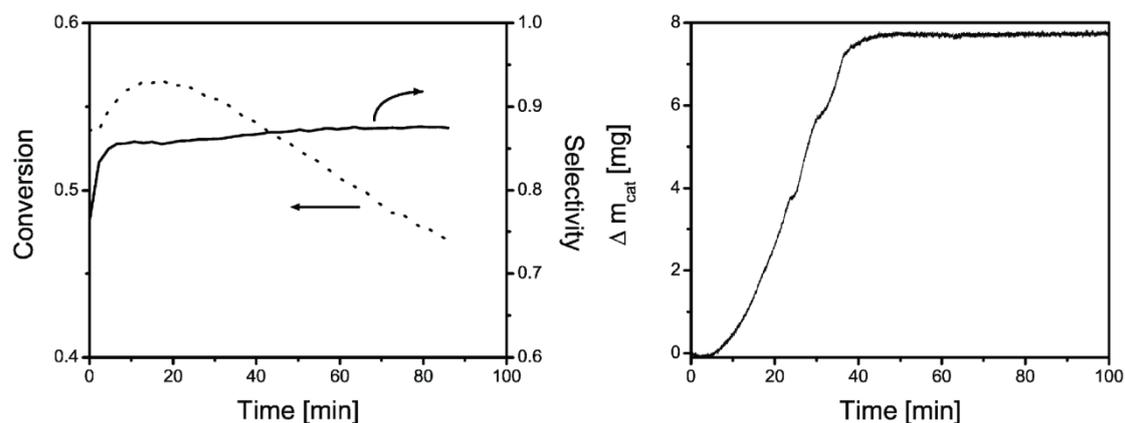


**Figure 1.17.** To the left, the conversion and selectivity for the dehydrogenation of propane on a 13 wt% CrO<sub>x</sub>/Al<sub>2</sub>O<sub>3</sub> catalyst over a 85 min period is shown. The conversion drops over time, while the selectivity remains stable after increasing during the initial stages of the reaction. To the right, the mass uptake of the catalyst as measured by a tapered element oscillating microbalance (TEOM) is shown as a function of time-on-stream. Over the first 40 min, the catalyst mass increases due to coke deposition, after which it remains stable. Reproduced from ref. 153, with permission from the PCCP Owner Societies.

#### 1.4.2.2 Catalyst deactivation

Over the course of a catalytic cycle,  $\text{CrO}_x$  dehydrogenation catalysts lose their activity due to the deposition of coke and as is the case with Pt-based catalysts, they need to be periodically regenerated. Experiments with a tapered element oscillating microbalance (TEOM), shown in Figure 1.17, revealed that the weight uptake of the catalyst takes place during the initial stages (10-40 min) of the reaction, after which no additional carbon is deposited. After this point, the conversion still drops, which is an indication that the carbon that is deposited becomes more detrimental to catalytic activity over time. Although the catalysts recover most of their activity after each reaction-regeneration cycle, the loss of activity is not entirely reversible. Indeed, the heat released through the combustion of coke during regeneration leads to the incorporation of chromia into the alumina framework, which causes the amount of catalytically active Cr species to decrease with each regeneration step.<sup>31</sup> This phenomenon has been measured by UV-Vis spectroscopy, as shown in Figure 1.18. In the Figure, a  $\text{CrO}_x/\text{Al}_2\text{O}_3$  catalyst is treated at 1200 °C for 12 h, which results in the bands corresponding to  $\text{Cr}^{3+}$  species to shift, signaling the incorporation of  $\text{Cr}^{3+}$  species into the alumina support. Consequently, the dehydrogenation activity shown by the catalyst drops, as an almost linear relationship has been found between activity and the amount of  $\text{Cr}^{6+}$  species on the catalyst surface (as measured after the regeneration step).<sup>133,139,153</sup>

Two processes are believed to lead to the dissolution of  $\text{Cr}^{3+}$  into the  $\text{Al}_2\text{O}_3$  carrier and result in catalytically inactive  $\text{Cr}^{3+}$  species. First, the sintering of the alumina may cause entrapment of the Cr species inside the bulk of the support. As an additional effect, the loss of alumina surface area reduces the ability of the support to stabilize  $\text{Cr}^{6+}$  species formed during the regeneration step.<sup>126,154</sup> For the second process,  $\text{Cr}^{3+}$  ions migrate into the support. Indeed, it is believed that the similar ionic radii and charge of  $\text{Al}^{3+}$  and  $\text{Cr}^{3+}$  facilitate the diffusion and subsequent incorporation of  $\text{Cr}^{3+}$  into the octahedral sites of alumina, which produces a type of chromia-alumina spinel that is inactive for the dehydrogenation reaction.<sup>118,155</sup> Of note is the fact that in the presence of  $\gamma$ -alumina, entrapment is believed to be the dominant process, while in its absence migration is favored.<sup>118,155</sup>

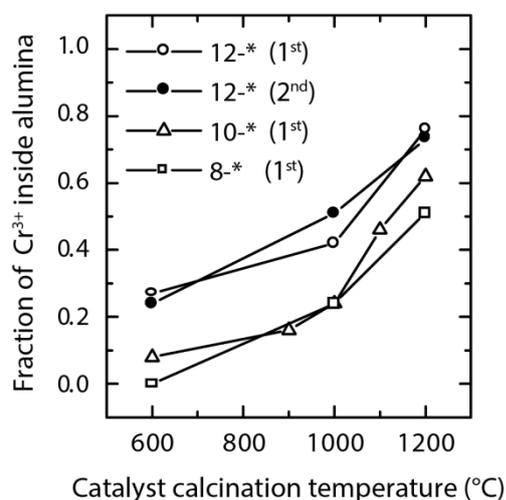
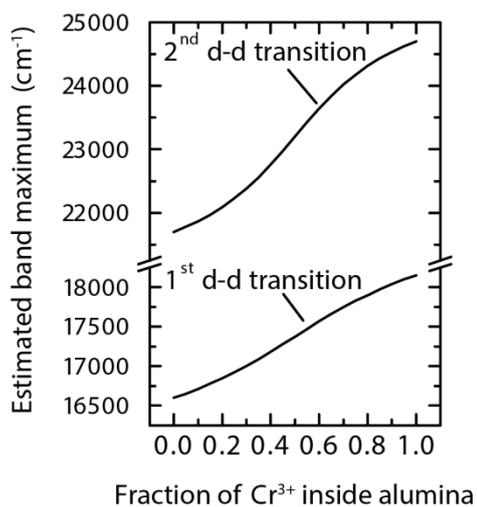
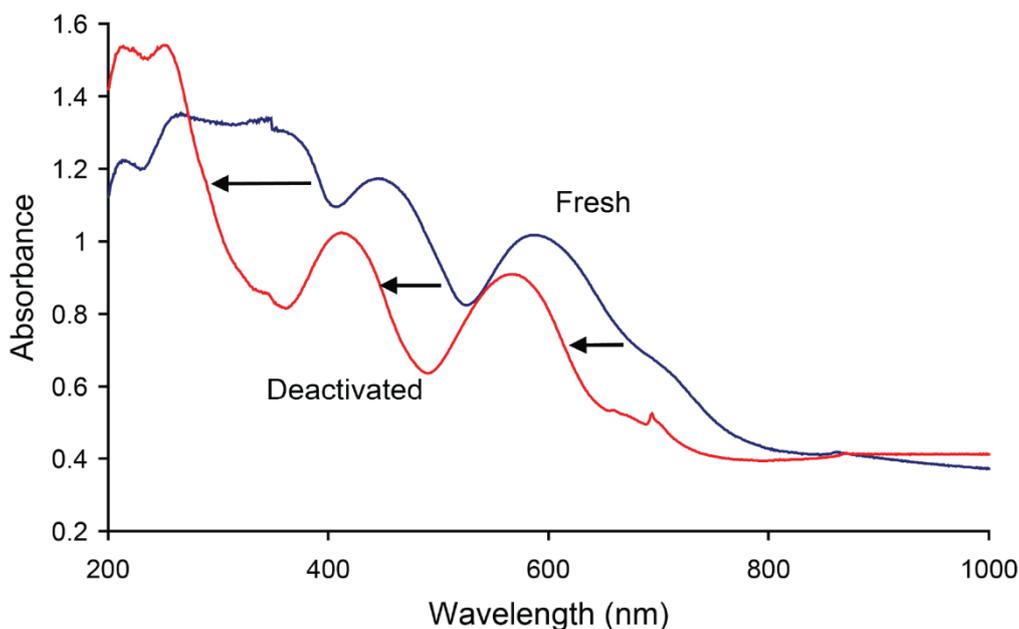


**Figure 1.18.** The top graph shows the ex-situ diffuse reflectance UV-Vis spectra of both fresh and deactivated  $\text{CrO}_x/\text{Al}_2\text{O}_3$ . The bottom left graph shows the extent of the shift for the bands at 600 and 450 nm, which correspond with the 1<sup>st</sup> and 2<sup>nd</sup> d-d transition, respectively. The bottom right graph shows that the fraction of  $\text{Cr}^{3+}$  incorporated into the alumina framework is strongly dependent on the calcination temperature. Reprinted from ref. 32 (top graph), copyright 2004, and ref 145 (bottom two graphs), copyright 2002, both with permission from Elsevier.

At elevated temperatures  $\gamma$ -alumina undergoes a thermodynamically driven transformation to  $\theta$ - or even  $\alpha$ -alumina, which have considerably lower surface areas. It is unknown whether the presence of chromia facilitates or hinders the sintering of

the alumina support, as some authors have found the presence of chromia to enhance sintering, while other research groups have observed the opposite.<sup>145,156–158</sup> The transformation of  $\gamma$ -alumina to  $\alpha$ -alumina can be restrained by doping the support with silica, zirconia, magnesia or lanthana. For example, Wachowski et al. observed that when a small amount of  $\text{La}_2\text{O}_3$  is added to  $\text{Al}_2\text{O}_3$ , the transition of  $\theta$ -alumina to  $\alpha$ -alumina occurs at a 136 °C higher relative to when no lanthana is added.<sup>159,160</sup> The authors found that the use of cations having larger ionic radius than  $\text{Al}^{3+}$ , which tend not to dissolve in  $\text{Al}_2\text{O}_3$ , in combination with a preparation method capable of affording high dopant dispersion, is most effective in preventing the formation of  $\alpha$ -alumina.

It is important to note that the advantages offered by the combustion of coke during the regeneration step far outweigh these unwanted side effects. First and foremost, the heat released in this step is harnessed to fuel the dehydrogenation reaction, making coke deposition not completely undesirable. Furthermore, oxidation of  $\text{Cr}^{3+}$  to  $\text{Cr}^{6+}$  during regeneration also accomplishes the re-dispersion of chromia crystallites. The latter is particularly important, given that the sintering of chromia under dehydrogenation conditions has also been reported to be a contributing factor to the reversible deactivation of chromium-based catalysts.<sup>144,145</sup>

Another interesting example of a deactivation phenomenon caused by a change in surface composition connected to the nature of the support has been observed on catalyst comprising mesoporous silica. Indeed, by analyzing this material via XPS before and after 6 h of time-on-stream, an important amount of  $\text{Cr}^{3+}$  species was found to be reduced to  $\text{Cr}^{2+}$  by the hydrogen evolved during the anoxic dehydrogenation reaction. In turn, the resulting  $\text{Cr}^{2+}$  species were found to be inactive in dehydrogenation.

#### 1.4.2.3 *Role of the support*

The nature of the support is important not only because it governs the mechanical properties of the catalyst, but also because the interaction of the carrier with the active phase can have a profound impact on catalyst activity and selectivity. Alumina is by far the most commonly used support and a variety of methods to produce chromia-alumina catalysts have been investigated. These include the incipient wetness impregnation of alumina with  $\text{CrO}_3$  or  $\text{Cr}(\text{NO}_3)_3$  solutions (if an alkali ion is added, an

aqueous solution of its chromate salt is used), the co-precipitation of  $\text{Al}(\text{OH})_3$  and  $\text{Cr}(\text{OH})_3$  from  $\text{Al}^{3+}$  and  $\text{Cr}^{3+}$  solutions, a type of chemical vapor deposition (CVD) involving volatile chromium compounds being deposited on alumina called “atomic layer deposition”, and the decomposition of complexes including both alumina and chromium. All these methods are followed by a calcination step at approximately 600 °C. Increasing the calcination temperature above 600 °C causes a loss of dehydrogenation activity, probably due to the incorporation of Cr into the  $\text{Al}_2\text{O}_3$  framework, as discussed in the preceding section.<sup>154</sup> Interestingly, increasing the pretreatment temperature of the alumina support has a positive effect on the TOF shown by the resulting catalyst, which has been attributed to an increase in the number of multinuclear  $\text{Cr}^{3+}$  sites.<sup>145</sup> In addition, this pretreatment will result in a more stable  $\text{Al}_2\text{O}_3$  polymorph, which is less likely to sinter. However, the use of alumina as support is not free of drawbacks. For instance,  $\text{Al}_2\text{O}_3$  can catalyze cracking and coking due to its surface acidity, which leads to a drop in both activity and selectivity. A solution for this is the doping of alumina-based dehydrogenation catalysts with alkali ions, which can effectively poison these undesirable acid sites.

The use of zirconia as an alternative support has also been investigated. Indeed, the low surface acidity of this oxide and the fact that chromia imparts an enhanced sintering resistance to  $\text{ZrO}_2$  make the latter a viable substitute for alumina.<sup>131,132</sup> De Rossi et al. have reported that catalysts with zirconia as the support are more active in the dehydrogenation of propane and isobutane than the corresponding catalysts supported on silica or alumina.<sup>140,141,153,161</sup> This has been attributed to an increase in the amount of surface  $\text{Cr}^{5+}$  that is produced during the regeneration of  $\text{Cr}_2\text{O}_3/\text{ZrO}_2$ . The latter improves activity since  $\text{Cr}^{5+}$  forms catalytically active mononuclear  $\text{Cr}^{3+}$  under reaction conditions, as has been mentioned previously. In turn, the high amount of  $\text{Cr}^{5+}$  on this catalyst has been assigned to the strong interaction between chromia and the basic support.<sup>143</sup> The choice of zirconia over alumina as the catalyst support offers the additional advantage of preventing the formation of Cr-Al mixed oxides. Nevertheless,  $\text{Cr}_2\text{O}_3/\text{ZrO}_2$  has been observed to deactivate faster than other less active catalysts including  $\text{Cr}_2\text{O}_3/\text{Al}_2\text{O}_3$ . This has been partially accredited to the higher coking rate displayed by  $\text{Cr}_2\text{O}_3/\text{ZrO}_2$ . Additionally, XPS studies suggest that chromia-zirconia catalysts also favor the formation of chromium carbides, which are inactive for dehydrogenation and consequently cause catalyst deactivation.<sup>143</sup>

De Rossi and co-workers have also concluded that albeit  $\text{CrO}_x/\text{ZrO}_2$  catalysts can outperform their alumina- and silica-supported counterparts, zirconia-supported formulations could be further improved by increasing the surface area and the thermal stability of  $\text{CrO}_x/\text{ZrO}_2$ . This has inspired other workers to produce chromium-based dehydrogenation catalysts with high surface areas and highly dispersed active sites. For example, Fajdala and Tilley have reported the use of a co-thermolysis method involving several thermolytic molecular precursors to produce a  $\text{CrO}_x/\text{SiO}_2/\text{ZrO}_2$  catalyst capable of showing propane conversions greater than 35 % and propylene selectivity exceeding 90 % at 450 °C.<sup>162</sup> According to the authors, the aforementioned values are among the best reported in the literature, particularly at such a low temperature. Korhonen et al. attempted to combine the high surface area of alumina with the basic nature of zirconia by covering an alumina support with a zirconia layer.<sup>163</sup> However, the resulting  $\text{CrO}_x/\text{ZrO}_2\text{-Al}_2\text{O}_3$  catalyst displayed inferior activity compared to the benchmark  $\text{CrO}_x/\text{ZrO}_2$  catalyst.

The use of silica as the support in chromia-based dehydrogenation catalysts requires a relative high surface area to stabilize  $\text{Cr}^{6+}$  sites.<sup>164</sup> For similar reasons, titania does not constitute a good support, as  $\text{CrO}_x$  easily sinters due to its weak interaction with  $\text{TiO}_2$ . However, an active and stable propane dehydrogenation catalyst has been obtained by preparing a titania mesoporous material with Cr dopants.<sup>150</sup>

Temperature programmed reduction (TPR) results suggest that there is a direct relationship between catalytic activity and the reducibility of the catalysts (see Figure 1.19).<sup>152</sup> Indeed, studies on the non-oxidative dehydrogenation of ethane have revealed that catalytic activity follows the order  $\text{CrO}_x/\gamma\text{-Al}_2\text{O}_3 > \text{CrO}_x/\text{SiO}_2 > \text{CrO}_x/\text{MCM41} \gg \text{CrO}_x/\text{MgO} \approx \text{CrO}_x/\text{Silicalite-2}$  (based on ethane conversion and ethylene yields), a reverse order being found for the reduction temperature of the chromium species on the aforementioned catalyst supports.

Cr-Mg-Al and Cr-Mg mixed oxides prepared using layered double hydroxide (LDH) precursors have been studied as catalysts for the non-oxidative dehydrogenation of ethane.<sup>165</sup> Some of these catalysts were found to achieve ethane conversions of 27-30 % and a selectivity towards ethylene of 71-75 %. The method used for introducing Cr into the LDH precursors was found to determine several properties of the resulting mixed oxides, such as surface area, catalytic performance, coking resistance and thermal stability against sintering.

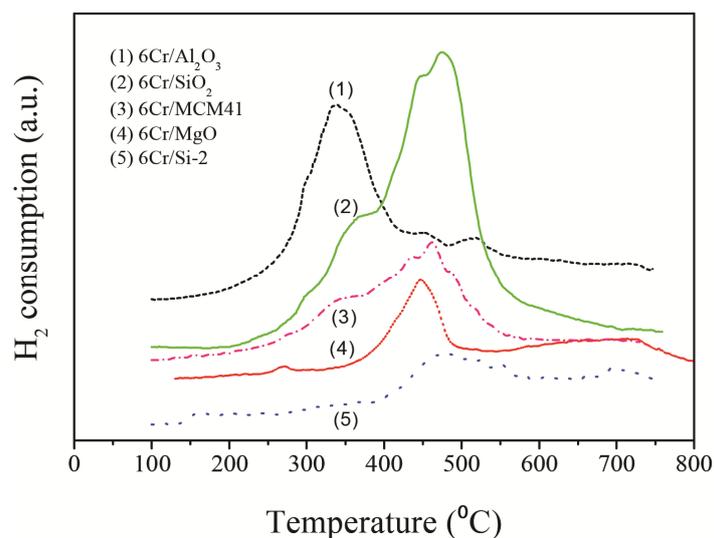


**Figure 1.19.** TPR profiles of 6 wt%  $\text{CrO}_x$  on different supports. The catalysts with a strong reduction peak at low temperatures show the highest catalytic activity. The figure is reproduced from ref. 152 with kind permission from Springer Science and Business Media.

Finally, the study of porous chromia-pillared  $\alpha$ -zirconium phosphate materials has been particularly informative with regards to the influence that acidity has on catalytic behavior. In the non-oxidative dehydrogenation of propane, catalysts based on these materials display an initial conversion of 18.1% with a selectivity towards propylene of 87.1 % at 550 °C.<sup>135</sup> Interestingly, it has been observed that while the selectivity towards cracking products of this material decreases with time-on-stream, its selectivity towards the alkene tends to remain constant. The latter has been explained by assigning the occurrence of cracking and dehydrogenation reactions to strong and medium strength acid sites, respectively. The authors argue that strong acid sites are rapidly deactivated, inhibiting cracking reactions and favoring the production of the alkene.

#### 1.4.2.4 Role of the promoters

Alkali metals, such as K, Rb and Cs, are known to promote both the activity and the selectivity of chromium-based dehydrogenation catalysts. This phenomenon has been attributed to the ability of large alkali cations to stabilize the structure of the support, to reduce surface acidity and/or to increase the number of active chromium sites.<sup>126</sup> Additionally, the presence of alkali metal promoters increases the dispersion of the

active phase by assisting the formation of  $\text{Cr}^{6+}$  complexes under oxidizing conditions that subsequently give rise to  $\text{Cr}^{3+}$  under a reducing atmosphere. A notable exception to this promotion effect has been found in the doping with  $\text{K}^+$  of several PDH catalysts, such as chromia-pillared  $\alpha$ -zirconium phosphate, gallium-chromium mixed oxides pillared  $\alpha$ -zirconium phosphate and chromia/zirconia.<sup>135,166</sup> For these materials, doping with  $\text{K}^+$  results in a dramatic decrease in catalytic activity. According to some authors, the latter indicates that oxygen ions play an active role in

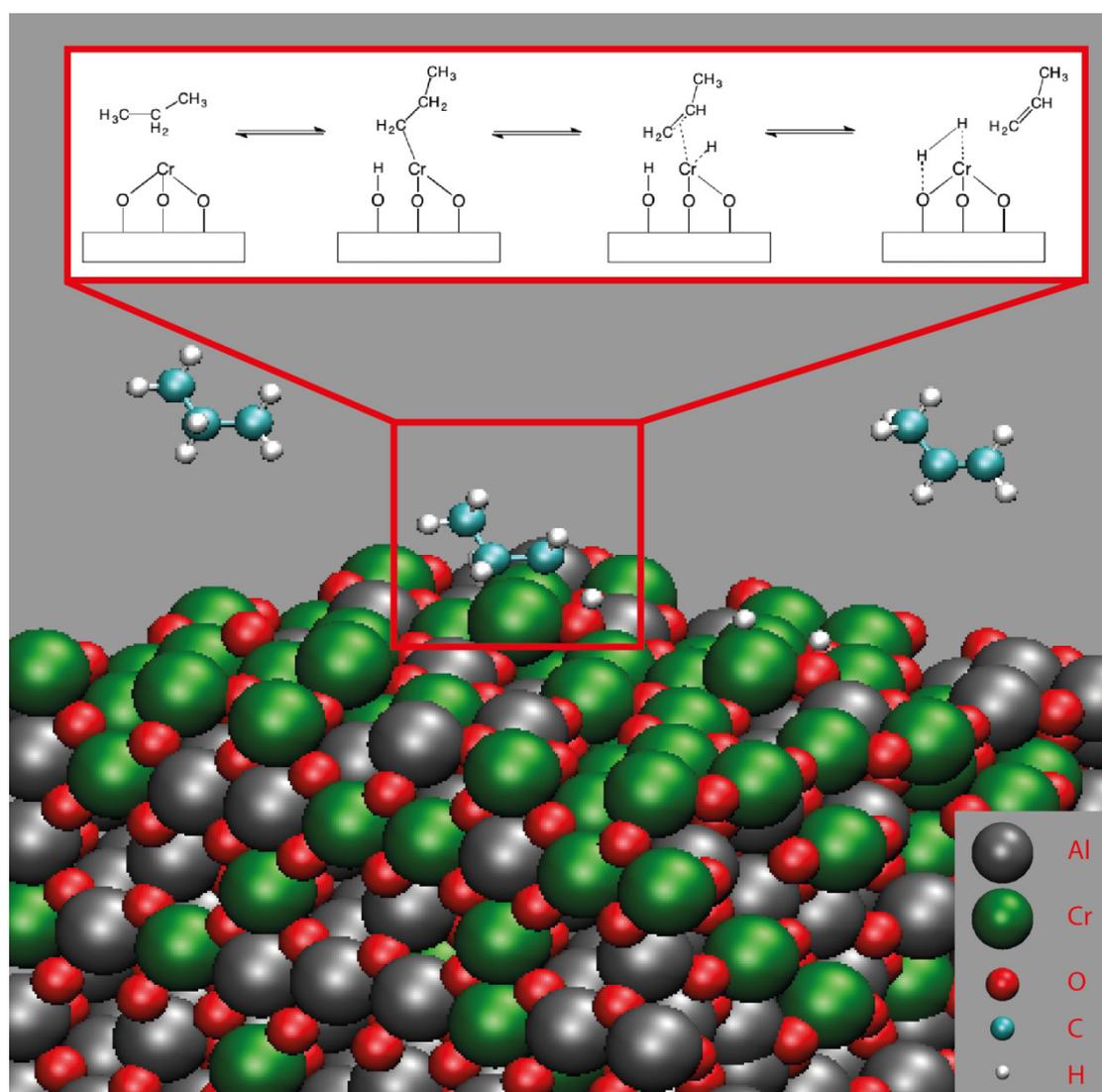


**Figure 1.20.** An artist's impression of the surface of a  $\text{CrO}_x/\text{Al}_2\text{O}_3$  catalyst in which coordinately unsaturated  $\text{Cr}^{3+}$  species catalyze the dehydrogenation reaction. Note that partially reduced  $\text{CrO}_x$  species are formed on the surface of the catalyst, and that the Cr is partially dissolved in the alumina support. The (simplified) reaction mechanism is shown in the inset.

the dissociative adsorption of propane and/or in the desorption of hydrogen. Indeed, these workers contend that in these catalysts, potassium bonds to oxygen anions, which causes some properties, such as Lewis acidity and coordinative unsaturation, of the latter to be altered in a way that hinders catalysis.<sup>153,161</sup> A similar argument has been used to explain the drop in activity observed when doping chromia/zirconia catalysts with sodium, although this effect has not been observed for alumina-based formulations.

To summarize the above discussions, an artist's impression of a  $\text{CrO}_x/\text{Al}_2\text{O}_3$  catalyst is shown in Figure 1.20, while Table S1.2 offers an overview of the different  $\text{CrO}_x$  catalysts discussed in the previous section.

### 1.5.3. Gallium Oxide-based Catalysts

The dehydrogenation activity of gallium oxide supported on ZSM-5, which was first reported in the late 1980's for the conversion of propane to aromatics<sup>167-170</sup>, has been the target of renewed attention in recent years. In the interim, both bulk and supported  $\text{Ga}_2\text{O}_3$  have been used as dehydrogenation catalysts. Nevertheless, this compound has been studied in much less depth than the other two catalysts and is therefore not as well understood.

The exact nature of the active sites in Ga-based dehydrogenation catalysts is still under debate. Akin to  $\text{Al}_2\text{O}_3$ ,  $\text{Ga}_2\text{O}_3$  has different polymorphs of which  $\beta\text{-Ga}_2\text{O}_3$  is not only the most stable, but also the most active Ga species in PDH according to some authors.<sup>171</sup>  $\beta\text{-Ga}_2\text{O}_3$  has a monoclinic structure, in which gallium atoms are equally distributed between tetrahedral and octahedral configurations. This crystal structure has a high concentration of weak Lewis acid sites (coordinatively unsaturated tetrahedral species on the surface of the material), which are deemed to be centers of dehydrogenation activity.<sup>172</sup> Indeed, a heterolytic dissociation reaction mechanism has been proposed where  $\text{H}^-$  adsorbs on a  $\text{Ga}^+$  Lewis acid site and  $\text{C}_3\text{H}_7^+$  on a neighboring oxygen, although these species can adsorb reversely as well.<sup>173,174</sup> The assignment of Lewis acid sites as the active species was substantiated by Chen et al.,<sup>175</sup> who by relating the results of  $\text{NH}_3$ -TPD measurements with activity data for different  $\text{Ga}_x\text{Al}_{10-x}\text{O}_{15}$  mixed oxides, showed that a high concentration of Lewis acid groups in the form of coordinatively unsaturated tetrahedral  $\text{Ga}^{3+}$  cations is a prerequisite for dehydrogenation activity (see Figure 1.21). Xu et al. reported dehydrogenation

activity on both Lewis and Brønsted acid sites on Ga<sub>2</sub>O<sub>3</sub>/H-ZSM-5. In fact, these workers observed a dual effect of the strong acidity, which on the one hand facilitated dehydrogenation, while on the other hand accelerated coke formation. A zeolitic support displaying a low concentration of medium and strong acid sites and a relatively high concentration of weak acid sites was found to lead to the most active and stable catalyst.<sup>176,177</sup> In addition, Michorczyk et al. concluded that acidic groups catalyze the reaction after observing that promotion with a base, such as potassium, resulted in a decrease in activity.<sup>178</sup>

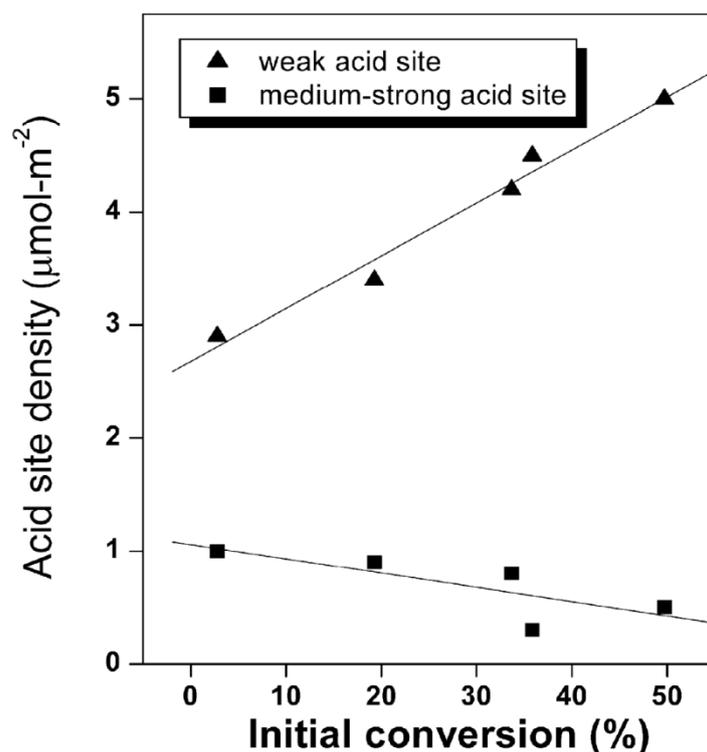


**Figure 1.21.** Concentration of Lewis acid sites versus propane conversion measured 15 min after the start of the PDH reaction on Ga<sub>x</sub>Al<sub>10-x</sub>O<sub>15</sub>. A clear correlation between the conversion and the surface density of weak Lewis acid sites is observed. For these experiments, CO<sub>2</sub> is used to improve conversion. Reprinted from ref. 175, copyright 2008, with permission from Elsevier.

Several authors have performed DFT calculations in an effort to understand the dehydrogenation reaction mechanism on Ga<sub>2</sub>O<sub>3</sub>. Studies by Liu et al. regarding propane dehydrogenation on a perfect Ga<sub>2</sub>O<sub>3</sub> (100) surface revealed that the C-H bond is activated by a surface oxygen that abstracts a hydrogen from the propane molecule,

thus forming a propyl species, which coordinates with a Ga surface site and a hydroxyl group. A second hydroxyl group is formed via  $\beta$ -hydrogen elimination, but for these hydroxyl groups to recombine, either as  $\text{H}_2\text{O}$  or  $\text{H}_2$ , a high energy barrier needs to be overcome. This barrier is much lower over a gallium hydride-hydroxide species, although the formation of the gallium hydride also involves a high energy barrier. Nevertheless, theoretical calculations by Pidko et al. indicate that these relatively stable  $[\text{H-Ga-OH}]^+$  sites are preferentially regenerated by water desorption resulting in a reduced active site.<sup>179</sup> Murata and co-workers have observed an increase in activity after a pre-reduction step with hydrogen at 550 °C, while a simultaneous increase of  $\text{Ga}^{\delta+}\text{H}$  and  $\text{Ga-OH}$  sites was observed via  $\text{NH}_3$  TPD. These authors proposed that these sites also form during reaction and may be responsible for the dehydrogenation activity of the silica supported  $\text{Ga}_2\text{O}_3$  catalyst.<sup>180,181</sup>

Contradictory information has been reported regarding the reducibility of  $\text{Ga}_2\text{O}_3$ . Rodriguez et al. reported that  $\text{Ga}_2\text{O}_3/\text{Al}_2\text{O}_3$  is not reduced by hydrogen at 700 °C, but the presence of Pd on the catalyst can assist in the reduction of  $\text{Ga}^{3+}$  to  $\text{Ga}^+$  and  $\text{Ga}^0$  at temperatures between 300 and 550 °C and form an alloy (in which  $\text{Ga}^0$  is immobilized). Indeed, it has been reported that the reduction of  $\text{Ga}_2\text{O}_3$  can be promoted by the proximity of other, more easily reduced metals, such as Pt and Pd.<sup>113,114,181,182</sup> For instance, on a Pt-Ga/H-beta catalyst, reduced gallium hydrides were observed after hydrogen reduction at 550 °C.<sup>183</sup> It has also been proposed that the reducibility of these species depends on the interaction of gallium oxide with the catalyst support, which is also the case with  $\text{CrO}_x$  (vide supra), where a weak metal-support interaction resulting in an increased reducibility. Indeed, Meitzner et al. showed that  $\text{Ga}_2\text{O}_3/\text{H-ZSM-5}$  could be reduced by hydrogen or hydrocarbons at dehydrogenation reaction conditions. Finally, regarding the reduction of  $\text{Ga}_2\text{O}_3$ , it is important to note that  $\text{Ga}_2\text{O}$  is gaseous and metallic gallium is liquid under dehydrogenation reaction conditions.<sup>184</sup>

A number of studies has shown that the addition of  $\text{CO}_2$  to the reactant feed improves the olefin yield.<sup>185–188</sup> Nakagawa et al. found that the addition of steam and  $\text{CO}_2$  decreased coke deposition on a  $\text{Ga}_2\text{O}_3/\text{TiO}_2$  catalyst by the Boudouart reaction, while also assisting ethylene desorption.<sup>185,186</sup> However, other authors claimed that the increase in activity was caused by the reverse water-gas shift reaction (RWGS).<sup>187,188</sup>

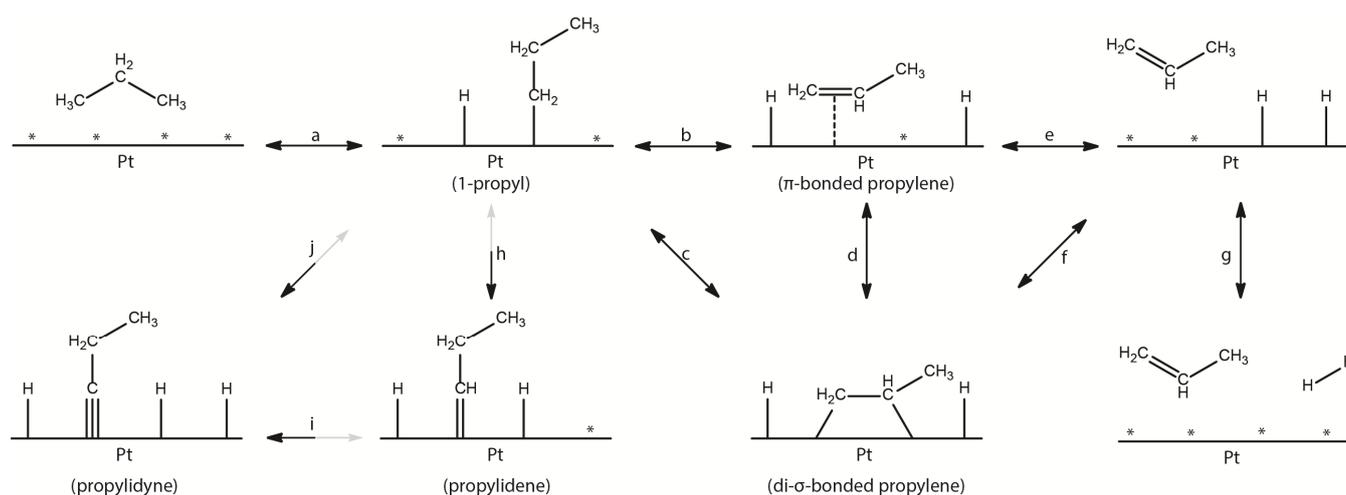
Additionally, Michorczyk et al. noted that this effect could only be seen at relative low levels of coke deposition.<sup>178</sup> It was suggested that CO<sub>2</sub> could also poison the basic sites required for the dissociative adsorption of the alkane.

Different carriers have been used in gallium oxide-based dehydrogenation catalysts, the inclusion of acid and basic sites on the support being important to achieve a high conversion. Xu et al. reported that in the absence of an oxidizing agent, the conversion obtained using Ga<sub>2</sub>O<sub>3</sub> supported on ZrO<sub>2</sub>, Al<sub>2</sub>O<sub>3</sub> and TiO<sub>2</sub> was high, medium and low, respectively, while SiO<sub>2</sub>- and MgO-supported Ga<sub>2</sub>O<sub>3</sub> were inactive in dehydrogenation.<sup>176</sup> The authors proposed activity to be dependent on the presence of acid sites of medium strength on the catalyst surface. However, a different trend was observed when CO<sub>2</sub> was present as an oxidizing agent, as conversion was observed to be high on Ga<sub>2</sub>O<sub>3</sub>/TiO<sub>2</sub> and low on Ga<sub>2</sub>O<sub>3</sub>/ZrO<sub>2</sub> and Ga<sub>2</sub>O<sub>3</sub>/Al<sub>2</sub>O<sub>3</sub>. This was attributed to the two contrary roles of CO<sub>2</sub>, which on the one hand removes H<sub>2</sub> from the surface of the catalyst by the reverse water-gas shift reaction, while on the other hand absorbs strongly on the basic sites of the support. Thus, the low conversion observed when zirconia or alumina were employed as the support can be ascribed to the relatively high amount of basic sites on these oxides. Notably, the structure of the support is also important, as a mesoporous Ga-Al mixed oxide exhibited an increased resistance to catalyst coking.<sup>189</sup>

Work on the promotion of GaO<sub>x</sub>-based dehydrogenation catalysts appears to be limited, although a patent by Iezzi et al. claims that a catalyst comprising 1.2 wt% Ga<sub>2</sub>O<sub>3</sub>, < 99 ppm of Pt and 1.6 wt% of SiO<sub>2</sub> on an Al<sub>2</sub>O<sub>3</sub> support represents a highly active formulation in the dehydrogenation reaction.<sup>190</sup> Indeed, when this catalyst is used for PDH, a conversion of 39% and a selectivity of 85% can be obtained after 150 h of time-on-stream at 580 °C, with frequent regenerations at 650°C. These values are the highest among those reported for Ga-based dehydrogenation catalyst. However, it is not completely clear which metal, whether Pt or Ga, is predominately responsible for the high activity of this catalyst. The catalytic data on the Ga-based formulations are summarized in Table S1.3.

## 1.5 Reaction and Deactivation Pathways

Even though the dehydrogenation reaction has been studied for almost a century, its exact mechanism is still a topic under debate, particularly because this reaction is catalyzed by an array of materials as different as noble metals and transition metal oxides. The so-called Horiuti-Polanyi mechanism, which was proposed in 1934, is most commonly used to describe catalytic dehydrogenation reactions.<sup>191</sup> This mechanism follows Langmuir-Hinshelwood kinetics, where all the surface sites of the catalyst are considered to be identical. The Horiuti-Polanyi mechanism consists of four main steps: dissociative adsorption of the paraffin, C-H cleavage of a second hydrogen atom, formation of a hydrogen molecule and subsequent desorption of both the hydrogen and the olefin, as is shown in Scheme 1.2.<sup>192</sup> Notably, both C-H



**Scheme 1.2.** Propane dehydrogenation mechanism as proposed by Horiuti and Polanyi on a Pt surface. The intermediates depicted have been observed by IR spectroscopy during the hydrogenation reaction at low temperatures and are supported by theoretical calculations. The dissociative adsorption of propane may also take place by the abstraction of the  $\beta$ -hydrogen, forming a 2-propyl intermediate, but for brevity this pathway is not shown. High paraffin pressures favor the formation of propylidyne species (step h-j), which are coke precursors. These species are relatively stable and can only be hydrogenated when high concentrations of hydrogen are present on the Pt surface.<sup>199–204</sup>

cleavage steps<sup>171,193–196</sup> and the dissociative adsorption of the paraffin have been suggested as the rate limiting step of the dehydrogenation reaction.<sup>81,83,117,197</sup> Whether this mechanism can explain the results of experimental and theoretical studies performed on both Pt and metal oxide systems will be discussed in the following section.

Several studies have been performed on Pt and Pt-Sn catalysts to gain a detailed understanding of the mechanism of the dehydrogenation reaction. First of all, isotopic labeling experiments have been used to identify the reaction intermediates. For example, co-feeding D<sub>2</sub> during ethane dehydrogenation resulted in a single deuterium being attached to the ethane molecules, suggesting an ethyl reaction intermediate.<sup>198</sup> However, since the dehydrogenation reaction is an equilibrium-controlled reaction, these compounds can react back and forth leading to isotopic scrambling, which complicates the interpretation of experimental results.

Infrared spectroscopy is another valuable tool to detect intermediates formed during dehydrogenation reactions on Pt based catalysts. Due to experimental limitations, this is done through the study of the reverse hydrogenation reaction, which has the same reaction intermediates, but takes place at considerably lower temperatures. During the adsorption of ethylene on both Pt and Pt-Sn surfaces at temperatures ranging from 173 to 300 K, ethylidyne (Pt<sub>3</sub>-C-CH<sub>3</sub>), as well as  $\pi$ -bonded and di- $\sigma$ -bonded ethylene species are detected.<sup>97,98,205,206</sup> Cremer et al. used sum frequency generation IR spectroscopy (SFGIR) to elucidate the role of these ethylene adspecies on a Pt (111) surface.<sup>207,208</sup> During ethylene hydrogenation, ethylidyne was found to be a spectator species, although one competing for active sites on the catalyst surface. On the other hand,  $\pi$ -bonded ethylene was determined to be the main intermediate of ethylene hydrogenation, although di- $\sigma$ -bonded ethylene was also found to be converted albeit at a lower rate.

Ethyl groups are only detected at very high hydrogen pressures, as these species readily convert to di- $\sigma$ -ethylene. Nevertheless, Zaera et al. have reported that the reaction mechanism of ethylene hydrogenation involves a  $\pi$ -bonded ethylene and an ethyl intermediate.<sup>209</sup> Furthermore, when propylene adsorption on Pt(111) was studied by reflection-absorption IR spectroscopy, most of the propylene was found to be coordinated as di- $\sigma$ -bonded, albeit  $\pi$ -bonded propylene was found to predominate at high surface coverages.<sup>199</sup> On the contrary, DFT calculations showed that propylene is

preferentially adsorbed in the di-sigma modus.<sup>60,95</sup> DFT calculations performed on Pt, Pt<sub>3</sub>Sn and Pt<sub>2</sub>Sn (111) surfaces during the PDH reaction pointed towards the dissociative adsorption of the alkane being the rate limiting step. In the presence of Sn, this energy barrier is increased, as is shown in Figure 1.22, therefore decreasing the activity of the catalyst.<sup>95,99</sup> On Pt(111) the dehydrogenation may proceed by both a 1- as a 2-propyl intermediate, while on the Pt-Sn alloys the 1-propyl intermediate is favored. The positive effect of Sn on the catalytic activity is explained by the facile desorption of propylene, preventing the further dehydrogenation of the adsorbed propylene.

Microcalorimetry has afforded complimentary information on the dehydrogenation mechanism over Pt-based catalysts, a lower heat of adsorption of ethylene being detected on the Pt-Sn relative to the Pt surface (94-135 kJ/mol and 157 kJ/mol,

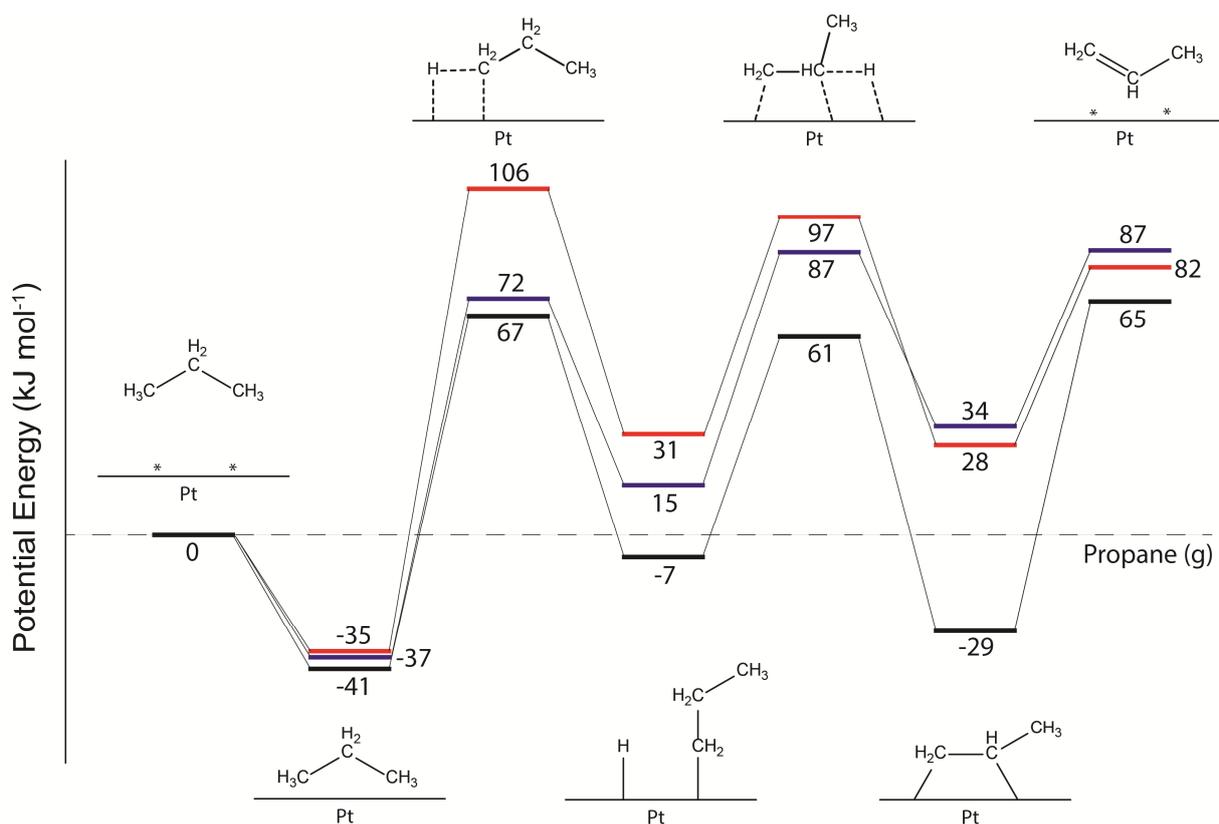
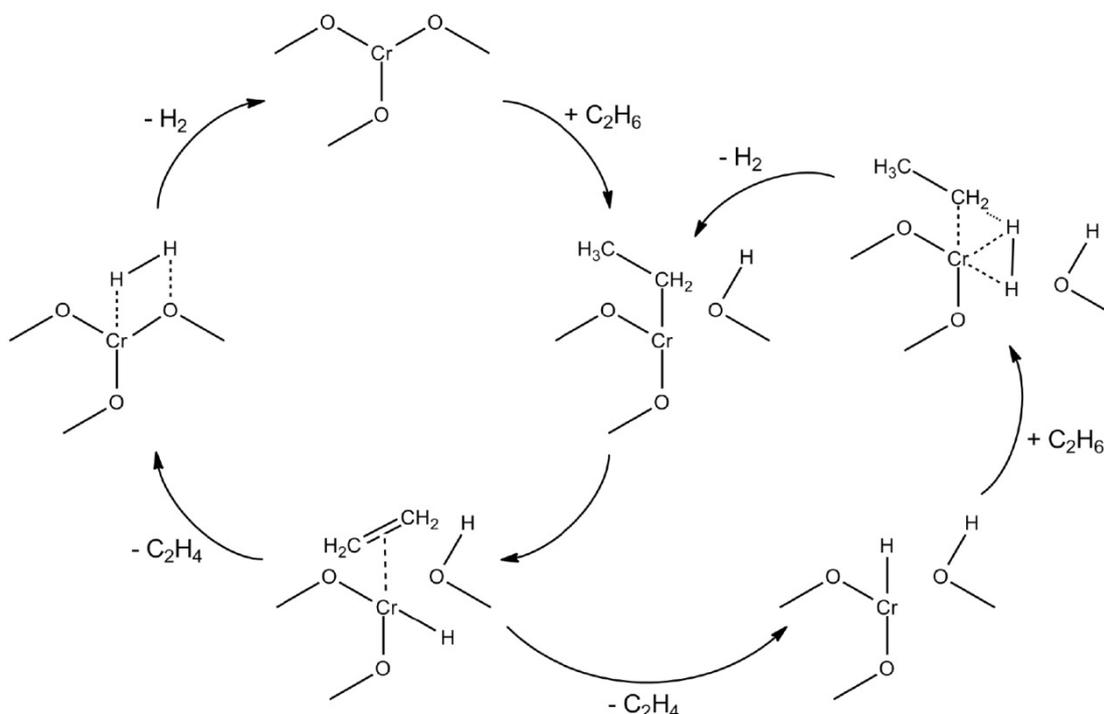


**Figure 1.22.** Energy profiles for propane dehydrogenation to propylene on Pt (111) (black), Pt<sub>3</sub>Sn (111) (blue) and Pt<sub>2</sub>Sn (111) (red) surfaces, as obtained by DFT calculations. The intermediates corresponding with each energy are shown. The recombination of the hydrogen ad-atoms is not considered.<sup>95</sup> All potential energies are shown relative to propane in the gas phase.

respectively).<sup>98</sup> Keeping in mind that Sn addition reduces the heat of adsorption, the formation of ethylidyne is hindered by the electron transfer taking place from Sn to Pt, as has been suggested by the results of density functional theory (DFT) calculations.<sup>99,196,210,211</sup> In addition, calculations have shown the presence of Sn reduces the amount of Pt step sites that are highly active for side reactions such as cracking.<sup>211</sup> The latter observation is rendered particularly noteworthy by the fact that isotopic labeling experiments, performed by Galvita et al. during ethane dehydrogenation, have revealed that ethylene can form methane and coke through cracking, the conversion proceeding via an ethylidyne intermediate.<sup>113,197</sup>

The dehydrogenation mechanism on chromia-based catalysts is somewhat different, as both the chromium and oxygen atoms of the oxide are believed to participate in the reaction mechanism.<sup>212</sup> Quantum chemical methods have been used by Lillehaug et al. to study the ethane dehydrogenation mechanism on mononuclear Cr<sup>3+</sup> surface sites on a silica support.<sup>213,214</sup> The first step they proposed is C-H activation via  $\sigma$ -bond metathesis resulting in the formation of Cr-C and O-H bonds. The second step is a  $\beta$ -H transfer to a Cr site, which was suggested to be the rate limiting step.<sup>213,215</sup> The final step proposed is the formation of hydrogen and the desorption of the latter and



**Scheme 1.3.** Proposed reaction mechanism for the dehydrogenation of ethane on CrO<sub>x</sub> catalysts.<sup>117,213,214</sup>

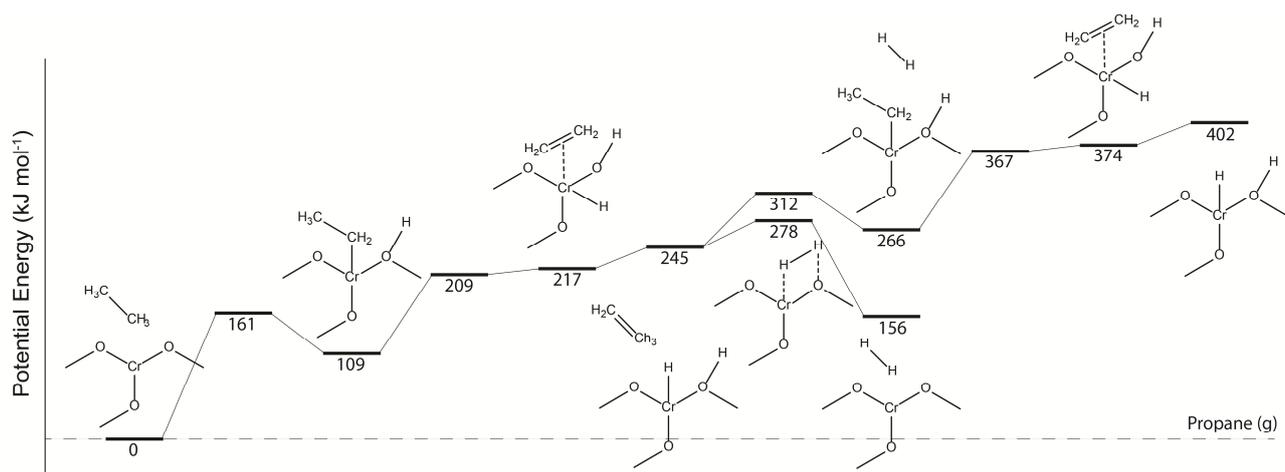


**Figure 1.23.** Energy profile for propane dehydrogenation to propylene on  $\text{CrO}_x$  catalyst obtained by DFT calculations. The intermediates from Scheme 1.3 are shown with their relative energies. Note that for the second section of the scheme, a second propane molecule is dehydrogenated.<sup>213,214</sup>

ethylene. An alternative mechanism in which a Cr-H species activates ethane by forming molecular hydrogen and an adsorbed ethyl species has been proposed based on the results of isotopic labeling experiments performed during ethane dehydrogenation on a  $\text{CrO}_x/\text{Al}_2\text{O}_3$  catalyst.<sup>117</sup> The two main mechanisms proposed for the dehydrogenation of light alkanes on chromia/alumina catalysts are shown in Scheme 1.3. In these mechanisms, either the dissociative adsorption<sup>117,212</sup> or  $\beta$ -H elimination are believed to be the rate limiting step.<sup>213,216,217</sup> Figure 1.23 shows two reaction cycles in an energy diagram, as calculated by Lillehaug et al. Indeed, the energy barrier is the highest for the initial C-H activation, although this energy is significantly lower when the bond is activated by the Cr-H intermediate (i.e. the right part of Scheme 1.3). Nevertheless, the desorption of hydrogen is preferred, as the energy barrier is lower.

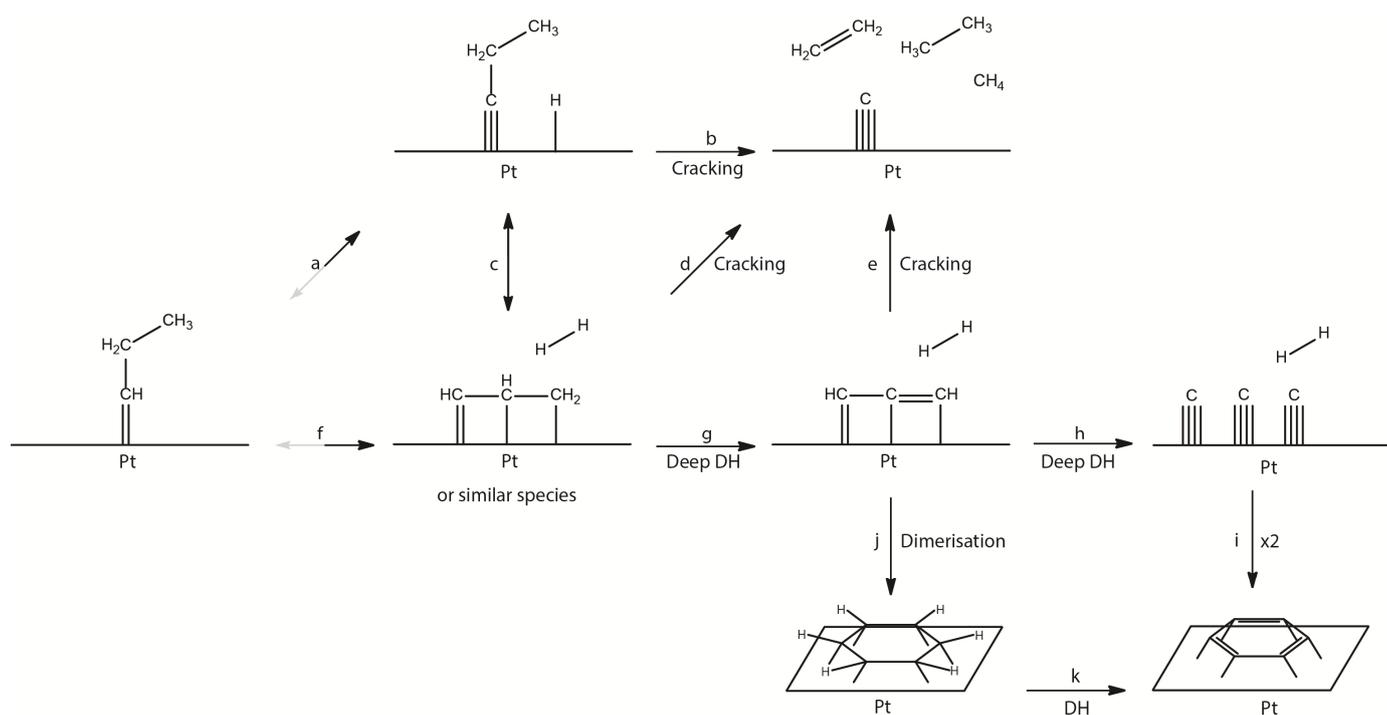
In-situ FTIR spectroscopy has provided evidence of the formation of acetaldehyde and acetone intermediates as ethane and propane are adsorbed on a mesoporous chromia-alumina catalyst.<sup>218</sup> Furthermore, during the dehydrogenation of propane on a  $\text{CrO}_x$  catalyst, surface species including aliphatic, unsaturated and aromatic carbon species, along with acetates and carboxylates, have been detected by diffuse reflectance infrared Fourier transform spectroscopy (DRIFTS).<sup>163,218,219</sup> This is consistent with a model in which the first step of the reaction is abstraction of



To summarize, most of the experimental results suggest that the dehydrogenation of light alkanes proceeds via the Horiuti-Polanyi mechanism, where either the dissociative adsorption of the alkane or the second C-H bond cleavage is the rate determining step. There is a lack of clear evidence of fundamental differences in the reaction mechanism on metal oxide and noble metal catalysts, although reports of mechanistic studies involving metal oxide catalysts are admittedly scant.

All dehydrogenation catalysts deactivate with time-on-stream, several processes being responsible for the deactivation of the various different types of catalysts discussed in this Chapter. However, there has been a clear consensus in the literature since the mid-1970's identifying coke deposition as the main cause of deactivation.<sup>62,221-223</sup>

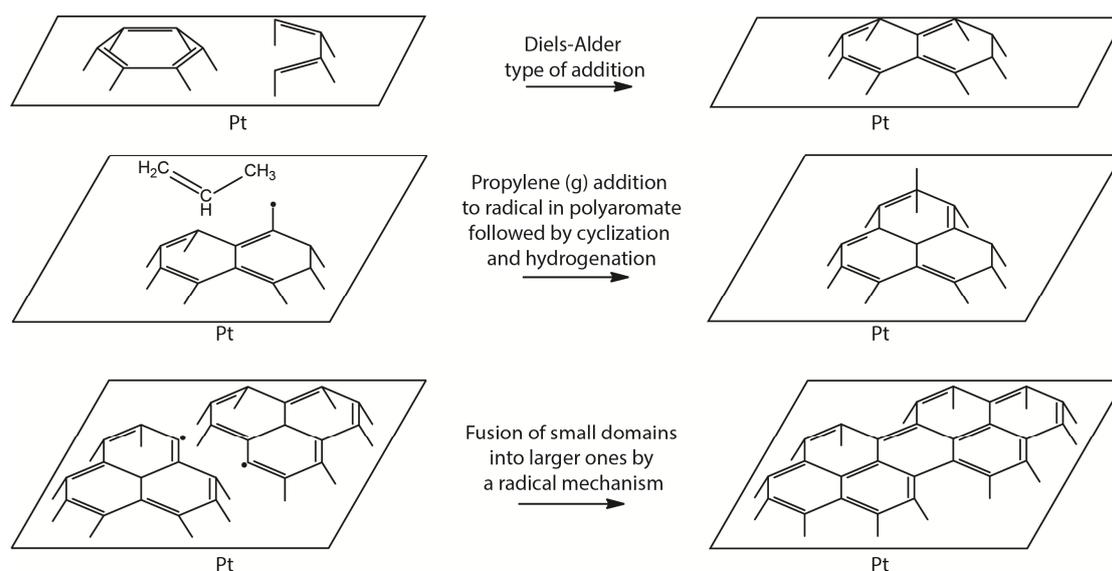
Coke is a collective name given to a large family of big hydrocarbon molecules that are highly graphitized and tend to form on the catalyst surface during the propane dehydrogenation reaction. Coke accumulation effectively hinders the diffusion of



**Scheme 1.4.** Proposed pathway linking the presence of strongly adsorbed propyl species to the formation of an aromatic ring through a series of cracking (a-e), deep dehydrogenation (f-i) and/or dimerisation (f,g,j,k) reactions.<sup>200,201,225</sup> Note that the adsorbed hydrocarbons shown in the scheme are examples of species formed on the Pt surface, and that they actually represent a family of similar species.

reactants to the catalyst surface by blocking both pores and active sites, which results in a drop in catalytic activity. Therefore, the detrimental effect of coke is largely dependent on catalyst design and the location of the coke deposits.<sup>224</sup>

The process of coke formation is very complex and not very well understood. Brønsted acid and others active sites of the catalysts serve as seeding points to which olefins and paraffins are added until large graphitic structures are formed. Indeed olefins in the stream can easily react with the carbocation intermediates formed on these acid sites. Additionally, strong adsorption of both reaction intermediates, such as the ethylidyne or ethyne species discussed above,<sup>60,113,197</sup> and products on active sites can also induce polymerization and lead to the formation of graphitic sheets. In Scheme 1.4, several pathways for the formation of the first aromatic ring structures from propylidyne and similar molecules are proposed, which include cracking, deep dehydrogenation and polymerization reactions.



**Scheme 1.5.** Proposed mechanism for the growth of polyaromatic species by either Diels-Alder-type addition, propylene addition via radical chemistry or fusion of small domains into larger ones.<sup>228,229</sup> The species will continue to grow in a similar fashion, and at a certain point are considered to be similar to graphite. The molecules in the scheme are only simplified hydrogen deficient coke precursors that may be present on the surface of the catalyst. Such species are directly bonded to the Pt surface and in reality will contain significant amounts of hydrogen, either by hydrogen terminated aromatic rings, or by aliphatic sidechains.

Coke species may grow from the resulting aromatic rings by either Diels-Alder-type addition, propylene addition to a radical, or fusion of smaller domains, as shown in Scheme 1.5. When these polyaromatics are still relatively small, they can also display some mobility over the catalyst surface and in fact, the addition of Sn to the Pt-based catalyst facilitates this migration.<sup>211,226,227</sup> In addition, acid sites present on the support may protonate these small polyaromatics, making them more reactive towards gas phase olefins.<sup>228,230</sup> Nevertheless, studies on these processes are scant, which is why the mechanism explaining the progression from adsorbed reaction intermediates to large graphitic sheets is still largely unknown.

The location of coke is very important, as coke on the support has a lesser negative effect on catalyst activity.<sup>224,226</sup> However, it is important to note that the presence of carbon deposits on the surface does not always negatively influence catalyst performance. Indeed, a low amount of coke deposition has been observed to increase the catalytic activity by facilitating the adsorption of the alkane near the active dehydrogenation site.<sup>224</sup> Furthermore, highly active sites responsible for side reactions, such as hydrogenolysis, are the first to be poisoned by coke, resulting in higher selectivities to the olefin product. Coke becomes detrimental when large graphitic sheets are formed that cover most of the catalytically active sites.<sup>146,231</sup> In order to address this coke-induced deactivation, a regeneration step under an oxidative atmosphere has been incorporated to industrial dehydrogenation processes. This process is relatively straightforward, as coke is easily combusted with air at dehydrogenation reaction temperatures. The ambivalent nature of coke deposits is further highlighted by the fact that their presence on deactivated catalysts is essential in the industrial processes that use coke combustion as the main source of the heat required to run the dehydrogenation reaction.

Several strategies have been applied to control coke formation. For example, coke deposition can be dramatically reduced by using a support with little to no Brønsted acidity, or by poisoning the acid sites. Changes in the reaction conditions, such as cofeeding steam, hydrogen or CO<sub>2</sub> can reduce coke formation,<sup>226,232,233</sup> whereas high partial pressures of olefins and paraffins exacerbate coke deposition. Even the nature of the alkane reactant has an effect, as coke formed during propane dehydrogenation on a Pt-Sn/Al<sub>2</sub>O<sub>3</sub> catalyst is reported to be more detrimental than coke formed during ethane dehydrogenation (although such a comparison difficult as both reactions run at different temperatures).<sup>113</sup> Alternatively, coke deposition can be reduced by adding a

promoter element, the addition of Sn to Pt-based dehydrogenation catalysts being the best-known example.

## 1.6 Comparing catalytic systems for propane dehydrogenation

As was discussed in the previous section, the Pt-, CrO<sub>x</sub>- and GaO<sub>x</sub>-based catalysts are profoundly different systems for propane dehydrogenation. Therefore, a comprehensive comparison of the activity and stability of these catalysts is desirable, particularly because said comparison stands to reveal qualitative differences between formulations. We have essayed this comparison focusing on three performance criteria, namely olefin yield (obtained at the start of the experiment), stability (expressed as the deactivation rate) and the space velocity at which the first two criteria were measured (expressed as weight hourly space velocity (WHSV)). In this approach, the effects of various factors, such as pressure, temperature, preparation method, promoter and catalyst support are not considered. The reasons to ignore these effects include the fact that this information is missing in many articles (pressure being a notable example), the absence of a clear trend (temperature) and an excessively large variance within a single variable to allow a meaningful comparison (catalyst preparation being an instance of such a variable). It is important to note that the catalysts were only included in this comparison if the space velocity, deactivation rate and initial yield could be determined from the original source.

In Tables S1.1 to S1.3 relevant catalytic data, including yield, space velocity and deactivation rate are summarized for Pt-, CrO<sub>x</sub>- and GaO<sub>x</sub>-based catalysts. The deactivation rate was calculated by assuming first order reaction kinetics, and comparing the conversion at the start and end of the reaction. In Figure 1.25, the (initial) yield of propylene for these materials is plotted versus the deactivation rate of these materials. The data points representing the catalytic performance the different metals are grouped around similar values, the initial yields being similar for Pt and CrO<sub>x</sub> and slightly higher for GaO<sub>x</sub>. Additionally, PDH results show that the different metals deactivate at different rates, with Pt being very stable, CrO<sub>x</sub> deactivating at a moderate rate and GaO<sub>x</sub> deactivating rapidly. Another interesting observation stemming from the PDH data is that within each type of catalyst high yields often coincide with relatively low deactivation rates, which is counterintuitive.

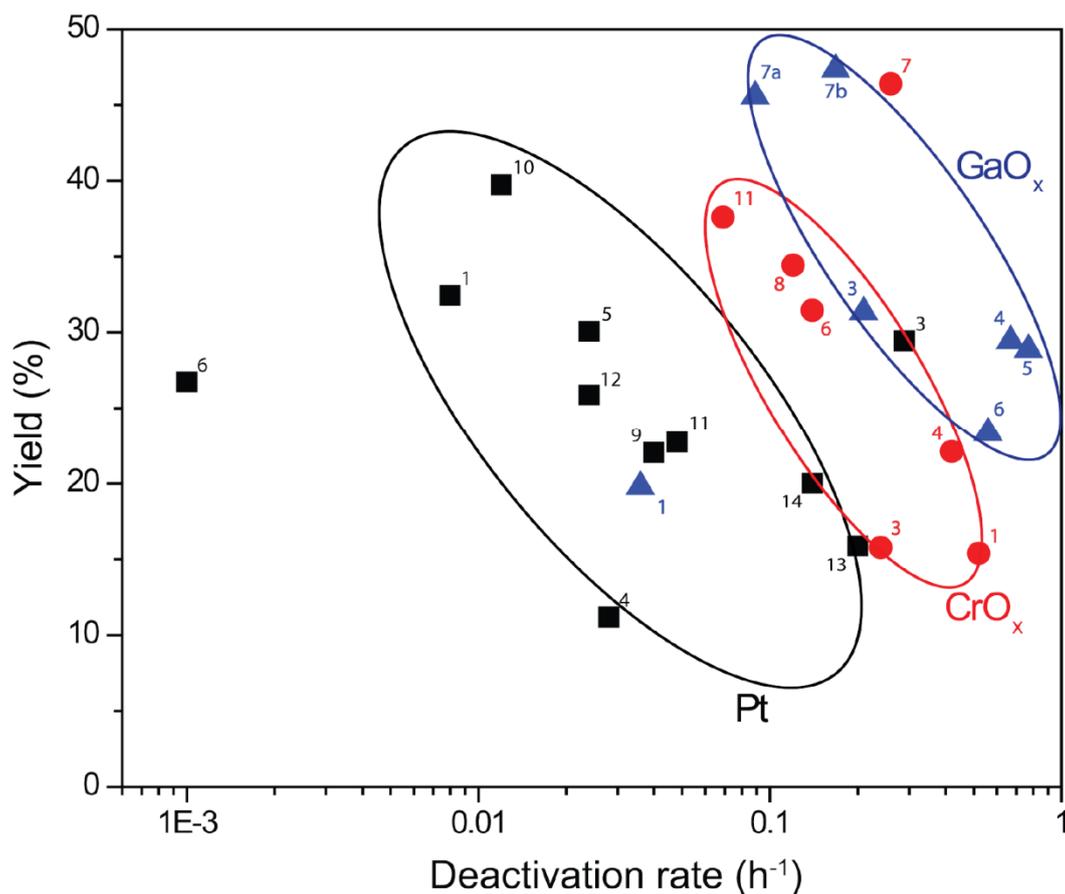


**Figure 1.25.** Yield of propylene during the dehydrogenation of propane versus deactivation rate of the catalysts included in Tables S1.1-1.3. Each data point is labeled with a number corresponding the first column of the respective tables, in order to distinguish between the different catalysts. Catalyst systems that present high yields combined with low deactivation rates are preferred.

Space velocity is the second important factor that is considered for comparing the performance of dehydrogenation catalysts. In Figure 1.26 propylene yield is plotted against the weight hourly space velocity (WHSV).

In order to be commercially attractive, dehydrogenation catalysts must provide high olefin yields at high space velocities. In other words, catalysts should display a high specific activity, which is to say good conversion at short contact times (moles of propane converted per moles of active phase per second). Figure 1.26 illustrates that while the yields obtained over GaO<sub>x</sub>-, CrO<sub>x</sub>-, and Pt-based propane dehydrogenation catalysts are comparable, the catalysts operate at relatively low, intermediate and high space velocities respectively.

Taking into account that Pt-based catalysts typically have low loadings (< 1 wt%), whereas GaO<sub>x</sub>- and CrO<sub>x</sub>-based catalysts generally have loadings between 5 and 20 wt%, it is clear that on a weight basis Pt represents the most active formulation in PDH. This is confirmed when the calculated net specific activity values from Tables S1.1-1.3 are compared with one another. Indeed, for the dehydrogenation of propane on Pt-based catalysts, the average specific activity is  $2.86 \times 10^{-1} \text{ s}^{-1}$ , which is considerably higher than the average specific activities over CrO<sub>x</sub> and GaO<sub>x</sub>, which are  $7.49 \times 10^{-5}$  and  $8.17 \times 10^{-5}$ , respectively. In Table 1.3, the proposed active sites for propane dehydrogenation of these three catalysts are shown. In the case of platinum-based catalysts, any Pt<sup>0</sup> atom located at the surface is believed to catalyze the reaction, while in CrO<sub>x</sub>- and GaO<sub>x</sub>- based catalysts Cr<sup>3+</sup> and Ga<sup>3+</sup> must be coordinately unsaturated in order to display catalytic activity. This similarity between the active

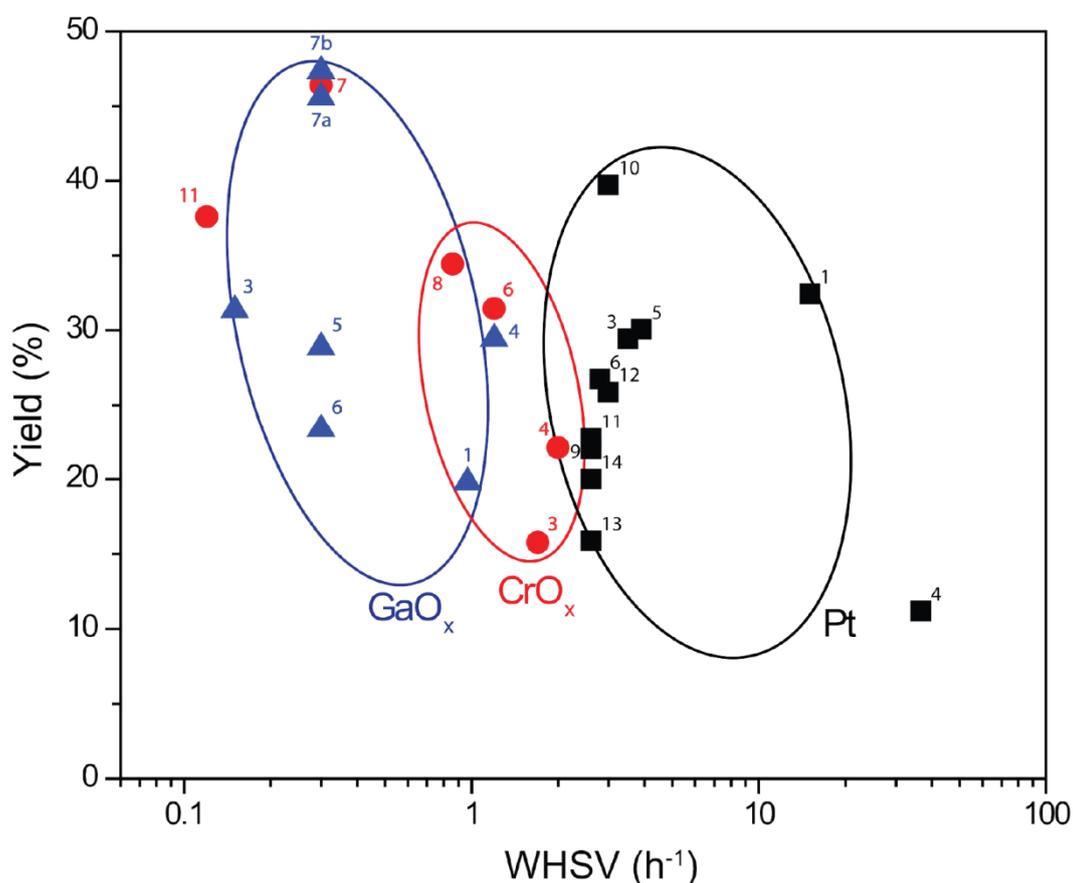


**Figure 1.26.** Yield of propylene versus WHSV of the catalysts included in Tables S1.1 to S1.3. High yields obtained at high space velocities are preferred; since Pt-based catalysts can afford comparable yields to catalysts based on metal oxides while operating at higher space velocities they are superior in this respect.

sites of Ga- and Cr-containing catalyst, and their difference to Pt, may therefore explain the relative specific activity values of these formulations. However, it should be noted that the specific activity values are a very rough approximation of the real TOF of these catalysts. In case of Pt catalysts, all Pt (not only Pt located at the surface of nanoparticles) is taken in account when calculating the specific activity, and additional errors are introduced for the metal oxides. In the case of CrO<sub>x</sub> catalysts, only coordinately unsaturated Cr<sup>3+</sup> species are active in the dehydrogenation reaction, yet in these specific activity calculations a considerable amount of species which are either coordinately saturated or in a different oxidation state are included. Although Ga<sup>3+</sup> is likely the only stable species during the dehydrogenation reaction, our specific activity calculation involving GaO<sub>x</sub> catalysts considers a significant amount of the Ga that is either present in the framework of the support or incorporated in larger Ga<sub>2</sub>O<sub>3</sub> crystallites. Nevertheless, the difference in specific activity calculated for Pt and the metal oxides is in the range of four orders of magnitude, which cannot be explained solely by the errors introduced in the calculations.

It is important to mention that catalysts tend to deactivate faster when higher space velocities are used. Notably, metal oxide-based catalysts deactivate faster than the Pt-based formulations, in spite of the fact that the latter are commonly used at higher space velocities, which highlights the remarkable stability of Pt catalysts.

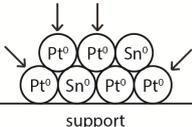
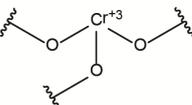
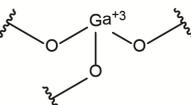
The differences in turn-over frequencies described previously could be explained by comparing the activation energies calculated by DFT methods, as was previously discussed in Chapter 1.5. In these calculations, the energy barrier for the rate limiting step on Pt-Sn system is lower (109 kJ/mol) than in the CrO<sub>x</sub> and GaO<sub>x</sub> catalysts (161 kJ/mol and 163 kJ/mol, respectively). E<sub>a</sub> affects the reaction rate, as described by the Arrhenius equation:

$$k = Ae^{\frac{-E_a}{RT}}$$

where k is the reaction rate constant, A is the pre-exponential factor, R is the gas constant and T the temperature. By calculating k/A at a temperature of 600 °C and assuming A is comparable for the three systems considered, the rate constant is ~10<sup>3</sup> times higher for the Pt-Sn catalysts compared to the metal oxide catalysts. The difference in reported specific activity for propane dehydrogenation on the Pt and metal oxide catalysts (Tables S1.1-1.3) is approximately 10<sup>4</sup>, as is shown in Table 1.3.

The higher activity observed for the Pt-based catalysts may therefore be explained by the significantly lower energy barrier of the rate-limiting step. However care must be taken when comparing these  $E_a$  values, as the methods used for obtaining these are not identical. Furthermore, these simulations assume model surfaces, that not resemble real catalyst systems and are therefore not necessarily representative for the experimentally observed reaction rates. Nevertheless, these combined theoretical and experimental data are very encouraging and highlight the need for more extensive studies on the reaction rate on Pt-based compared to metal oxide dehydrogenation catalysts.

**Table 1.3.** Proposed active sites for the Pt-,  $\text{CrO}_x$ - and  $\text{GaO}_x$ -based propane dehydrogenation catalysts discussed above, along with the order of magnitude of their calculated specific activity, and the reaction rates ( $k/A$ ) calculated by DFT.

	Pt-Sn	$\text{CrO}_x$	$\text{GaO}_x$
(Proposed) active site			
Typical specific activity PDH (mol olefin per mol metal per s)	$\sim 10^{-1}$	$\sim 10^{-5}$	$\sim 10^{-5}$
$k/A (=e^{E_a/RT})$ (determined by DFT)	$\sim 3 \times 10^{-7}$	$\sim 2 \times 10^{-10}$	$\sim 2 \times 10^{-10}$

To summarize, although metal oxide-based catalysts can afford comparable yields to those obtained using Pt-based formulations, the latter can operate at higher space velocities and exhibits lower deactivation rates than metal oxide catalysts.

## 1.7 Scope of this PhD Thesis

As was shown in the preceding sections, the catalytic dehydrogenation of propane has been extensively researched on Pt-, CrO<sub>x</sub>- and GaO<sub>x</sub>-based catalysts. In this PhD thesis, a spectroscopic approach will be used to further our knowledge on the deactivation of these catalyst materials, and to gain a better understanding of the process of coke deposition. More specifically, the effects of catalyst composition and experimental conditions on the chemical nature of these coke deposits is one of our targets. To further emphasize the value of spectroscopic techniques, they are applied in a pilot plant setup to study the deactivation of these catalyst materials under relevant reaction conditions.

In Section 1.4 of this Chapter, it was shown that the deposition of coke can be decreased by adding hydrogen or steam to the feed. However, little is known how this affects the chemical structure of these carbon deposits. Raman spectroscopy is known to be a valuable tool to examine such structural changes of coke. Therefore operando Raman spectroscopy is used in **Chapter 2** to study the influence of co-feeding varying amounts of hydrogen on the chemical nature of the coke species formed.

In **Chapter 3**, this analysis is taken a step further, as the coke deposits formed on different catalysts materials (Pt, Pt-Sn, Ga or Pt-Ga supported on alumina) are studied by operando Raman spectroscopy and TGA. With this approach, the coking process on these different materials can be compared. However, these techniques provide information of the bulk of the catalyst material, but since catalysis takes place on a nano-scale, it is desirable to obtain additional chemical information on a similar length scale. Hence, we applied scanning transmission X-ray spectroscopy (STXM) to investigate the coke deposits in more detail.

In Section 1.6 of this Chapter, a comparison is made between the Pt-, GaO<sub>x</sub>- and CrO<sub>x</sub>-based propane dehydrogenation catalysts. It is clear from literature, that the Pt-based formulations display higher activities and stabilities compared to the metal oxide catalysts. In **Chapter 4**, a novel Pt-promoted GaO<sub>x</sub> catalyst is described, which exhibits excellent catalytic performance that rivals the highly active Pt-Sn system. The advantage of this system, however, is that the Pt content is significantly lower, while exhibiting a stability superior to other catalyst formulations. From the

experiments performed, it was apparent that Ga was responsible for the C-H activation, while Pt acted as a promotor. A broad collection of techniques was employed to explain the reason behind the unique behavior of this catalyst material. The results indicated that a mixed Al-Ga oxide was formed, that was highly stable and active for the dehydrogenation of propane, while highly dispersed Pt is assisting with the desorption of hydrogen from the Ga active sites.

The combination of operando Raman and UV-Vis spectroscopy is a powerful tool to study the deposition of coke deposits on catalyst materials. For the industrial propane dehydrogenation processes it is very important to carefully control the deposition of coke deposits. As was discussed above, the combustion of coke serves as the main source of heat for the Catofin system, although when too much coke is present on the catalyst, an excessive amount of heat is generated that irreversibly deactivates the  $\text{CrO}_x$  catalyst by incorporation of the Cr in the bulk of the support. Therefore, it would be desirable to know precisely the amount of coke is present at any time during the dehydrogenation reaction, so the regeneration step can be started at the optimal time by using an on-line control system based on operando spectroscopy. Nevertheless, the tools required to do such analysis were not available until now. In this work, we have designed and tested novel probes for operando UV-Vis and Raman spectroscopy which can be inserted in a pilot-scale reactor in order to measure the active catalyst material under relevant reaction conditions. The findings of this approach are discussed in **Chapter 5** for the UV-Vis probes, and in **Chapter 6** for the combination of UV-Vis and Raman probes.

Finally, **Chapter 7** will serve as a summary of the work performed in this PhD thesis, including some future perspectives.

## 1.8 Acknowledgements

Eduardo Santillan Jimenez (currently working at the University of Kentucky) and Javier Ruiz Martinez (Utrecht University) are thanked for their contributions to the literature study this Chapter is based on.

## 1.9 References

- (1) Budavari, S.; O'Neil, M.; Smith, A.; Heckelman, P.; Obenchain, J. *The Merck Index*; Budavari, S., Ed.; 12th ed.; Merck & Co.: New Jersey, 1996; pp. 1348–1349.
- (2) McCoy, M.; Reisch, M.; Tullo, A. H.; Short, P. L.; Tremblay, J.-F. *Chem. Eng. News* **2006**, *84*, 59.
- (3) Ethylene Uses and Market Data  
<http://www.icis.com/Articles/2007/11/05/9075777/ethylene-uses-and-market-data.html> (accessed Oct 25, 2013).
- (4) Market Study: Propylene (UC-1705) <http://www.ceresana.com/en/market-studies/chemicals/propylene/> (accessed Oct 25, 2013).
- (5) The Global Olefins and Polyolefins Markets in 2011 - Slow Growth in Demand Amid Political and Economical Crisis  
[http://www.researchandmarkets.com/research/bdd2c0/the\\_global\\_olefins](http://www.researchandmarkets.com/research/bdd2c0/the_global_olefins) (accessed Oct 25, 2013).
- (6) Radcliffe, C. The FCC unit as a propylene source  
<http://www.digitalrefining.com/article/1000312#.UmpROtK8BWQ> (accessed Oct 25, 2013).
- (7) Nexant. Industry Report - Independent Market Report on the Global and Indonesian Petrochemicals Industry [http://www.chandra-asri.com/UserFiles/201105151926340.Nexant Industry Report 2011.pdf](http://www.chandra-asri.com/UserFiles/201105151926340.Nexant%20Industry%20Report%202011.pdf) (accessed Oct 20, 2013).
- (8) Tullo, A. H. *Chem. Eng. News* **2012**, *90*, 10.
- (9) McFarland, E. *Science* **2012**, *338*, 340.
- (10) Bullin, K.; Krouskop, P. Composition Variety Complicates Processing Plans for US Shale Gas [http://www.bre.com/portals/0/technicalarticles/Keith Bullin - Composition Variety\\_ US Shale Gas.pdf](http://www.bre.com/portals/0/technicalarticles/Keith%20Bullin%20-%20Composition%20Variety%20US%20Shale%20Gas.pdf) (accessed Oct 21, 2013).
- (11) Chemical Composition of Natural Gas <http://www.uniongas.com/about-us/about-natural-gas/Chemical-Composition-of-Natural-Gas#L> (accessed Oct 23, 2013).
- (12) Schut, J. H. How Shale Gas Is Changing Propylene  
<http://plasticsengineeringblog.com/2013/02/20/how-shale-gas-is-changing-propylene/> (accessed Oct 23, 2013).

- (13) Propylene from Propane via Dehydrogenation (similar to UOP Oleflex)  
<http://base.intratec.us/home/chemical-processes/propylene/propylene-from-propane-via-dehydrogenation> (accessed Oct 23, 2013).
- (14) Propylene from Propane via Dehydrogenation (similar to Lummus CATOFIN)  
<http://base.intratec.us/home/chemical-processes/propylene/propylene-from-propane-via-dehydrogenation-2> (accessed Oct 23, 2013).
- (15) Buonomo, F.; Sanfilippo, D.; Trifiro, F. In *Handbook of Heterogeneous Catalysis*; Ertl, G.; Knozinger, H.; Weitkamp, J., Eds.; Wiley-VHC Verlag GmbH: Weinheim, Germany, 1997; pp. 2140–2151.
- (16) Alperowicz, N. Engineering & construction: Shale boom reinvigorates the industry, could lead to shortage of labor resources  
[http://www.chemweek.com/lab/Engineering-and-construction-Shale-boom-reinvigorates-the-industry-could-lead-to-shortage-of-labor-resources\\_52648.html](http://www.chemweek.com/lab/Engineering-and-construction-Shale-boom-reinvigorates-the-industry-could-lead-to-shortage-of-labor-resources_52648.html) (accessed Oct 23, 2013).
- (17) Hua, L. China propane imports to surge on new PDH projects  
<http://www.icis.com/Articles/2013/05/21/9670487/china-propane-imports-to-surge-on-new-pdh-projects.html> (accessed Oct 23, 2013).
- (18) Shale Gas, Competitiveness, and New US Chemical Industry Investment: An Analysis Based on Announced Projects.  
<http://chemistrytoenergy.com/sites/chemistrytoenergy.com/files/shale-gas-full-study.pdf> (accessed Oct 23, 2013).
- (19) Pujadó, P. R.; Vora, B. V. *Hydrocarb. Process.* **1990**, *69*, 65.
- (20) Buyanov, R. A.; Pakhomov, N. A. *Kinet. Catal.* **2001**, *42*, 64.
- (21) Altani, A. M. *Oil Gas Eur. Mag.* **2004**, *30*, 36.
- (22) Tinnemans, S. J. Combined operando Raman/UV-Vis-NIR spectroscopy as a tool to study supported metal oxide catalysts at work, PhD Thesis, Utrecht University, 2006.
- (23) Research and Markets: China Propylene Market, 2013-2015  
<http://www.businesswire.com/news/home/20130913005218/en/Research-Markets-China-Propylene-Market-2013-2015> (accessed Oct 23, 2013).
- (24) Ondrey, G. UOP's C3 Oleflex process selected for propylene plant in the U.S. Gulf Coast [http://www.che.com/only\\_on\\_che/latest\\_news/UOPs-C3-Oleflex-process-selected-for-propylene-plant-in-the-U-S-Gulf-Coast\\_10539.html](http://www.che.com/only_on_che/latest_news/UOPs-C3-Oleflex-process-selected-for-propylene-plant-in-the-U-S-Gulf-Coast_10539.html) (accessed Oct 23, 2013).
- (25) Boswell, C. On-purpose technologies ready to fill propylene gap  
<http://www.icis.com/Articles/2012/04/16/9549968/on-purpose-technologies-ready-to-fill-propylene-gap.html> (accessed Oct 23, 2013).

- (26) Yu, L.; Chen, K. China Insight: Propane dehydrogenation projects boom, but risks loom <http://www.icis.com/Articles/2012/04/02/9546232/China-Insight-Propane-dehydrogenation-projects-boom-but-risks.html> (accessed Oct 23, 2013).
- (27) Bhasin, M. M.; McCain, J. H.; Vora, B. V.; Imai, T.; Pujadó, P. R. *Appl. Catal. A-Gen.* **2001**, *221*, 397.
- (28) CATOFIN Dehydrogenation [http://www.cbi.com/images/uploads/tech\\_sheets/CatofinDehydrogenation-12.pdf](http://www.cbi.com/images/uploads/tech_sheets/CatofinDehydrogenation-12.pdf) (accessed Oct 23, 2013).
- (29) Ercan, C.; Gartside, R. J. *Can. J. Chem. Eng.* **1996**, *74*, 626.
- (30) Sanfilippo, D.; Miracca, I. In *Proceedings of the DGMK Conference "Oxidation and Functionalization: Classical and Alternative Routes and Sources"*; Ernst, S.; Gallei, E.; Lercher, J. A.; Rossini, S.; Santacesaria, E., Eds.; German Society for Petroleum and Coal Science and Technology (DGMK): Hamburg, 2005; p. 773.
- (31) Weckhuysen, B. M.; Schoonheydt, R. A. *Catal. Today* **1999**, *51*, 223.
- (32) Nijhuis, T. A.; Tinnemans, S. J.; Visser, T.; Weckhuysen, B. M. *Chem. Eng. Sci.* **2004**, *59*, 5487.
- (33) UOP Oleflex process for light olefin production <http://pet-oil.blogspot.nl/2012/10/uop-oleflex-process-for-light-olefin.html> (accessed Oct 23, 2013).
- (34) Honeywell's UOP Technology Selected For Petrochemical Production In China <http://www.dailyfinance.com/rtn/pr/honeywell-s-uop-technology-selected-for-petrochemical-production-in-china/rfid637412763/> (accessed Oct 23, 2013).
- (35) CCR Platforming & Oleflex <http://www.uop.com/products/equipment/ccr-regeneration/> (accessed Oct 23, 2013).
- (36) New Clariant CATOFIN Propane Dehydrogenation Catalysts Delivers Significant Savings <http://newsroom.clariant.com/new-clariant-catofin-propane-dehydrogenation-catalyst-delivers-significant-savings/> (accessed Oct 23, 2013).
- (37) Sanfilippo, D.; Miracca, I.; Trifiro, F. In *Encyclopedia of Hydrocarbons: Refining and Petrochemicals*; Amadei, C., Ed.; ENI: Rome, 2006; Vol. II, pp. 687–700.
- (38) Jensen, S. F.; Roennekleiv, M.; Rytter, E.; Souraker, P. International Patent WO 2000072967 A1. WO 2000072967 A1, 2000.

- (39) Caspary, K. J.; Gehrke, H.; Heinritz-Adrian, M.; Schwefel, M. In *Handbook of Heterogeneous Catalysis*; Ertl, G.; Knozinger, H.; Weitkamp, J., Eds.; Wiley-VHC Verlag GmbH: Weinheim, Germany, 2008; pp. 3206–3229.
- (40) The Uhde STAR process: Oxydehydrogenation of light paraffins to olefins [http://www.thyssenkrupp-uhde.de/fileadmin/documents/brochures/uhde\\_brochures\\_pdf\\_en\\_12.pdf](http://www.thyssenkrupp-uhde.de/fileadmin/documents/brochures/uhde_brochures_pdf_en_12.pdf) (accessed Oct 23, 2013).
- (41) Sinfelt, J. H. *J. Phys. Chem.* **1964**, *68*, 344.
- (42) Cortright, R. D.; Watwe, R. M.; Dumesic, J. A. *J. Mol. Catal. A-Chem.* **2000**, *163*, 91.
- (43) Willems, P. A.; Froment, G. F. *Ind. Eng. Chem. Res.* **1988**, *27*, 1966.
- (44) Olah, G. A.; Molnar, A. In *Hydrocarbon Chemistry, Second Edition*; Wiley inc.: Hoboken, New Jersey, 2003; pp. 30–37.
- (45) Rahimi, N.; Karimzadeh, R. *Appl. Catal. A-Gen.* **2011**, *398*, 1.
- (46) Barron, Y.; Maire, G.; Muller, J. M.; Gault, F. G. *J. Catal.* **1966**, *5*, 428.
- (47) Garin, F.; Aeiyaeh, S.; Legare, P.; Maire, G. *J. Catal.* **1982**, *77*, 323.
- (48) Olah, G. A.; Molnar, A. In *Hydrocarbon Chemistry, Second Edition*; Wiley inc.: Hoboken, New Jersey, 2003; pp. 161–185.
- (49) Jackson, S. D.; Stair, P. C.; Gladden, L. F.; McGregor, J. In *Metal Oxide Catalysis*; Jackson, S. D.; Hargreaves, J. S. J., Eds.; Wiley-VHC Verlag GmbH: Weinheim, Germany, 2009; pp. 595–612.
- (50) Grasselli, R. K. *Catal. Today* **1999**, *24*, 141.
- (51) Dittmeyer, R.; Höllein, V.; Daub, K. *J. Mol. Catal. A-Chem.* **2001**, *173*, 135.
- (52) Ravanchi, M. T.; Kaghazchi, T.; Kargari, A. *Desalination* **2009**, *235*, 199.
- (53) Sheintuch, M.; Simakov, D. S. A. In *Membrane Reactors for Hydrogen Production Processes*; De Falco, M.; Marrelli, L.; Iaquaniello, G., Eds.; Springer-Verlag Ltd.: London, 2011; pp. 183–200.
- (54) Rioux, R. M.; Song, H.; Hoefelmeyer, J. D.; Yang, P.; Somorjai, G. A. *J. Phys. Chem. B* **2005**, *109*, 2192.
- (55) Song, H.; Rioux, R. M.; Hoefelmeyer, J. D.; Komor, R.; Niesz, K.; Grass, M.; Yang, P.; Somorjai, G. A. *J. Am. Chem. Soc.* **2006**, *128*, 3027.
- (56) Santhosh Kumar, M.; Chen, D.; Walmsley, J. C.; Holmen, A. *Catal. Commun.* **2008**, *20*, 747.

- (57) Yang, M.-L.; Zhu, Y.-A.; Fan, C.; Sui, Z.-J.; Chen, D.; Zhou, X.-G. *Phys. Chem. Chem. Phys.* **2011**, *13*, 3257.
- (58) Cortright, R. D.; Dumesic, J. A. *J. Catal.* **1994**, *148*, 771.
- (59) Spivey, J. J.; Roberts, G. W.; Goodwin, J. G.; Kim, S.; Rhodes, W. D. In *Catalysis*; Spivey, J. J.; Roberts, G. W., Eds.; The Royal Society of Chemistry, 2004; pp. 320–348.
- (60) Yang, M.-L.; Zhu, Y.-A.; Fan, C.; Sui, Z.-J.; Chen, D.; Zhou, X.-G. *J. Mol. Catal. A-Chem.* **2010**, *321*, 42.
- (61) Fiedorow, R. M. J.; Chahar, B. S.; Wanke, S. E. *J. Catal.* **1978**, *51*, 193.
- (62) Moulijn, J. A.; van Diepen, A. E.; Kapteijn, F. *Appl. Catal. A-Gen.* **2001**, *212*, 3.
- (63) Nagai, Y.; Hirabayashi, T.; Dohmae, K.; Takagi, N.; Minami, T.; Shinjoh, H.; Matsumoto, S. *J. Catal.* **2006**, *242*, 103.
- (64) Adler, S. F.; Keavney, J. J. *J. Phys. Chem.* **1960**, *64*, 208.
- (65) Lieske, H.; Lietz, G.; Spindler, H.; Völter, J. *J. Catal.* **1983**, *81*, 8.
- (66) Lee, T. J.; Kim, Y. G. *J. Catal.* **1984**, *90*, 279.
- (67) Le Normand, F.; Borgna, A.; Garetto, T. F.; Apesteguia, C. R.; Moraweck, B. *J. Phys. Chem.* **1996**, *100*, 9068.
- (68) Monzon, A.; Garetto, T. F.; Borgna, A. *Appl. Catal. A-Gen.* **2003**, *248*, 279.
- (69) Bocanegra, S. A.; Castro, A. A.; Guerrero-Ruíz, A.; Scelza, O. A.; de Miguel, S. R. *Chem. Eng. J.* **2006**, *118*, 161.
- (70) Zhang, Y.; Zhou, Y.; Shi, J.; Zhou, S.; Sheng, X.; Zhang, Z.; Xiang, S. *J. Mol. Catal. A-Chem.* **2014**, *381*, 138.
- (71) Casella, M. L.; Siri, G. J.; Santori, G. F.; Ferretti, O. A.; Ramirez-Corredores, M. M. *Langmuir* **2000**, *16*, 5639.
- (72) Siri, G. J.; Bertolini, G. R.; Casella, M. L.; Ferretti, O. A. *Mater. Lett.* **2005**, *59*, 2319.
- (73) De Miguel, S. R.; Bocanegra, S. A.; Vilella, I. M. J.; Guerrero-Ruíz, A.; Scelza, O. A. *Catal. Lett.* **2007**, *119*, 5.
- (74) Tasbihi, M.; Feyzi, F.; Amlashi, M. A.; Abdullah, A. Z.; Mohamed, A. R. *Fuel. Process. Technol.* **2007**, *88*, 883.
- (75) Rennard, R. J.; Freil, J. *J. Catal.* **1986**, *98*, 235.

- (76) Aguilar-Rios, G.; Valenzuela, M. A.; Armendariz, H.; Salas, P.; Domínguez, J. M.; Acosta, D. R.; Schifter, I. *Appl. Catal. A-Gen.* **1992**, *90*, 25.
- (77) Bocanegra, S. A.; Guerrero-Ruíz, A.; de Miguel, S. R.; Scelza, O. A. *Appl. Catal. A-Gen.* **2004**, *277*, 11.
- (78) Lai, Y.; He, S.; Li, X.; Sun, C.; Seshan, K. *Appl. Catal. A-Gen.* **2014**, *469*, 74.
- (79) Mironenko, R. M.; Belskaya, O. B.; Talsi, V. P.; Gulyaeva, T. I.; Kazakov, M. O.; Nizovskii, A. I.; Kalinkin, A. V.; Bukhtiyarov, V. I.; Lavrenov, A. V.; Likhobolov, V. A. *Appl. Catal. A-Gen.* **2014**, *469*, 472.
- (80) Cortright, R. D.; Dumesic, J. A. *Appl. Catal. A-Gen.* **1995**, *129*, 101.
- (81) Cortright, R. D.; Levin, P. E.; Dumesic, J. A. *Ind. Eng. Chem. Res.* **1998**, *37*, 1717.
- (82) Hill, J. M.; Cortright, R. D.; Dumesic, J. A. *Appl. Catal. A-Gen.* **1998**, *168*, 9.
- (83) Cortright, R. D.; Hill, J. M.; Dumesic, J. A. *Catal. Today* **2000**, *55*, 213.
- (84) Li, X.; Iglesia, E. *Chem. Commun.* **2008**, *8*, 594.
- (85) Lieske, H.; Sárkány, A.; Völter, J. *Appl. Catal.* **1987**, *30*, 69.
- (86) Wu, J.; Peng, Z.; Bell, A. T. *J. Catal.* **2014**, *311*, 161.
- (87) Virnovskaia, A.; Morandi, S.; Rytter, E.; Ghiotti, G.; Olsbye, U. *J. Phys. Chem. C* **2007**, *111*, 14732.
- (88) Nagaraja, B. M.; Shin, C.-H.; Jung, K.-D. *Appl. Catal. A-Gen.* **2013**, *467*, 211.
- (89) Boudart, M.; Aldag, A.; Benson, J. E.; Dougharty, N. A.; Girvin Harkins, C. *J. Catal.* **1966**, *6*, 92.
- (90) Cardona-Martinez, N.; Dumesic, J. A. *Adv. Catal.* **1992**, *38*, 149.
- (91) Ruiz-Martínez, J.; Sepúlveda-Escribano, A.; Anderson, J. A.; Rodríguez-Reinoso, F. *Catal. Today* **2007**, *123*, 235.
- (92) Ruiz-Martínez, J.; Coloma, F.; Sepúlveda-Escribano, A.; Anderson, J. A.; Rodríguez-Reinoso, F. *Catal. Today* **2008**, *133-135*, 35.
- (93) Ruiz-Martínez, J.; Sepúlveda-Escribano, A.; Anderson, J. A.; Rodríguez-Reinoso, F. *Phys. Chem. Chem. Phys.* **2009**, *11*, 917.
- (94) Soares, O. S. G. P.; Órfão, J. J. M.; Ruiz-Martínez, J.; Silvestre-Albero, J.; Sepúlveda-Escribano, A.; Pereira, M. F. R. *Chem. Eng. J.* **2010**, *165*, 78.
- (95) Yang, M.; Zhu, Y.; Zhou, X.; Sui, Z.; Chen, D. *ACS Catal.* **2012**, *2*, 1247.

- (96) Cortright, R. D.; Dumesic, J. A. *J. Catal.* **1995**, *157*, 576.
- (97) Natal-Santiago, M. A.; Podkolzin, S. G.; Cortright, R. D.; Dumesic, J. A. *Catal. Lett.* **1997**, *45*, 155.
- (98) Shen, J.; Hill, J. M.; Watwe, R. M.; Spiewak, B. E.; Dumesic, J. A. *J. Phys. Chem. B* **1999**, *103*, 3923.
- (99) Nykänen, L.; Honkala, K. *J. Phys. Chem. C* **2011**, *115*, 9578.
- (100) Gao, J.; Zhao, H.; Yang, X.; Koel, B. E.; Podkolzin, S. G. *Angew. Chem. Int. Ed.* **2014**, *53*, 3641.
- (101) Siri, G. J.; Ramallo-López, J. M.; Casella, M. L.; Fierro, J. L. G.; Requejo, F. G.; Ferretti, O. A. *Appl. Catal. A-Gen.* **2005**, *278*, 239.
- (102) Fearon, J.; Watson, G. W. *J. Mater. Chem.* **2006**, *16*, 1989.
- (103) Iglesias-Juez, A.; Beale, A. M.; Maaijen, K.; Weng, T. C.; Glatzel, P.; Weckhuysen, B. M. *J. Catal.* **2010**, *276*, 268.
- (104) Deng, L.; Shishido, T.; Teramura, K.; Tanaka, T. *Catal. Today* **2013**, *232*, 33.
- (105) Silvestre-Albero, J.; Sanchez-Castillo, M. A.; He, R.; Sepúlveda-Escribano, A.; Rodríguez-Reinoso, F.; Dumesic, J. A. *Catal. Lett.* **2001**, *74*, 17.
- (106) Silvestre-Albero, J.; Serrano-Ruiz, J. C.; Sepúlveda-Escribano, A.; Rodríguez-Reinoso, F. *Appl. Catal. A-Gen.* **2005**, *292*, 244.
- (107) De Cola, P. L.; Gläser, R.; Weitkamp, J. *Appl. Catal. A-Gen.* **2006**, *306*, 85.
- (108) Yu, C.; Xu, H.; Ge, Q.; Li, W. *J. Mol. Cat. A-Chem.* **2007**, *266*, 80.
- (109) Silvestre-Albero, J.; Serrano-Ruiz, J. C.; Sepúlveda-Escribano, A.; Rodríguez-Reinoso, F. *Appl. Catal. A-Gen.* **2008**, *351*, 16.
- (110) Vu, B. K.; Song, M. B.; Ahn, I. Y.; Suh, Y.-W.; Suh, D. J.; Kim, W.-I.; Koh, H.-L.; Choi, Y. G.; Shin, E. W. *Appl. Catal. A-Gen.* **2011**, *400*, 25.
- (111) Jablonski, E. L.; Castro, A. A.; Scelza, O. A.; de Miguel, S. R. *Appl. Catal. A-Gen.* **1999**, *183*, 189.
- (112) Sun, P.; Siddiqi, G.; Chi, M.; Bell, A. T. *J. Catal.* **2010**, *274*, 192.
- (113) Siddiqi, G.; Sun, P.; Galvita, V.; Bell, A. T. *J. Catal.* **2010**, *274*, 200.
- (114) Sun, P.; Siddiqi, G.; Vining, W. C.; Chi, M.; Bell, A. T. *J. Catal.* **2011**, *282*, 165.

- (115) Ballarini, A. D.; de Miguel, S. R.; Castro, A. A.; Scelza, O. A. *Appl. Catal. A-Gen.* **2013**, *467*, 235.
- (116) Frey, F. E.; Huppke, W. F. *Ind. Eng. Chem. Res.* **1933**, *25*, 54.
- (117) Olsbye, U.; Virnovskaia, A.; Prytz, Ø.; Tinnemans, S. J.; Weckhuysen, B. M. *Catal. Lett.* **2005**, *103*, 143.
- (118) Weckhuysen, B. M.; de Ridder, L. M.; Schoonheydt, R. A. *J. Phys. Chem* **1993**, *97*, 4756.
- (119) Weckhuysen, B. M.; Schoonheydt, R. A.; Mabbs, F. E.; Collison, D. *J. Chem. Soc. Faraday Trans.* **1996**, *92*, 2431.
- (120) Cavani, F.; Koutyrev, M.; Trifiro, F.; Bartolini, A.; Ghisletti, D.; Iezzi, R.; Santucci, A.; Del Piero, G. *J. Catal.* **1996**, *158*, 236.
- (121) Weckhuysen, B. M.; Wachs, I. E. *J. Chem. Soc. Faraday Trans.* **1996**, *92*, 1969.
- (122) Santhosh Kumar, M.; Hammer, N.; Ronning, M.; Holmen, A.; Chen, D.; Walmsley, J. C.; Oye, G. *J. Catal.* **2009**, *261*, 116.
- (123) Weckhuysen, B. M.; Wachs, I. E. *J. Phys. Chem* **1996**, *100*, 14437.
- (124) Weckhuysen, B. M.; Bensalem, A.; Schoonheydt, R. A. *J. Chem. Soc. Faraday Trans.* **1998**, *94*, 2011.
- (125) Weckhuysen, B. M.; Verberckmoes, A. A.; Debaere, J.; Ooms, K.; Langhans, I.; Schoonheydt, R. A. *J. Mol. Catal. A-Chem.* **2000**, *151*, 115.
- (126) Marcilly, C.; Delmon, B. *J. Catal.* **1972**, *24*, 336.
- (127) Ashmawy, F. M. *J. Chem. Soc. Faraday Trans.* **1980**, *76*, 2096.
- (128) Lugo, H. J.; Lunsford, J. H. *J. Catal.* **1985**, *91*, 155.
- (129) Grünert, W.; Saffert, W.; Feldhaus, R.; Anders, K. *J. Catal.* **1986**, *99*, 149.
- (130) Selwood, P. W. *J. Am. Chem. Soc.* **1970**, *92*, 39.
- (131) Cimino, A.; Cordischi, D.; De Rossi, S.; Ferraris, G.; Gazzoli, D.; Indovina, V.; Minelli, G.; Occhiuzzi, M.; Valigi, M. *J. Catal.* **1991**, *127*, 744.
- (132) Bruckner, A.; Radnik, J.; Hoang, D. L.; Lieske, H. *Catal. Lett.* **1999**, *60*, 183.
- (133) Michorczyk, P.; Ogonowski, J.; Zeńczak, K. *J. Mol. Catal. A-Chem.* **2011**, *349*, 1.

- (134) Mimura, N.; Okamoto, M.; Yamashita, H.; Oyama, S. T.; Murata, K. *J. Phys. Chem. B* **2006**, *110*, 21764.
- (135) Pérez-Reina, F. J.; Rodríguez-Castellón, E.; Jiménez-López, A. *Langmuir* **1999**, *15*, 8421.
- (136) Hakuli, A.; Kytökivi, A.; Krause, A. O. I. *Appl. Catal. A-Gen.* **2000**, *190*, 219.
- (137) Kytökivi, A.; Jacobs, J. P.; Hakuli, A.; Meriläinen, J.; Brongersma, H. H. *J. Catal.* **1996**, *162*, 190.
- (138) Michorczyk, P.; Pietrzyk, P.; Ogonowski, J. *Micropor. Mesopor. Mat.* **2012**, *161*, 56.
- (139) Hakuli, A.; Kytökivi, A.; Krause, A. O. I.; Suntola, T. *J. Catal.* **1996**, *161*, 393.
- (140) De Rossi, S.; Ferraris, G.; Fremoiotti, S.; Garrone, E.; Ghiotti, G.; Campa, M. C.; Indovina, V. *J. Catal.* **1994**, *148*, 36.
- (141) De Rossi, S.; Casaletto, M. P.; Ferraris, G.; Cimino, A.; Minelli, G. *Appl. Catal. A-Gen.* **1998**, *167*, 257.
- (142) Gaspar, A. B.; Brito, J. L. F.; Dieguez, L. C. *J. Mol. Catal. A-Chem.* **2003**, *203*, 251.
- (143) Zhang, X.; Yue, Y.; Gao, Z. *Catal. Lett.* **2002**, *83*, 19.
- (144) Airaksinen, S. M. K.; Kanervo, J. M.; Krause, A. O. I. *Stud. Surf. Sci. Catal.* **2001**, *136*, 153.
- (145) Puurunen, R. L.; Weckhuysen, B. M. *J. Catal.* **2002**, *210*, 418.
- (146) Nijhuis, T. A.; Tinnemans, S. J.; Visser, T.; Weckhuysen, B. M. *Phys. Chem. Chem. Phys.* **2003**, *5*, 4361.
- (147) Takehira, K.; Ohishi, Y.; Shishido, T.; Kawabata, T.; Takaki, K.; Zhang, Q.; Wang, Y. *J. Catal.* **2004**, *224*, 404.
- (148) Shi, X.; Ji, S.; Wang, K. *Catal. Lett.* **2008**, *125*, 331.
- (149) Michorczyk, P.; Ogonowski, J.; Niemczyk, M. *Appl. Catal. A-Gen.* **2010**, *374*, 142.
- (150) Ma, F.; Chen, S.; Wang, Y.; Chen, F.; Lu, W. *Appl. Catal. A-Gen.* **2012**, *427-428*, 145.
- (151) Shishido, T.; Shimamura, K.; Teramura, K.; Tanaka, T. *Catal. Today* **2012**, *185*, 151.

- (152) Yang, H.; Xu, L.; Ji, D.; Wang, Q.; Lin, L. *React. Kinet. Catal. Lett.* **2002**, *76*, 151.
- (153) De Rossi, S.; Ferraris, G.; Fremiotti, S.; Cimino, A.; Indovina, V. *Appl. Catal. A-Gen.* **1992**, *81*, 113.
- (154) Puurunen, R. L.; Beheydt, B. G.; Weckhuysen, B. M. *J. Catal.* **2001**, *204*, 253.
- (155) Weckhuysen, B. M.; De Ridder, L. M.; Grobet, P. J.; Schoonheydt, R. A. *J. Phys. Chem.* **1995**, *99*, 320.
- (156) Vuurman, M. A.; Hardcastle, F. D.; Wachs, I. E. *J. Mol. Catal.* **1993**, *84*, 193.
- (157) Simon, S.; van der Pol, A.; Reijerse, E. J.; Kentgens, A. P. M. *J. Chem. Soc. Faraday Trans.* **1995**, *91*, 1519.
- (158) El-Shobaky, H. G.; Ghozza, A. M.; El-Shobaky, G. A.; Mohamed, G. M. *Coll. Surf. A.* **1999**, *152*, 315.
- (159) Wachowski, L.; Kirszensztejn, P.; Lopatka, R.; Czajka, B. *Mater. Chem. Phys.* **1994**, *37*, 29.
- (160) Rossignol, S.; Kappenstein, C. *J. Inorg. Mater.* **2001**, *3*, 52.
- (161) De Rossi, S.; Ferraris, G.; Fremiotti, S.; Indovina, V.; Cimino, A. *Appl. Catal. A-Gen.* **1993**, *106*, 125.
- (162) Furdala, K.; Tilly, T. D. *J. Catal.* **2003**, *218*, 123.
- (163) Korhonen, S. T.; Airaksinen, S. M. K.; Banares, M. A.; Krause, A. O. I. *Appl. Catal. A-Gen.* **2007**, *333*, 30.
- (164) Martyanov, I.; Sayari, A. *Catal. Lett.* **2008**, *126*, 164.
- (165) Tsyganok, A.; Green, R. G.; Giorgi, J. B.; Sayari, A. *Catal. Commun.* **2007**, *8*, 2186.
- (166) Alcántara-Rodríguez, M.; Rodríguez-Castellón, E.; Jiménez-López, A. *Langmuir* **1999**, *15*, 1115.
- (167) Gnep, N. S.; Doyemet, J. Y.; Seco, A. M.; Ribeiro, F. R.; Guisnet, M. *Appl. Catal.* **1988**, *43*, 155.
- (168) Meriaudeau, P.; Naccache, C. *J. Mol. Catal.* **1989**, *50*, L7.
- (169) Price, G. L.; Kanazirev, V. *J. Catal.* **1990**, *126*, 267.
- (170) Meitzner, G. D.; Iglesia, E.; Baumgartner, J. E.; Huang, E. S. *J. Catal.* **1993**, *140*, 209.

- (171) Zheng, B.; Hua, W.; Yue, Y.; Gao, Z. *J. Catal.* **2005**, *232*, 143.
- (172) Nesterenko, N. S.; Ponomoreva, O. A.; Yuschenko, V. V.; Ivanova, I. I.; Testa, F.; Di Renzo, F.; Fajula, F. *Appl. Catal. A-Gen.* **2003**, *254*, 261.
- (173) Copéret, C. *Chem. Rev.* **2010**, *110*, 656.
- (174) Liu, Y.; Li, Z. H.; Lu, J.; Fan, K. *J. Phys. Chem. C* **2008**, *112*, 20382.
- (175) Chen, M.; Xu, J.; Su, F.; Liu, Y.; Cao, Y.; He, H.; Fan, K. *J. Catal.* **2008**, *256*, 293.
- (176) Xu, B.; Zheng, B.; Hua, W.; Yue, Y.; Gao, Z. *J. Catal.* **2006**, *239*, 470.
- (177) Xu, B.; Li, T.; Zheng, B.; Hua, W.; Yue, Y.; Gao, Z. *Catal. Lett.* **2007**, *119*, 283.
- (178) Michorczyk, P.; Ogonowski, J. *Appl. Catal. A-Gen.* **2003**, *251*, 425.
- (179) Pidko, E. A.; Hensen, E. J. M.; van Santen, R. A. *J. Phys. Chem. C* **2007**, *111*, 13068.
- (180) Takahara, I.; Saito, M.; Inaba, M.; Murata, K. *Catal. Lett.* **2004**, *96*, 29.
- (181) Rodríguez, L.; Romero, D.; Rodríguez, D.; Sánchez, J.; Domínguez, F.; Arteaga, G. *Appl. Catal. A-Gen.* **2010**, *373*, 66.
- (182) Sun, P.; Siddiqi, G.; Chi, M.; Bell, A. T. *J. Catal.* **2010**, *274*, 192.
- (183) Chao, K. J.; Wei, A. C.; Wu, H. C.; Lee, J. F. *Micropor. Mesopor. Mat.* **2000**, *35-36*, 413.
- (184) Butt, D. P.; Park, Y.; Taylor, T. N. *J. Nucl. Mater.* **1999**, *264*, 71.
- (185) Nakagawa, K.; Okamura, M.; Ikenaga, N.; Kobayashi, T. *Chem. Commun.* **1998**, *3*, 1025.
- (186) Nakagawa, K.; Kajita, C.; Okumura, K.; Ikenaga, N.; Nishitani-Gamo, M.; Ando, T.; Kobayashi, T.; Suzuki, T. *J. Catal.* **2001**, *203*, 87.
- (187) Li, H.; Yue, Y.; Miao, C.; Xie, Z.; Hua, W.; Gao, Z. *Catal. Commun.* **2007**, *8*, 1317.
- (188) Shen, Z.; Liu, J.; Xu, H.; Yue, Y.; Hua, W.; Shen, W. *Appl. Catal. A-Gen.* **2009**, *356*, 148.
- (189) Michorczyk, P.; Kuśtrowski, P.; Kolak, A.; Zimowska, M. *Catal. Commun.* **2013**, *35*, 95.
- (190) Iezzi, R.; Bartolini, A.; Buonomo, F. U.S. Patent 0198428, 2002.

- (191) Horiuti, I.; Polanyi, M. *Trans. Faraday Soc.* **1934**, *30*, 1164.
- (192) Biloen, P.; Dautzenberg, F. M.; Sachtler, W. M. H. *J. Catal.* **1977**, *50*, 77.
- (193) Chen, K.; Iglesia, E.; Bell, A. T. *J. Catal.* **2000**, *192*, 197.
- (194) Li, Q.; Sui, Z.; Zhou, X.; Chen, D. *App. Catal. A-Gen.* **2011**, *398*, 18.
- (195) Sokolov, S.; Stoyanova, M.; Rodemerck, U.; Linke, D.; Kondratenko, E. V. *J. Catal.* **2012**, *293*, 67.
- (196) Hauser, A. W.; Gomes, J.; Bajdich, M.; Head-Gordon, M.; Bell, A. T. *Phys. Chem. Chem. Phys.* **2013**, *15*, 20727.
- (197) Galvita, V.; Siddiqi, G.; Sun, P.; Bell, A. T. *J. Catal.* **2010**, *271*, 209.
- (198) Virnovskaia, A.; Rytter, E.; Olsbye, U. *Ind. Eng. Chem. Res.* **2008**, *47*, 7167.
- (199) Zaera, F.; Chrysostomou, D. *Surf. Sci.* **2000**, *457*, 71.
- (200) Zaera, F.; Chrysostomou, D. *Surf. Sci.* **2000**, *457*, 89.
- (201) Chrysostomou, D.; Zaera, F. *J. Phys. Chem. B* **2001**, *105*, 1003.
- (202) Valcarcel, A.; Ricart, J.; Clotet, A.; Illas, F.; Markovits, A.; Minot, C. *J. Catal.* **2006**, *241*, 115.
- (203) Watwe, R. M.; Spiewak, B. E.; Cortright, R. D.; Dumesic, J. A. *J. Catal.* **1998**, *180*, 184.
- (204) Chrysostomou, D.; Chou, A.; Zaera, F. *J. Phys. Chem. B* **2001**, *105*, 5968.
- (205) Ohtani, T.; Kubota, J.; Kondo, J. N.; Hirose, C.; Domen, K. *J. Phys. Chem. B* **1999**, *103*, 4562.
- (206) De La Cruz, C.; Sheppard, N. *J. Chem. Soc. Faraday Trans.* **1997**, *93*, 3569.
- (207) Cremer, P. S.; Su, X.; Shen, Y. R.; Somorjai, G. A. *J. Am. Chem. Soc.* **1996**, *118*, 2942.
- (208) Cremer, P. S.; Stanners, C.; Niemantsverdriet, J. W.; Shen, Y. R.; Somorjai, G. A. *Surf. Sci.* **1995**, *328*, 111.
- (209) Zaera, F.; Janssens, T. V. W.; Ofner, H. *Surf. Sci.* **1996**, *368*, 371.
- (210) Shen, J.; Hill, J. M.; Watwe, R. M.; Spiewak, B. E.; Dumesic, J. A. *J. Phys. Chem. B* **1999**, *103*, 3934.
- (211) Nykanen, L.; Honkala, K. *ACS Catal.* **2013**, *3*, 3026.

- (212) Airaksinen, S. M. K.; Harlin, M. E.; Krause, A. O. I. *Ind. Eng. Chem. Res.* **2002**, *41*, 5619.
- (213) Lillehaug, S.; Børve, K. J.; Sierka, M.; Sauer, J. J. *Phys. Org. Chem.* **2004**, *17*, 990.
- (214) Lillehaug, S.; Jensen, V. R.; Børve, K. J. *J. Phys. Org. Chem.* **2006**, *19*, 25.
- (215) Carra, S.; Forni, L.; Vintani, C. *J. Catal.* **1967**, *9*, 154.
- (216) Kao, J. Y.; Piet-Lahanier, H.; Walter, E.; Happel, J. J. *Catal.* **1992**, *133*, 383.
- (217) Suzuki, I.; Kaneko, Y. *J. Catal.* **1977**, *47*, 239.
- (218) Shee, D.; Sayari, A. *Appl. Catal. A-Gen.* **2010**, 389, 155.
- (219) Airaksinen, S. M. K.; Banares, M. A.; Krause, A. O. I. *J. Catal.* **2005**, *230*, 507.
- (220) Kazansky, V. B.; Subbotina, I. R.; Pronin, A. A.; Schlögl, R.; Jentoft, F. C. *J. Phys. Chem. B* **2006**, *110*, 7975.
- (221) Noda, H.; Tone, S.; Otake, T. *J. Chem. Eng. Jap.* **1973**, *7*, 1974.
- (222) Toei, R.; Nakanishi, K.; Yamada, K.; Okazaki, M. *J. Chem. Eng. Jap.* **1975**, *8*, 131.
- (223) Swift, H. E.; Beuther, H.; Rennard, R. J. *Ind. Eng. Chem. Prod. Res. Dev.* **1976**, *15*, 131.
- (224) Menon, P. G. *J. Mol. Catal.* **1990**, *59*, 207.
- (225) Chen, Y.; Vlachos, D. G. *J. Phys. Chem. C* **2010**, *114*, 4973.
- (226) Larsson, M.; Hulten, M.; Blekkan, E. A.; Andersson, B. *J. Catal.* **1996**, *164*, 44.
- (227) Li, Q.; Sui, Z.; Zhou, X.; Zhu, Y.; Zhou, J.; Chen, D. *Top. Catal.* **2011**, *54*, 888.
- (228) Wang, B.; Ma, X.; Caffio, M.; Schaub, R.; Li, W.-X. *Nano Lett.* **2011**, *11*, 424.
- (229) Otero, G.; González, C.; Pinardi, a. L.; Merino, P.; Gardonio, S.; Lizzit, S.; Blanco-Rey, M.; Van de Ruit, K.; Flipse, C. F. J.; Méndez, J.; de Andrés, P. L.; Martín-Gago, J. A. *Phys. Rev. Lett.* **2010**, *105*, 216102.
- (230) Land, T. A.; Michely, T.; Behm, R. J.; Hemminger, J. C. *Surf. Sci.* **1992**, *264*, 261.
- (231) Tinnemans, S. J.; Kox, M. H. F.; Nijhuis, T. A.; Visser, T.; Weckhuysen, B. M. *Phys. Chem. Chem. Phys.* **2005**, *7*, 211.

- (232) Li, Q.; Sui, Z.; Zhou, X.; Chen, D. *Appl. Catal. A-Gen.* **2011**, 398, 18.
- (233) Sattler, J. J. H. B.; Beale, A. M.; Weckhuysen, B. M. *Phys. Chem. Chem. Phys.* **2013**, 15, 12085.

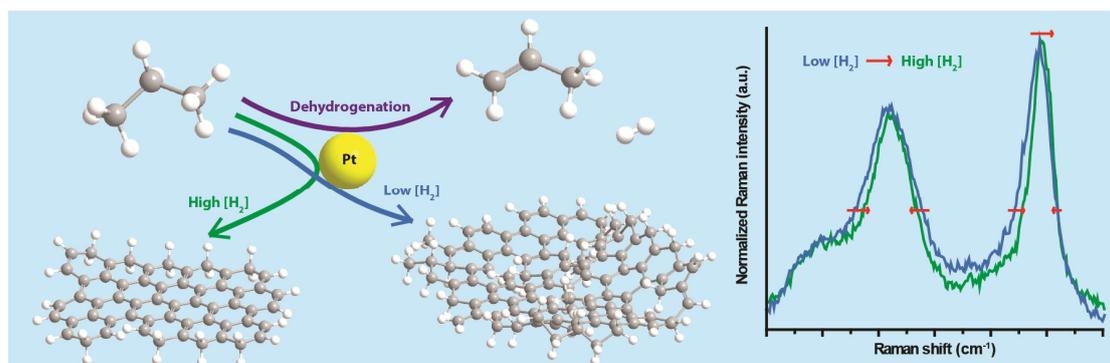


## **Part 1**



## Chapter 2

# Operando Raman Spectroscopy during the Deactivation of Pt and Pt-Sn/Al<sub>2</sub>O<sub>3</sub> Propane Dehydrogenation Catalysts in a Lab-Scale Setup



The deactivation of 0.5 wt% Pt/Al<sub>2</sub>O<sub>3</sub> and 0.5 wt% Pt - 1.5 wt% Sn/Al<sub>2</sub>O<sub>3</sub> catalysts was studied by operando Raman spectroscopy during the dehydrogenation of propane. By altering the reaction feed composition, the deposition of carbon species could be either suppressed or enhanced, influencing the performance of the catalyst materials. A high H<sub>2</sub> partial pressure resulted in changes in the position, intensity and width of the characteristic Raman bands of coke deposits. These trends imply that smaller graphitic crystallites were formed, which contained less defects.

This Chapter is based on the manuscript: J.J.H.B. Sattler, A.M. Beale, B.M. Weckhuysen, Operando Raman spectroscopic study on the deactivation of Pt and Pt-Sn/Al<sub>2</sub>O<sub>3</sub> propane dehydrogenation catalysts, *Phys. Chem. Chem. Phys.* **15** (2013) 12095-12103.

## 2.1 Introduction

As was discussed in Chapter 1, the deposition of carbon is the first and foremost cause of short-term catalyst deactivation for alkane dehydrogenation catalysts.<sup>1-4</sup> This so-called coking process originates from the polymerization of (strongly) adsorbed reaction intermediates on the catalyst surface, forming large, graphite-like structures that cover alkane dehydrogenation sites and hamper the diffusion of reactants.<sup>5-7</sup> Several parameters are known to influence the process. For example, the composition of the gas atmosphere is known to be important, as high hydrocarbon partial pressures result in more severe catalyst coking, while the coking process can be inhibited by the addition of steam or hydrogen.<sup>4,8,9</sup> Secondly, doping a Pt/Al<sub>2</sub>O<sub>3</sub> catalysts with Sn results in a more robust alkane dehydrogenation catalyst, as the catalyst remains active for longer times.<sup>10-13</sup>

In this Chapter, the deposition of carbon on a Pt/Al<sub>2</sub>O<sub>3</sub> and a Pt-Sn/Al<sub>2</sub>O<sub>3</sub> catalyst is compared during the dehydrogenation of propane by operando Raman spectroscopy, thermogravimetric analysis (TGA) and on-line gas chromatography (GC). The advantage of using operando Raman spectroscopy is that the technique is non-invasive, allowing to monitor the deactivation of the catalyst during the actual dehydrogenation reaction.<sup>12,14-17</sup> Coke species formed on the catalyst typically display two distinct Raman signals, at approximately 1320 and 1590 cm<sup>-1</sup>, commonly referred to as the D and G band, respectively.<sup>18-20</sup> These bands originate from the ring breathing vibration of a perfect graphitic lattice (G) and sp<sup>3</sup> hybridized carbon atoms at the edges of graphene sheets or at defects within in the graphene lattice (D). By continuously collecting Raman spectra, changes over time in the nature of these carbon deposits are observed. These spectra can be correlated with the activity data obtained by on-line GC analysis. Lastly, the amount of coke can be quantified by isolating the deactivated catalyst from the reactor and measuring the loss of weight with TGA during the combustion of the coke.

In addition, the effect of the composition of the reaction mixture on the coke deposition is studied by varying the ratio of hydrogen to propane or propylene. In literature, the coke inhibiting effect of hydrogen on the formation of carbon deposits has already been described, and was attributed to the competitive adsorption of

hydrogen and hydrocarbons: as the partial pressure of hydrogen is increased, the amount of adsorbed hydrocarbons on the catalyst surface decreases, effectively reducing the likelihood that reaction intermediates oligomerize towards coke precursors.<sup>21,22</sup> Density functional theory (DFT) studies have been performed on the adsorption of hydrogen, propane, propylene and carbon (coke) on Pt and Pt-Sn surfaces.<sup>23–25</sup> These calculations revealed that both hydrogen and carbon would adsorb more strongly on Pt than propylene or propane. The heat of adsorption of propylene and propane is further decreased with the addition of Sn, while the adsorption of hydrogen or coke was not significantly altered.<sup>26–28</sup> Nevertheless, the effect of hydrogen on the nature of the carbon deposits formed is not yet understood, which is the topic of this Chapter.

## 2.2 Experimental

### 2.2.1 Catalyst Preparation

0.5 wt% Pt/Al<sub>2</sub>O<sub>3</sub> and 0.5 wt% Pt - 1.5 wt% Sn/Al<sub>2</sub>O<sub>3</sub> catalysts were prepared by (co-) impregnating an ethanol solution (99.9%) containing H<sub>2</sub>PtCl<sub>6</sub>×(H<sub>2</sub>O)<sub>x</sub> (39.96 wt% Pt, Degussa) and SnCl<sub>2</sub>×(H<sub>2</sub>O)<sub>2</sub> (Merck, p.a.) onto a commercial alumina carrier (Norton, 89 m<sup>2</sup>/g). The catalyst was dried by evaporating the ethanol by using a rotavap (50 °C, 20 mbar) and the obtained catalysts were calcined at 560 °C for 3 h.

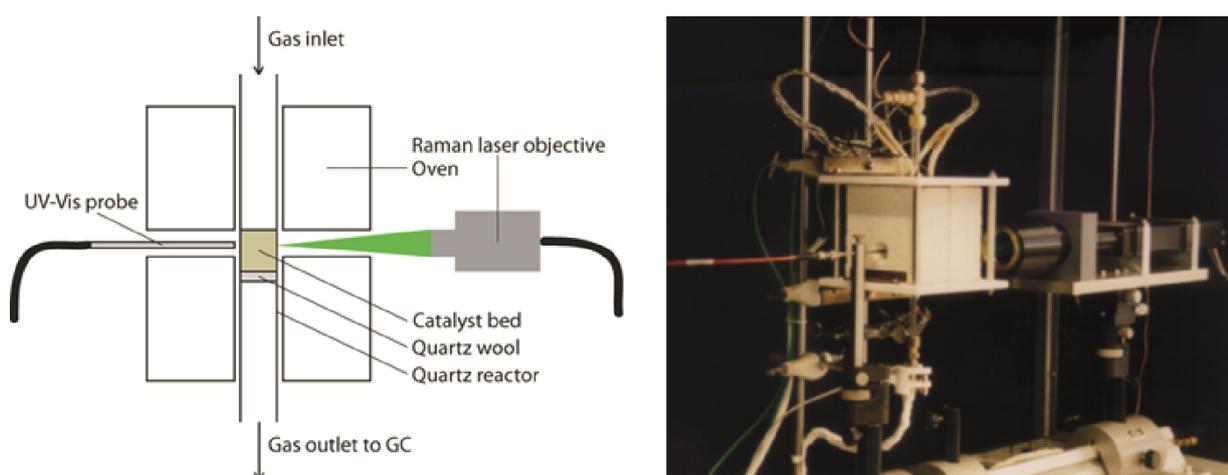


**Figure 2.1.** Scheme and photograph for the combined operando Raman/UV-Vis spectroscopy setup. The gas flow leaving the reactor is analyzed by an on-line GC.

### 2.2.2 Dehydrogenation Reaction

Catalytic data and operando Raman spectroscopy data were obtained with a combined Raman/UV-Vis spectroscopy setup equipped with an on-line gas chromatograph, which is shown in Figure 2.1. A packed bed reactor, consisting of a cylindrical quartz tube is placed inside an oven. Inside the tube, 0.3 g of catalyst material is loaded on top of a bed of quartz wool. The quartz reactor includes optical grade windows, that are aligned with two holes in the oven. A Kaiser Optical Systems Inc. Raman spectrometer with a 532 nm laser is aligned with one of these holes and an Avantes optical probe connected to a deuterium-halogen light source and Avantes 2048 UV-Vis spectrometer to the other. The reactor is connected with an Interscience compact GC, equipped with a flame ionization detector (FID, Porabond-Q column) and a thermal conductivity detector (TCD, Carboxan column) to study the composition of the reactor stream. The former detector is used to quantify the flammable gases in the product stream (with the exception of hydrogen), which are  $\text{CH}_4$ ,  $\text{C}_2\text{H}_4$ ,  $\text{C}_2\text{H}_6$ ,  $\text{C}_3\text{H}_6$  and  $\text{C}_3\text{H}_8$ . The latter detector is used to quantify the other gases present in the system based on thermal conductivity:  $\text{H}_2$ ,  $\text{O}_2$ ,  $\text{CO}$ ,  $\text{CH}_4$  and  $\text{CO}_2$ . The chromatograph is set up to provide optimal separation between the signals of the aforementioned molecules and producing one chromatograph every 5 min.

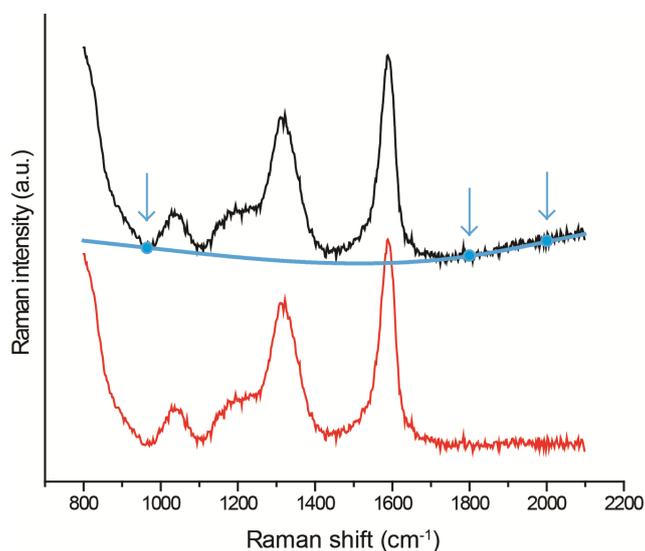


**Figure 2.2.** The deconvolution operation is performed by taking three points at fixed positions (blue spots) on the original spectrum (black line). A smooth line is drawn through these points, which then serves as a baseline (blue line). The resultant spectrum (red line) is then further analyzed.

For each experiment the catalyst first has to be pretreated in order to reduce any catalytically inactive  $\text{PtO}_x$ . This is done by increasing the temperature from room temperature to 600 °C with a ramp of 10 °C/min under a  $\text{H}_2$  flow of 9 ml/min, after which the reactor is purged with He for 5 min. During the second step, the actual dehydrogenation reaction takes place at 600 °C for 6 h, by flowing 9 ml/min consisting of 100, 75, 50 or 25% of either propane or propylene diluted with  $\text{H}_2$  (WHSV = 3.2 for 100% propane). The flow is humidified by 9 v/v% steam, which reduces coke deposition. Following the reaction, the reactor is flushed for 5 min with He, and the coked catalyst regenerated by flowing 9 ml/min of a mixture of 20%  $\text{O}_2$  in He for 2 h. In all cases, this treatment was sufficient to remove all the carbon deposited, as no  $\text{CO}_x$  is detected at the end of the regeneration step. After flushing the reactor again with He, the catalyst is reactivated by introducing a flow of 20%  $\text{H}_2$  in He in the reactor for 1 h. These steps are repeated until 10 dehydrogenation cycles are performed.

For the thermogravimetical analysis, a Perkin-Elmer 1 instrument was used. For this purpose, 10-25 mg of the spent catalysts, obtained after 3 propane dehydrogenation-regeneration cycles, was heated from room temperature to 800 °C at a rate of 10 °C under 10 ml/min of oxygen.

### 2.2.3 Raman Spectroscopy and Data Analysis

Data acquisition was done using the Holograms 4.0 program with an exposure time of 7 s and 11 accumulations. For each Raman spectrum collected, a separate background is measured, and the cosmic ray filter option in the software is used to prevent spikes in the Raman spectra, resulting in one spectrum being collected every 5 min. The resulting Raman spectra are processed with the Fityk v.0.8.6 software package, by means of a baseline correction in order to subtract the fluorescence background and perform a deconvolution operation.

The baseline correction is necessary because the fluorescence background varies strongly during the experiment, which would make it very challenging to compare the spectra otherwise. Nevertheless, performing this subtraction in a reproducible manner is very important. The Fityk program draws a line through three specific points in the spectra, at 950, 1800 and 2000  $\text{cm}^{-1}$  (shifts where no Raman signal is observed),

which is subtracted from the original spectrum. As is shown in Figure 2.2, this procedure does not alter the shape or intensity of the bands in the region of interest, i.e. 1000-1700  $\text{cm}^{-1}$ .

When the background subtracted spectrum is obtained, a deconvolution operation is performed to describe the position, width and intensity of the respective bands more effectively. A set of bands is manually fitted, after which the program optimizes the fit.

## 2.3 Results and Discussion

### 2.3.1 Effect of Hydrogen Addition

In Fig. 2.3a the conversion of propane during the first, third and tenth dehydrogenation-regeneration cycle of the Pt/ $\text{Al}_2\text{O}_3$  catalyst at different propane/ $\text{H}_2$  ratios is shown. A strong effect of the hydrogen concentration was observed, as an increase in hydrogen partial pressure results in a higher conversion of propane. However, the drop of conversion within a cycle, which is caused by carbon deposition and Pt sintering, remains unaffected. In Figure 2.3b, the conversion as obtained at the end of each of the 10 dehydrogenation cycles is shown. The end of the different cycles were compared, since the catalyst has attained a relatively steady state here. The conversion measured drops significantly for the first three or four cycles, after which it remains more or less stable. The drop between cycles is explained by sintering of the Pt nanoparticles, as was described in earlier work.<sup>12</sup>

The corresponding selectivity towards propylene is shown in Figure 2.3c and d. During the first two cycles, the addition of  $\text{H}_2$  has a negative effect on the selectivity towards propylene: at the start of the first cycle, only cracking products are detected in the case where 25% propane is present in the feed. However, for the following cycles the selectivity is improved to the point where hydrogen addition becomes beneficial. For the tenth cycle for example, the selectivity to propylene is 43% in the absence of hydrogen, while this is increased to 73% by adding 50% hydrogen in the feed. The corresponding yield is shown in Figure 2.3e and f. From the fourth cycle onward, the yield increases as more  $\text{H}_2$  is added.

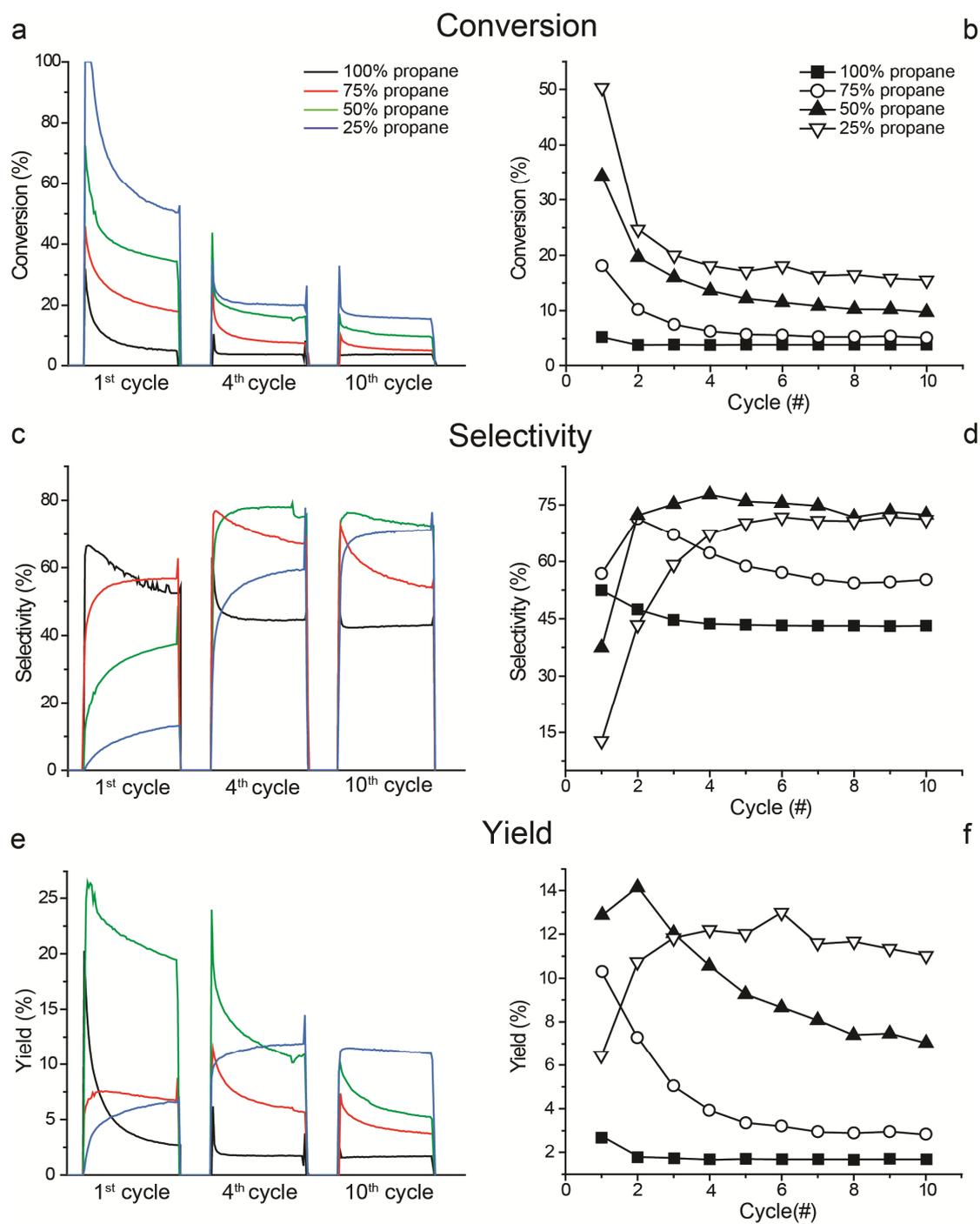


**Figure 2.3.** Propane conversion (a), selectivity to propylene (c) and propylene yield (e) of a Pt/Al<sub>2</sub>O<sub>3</sub> catalyst for the first, third and tenth dehydrogenation cycle at different H<sub>2</sub> and propane ratios. Additionally, the values for conversion (b), selectivity (d) and yield (f), obtained at the end of each of the 10 cycles are shown for the different H<sub>2</sub> and propane ratios.

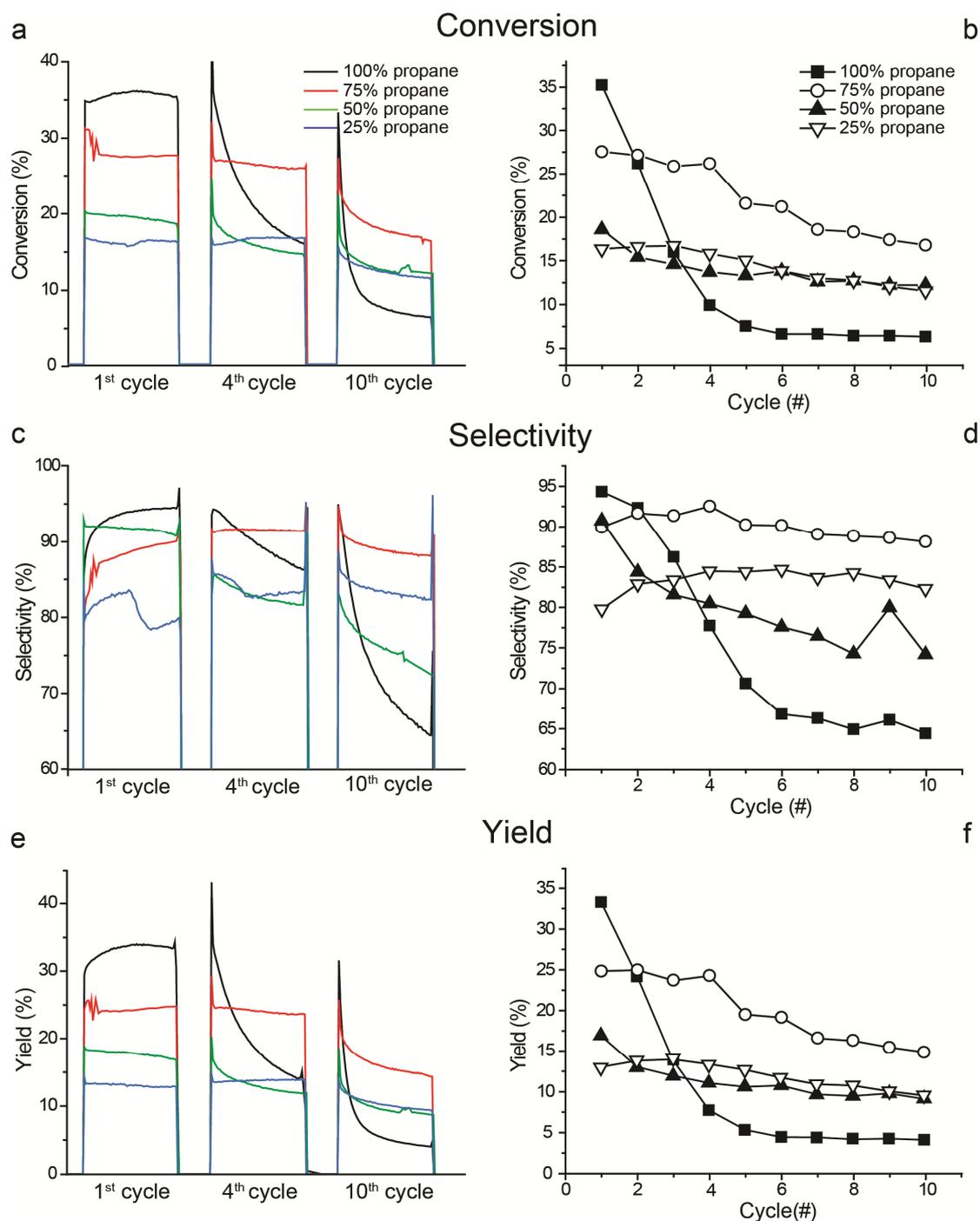


**Figure 2.4.** Propane conversion (a), selectivity to propylene (c) and propylene yield (e) of a Pt-Sn/Al<sub>2</sub>O<sub>3</sub> catalyst for the first, third and tenth dehydrogenation cycle at different H<sub>2</sub> and propane ratios. Additionally, the values for conversion (b), selectivity (d) and yield (f), obtained at the end of each of the 10 cycles are shown for the different H<sub>2</sub> and propane ratios.

In Figure 2.4, the catalytic data of the Pt-Sn/Al<sub>2</sub>O<sub>3</sub> catalyst is shown for the 10 cycle dehydrogenation experiment. The conversion (a), selectivity (c) and yield (e) for the first, third and tenth cycle are considerably higher compared to the Pt/Al<sub>2</sub>O<sub>3</sub>, which is in agreement with what has been reported in literature.<sup>12,29</sup> The positive effects of Sn addition are explained by reduced coke formation and the so-called flow off effect, which consists of the migration of coke precursors away from the metallic particles to the support, effectively preventing the blocking of the active sites by coke. The respective values for the conversion, selectivity and yield obtained at the end of each cycle are shown in Fig. 2.4b, d and f, respectively. The addition of H<sub>2</sub> increases catalyst stability, meaning the drop of conversion and selectivity within, but also between cycles, is less. The feed containing 100% propane displayed the highest conversion and selectivity during the first cycle, but drops strongly during subsequent cycles. With the addition of hydrogen, this drop becomes much smaller and from the 4<sup>th</sup> cycle onwards, a higher conversion and selectivity is obtained, regardless of the concentration of hydrogen. In the end, the Pt-Sn catalyst performs best when a feed consisting of 75% propane and 25% hydrogen is used.

Because the total flow of gases remains constant, the flow of propane is effectively diluted by hydrogen. Therefore, the use of nitrogen as a diluent was investigated. It was found that nitrogen addition did not change the conversion and selectivity of the propane dehydrogenation catalysts discussed above (additionally no changes were observed in the Raman spectra). The trends observed are therefore caused by the addition of hydrogen, which affect the chemistry of the system. As hydrogen is produced by the dehydrogenation reaction, the addition of hydrogen to the feed should shift the equilibrium of the reaction to the competing hydrogenation reaction, effectively reducing propylene yield. Indeed, when the theoretical yield was calculated, the propylene yield was 27% and 47% for the feed consisting of 100% propane and 25% propane respectively, at 600 °C and 1 bar. The catalyst operates therefore closer to the equilibrium when hydrogen is added to the feed.

Several processes that affect catalyst deactivation may be influenced by an increase in the partial pressure of hydrogen. First of all, the increase in hydrogen partial pressure would lead to a higher concentration of adsorbed hydrogen on the platinum, effectively reducing the probability of the formation of coke precursors that make dehydrogenation sites permanently unavailable for the dehydrogenation reaction.

In addition, Iglesia-Juez et al. have previously shown by operando high energy resolution fluorescence detected X-ray absorption spectroscopy (HERFD-XAS), that sintering of the nanoparticles occurs during the calcination step.<sup>12</sup> During this step, the Pt-Sn alloy segregates into SnO<sub>2</sub> and Pt nanoparticles. During the following reduction and dehydrogenation step, the Pt-Sn alloy is reformed. During the repeated cycling, the Pt-Sn nanoparticles become enriched with Sn, reducing the amount of Pt on the exterior of the nanoparticles. As less active sites are in each other's proximity, the probability of the polymerization of reaction intermediates becomes less likely. As a second effect, Sn donates electron density to Pt, reducing the strength of adsorption of propane and other hydrocarbons. The formation of the alloy is due to hydrogen spillover from the Pt to the SnO<sub>x</sub> located on the support, reducing the Sn which gets incorporated in the nanoparticle. The reduction of the SnO<sub>x</sub> during the dehydrogenation step is possibly affected by the partial pressure of hydrogen. Finally, as the coke on the deactivated catalyst is combusted, a significant amount of heat is released. This results in hot spots on the catalyst surface that may increase Pt sintering. Therefore, when less coke is formed, the sintering of Pt nanoparticles is reduced, therefore resulting in a more stable catalyst.

### 2.3.2 Effect of Hydrogen on Propylene Hydrogenation

On the same catalyst materials, the hydrogenation of propylene is attempted under identical reaction conditions. For both catalyst materials the selectivity to propane and conversion of propylene increased as more hydrogen was added to the feed. Catalyst cycling decreased the conversion for all propylene/hydrogen ratios. The Pt-Sn/Al<sub>2</sub>O<sub>3</sub> catalyst again displayed a higher conversion and selectivity compared to the Pt/Al<sub>2</sub>O<sub>3</sub> catalyst. The deactivation behavior of both catalysts is very similar during the hydrogenation of propylene as compared to the dehydrogenation of propane. The Pt-Sn/Al<sub>2</sub>O<sub>3</sub> catalyst is more resistant to catalyst deactivation during the first few cycles. Concluding, the same processes of catalyst deactivation are likely responsible.

### 2.3.3 Coke Analysis by Operando Raman Spectroscopy

From the activity measurements discussed above it is clear that both the addition of Sn and hydrogen influence the deposition of coke on the catalysts. Operando Raman

spectroscopy is a valuable tool to find links between the activity data discussed before and the chemical nature of the coke deposits. In Figure 2.5 therefore Raman spectra obtained during the first, third and tenth dehydrogenation cycle on the Pt/Al<sub>2</sub>O<sub>3</sub> are shown. The evolution and general shape of the Raman bands shown in the Figure are typical for all experiments discussed in this Chapter. Four different bands can be distinguished: the first two bands at 1040 and 1166 cm<sup>-1</sup> bands originate from the quartz reactor, while the other two bands, the D band at ~1320 cm<sup>-1</sup> and the G band at ~1590 cm<sup>-1</sup>, have been reported for a wide array of carbon materials and are assigned to the coke deposits.<sup>20,30-33</sup> These bands appear immediately after the catalyst material is exposed to propane, and their intensity increases very rapidly for the first few minutes of the dehydrogenation reaction. After this short period, the intensity of the

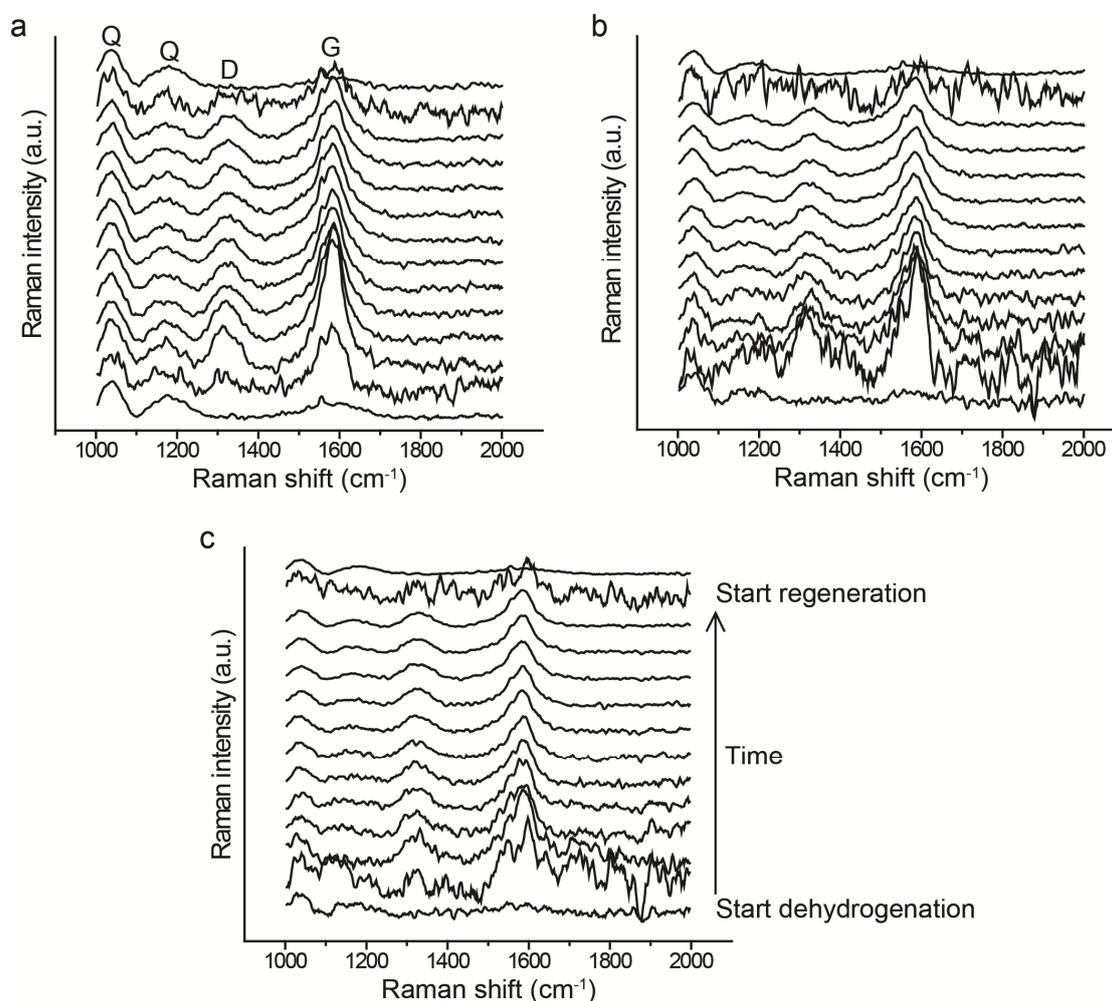


**Figure 2.5.** Operando Raman spectra obtained during the first, third and tenth dehydrogenation cycle, including the regeneration in air, over the Pt/Al<sub>2</sub>O<sub>3</sub> catalyst with a feed consisting of 100% propane.

bands drops to stabilize after approximately one hour into the reaction. This drop in intensity is caused by the catalyst slowly turning black, resulting in self-absorption of the Raman signal. When the catalyst is regenerated, both the D and G bands disappear. During the initial stages of the dehydrogenation, as well as during the regeneration step, a strong fluorescence background is observed that results in the relatively low signal to noise ratio of these spectra. The composition of the feed and the catalyst material under study influence the shape of the coke bands in the Raman spectra.

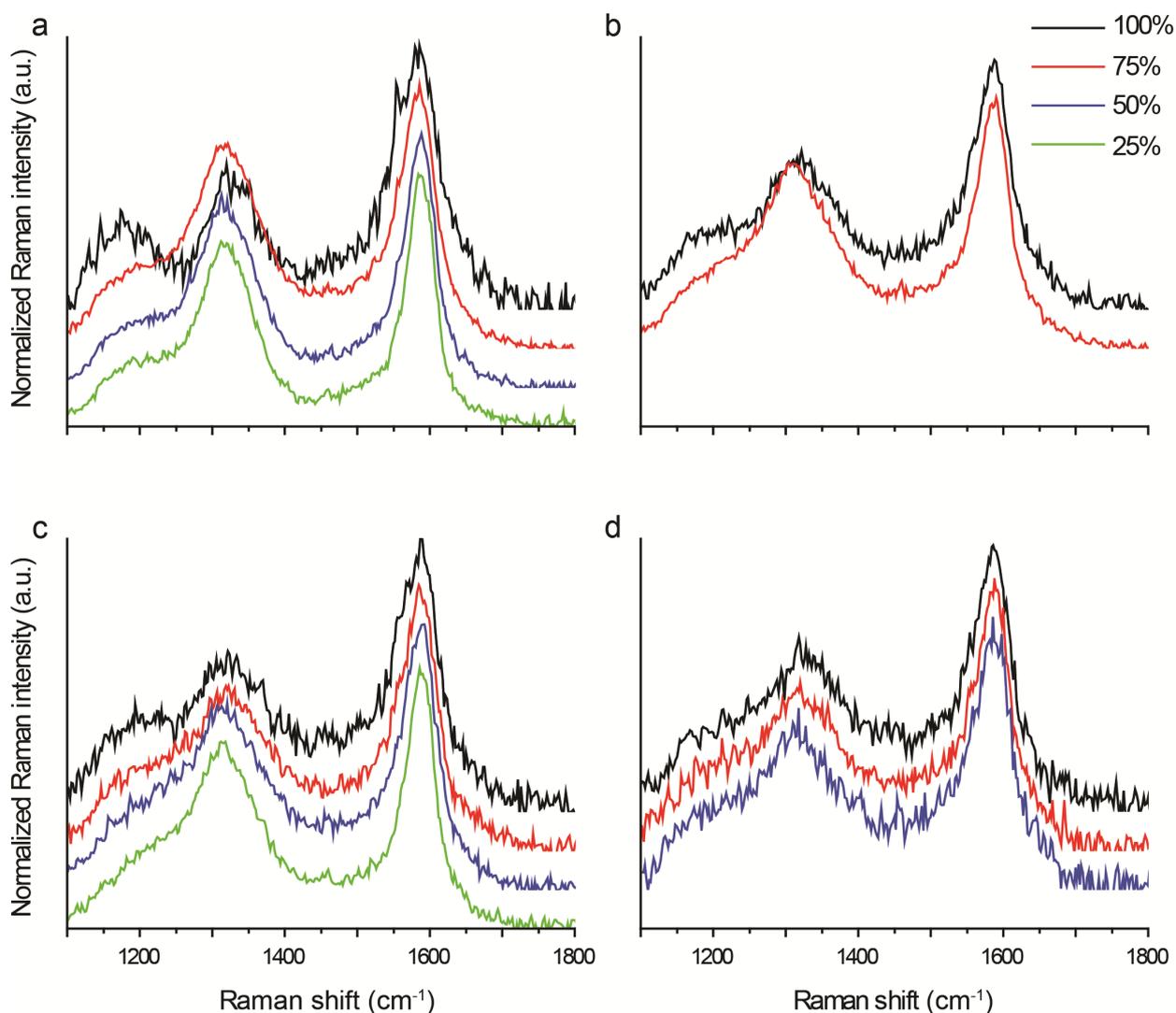


**Figure 2.6.** Operando Raman spectra of coked Pt/Al<sub>2</sub>O<sub>3</sub> (a, c) and Pt-Sn/Al<sub>2</sub>O<sub>3</sub> (b, d) catalyst materials with feeds of propane (a, b) and propylene (c, d) for different hydrocarbon- hydrogen ratios. The spectra were all obtained at the end of the first reaction cycle. The color of the spectra indicates the concentration of the hydrocarbon in the feed.

In Figure 2.6, operando Raman spectra of the deactivated Pt/Al<sub>2</sub>O<sub>3</sub> (a, c) and Pt-Sn/Al<sub>2</sub>O<sub>3</sub> catalysts (b, d) are shown. These spectra were collected at the end of the first cycle, where the catalyst is more or less at a steady state. The feeds used in this instance consisted of propane (a, b) and propylene (c, d) diluted with 0, 25, 50 or 75% of hydrogen. As the intensity of the Raman signal differs between the experiments, the signal has been normalized with respect to the G band, which had the highest intensity in all cases. In some experiments the coke signal could not be distinguished from the (very strong) fluorescent background, and are therefore omitted from the Figure. When examining the effect of the increasing hydrogen content in the feed, some trends are observed. First of all, the D band becomes more prominent with respect to the G band. Secondly, the Raman bands become narrower and their position appears to shift. As these observations are made with the naked eye a more thorough analysis is required. Careful analysis of coke related compounds, such as soot, graphene, graphite and carbon nanofibers has shown that the Raman spectra of these materials consist of an overlapping set of four or five bands in the 1200-1650 cm<sup>-1</sup> region.<sup>20,34,35</sup> Similar data analysis was therefore performed on the coke deposits reported herein by deconvoluting the spectra. A combination of 6 different bands was used to fit the Raman spectra, of which two originated from the quartz of the reactor, and four bands from the carbonaceous deposits. The parameters used for this fitting operation are summarized in Table 2.1. The set of Raman bands used for this fitting operation could be applied to all spectra obtained.

For the analysis of the coke Raman bands the nomenclature, which was proposed by Sadezky et al. for the analysis of soot-based samples, was used.<sup>34</sup> In this interpretation, the so-called G band at ~1587 cm<sup>-1</sup> corresponds with the doubly degenerate phonon mode with a E<sub>2g</sub> symmetry at the Brillouin zone for a perfect graphite lattice. The second most intense band is the D<sub>1</sub> band, which originates from a double resonant Raman scattering process consisting of a defect and an in-plane transverse optic phonon mode in the graphene lattice. The intensity of the D<sub>1</sub> band relative to the G band is increased as the amount of defects in the graphitic lattice increases or when the size of the graphite crystallites decreases, since the latter results in a relatively stronger contribution of the graphene layer edges. In addition, The D<sub>3</sub> band is believed to correspond to amorphous carbon, while the D<sub>4</sub> band is assigned to disordered graphitic lattice of an A<sub>1g</sub> symmetry. The D<sub>2</sub> band (1620 cm<sup>-1</sup>), as proposed by Sadezky and coworkers,<sup>34</sup> was not detected in the Raman spectra of the coke

**Table 2.1.** Characteristics of the Raman bands obtained by the deconvolution operation, with the nomenclature proposed by Sadezky et al.<sup>34</sup>

Band	Position (cm <sup>-1</sup> )	Shape	Assignment
Q <sub>1</sub>	1040	Gaussian	Si-O stretch of quartz
Q <sub>2</sub>	1166	Gaussian	Si-O stretch of quartz
G	1587	Lorentzian	Ring breathing vibration of ideal graphite lattice
D <sub>1</sub>	1320	Lorentzian	Ring vibrations of disordered graphitic lattice (graphene layer edges and defects in graphite plane)
D <sub>3</sub>	1500	Gaussian	Amorphous carbon
D <sub>4</sub>	1220	Gaussian	Disordered graphitic lattice

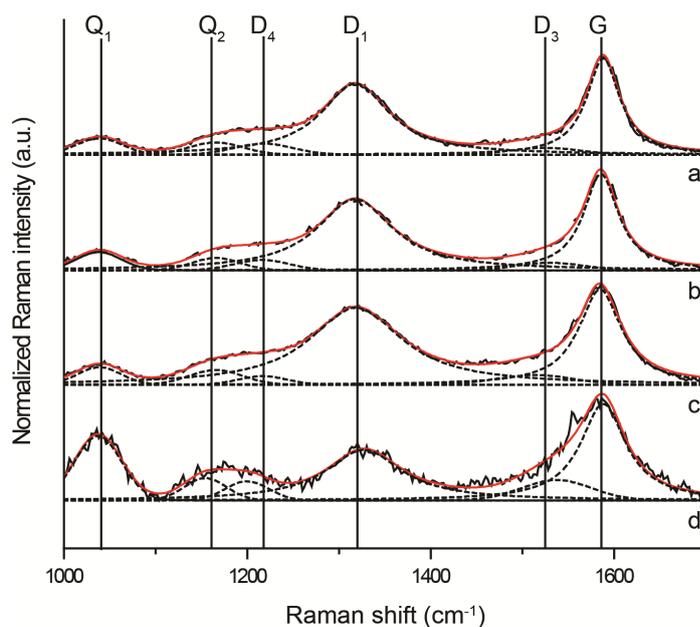


**Figure 2.7.** Deconvoluted operando Raman spectra of the carbon deposits formed on the surface of a Pt/Al<sub>2</sub>O<sub>3</sub> catalyst material for the 25% (a), 50% (b), 75% (c) and 100% (d) propane feed obtained under propane dehydrogenation conditions.

deposits. Lorentzian line shapes are used to fit the D<sub>1</sub> and G bands, while the other bands were fitted using Gaussian functions. As an example, the operando Raman

spectra shown in Fig. 2.5a have been analyzed in this manner and are shown in Figure 2.7.

The Raman spectra of all the catalyst materials, discussed in Figure 2.6, are deconvoluted in an identical manner. The obtained values for the position (a, b) and width (c, d) (half width half maximum (HWHM)) of the D<sub>1</sub> and G bands of these spectra are shown in Figure 2.8. This analysis is performed on ten consecutive spectra obtained at the end of the first cycle. This period was chosen for comparing the catalyst materials as the catalysts are in a relatively steady state, and the continuous cycling operation does not affect each catalyst in the same way. To illustrate this, the

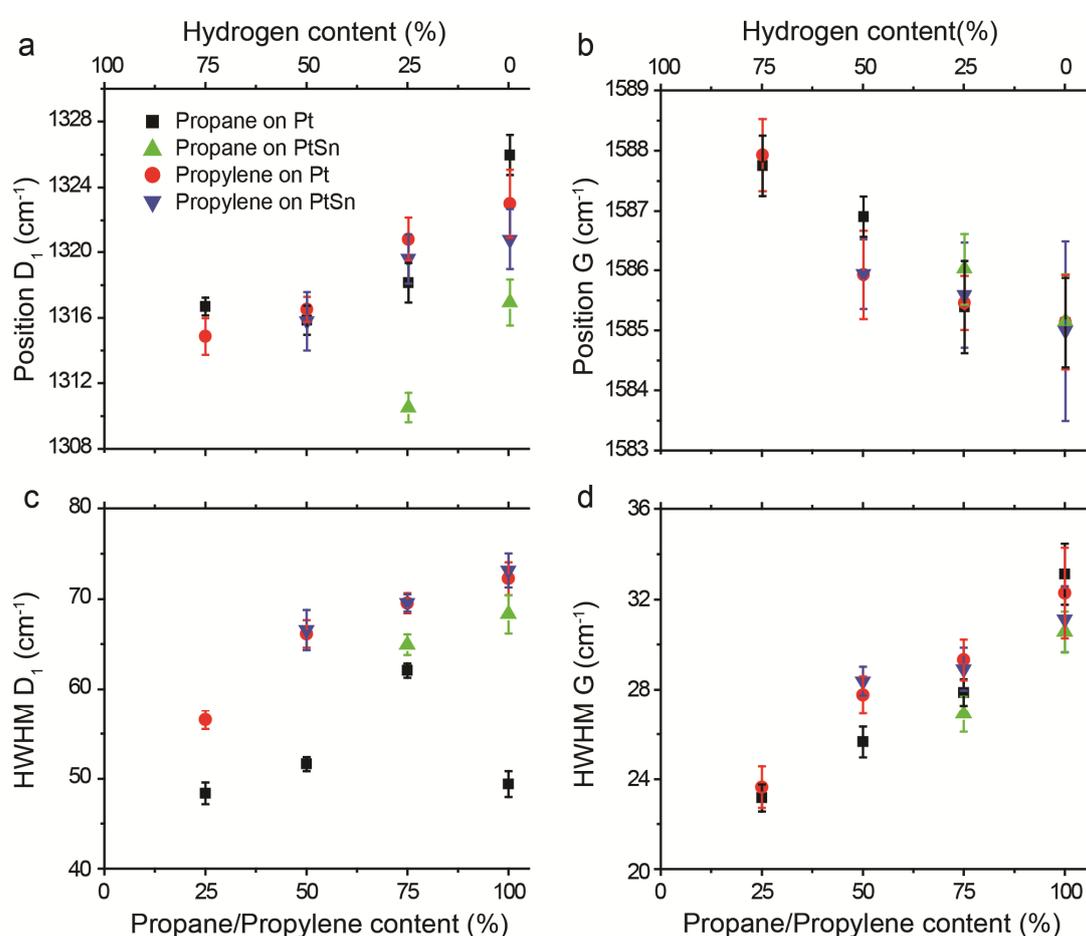


**Figure 2.8.** Positions (a, b) and values of the half width half maximum (HWHM) (c, d) of the D<sub>1</sub> (a, c) and G (b, d) bands of the Raman spectra obtained at the end of the first cycle, while using feeds containing propane/propylene diluted with different concentrations of hydrogen. Furthermore, the Figure includes experiments performed on the Pt catalyst using propane (■) and propylene (●), and the Pt-Sn/Al<sub>2</sub>O<sub>3</sub> catalyst using propane (▲) and propylene (▼).

values for the width, position and relative intensity expressed as the  $D_1/G$  ratio have been determined for the deactivated Pt and Pt-Sn catalyst for the first, third and tenth cycle, when a feed consisting of 100% propane was used. The results are summarized in Table 2.2.

**Table 2.2.** HWHM (half width at half maximum) and position of the  $D_1$  and G bands of the coke formed on the catalyst materials at the end of the first, third and tenth dehydrogenation cycle for the feed consisting of 100% propane. The average value of 10 consecutive spectra at the end of the cycle is shown, with the standard deviation between brackets.

Catalyst sample	Cycle	HWHM $D_1$ ( $\text{cm}^{-1}$ )	Position $D_1$ ( $\text{cm}^{-1}$ )	HWHM G ( $\text{cm}^{-1}$ )	Position G ( $\text{cm}^{-1}$ )	$D_1/G$
Pt/ $\text{Al}_2\text{O}_3$	1 <sup>st</sup>	49.4 (1.4)	1326.0 (1.2)	33.1 (1.3)	1585.1 (0.7)	0.54 (0.015)
Pt/ $\text{Al}_2\text{O}_3$	3 <sup>rd</sup>	54.6 (2.7)	1326.3 (0.9)	35.2 (1.8)	1583.1 (0.9)	0.58 (0.022)
Pt/ $\text{Al}_2\text{O}_3$	10 <sup>th</sup>	54.3 (3.2)	1323.6 (1.5)	32.4 (2.8)	1583.8 (0.9)	0.66 (0.020)
Pt-Sn/ $\text{Al}_2\text{O}_3$	1 <sup>st</sup>	68.3 (2.1)	1316.9 (1.4)	30.6 (0.9)	1585.2 (0.8)	0.67 (0.015)
Pt-Sn/ $\text{Al}_2\text{O}_3$	3 <sup>rd</sup>	68.1 (2.3)	1318.5 (1.4)	32.5 (0.9)	1585.9 (0.9)	0.68 (0.014)
Pt-Sn/ $\text{Al}_2\text{O}_3$	10 <sup>th</sup>	68.3 (1.5)	1316.6 (1.8)	31.7 (0.6)	1587.7 (1.1)	0.69 (0.027)

It can be concluded that, as the hydrogen content in the feed is increased, the  $D_1$  band shifts towards lower wavenumbers, while the G band shifts to higher wavenumbers. The spectral shifts appear to be unaffected by the presence of Sn or whether propane or propylene is used in the feed. In literature, the position of the Raman bands have been reported to shift as a function of temperature or incident photon energy. However, this cannot account for the trends observed here, as the temperature and incident photon energy are identical for each experiment reported here. Tuinstra and Koenig have reported that the G band for perfect, large graphite crystals is positioned at  $1575 \text{ cm}^{-1}$ .<sup>18</sup> When small graphite crystallites were measured at the same conditions, the position of the G band had shifted to  $1590 \text{ cm}^{-1}$ . As a similar change

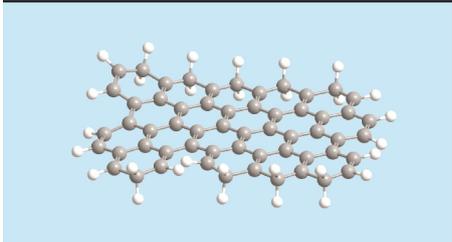
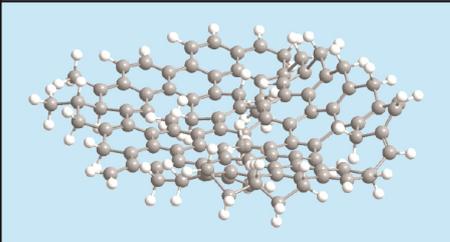
towards higher Raman shifts is observed here, it would imply that the addition of hydrogen decreases the crystallite size of the graphite particles. The reason of the change of the D<sub>1</sub> band towards lower Raman shifts is not understood at this point. In Figure 2.8c and d, the HWHM of the D<sub>1</sub> and G Raman bands is shown. The general trend is that both Raman bands become narrower as the H<sub>2</sub> content in the feed is increased. This effect is visible for all operando Raman spectra measured. The narrowing of these bands indicate a more ordered carbon structure with fewer defects on the catalyst. The D<sub>1</sub>/G ratio obtained at the end of the first, third and tenth cycle is summarized in Table 2.3 for every concentration of propane and propylene used. As the hydrocarbon concentration is decreased, the D<sub>1</sub>/G ratio increases for the first cycle, indicating that either smaller graphitic crystallites are formed, or that these graphitic sheets contain more defects.

**Table 2.3.** D<sub>1</sub>/G ratios for Pt/Al<sub>2</sub>O<sub>3</sub> and Pt-Sn/Al<sub>2</sub>O<sub>3</sub> catalysts for different feeds obtained at the end of the first, third and tenth cycle.

Propane/propylene concentration (%)	cycle	Pt/Al <sub>2</sub> O <sub>3</sub>		Pt-Sn/Al <sub>2</sub> O <sub>3</sub>	
		Propane	Propylene	Propane	Propylene
100	1	0.54	0.60	0.67	0.62
	3	0.58	0.58	0.68	0.57
	10	0.66	0.63	0.69	0.64
75	1	0.81	0.64	0.78	0.63
	3	0.80	0.64	0.68	0.65
	10	0.87	0.61	0.35	0.67
50	1	0.74	0.71	(-)	0.65
	3	0.62	0.74	(-)	0.71
	10	(-)	0.70	(-)	0.71
25	1	0.74	0.72	(-)	(-)
	3	0.60	0.72	(-)	(-)
	10	0.37	0.71	(-)	(-)

Summarizing, three trends are observed in the Raman spectra as a function of increasing hydrogen concentration: First of all, the Raman bands become more narrow, suggesting a more ordered system. Moreover, a shift in the position of the G band was observed, suggesting a decrease in the size of the graphite crystallites. Finally, the  $D_1/G$  ratio increases as a function of the hydrogen concentration. Since this value signifies the ratio between carbon present on the edges and defects of the coke ( $D_1$ ) and carbon in the bulk of the graphite sheet (G), this can be interpreted as graphite sheets becoming smaller. These findings are summarized in Table 2.4.

**Table 2.4.** Summary of the effects of a high and low hydrogen pressure on the chemical nature of coke deposits formed on the Pt and Pt-Sn/ $Al_2O_3$  catalyst material, as observed by operando Raman spectroscopy. As is shown in the bottom of the scheme, smaller, more ordered coke species are formed at a high partial pressure of hydrogen.

High hydrogen partial pressure	Low hydrogen partial pressure
G band at high Raman shifts	G band at low Raman shifts
Narrow Raman bands	Broad Raman bands
Low $D_1/G$	High $D_1/G$
	

The amount of amorphous coke, as shown by the intensity of the  $D_3$  band, becomes less as more hydrogen is added. However, the variance for both the position and width of this band is very large for these measurements, which is why this band was not investigated in detail. Catalyst cycling does not strongly affect the Raman band positions, band widths and the ratio between the  $D_1$  and G bands in most experiments performed, with the exception of experiments with 50 and 25% propane on the Pt/ $Al_2O_3$  catalyst and 75% propane feed on the Pt-Sn/ $Al_2O_3$  catalyst. In these cases, three trends are observed during the catalyst cycling: First of all, the relative intensity

of the coke bands drops for each consecutive cycle. Furthermore, the  $D_1/G$  ratio drops from ca. 0.75 to 0.35. Finally, the width of the  $D_1$  and G bands increases. These trends suggest that less coke of a more graphitic nature is deposited after each consecutive cycle. In addition, for the experiments with 50 and 25% propane on the Pt-Sn/ $\text{Al}_2\text{O}_3$  catalyst only fluorescence was detected. Our experiments have also shown that the formation and maturing of coke quenches fluorescence and that fluorescence is relatively strong at the initial stages of each cycle and during the oxidation step. Therefore the presence of very strong fluorescence seems to be an indication that the amount of coke on the catalyst surface is relatively low and reactive. To investigate this in more detail, additional experiments have been performed while using operando UV-Vis spectroscopy to track the darkening of the catalyst during the dehydrogenation reaction for feeds consisting of 100% propane and 25% propane in hydrogen on the Pt-Sn catalyst. As is shown in Figure 2.9, indeed the absorption of UV-Vis light increases less when 25% propane is present in the reactor feed compared to 100% propane, which is a strong indication that less coke has been deposited.

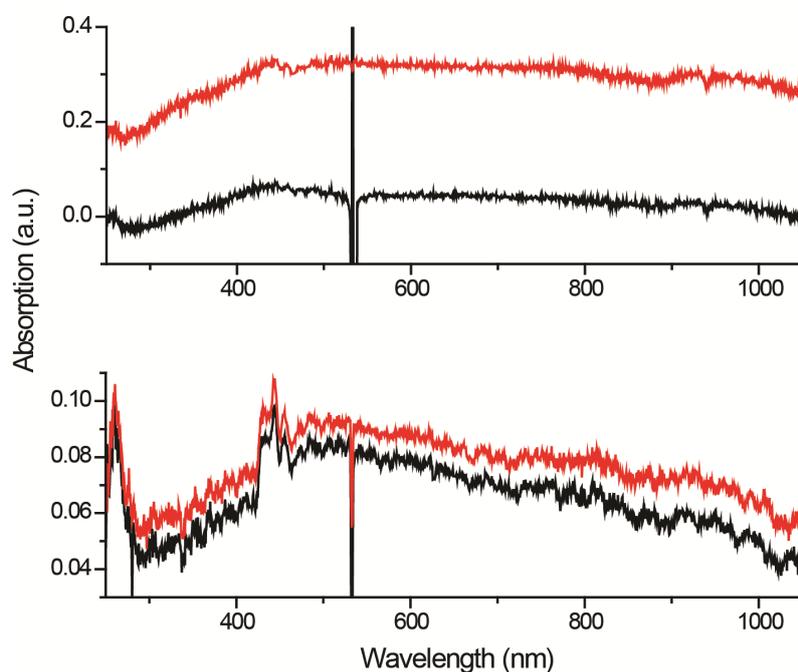


**Figure 2.9.** UV-Vis absorption spectra obtained at the start (black spectrum) and at the end (red spectrum) of the dehydrogenation reaction on the Pt-Sn catalyst using a feed consisting of 100% propane (top) and 25% propane diluted with hydrogen (bottom). The feature observed around 532 nm is caused by diffusely scattered light of the Raman light source.

When correlating observations made with Raman spectroscopy with the activity data, the increase in propane conversion at higher hydrogen contents, can be attributed to a decrease in the amount of coke deposited. The low initial selectivity observed on the Pt/Al<sub>2</sub>O<sub>3</sub> catalyst can be explained by the fact that highly active sites (i.e. corners, edges, etc.) are present on the catalyst that catalyze cracking and hydrogenolysis in the presence of hydrogen. As the cycle progresses in time, these sites become poisoned by the deposition of coke, quenching the formation of these cracking products. After the catalyst is cycled a few times, these sites are permanently deactivated because the morphology of the Pt particles is altered due to sintering. In contrast with dehydrogenation, hydrogenolysis is a structure sensitive reaction, which is favored on smaller Pt crystallites, which contain more highly reactive kink sites.<sup>36,37</sup> Finally, the experiments with propane concentrations of 25 and 50% show a strong increase in selectivity for each consecutive cycle. This change coincides with the coke deposits becoming more graphitic, which suggests a link between the presence of relatively disordered coke deposits and side reactions, such as cracking.

#### 2.3.4 Thermogravimetric Analysis

Thermogravimetric analysis (TGA) experiments, shown in Figure 2.10 on deactivated Pt/Al<sub>2</sub>O<sub>3</sub> and Pt-Sn/Al<sub>2</sub>O<sub>3</sub> catalysts (obtained after three dehydrogenation cycles, excluding an oxidation step for the last cycle), support the findings obtained by the operando Raman measurements. In the Figure, the loss of weight per temperature step is shown. The signal between 400 and 600 °C corresponds with the loss of weight due to the combustion of coke. This loss of weight is lower for the catalyst where H<sub>2</sub> is added to the feed. In the case of the Pt catalyst, 1.44 wt% of coke is measured, while this is decreased to 0.34 wt% when 50% H<sub>2</sub> is added (1.32 and 0.53 wt% coke for the Pt-Sn catalyst, respectively). Also, the coke on both catalysts combusts at different temperatures: for 100% propane the signal is centered around 475 °C and for 50% at 600 °C. It has been reported in literature that disordered carbon combusts at lower temperatures than highly graphitic coke deposits, since the latter species is thermally more stable.<sup>38-40</sup> This indicates that the coke deposits formed in the presence of hydrogen are more graphitic, which is in agreement with the Raman data. A second

signal is observed for both coked materials at 425 °C. The considerably lower combustion temperature is explained by the fact that this coke is in proximity of the Pt nanoparticles, which assists in the combustion of these species.<sup>41,42</sup> Apparently on the Pt catalyst, only part of the coke is in proximity of the Pt nanoparticles. On the Pt-Sn catalyst, only a single signal corresponding with the combustion of coke is observed, which is centered around 450 and 605 °C, when using a feed of 100 or 50% propane. On this catalyst material apparently coke is present solely on the support of the material. During propylene dehydrogenation, much larger quantities of coke are deposited (around 20 wt%). Propylene can readily polymerize to form coke on Brønsted acid sites, when present in large concentrations at high temperatures, which is the case here.<sup>37</sup>

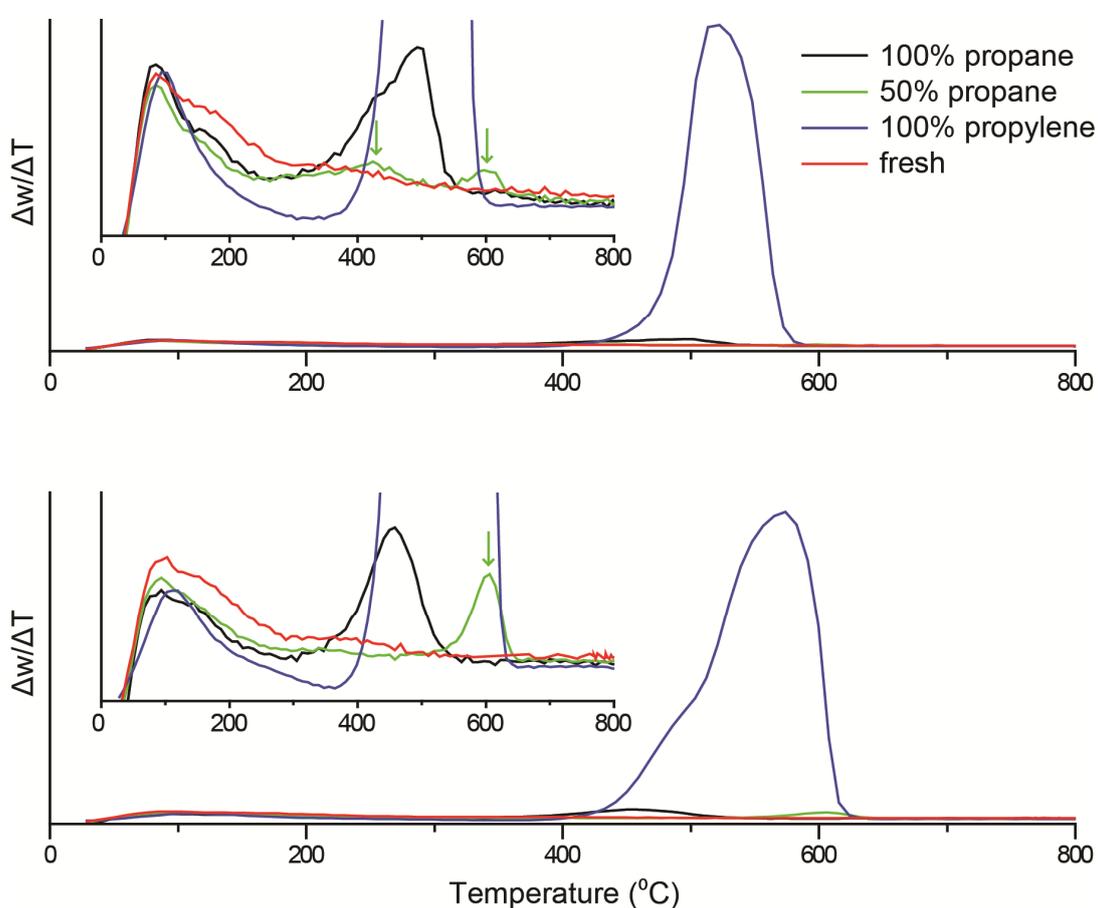


**Figure 2.10.** Thermogravimetric analysis on spent Pt/Al<sub>2</sub>O<sub>3</sub> (top) and Pt-Sn/Al<sub>2</sub>O<sub>3</sub> (bottom) catalysts, deactivated by feeds consisting of either 100% propane, 50% propane and 50% hydrogen, or 100% propylene. The inset shows a zoomed-in view of the signal corresponding with coke.

## 2.4 Conclusions

The deposition of coke species on Pt/Al<sub>2</sub>O<sub>3</sub> and Pt-Sn/Al<sub>2</sub>O<sub>3</sub> catalyst materials has been studied during 10 successive propane dehydrogenation-regeneration cycles by operando Raman spectroscopy, on-line activity measurements and thermogravimetric analysis. The effect of the hydrogen content of the reactor feed on coke deposition was of special interest. It was found that the Raman bands originating from coke deposits become narrower as hydrogen is added to the feed. Furthermore, the position of the G band shifts to higher wavenumbers, and the ratio of the D<sub>1</sub> and G band increases. This points towards the formation of less coke, which has a more graphitic nature when hydrogen is co-fed. The corresponding on-line activity data shows that the addition of hydrogen to the feed increases the conversion and selectivity of the Pt/Al<sub>2</sub>O<sub>3</sub> catalyst. The deactivation of the Pt-Sn/Al<sub>2</sub>O<sub>3</sub> catalyst was slowed down significantly by the addition of hydrogen, resulting in a significantly more stable catalyst. The increase in catalytic performance is attributed to hydrogen assisting in keeping the active sites for dehydrogenation free of coke deposits.

## 2.5 Acknowledgements

Marjan Versluijs (Utrecht University) is kindly thanked for performing the TGA experiments.

## 2.6 References

- (1) Noda, H.; Tone, S.; Otake, T. *J. Chem. Eng. Jap.* **1973**, *7*, 1974.
- (2) Toei, R.; Nakanishi, K.; Yamada, K.; Okazaki, M. *J. Chem. Eng. Jap.* **1975**, *8*, 131.

- (3) Swift, H. E.; Beuther, H.; Rennard, R. J. *Ind. Eng. Chem. Prod. Res. Dev.* **1976**, *15*, 131.
- (4) Moulijn, J. A.; van Diepen, A. E.; Kapteijn, F. *Appl. Catal. A-Gen.* **2001**, *212*, 3.
- (5) Menon, P. G. *J. Mol. Catal.* **1990**, *59*, 207.
- (6) Duan, Y.; Zhou, Y.; Zhang, Y.; Sheng, X.; Xue, M. *Catal. Lett.* **2011**, *141*, 120.
- (7) Li, Q.; Sui, Z.; Zhou, X.; Zhu, Y.; Zhou, J.; Chen, D. *Top. Catal.* **2011**, *54*, 888.
- (8) Larsson, M.; Hulten, M.; Blekkan, E. A.; Andersson, B. *J. Catal.* **1996**, *164*, 44.
- (9) Li, Q.; Sui, Z.; Zhou, X.; Chen, D. *Appl. Catal. A-Gen.* **2011**, *398*, 18.
- (10) Larese, C. *J. Catal.* **2002**, *208*, 467.
- (11) Santhosh Kumar, M.; Chen, D.; Holmen, A.; Walmsley, J. C. *Catal. Today* **2009**, *142*, 17.
- (12) Iglesias-Juez, A.; Beale, A. M.; Maaijen, K.; Weng, T. C.; Glatzel, P.; Weckhuysen, B. M. *J. Catal.* **2010**, *276*, 268.
- (13) Sun, P.; Siddiqi, G.; Vining, W. C.; Chi, M.; Bell, A. T. *J. Catal.* **2011**, *282*, 165.
- (14) Nijhuis, T. A.; Tinnemans, S. J.; Visser, T.; Weckhuysen, B. M. *Phys. Chem. Chem. Phys.* **2003**, *5*, 4361.
- (15) Nijhuis, T. A.; Tinnemans, S. J.; Visser, T.; Weckhuysen, B. M. *Chem. Eng. Sci.* **2004**, *59*, 5487.
- (16) Bennici, S. M.; Vogelaar, B. M.; Nijhuis, T. A.; Weckhuysen, B. M. *Angew. Chem. Int. Ed.* **2007**, *46*, 5412.
- (17) Santhosh Kumar, M.; Chen, D.; Walmsley, J. C.; Holmen, A. *Catal. Commun.* **2008**, *20*, 747.
- (18) Tuinstra, F.; Koenig, J. L. *J. Chem. Phys.* **1970**, *53*, 1126.
- (19) Chua, Y. T.; Stair, P. C. *J. Catal.* **2003**, *213*, 39.
- (20) Bernard, S.; Beyssac, O.; Benzerara, K.; Findling, N.; Tzvetkov, G.; Brown Jr., G. E. *Carbon N. Y.* **2010**, *48*, 2506.
- (21) Bartholomew, C. H. *Appl. Catal. A-Gen.* **2001**, *212*, 17.

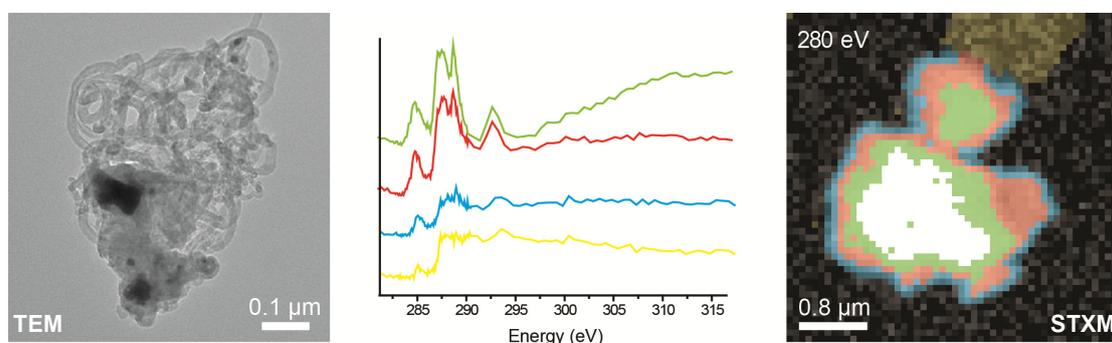
- (22) Fearon, J.; Watson, G. W. *J. Mater. Chem.* **2006**, *16*, 1989.
- (23) Virnovskaia, A.; Rytter, E.; Olsbye, U. *Ind. Eng. Chem. Res.* **2008**, *47*, 7167.
- (24) Nykänen, L.; Honkala, K. *J. Phys. Chem. C* **2011**, *115*, 9578.
- (25) Hauser, A. W.; Gomes, J.; Bajdich, M.; Head-Gordon, M.; Bell, A. T. *Phys. Chem. Chem. Phys.* **2013**, *15*, 20727.
- (26) Vincent, R.; Lindstedt, R.; Malik, N.; Reid, I.; Messenger, B. *J. Catal.* **2008**, *260*, 37.
- (27) Yang, M.-L.; Zhu, Y.-A.; Fan, C.; Sui, Z.-J.; Chen, D.; Zhou, X.-G. *J. Mol. Catal. A-Chem.* **2010**, *321*, 42.
- (28) Yang, M.-L.; Zhu, Y.-A.; Fan, C.; Sui, Z.-J.; Chen, D.; Zhou, X.-G. *Phys. Chem. Chem. Phys.* **2011**, *13*, 3257.
- (29) Galvita, V.; Siddiqi, G.; Sun, P.; Bell, A. T. *J. Catal.* **2010**, *271*, 209.
- (30) Jawhari, T. *Carbon N. Y.* **1995**, *33*, 1561.
- (31) Buijnsters, J. G.; Gago, R.; Jiménez, I.; Camero, M.; Agulló-Rueda, F.; Gómez-Aleixandre, C. *J. Appl. Phys.* **2009**, *105*, 093510.
- (32) Pimenta, M. A.; Dresselhaus, G.; Dresselhaus, M. S.; Cançado, L. G.; Jorio, A.; Saito, R. *Phys. Chem. Chem. Phys.* **2007**, *9*, 1276.
- (33) Hof, F.; Bosch, S.; Englert, J. M.; Hauke, F.; Hirsch, A. *Angew. Chem. Int. Ed.* **2012**, *51*, 1.
- (34) Sadezky, A.; Muckenhuber, H.; Grothe, H.; Niessner, R.; Poschl, U. *Carbon*, **2005**, *43*, 1731.
- (35) McGregor, J.; Huang, Z.; Parrott, E. P. J.; Zeitler, J. A.; Nguyen, K. L.; Rawson, J. M.; Carley, A.; Hansen, T. W.; Tessonnier, J.-P.; Su, D. S.; Teschner, D.; Vass, E. M.; Knop-Gericke, A.; Schlögl, R.; Gladden, L. F. *J. Catal.* **2010**, *269*, 329.
- (36) Cortright, R. D.; Watwe, R. M.; Dumesic, J. A. *J. Mol. Catal. A-Chem.* **2000**, *163*, 91.
- (37) Bhasin, M. M.; McCain, J. H.; Vora, B. V.; Imai, T.; Pujadó, P. R. *Appl. Catal. A-Gen.* **2001**, *221*, 397.
- (38) Afonso, J.; Schmal, M.; Frety, R. *Fuel Process. Technol.* **1994**, *41*, 13.
- (39) Stagg, S. M.; Querini, C. A.; Alvarez, W. E.; Resasco, D. E. *J. Catal.* **1997**, *168*, 75.

- (40) Bai, L.; Zhou, Y.; Zhang, Y.; Liu, H.; Sheng, X. *Ind. Eng. Chem. Res.* **2009**, *48*, 9885.
- (41) Sahoo, S. K.; Rao, P. V. C.; Rajeshwer, D.; Krishnamurthy, K. R.; Singh, I. D. *Appl. Catal. A-Gen.* **2003**, *244*, 311.
- (42) Vu, B. K.; Song, M. B.; Ahn, I. Y.; Suh, Y.-W.; Suh, D. J.; Kim, J. S.; Shin, E. *W. J. Ind. Chem Eng.* **2011**, *17*, 71.



## Chapter 3

# Nano-Scale Chemical Imaging of Individual Catalyst Particles for Studying the Coke Formed During Propane Dehydrogenation



STXM, TGA and operando Raman spectroscopy were used to gain insight in the chemical nature of the carbon deposits formed on four propane dehydrogenation catalyst materials, namely Pt, Pt-Sn, Ga and Pt-Ga supported on  $\text{Al}_2\text{O}_3$ . STXM analysis on individual catalyst particles revealed that carbon deposits formed on the Ga-based catalyst was more graphitic in nature compared to coke formed on Pt-based catalysts. Furthermore, the coke species formed on the exterior of the catalyst particles was distinctly different from the coke species formed within the interior of the catalyst particles.

This Chapter is based on the manuscript: J.J.H.B. Sattler, I.D. Gonzalez Jimenez, B.M. Weckhuysen, *in preparation*.

### 3.1 Introduction

Chemical information on the carbon species deposited on catalyst materials is generally obtained by using bulk analysis techniques (e.g., UV-Vis, Raman and infrared (IR) spectroscopy, thermo-gravimetric analysis (TGA),  $^{13}\text{C}$  nuclear magnetic resonance (NMR) or X-ray absorption near edge structure (XANES)<sup>1-5</sup>) as well as surface science methods (e.g., X-ray photoelectron spectroscopy (XPS), ultraviolet photoelectron spectroscopy (UPS) and secondary ion mass spectrometry (SIMS)<sup>6-9</sup>). However, it is desirable to obtain chemical information at the resolution of individual catalyst particles and even below. Hence, microscopy techniques are required to study the catalyst materials at the length scales of micro- and nanometers. Transmission electron microscopy (TEM) is generally used to study individual catalyst particles in great detail, but no detailed chemical information on the nature of carbon deposits on catalyst materials has yet been obtained, although in principle electron energy loss spectroscopy (EELS) could assist in this endeavour.<sup>3,10</sup> A microscope has often been combined with spectroscopic techniques to obtain spectral information, but due to the diffraction limit of visible and infrared light, the spatial resolution of most of the bulk aforementioned spectroscopic techniques, such as Raman, UV-Vis and IR microscopy, is practically limited to the micron-range.<sup>11-13</sup> In contrast, by using X-rays as a light source, much higher spatial resolutions can be obtained. Scanning transmission X-ray microscopy (STXM) is a technique that uses a focused beam of soft X-rays to scan a sample in a continuous fashion, while slightly changing the energy of the photons for each following scan. In this way, a map of the catalyst material can be obtained where every pixel consists of a X-ray absorption spectrum over a wide range of energies.<sup>14</sup> The practical spectral resolution obtained depends on the zone plate used and the selected energies of the X-rays. The optimal spatial resolution that can be achieved nowadays with STXM is approximately 30 nm. Such a spatial resolution is high enough to observe distinct differences in the chemical nature of e.g. coke deposits within individual catalyst particles, which has been recently illustrated for the methanol-to hydrocarbons (MTH) process over individual H-ZSM-5 and H-SAPO-34 catalyst particles.<sup>15-17</sup>

The goal of this Chapter is to show that STXM is a powerful addition to the current toolbox for the study of coke deposits formed under relevant reaction conditions on individual catalyst particles active in the dehydrogenation of propane. For this purpose, four catalyst materials, namely Pt, Pt-Sn, Ga and Pt-Ga supported on a porous alumina carrier, were chosen as their activity in the dehydrogenation reaction and their deactivation behavior is clearly different. These differences in activity are believed to be related to the process of coke formation. This is why the type and amount of the formed carbon deposits were analyzed by a combination of bulk and local characterization techniques. The four materials were tested for the catalytic dehydrogenation of propane, and during the catalytic reaction the formation of coke deposits was tracked by combined operando Raman spectroscopy. After certain times of dehydrogenation, the deactivated catalyst material was collected from the reactor and examined by TGA and STXM. The bulk characterization techniques revealed differences between the different deactivated catalyst samples, while with STXM insight was gained in the chemical differences between coke formed on the exterior and in the interior of individual catalyst particles.

## 3.2 Experimental

### 3.2.1 Catalyst Preparation and Characterization

Four different catalyst materials, i.e., 0.5 wt% Pt/Al<sub>2</sub>O<sub>3</sub>, 0.5 wt% Pt - 1.5 wt% Sn/Al<sub>2</sub>O<sub>3</sub>, 1.5 wt% Ga/Al<sub>2</sub>O<sub>3</sub> and 0.5 wt% Pt - 1.5 wt% Ga/Al<sub>2</sub>O<sub>3</sub>, were prepared by the incipient wetness impregnation method. The catalyst precursors used were H<sub>2</sub>PtCl<sub>6</sub>×(H<sub>2</sub>O)<sub>x</sub> (38 wt% Pt, Sigma-Aldrich), SnCl<sub>2</sub>×(H<sub>2</sub>O)<sub>2</sub> (98%, VWR int.) and Ga(NO<sub>3</sub>)<sub>3</sub>×(H<sub>2</sub>O)<sub>x</sub> (99.9998% on metal base, Acros Organics) and puralox alumina (Sasol) was used as the support. After impregnation, the catalyst materials were dried for 2 h at 60 °C and overnight at 120 °C. Subsequently, the catalysts were calcined at 560 °C for 3 h. Note that the Pt and Pt-Sn/Al<sub>2</sub>O<sub>3</sub> catalysts reported here, are not the same as those studied in the Chapter 2. The catalysts have been characterized by transmission electron microscopy (TEM), X-ray diffraction (XRD) and N<sub>2</sub>-physisorption and NH<sub>3</sub> temperature programmed desorption (TPD). A Tecnai 20 instrument equipped with a 200 keV field emission gun was used to perform bright field TEM analysis. The dark field TEM images were collected with a JEOL 2010F

200kV TEM apparatus equipped with an Oxford Energy Dispersive Spectroscopy system for elemental analysis. A Bruker D2 Phaser, equipped with a Co ( $K\alpha$ ) anode, was used for the collection of XRD diffractograms.  $N_2$  physisorption experiments were performed with a TriStar 3000 V6.08 A at  $-196\text{ }^\circ\text{C}$  after drying the samples overnight. Ammonia TPD was performed on a Micromeritics AutoChem II instrument. Approximately 0.1 g of catalyst material pretreated under a flow of Ar at  $350\text{ }^\circ\text{C}$ , after which ammonia was chemisorbed by pulsing at  $100\text{ }^\circ\text{C}$  until equilibrium is reached. The sample is then heated under a ramp of  $5\text{ }^\circ\text{C}/\text{min}$  up to  $600\text{ }^\circ\text{C}$ , while the desorbed  $NH_3$  is detected by a TCD detector.

### 3.2.2 Catalytic Dehydrogenation of Propane

Catalytic tests were performed in a setup, which allowed for the collection of catalytic performance data, including activity, selectivity and stability, by on-line gas chromatography as well as of operando Raman and UV-Vis spectroscopic data.<sup>18</sup> A tubular quartz reactor was filled with 0.3 g of catalyst material and placed inside an oven. The reactor contains optical grade quartz windows which, when aligned with holes in the oven, allow for the collection of high-quality spectroscopic data. The catalyst material was heated for 1 h to  $600\text{ }^\circ\text{C}$  under  $H_2$  in order to obtain the catalytically active metallic Pt, after which a 6 h dehydrogenation cycle was started by flowing 9 ml/min of propane (100%) through the catalyst bed ( $WHSV = 3.2\text{ h}^{-1}$ ). The deactivated catalyst was then regenerated by flowing a mixture of He and  $O_2$  over the catalyst, followed by a 45 min reduction step with  $H_2$ . Gas chromatographs are collected at a 5 min interval: the apparatus is equipped with a FID (Porabond-Q column) and TCD (Carboxan column) detector that allow for full analysis of the feed composition. A Kaiser Optical Systems Raman spectrometer (11 accumulations of 7 s exposure time, collected at a 5 min interval) was used to collect spectra continuously during propane dehydrogenation.

### 3.2.3 Analysis of the Carbon deposits

In total 10 dehydrogenation-regeneration cycles are performed (after the final cycle the catalyst material is not regenerated), after which the deactivated catalyst is collected and used for further analysis, including scanning transmission X-ray microscopy (STXM) and thermogravimetric analysis (TGA). More specifically, catalyst samples were collected from the PDH reactor for Pt-Ga after the 1<sup>st</sup>, 3<sup>rd</sup> and

10<sup>th</sup> cycle, and for Pt, Pt-Sn and Ga after the 10<sup>th</sup> cycle. TGA analysis on these collected samples was performed on a Perking-Elmer 1 TGA apparatus, by drying the catalyst (10-25 mg) at 150 °C under argon, followed by heating the catalyst under O<sub>2</sub> from room temperature to 900 °C at a 10 °C/min ramp. STXM experiments were performed at the PolLux STXM microscope (beamline X07DA) at the Swiss Light Source (SLS), Paul Scherrer Institute (PSI), Villigen, Switzerland. Images were collected of the carbon K-edge (280-315 eV) and the oxygen K-edge (520-550 eV), using a 25 nm zone plate that has been maintained free of carbon. The transmitted X-rays were detected by a photomultiplier tube, while data processing was performed using the aXis2000 and TXM-XANES Wizard software.

### 3.3 Results and Discussion

#### 3.3.1 Catalyst Characterization

N<sub>2</sub>-physisorption was used to determine the BET surface area and pore volume of the four catalyst materials under study and the results are summarized in Table 3.1, including the catalyst sample names. The surface area and pore volume are very similar for the Pt, Pt-Sn, Ga and Pt-Ga materials, so the applied impregnation procedure does not significantly alter these physical properties of the catalyst materials prepared.

**Table 3.1.** N<sub>2</sub>-physisorption results on the four propane dehydrogenation catalyst materials under investigation.

Catalyst (supported on Al <sub>2</sub> O <sub>3</sub> )	Catalyst name	BET surface area (m <sup>2</sup> /g)	Pore volume (cm <sup>3</sup> /g)
0.5 wt% Pt	Pt	190	0.48
0.5 wt% Pt-1.5 wt% Sn	Pt-Sn	202	0.50
1.5 wt% Ga	Ga	201	0.51
0.5 wt% Pt, 1.5 wt% Ga	Pt-Ga	188	0.48

The prepared catalyst materials were also characterized by a series of analytical methods. The XRD diffractograms of the freshly prepared catalyst materials are shown in Figure 3.1. Only diffraction peaks corresponding with the  $\gamma$ -alumina support are detected, so no detectable crystalline Pt, Sn or Ga phases have been formed.

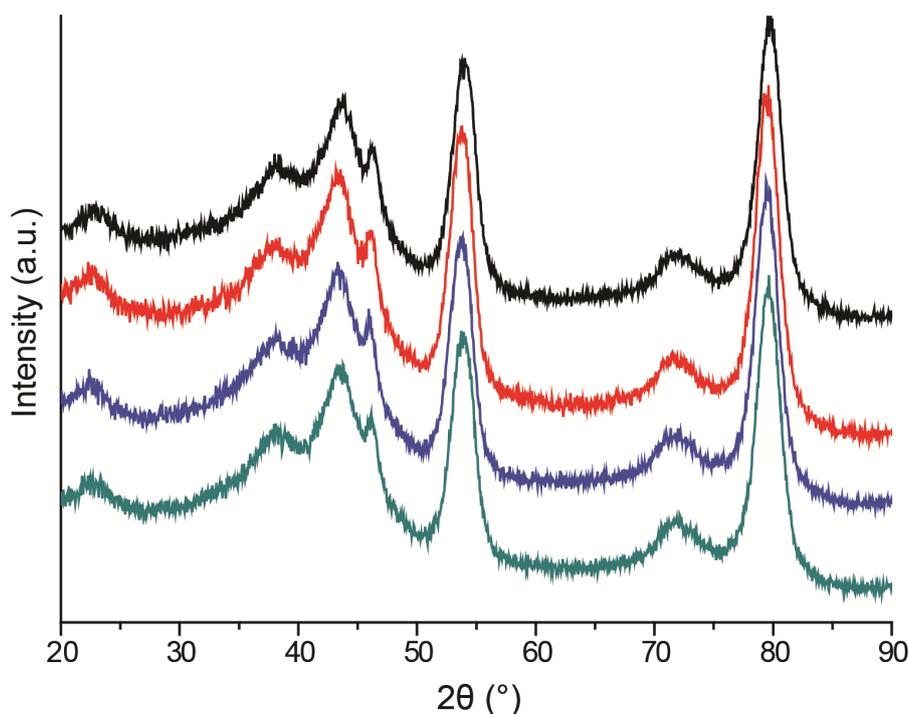


**Figure 3.1.** XRD diffractograms of the Pt (black), Pt-Sn (red), Ga (blue) and Pt-Ga (turquoise) supported on the puralox alumina support. Other than the puralox support, no crystalline phases are observed.

Acid sites on the surface of the catalyst materials are known to play a key role in catalyst deactivation by coke deposition,<sup>19</sup> which is why temperature programmed desorption (TPD) of  $\text{NH}_3$  was used to probe the acidity of the catalyst materials. Ammonia adsorbs on the acid sites of catalyst material, where the strength of adsorption is directly related to the strength of the acid site.<sup>20</sup> By heating the catalyst material in a controlled manner, the ammonia desorption profile will reveal the relative strengths of different acid sites present. This analysis has been performed for the four catalyst materials and the results are shown in Figure 3.2.

It was found that ammonia desorption from the catalyst materials takes place between 100 and 500 °C and is the strongest around 150 and 375 °C. At these temperatures, ammonia desorbs from weak and strong acid sites, respectively.<sup>20</sup> The  $\text{NH}_3$  TPD

profiles of the Pt, Pt-Sn, Ga and Pt-Ga catalysts are quite similar. For the Pt-Sn catalyst, however the peak at 375 °C shifts to lower temperatures, suggesting the strongest acid sites are being poisoned by the SnO<sub>x</sub>. Furthermore, for the Ga/Al<sub>2</sub>O<sub>3</sub> catalyst, this signal has almost completely disappeared, and is replaced with one at 275 °C, which can be attributed to the presence of acid sites of a medium strength. GaO<sub>x</sub> is known to have Lewis acid sites of medium strength on the surface, which corresponds with the broad signal between 150 and 300 °C.<sup>21,22</sup>

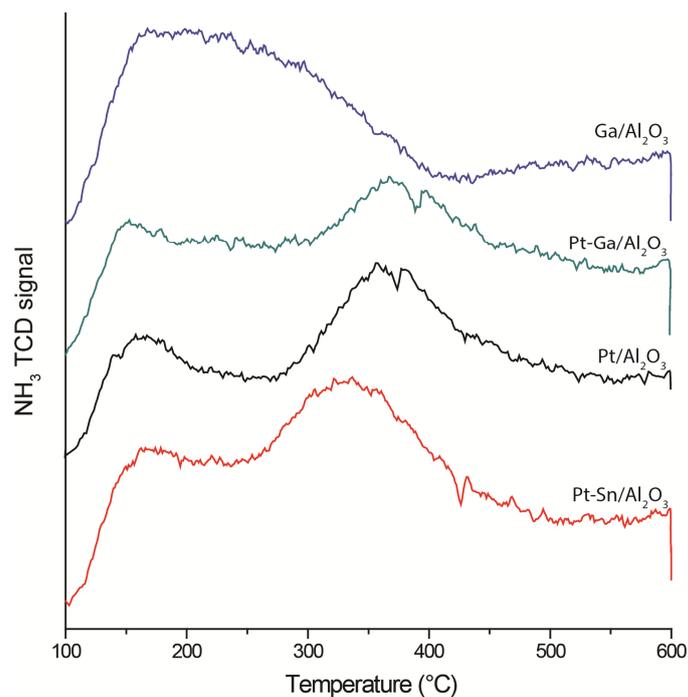


**Figure 3.2.** Temperature programmed desorption (TPD) of ammonia profiles of the Pt, Ga, Pt-Ga and Pt-Sn propane dehydrogenation catalysts.

### 3.3.2 Propane Dehydrogenation Activity, Selectivity and Stability

First, the catalytic performance of the four materials was tested by performing a prolonged propane dehydrogenation experiment, consisting of 10 dehydrogenation-regeneration cycles of 8 h each (6 h of actual dehydrogenation), at a temperature of 600 °C and a pressure of 1 bar. The propane conversion and selectivity towards propylene, as determined by on-line GC analysis, are summarized in Table 3.2 and Figure 3.3. The three catalyst materials containing Pt, display a similar high propane conversion at the start of the first cycle, with the Ga catalyst being significantly less active. Over time, the propane conversion drops as the catalyst materials start to

deactivate. The changes over time in the conversion of propane are different for each catalyst material under investigation. First of all, the Pt-Sn catalyst exhibits a stable and high conversion during the first cycle. From the second cycle onwards however, the conversion starts to drop during each cycle with increasing severity. On the other hand, the Ga catalyst shows a low initial conversion during the first cycle that also drops over the course of the cycle. However, continuous cycling does not change the catalyst performance. The Pt catalyst on the other hand has initially the same conversion as the Pt-Sn catalyst, but the conversion rapidly drops. This high performance at the start of the experiment cannot be retained by simple regeneration of the material and from the third cycle onwards the catalyst displays the lowest propane conversion. Lastly, the Pt-Ga catalyst initially behaves similar to the Pt catalyst, albeit at higher conversions. For the following cycles the performance drops: for the ninth and tenth cycle the catalyst has the same conversion and selectivity as the

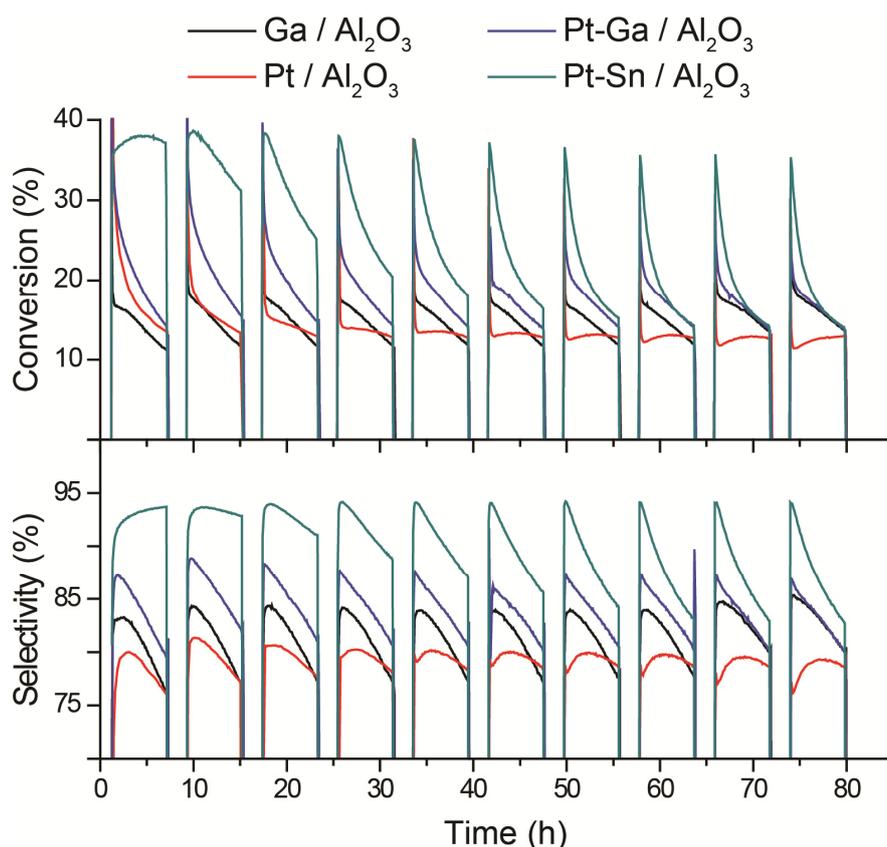


**Figure 3.3.** Conversion and selectivity obtained for the propane dehydrogenation catalyst materials under investigation during a 10-cycle propane dehydrogenation experiment. In between the cycles, the catalyst materials are regenerated by combusting the coke deposits formed.

Ga catalyst. Similar to the conversion, the selectivity towards propylene is generally the highest at the start of the cycle after which it drops over time. It was found that the Pt-Sn catalyst shows the highest selectivity towards propylene, while the Pt-Ga and Ga catalysts have an intermediate selectivity towards propylene and finally the Pt catalyst is the least selective towards propylene.

**Table 3.2.** Conversion of propane (X) and selectivity to propylene (S) on the four catalyst materials under study at different points in time during the 10 cycle propane dehydrogenation-regeneration experiment at a temperature of 600 °C and a pressure of 1 bar.

Time	Pt		Pt-Sn		Pt-Ga		Ga	
	X (%)	S (%)						
Start cycle 1	35.0	72.1	35.6	88.5	35.4	83.5	18.6	81.6
End cycle 1	13.5	76.0	37.2	93.7	14.2	79.5	11.2	76.1
Start cycle 3	17.1	80.6	38.2	92.9	30.9	88.0	19.6	83.1
End cycle 3	12.9	77.7	25.2	91.1	14.7	81.0	11.6	77.0
Start cycle 10	13.9	77.2	35.4	94.0	22.7	86.9	22.5	85.0
End cycle 10	12.9	78.6	14.1	82.8	13.8	80.0	13.5	80.0

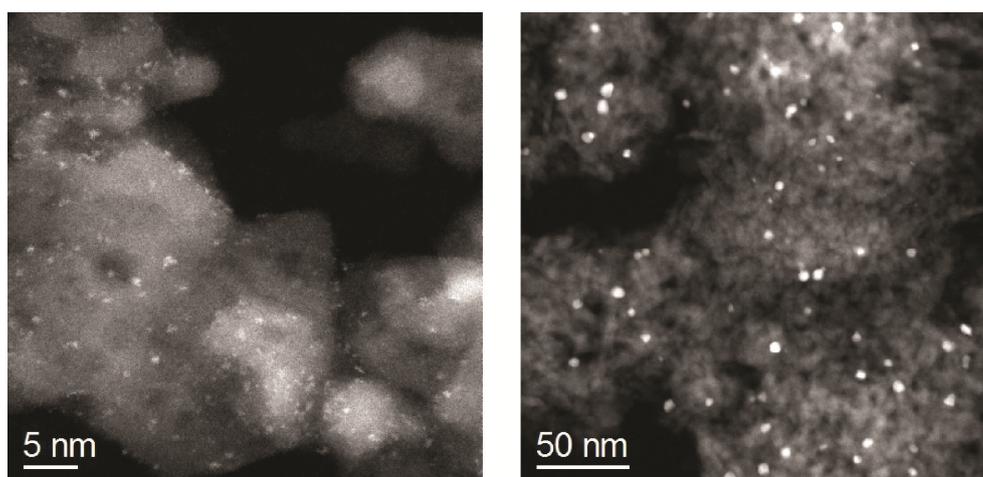


**Figure 3.4.** TEM images of a fresh (left) and deactivated Pt/Al<sub>2</sub>O<sub>3</sub> catalyst. The average size of the Pt nanoparticles increases from 0.6 (± 0.2) to 6.0 (± 1.9) nm.

TEM images of the fresh and deactivated (after 10 dehydrogenation cycles) Pt, Pt-Ga and Pt-Sn were collected, where the Pt/Al<sub>2</sub>O<sub>3</sub> catalyst is shown in Figure 3.4. For the fresh catalyst, the Pt nanoparticles are highly dispersed, resulting in an average size of 0.6 nm, with a standard deviation of 0.2 nm. After 10 dehydrogenation cycles, the size of the nanoparticles has significantly increased to an average of 6.0 nm with a standard deviation of 1.9 nm. The sintering of the Pt is also observed for the Pt-Ga and to a lesser extent for the Pt-Sn catalyst, and is partially responsible for the irreversible deactivation.

### 3.3.3 Bulk Characterization of the Coke Deposits

During the dehydrogenation experiments discussed above, operando Raman spectra are collected in a continuous fashion. In Figure 3.5, the Raman spectra obtained during the initial dehydrogenation cycle including the oxidation step on the Pt-Ga/Al<sub>2</sub>O<sub>3</sub> catalyst are shown. The two Raman bands at 1040 and 1160 cm<sup>-1</sup> are caused by Si-O vibrations of the quartz from the reactor tube. The other two bands in the spectra, at 1320 and 1590 cm<sup>-1</sup>, originate from the coke deposits formed on the catalyst. Two bands, the so-called D<sub>1</sub> and G bands respectively, corresponding with ring vibrations of disordered coke species and the ‘perfect’ graphitic lattice, can be separated by spectral deconvolution, as was discussed in detail in Chapter 2.<sup>23–25</sup> During the initial stages of the dehydrogenation reaction, the coke bands quickly increase in intensity, after which their intensity gradually drops over time. This drop is due to the self-absorption of the Raman signal, since the catalyst material gradually turns dark during the dehydrogenation reaction. While the catalyst is regenerated, the carbon deposits are combusted and the Raman bands corresponding with coke deposits disappear. As was discussed in Chapter 2, the width and position of the D<sub>1</sub> and G bands, and the ratio in intensity of the two main Raman bands observed provides information of the chemical nature of the coke deposits, with a low value corresponding to a more graphitic type of coke being present.

In Table 3.3 the D<sub>1</sub>/G ratio is summarized for the coke deposits formed on the deactivated catalyst materials under investigation. Each D<sub>1</sub>/G ratio is the averaged value for 10 consecutive spectra, and the variance is shown within brackets. The D<sub>1</sub>/G is calculated for three points during the cycling operation, in order to make the

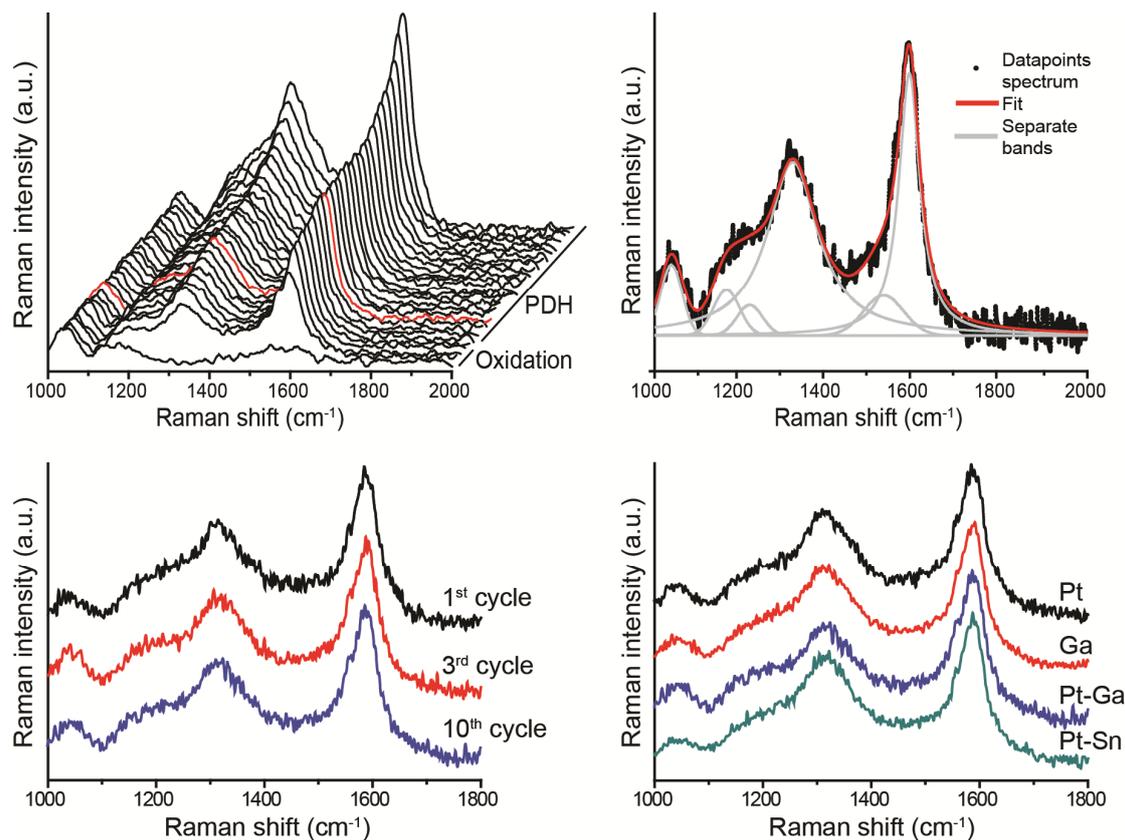


**Figure 3.5.** Operando Raman spectra of the Pt-Ga/Al<sub>2</sub>O<sub>3</sub> catalyst collected during the first propane dehydrogenation cycle (top left). Secondly, the red spectrum has been deconvoluted (top right). The Raman bands at around 1320 (D<sub>1</sub>) and 1590 (G) cm<sup>-1</sup> correspond with coke species, while the Raman bands at 1040 and 1160 cm<sup>-1</sup> originate from the quartz reactor window. At the bottom left, typical Raman spectra collected at the end of the first, third and tenth dehydrogenation cycle on the Pt-Ga catalyst are shown. At the bottom right, spectra collected at the end of the tenth dehydrogenation cycle for each of the four catalyst materials are shown.

comparison with the collected samples from the propane dehydrogenation reactor. Even though the D<sub>1</sub>/G ratio increases slightly as a function of cycling, the values and therefore the graphiticity of the coke deposits are very similar. When the D<sub>1</sub>/G ratios of the coke deposits formed on the four different catalysts (Pt, Pt-Ga, Pt-Sn and Ga) are compared, it is observed that coke formed on the Pt-Ga and Ga catalysts is slightly more graphitic in nature, compared to coke formed on Pt and Pt-Sn/Al<sub>2</sub>O<sub>3</sub>. By comparing the D<sub>1</sub>/G ratio on the Pt and Pt-Sn catalysts with those reported in Table 2.2, it is observed that coke formed on these materials is more disordered, which is

likely related to the addition of steam to the feed. The width and positions of the D<sub>1</sub> and G bands were also determined, and are included in Table 3.3. As a function of cycling or catalyst composition, no clear trend in the shape and position of the Raman bands is observed.

**Table 3.3.** HWHM (half width at half maximum), position of the D<sub>1</sub>/G and the D<sub>1</sub>/G ratio of the coke formed on the catalyst materials at the end of the first, third and tenth dehydrogenation cycle. The values are averaged by comparing 10 consecutively collected Raman spectra and within brackets the standard deviation is shown.

Catalyst sample	Cycle	HWHM D <sub>1</sub> (cm <sup>-1</sup> )	Position D <sub>1</sub> (cm <sup>-1</sup> )	HWHM G (cm <sup>-1</sup> )	Position G (cm <sup>-1</sup> )	D <sub>1</sub> /G
Pt-Ga/Al <sub>2</sub> O <sub>3</sub>	1 <sup>st</sup>	68.7 (1.8)	1316.7 (1.6)	29.1 (0.8)	1586.8 (0.6)	0.67 (0.014)
Pt-Ga/Al <sub>2</sub> O <sub>3</sub>	3 <sup>rd</sup>	66.2 (2.9)	1317.4 (1.8)	24.4 (0.5)	1589.2 (0.5)	0.69 (0.018)
Pt-Ga/Al <sub>2</sub> O <sub>3</sub>	10 <sup>th</sup>	68.9 (3.9)	1316.7 (2.2)	25.1 (1.0)	1589.0 (0.7)	0.69 (0.017)
Ga/Al <sub>2</sub> O <sub>3</sub>	1 <sup>st</sup>	72.6 (1.7)	1316.5 (0.6)	29.7 (1.4)	1587.0 (0.5)	0.70 (0.011)
Ga/Al <sub>2</sub> O <sub>3</sub>	3 <sup>rd</sup>	69.1 (1.0)	1316.6 (1.3)	26.7 (0.3)	1587.6 (0.4)	0.71 (0.013)
Ga/Al <sub>2</sub> O <sub>3</sub>	10 <sup>th</sup>	69.8 (0.9)	1316.0 (1.1)	26.8 (0.2)	1587.8 (0.3)	0.72 (0.012)
Pt/Al <sub>2</sub> O <sub>3</sub>	1 <sup>st</sup>	67.2 (1.7)	1315.4 (1.0)	26.9 (1.3)	1587.8 (0.6)	0.70 (0.026)
Pt/Al <sub>2</sub> O <sub>3</sub>	3 <sup>rd</sup>	68.6 (0.7)	1315.0 (1.0)	25.5 (1.0)	1588.4 (0.6)	0.74 (0.015)
Pt/Al <sub>2</sub> O <sub>3</sub>	10 <sup>th</sup>	67.9 (1.0)	1315.9 (1.5)	27.4 (0.7)	1588.2 (0.7)	0.73 (0.016)
Pt-Sn/Al <sub>2</sub> O <sub>3</sub>	1 <sup>st</sup>	65.9 (4.1)	1317.5 (1.4)	26.1 (0.6)	1587.4 (1.0)	0.70 (0.014)
Pt-Sn/Al <sub>2</sub> O <sub>3</sub>	3 <sup>rd</sup>	69.7 (1.7)	1315.2 (0.5)	24.8 (0.7)	1588.5 (0.7)	0.72 (0.015)
Pt-Sn/Al <sub>2</sub> O <sub>3</sub>	10 <sup>th</sup>	68.0 (0.5)	1315.9 (1.1)	26.8 (0.5)	1587.9 (0.7)	0.75 (0.014)

In a next step, thermogravimetric analysis (TGA) was used to quantify the amount of coke present on the deactivated catalyst materials collected from the propane

dehydrogenation reactor. During TGA, a flow of oxygen is used to combust the carbon deposits on the catalyst, and the resultant loss of weight is measured as a function of temperature. This is an accurate method for determining the amount of coke species, while the temperature of combustion may reveal information on the chemical nature or location of the coke species.<sup>1,26,27</sup> In Table 3.4, the amount of coke measured on different deactivated catalysts is summarized. The weight loss as a function of temperature is shown in Figure 3.6 as well, for each of the four materials after 1 and 10 propane dehydrogenation cycles. In all cases, the combustion of coke takes place between 310 and 550 °C with a varying maximum.

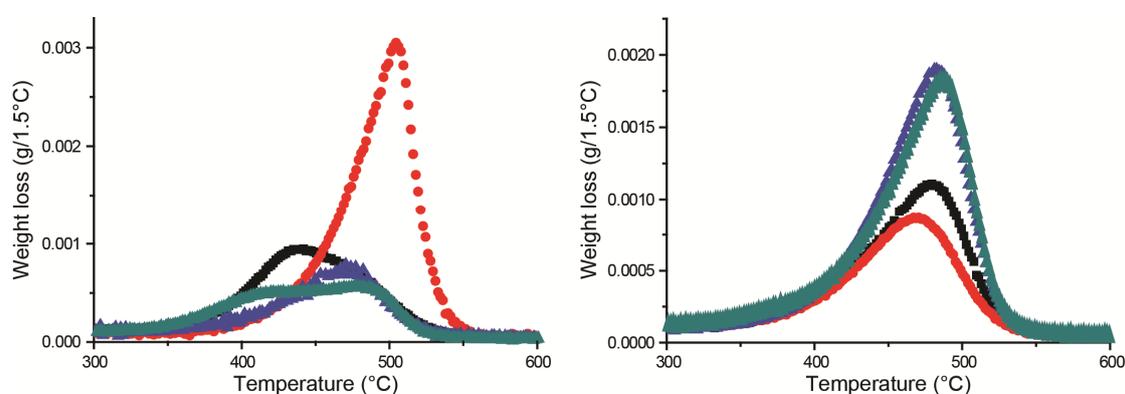


**Figure 3.6.** The derivative of the weight loss over time as a function of temperature is shown for the four deactivated catalysts under study, as measured by TGA. The catalysts were obtained after the first (left) and tenth (right) propane dehydrogenation cycle.

During the first cycle, the most coke is deposited on the Pt-Sn catalyst (10.5 wt%), and the least on the Pt-Ga and Ga catalyst (5.0; 4.0 wt%). During the tenth cycle however, the opposite is observed as significantly more coke is formed on the Pt-Ga and Ga catalysts (9.1, 8.9 vs 5.0 wt%). In both cases, an intermediate amount of coke (6.2, 6.4 wt%) is formed on the Pt/Al<sub>2</sub>O<sub>3</sub> catalyst.

Several differences are observed, when looking at the combustion temperature of the four catalysts for the first cycle. First of all, the combustion takes place at considerably lower temperatures on Pt compared to Pt-Sn/Al<sub>2</sub>O<sub>3</sub>. Operando Raman spectroscopy revealed that the coke deposits formed on these two materials were very similar, so the difference in the combustion should be related to the location of the

**Table 3.4:** Weight loss (in wt%) as measured by thermogravimetric analysis (TGA) of the collected catalyst samples from the propane dehydrogenation reactor. In all cases, the combustion takes place between 325 and 550 °C. The amount of coke formed after three dehydrogenation cycles was only determined on the Pt-Ga catalyst.

Catalyst sample	Weight loss (wt%)			T <sub>combustion</sub> (°C)	
	1 <sup>st</sup> cycle	3 <sup>rd</sup> cycle	10 <sup>th</sup> cycle	1 <sup>st</sup> cycle	10 <sup>th</sup> cycle
Pt-Ga/Al <sub>2</sub> O <sub>3</sub>	5.0	9.2	9.1	415, 480	485
Ga/Al <sub>2</sub> O <sub>3</sub>	4.0	(-)	8.9	470	480
Pt/Al <sub>2</sub> O <sub>3</sub>	6.2	(-)	6.4	440	480
Pt-Sn/Al <sub>2</sub> O <sub>3</sub>	10.5	(-)	5.0	505	470

coke. This means that on Pt/Al<sub>2</sub>O<sub>3</sub> the coke is present on the active sites, while on the Pt-Sn it is likely located on the support. This has been reported in literature previously and has been attributed to the flow-off effect of the Sn.<sup>6,9,28</sup> Coke formed on the Ga/Al<sub>2</sub>O<sub>3</sub> catalysts is combusted at intermediate temperatures, suggesting the coke is not in proximity of the active site, or that GaO<sub>x</sub> active sites are less prone to assist in the burning of the coke deposits. The combustion profile of the Pt-Ga catalyst displays two maxima, one likely corresponding with coke in proximity of the Pt nanoparticles, and the second with coke located on the support or near Ga surface species. After ten propane dehydrogenation-regeneration cycles, the combustion profiles have changed significantly, and have become quite similar. At this point, most of the Pt nanoparticles have sintered, which makes Pt-assisted combustion of the coke deposits more unlikely. As the coke is predominately located on the support now, the small differences in combustion temperature can be explained by the variations differences in the D<sub>1</sub>/G ratio, where a high value corresponds with a lower combustion temperature.

Although surface acidity is often considered to play an important factor in the deposition of coke, no correlation could be found between the surface acidity as determined by NH<sub>3</sub> TPD, and the amount, or nature of the coke deposits.

In Chapter 2, the coke deposition on similar Pt and Pt-Sn/Al<sub>2</sub>O<sub>3</sub> catalysts was studied by TGA and Raman spectroscopy. As was mentioned before, the values of the D<sub>1</sub>/G ratio at 100% propane feed for the first, third and tenth cycle on both catalyst

materials from Table 2.3 are lower than those reported in Table 3.3, meaning that the coke deposits reported in the latter are more disordered. The only difference between the experimental conditions are that steam is added to the feed in Chapter 2, which is known to hamper the formation of coke deposits. Indeed, by TGA considerably less coke is detected. Note however, that the TGA data in Figure 2.10 are collected after 3 dehydrogenation cycles, while in this Chapter they are measured after 1 and 10 dehydrogenation cycles. Nevertheless, the difference is very large, for example 1.44 wt% of coke formed on Pt in the presence of steam after 3 cycles, versus 6.2 and 6.4 wt% in the absence of steam.

The amount of coke was found to have an effect on the chemical nature of the coke deposits formed. In Figure 3.7, the parameters in the Raman spectra that reveal information of the chemistry of the coke deposits are plotted against the amount of coke deposits measured by TGA. The data points in the graph are directly obtained from Tables 3.3 and 3.4. As more coke is formed on the catalyst material, the  $D_1/G$  slightly increases and the position of the G band shifts to higher wavenumbers, while the Raman bands become more narrow. Similar trends were observed as a function of increasing hydrogen content in Chapter 2, and were believed to originate from the formation of relatively smaller, more ordered graphite sheets. In this case however, the feed is exactly the same for all the data points in the Figure, the variables being the amount of coke, and the fact that each catalyst material is different (4 different materials, each having performed 1, 3 or 10 dehydrogenation cycles). Many processes, such a sintering of the support or Pt nanoparticles and the poisoning of active or acid sites, may change the surface composition and therefore the process of coke deposition of the catalyst material. It is very difficult to determine of the trends observed by Raman spectroscopy are truly due to differences in the amount of coke formed, or whether there is really an effect of differences in the chemistry on the catalyst surface. Nevertheless, this interesting observation warrants a more thorough study on the relationship between the chemical nature of coke deposits and the amount of coke formed.

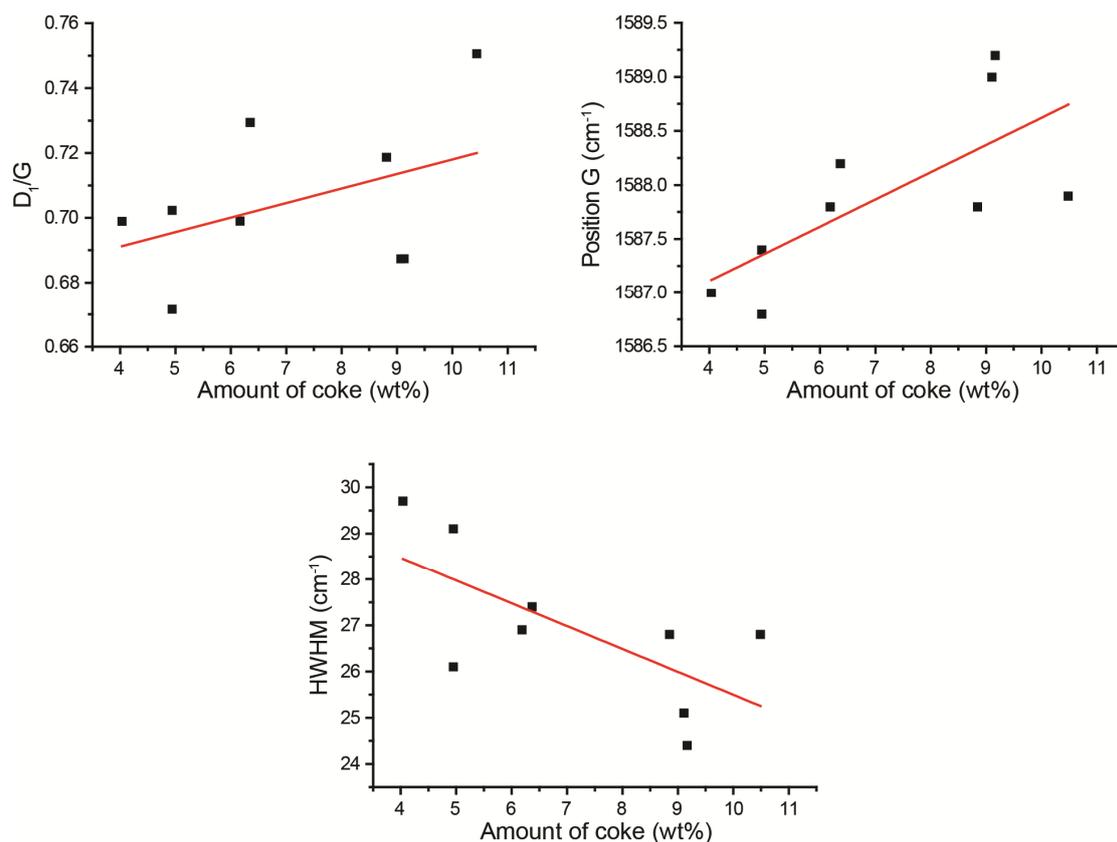


**Figure 3.7.** The amount of coke is plotted against the D<sub>1</sub>/G ratio in the top left graph, at the top right versus the position of the G band, and against the width of the G band at the bottom. The spread between the data points is large, which is why trend lines are added to visualize the trends more clearly.

### 3.3.4 STXM Analysis of Coke Deposits within a Single Catalyst Particle

Next, the deactivated catalyst materials collected from the propane dehydrogenation reactor were investigated with STXM at the carbon and oxygen K-edges. The carbon K-edge reveals specific information on the chemical bonds present in the formed coke deposits on the catalyst particles, while the oxygen K-edge is used to locate the Al<sub>2</sub>O<sub>3</sub> support constituting the catalyst particles under study precisely.

During a specific STXM experiment, a series of X-ray absorption maps of a catalyst particle at slightly alternating energies have been collected. In this way, each pixel of the image contains an X-ray absorption near edge spectrum (XANES). The spatial resolution of the STXM technique depends on the energy of the X-rays employed and the overall quality of the zone plate, and is in this case 40 nm. The next step in the spectral analysis is to group similar XANES spectra together, which is done

mathematically by performing a principle component analysis (PCA) data analysis step.<sup>29</sup> In this manner, spectral differences between different parts of the catalyst particle can be discerned. In addition, by taking the average XANES spectrum of such a cluster, the spectral quality can be significantly improved.

In Figure 3.8, the carbon K-edge X-ray absorption maps and corresponding XANES spectra are shown for the coked Pt-Ga catalyst material at the end of the first, third and tenth dehydrogenation cycle. The spectra and their corresponding regions of the catalyst particle are displayed in identical colors. Three peaks, at 285, 288.9 and 293 eV, are observed in each spectrum. The first peak at 285 eV corresponds with the transition of an electron from the 1s orbital to a  $\pi^*$  molecular orbital of a C=C bond. The second peak, at 288.9 eV, can be attributed to either a transition to a  $\pi^*$  molecular orbital of a C=C bond, or a transition to a  $\sigma^*$  molecular orbital of a  $sp^3$  hybridized C-C bond. The final peak corresponds with the transition of an electron from the 1s orbital to an unoccupied C=C  $\sigma^*$  orbital.<sup>3,13,25,30-34</sup> For the coke deposits formed after three and ten dehydrogenation cycles, an additional signal is observed at  $\sim 287.5$  eV. Several explanations for this signal have been presented in literature, including the transition of a 1s electron to the  $\sigma^*$  orbital of either C-H or C-O moieties.<sup>3,25,31-33</sup> Furthermore, interlayer states from misaligned graphene layers have been used as an explanation for this peak as well.<sup>25,32,35</sup> Finally, features between 290-310 eV can be attributed to the transition to an unoccupied C-C anti-bonding  $\sigma$ -orbital.<sup>34</sup>

When comparing the XANES spectra corresponding with the different regions obtained by PCA, the carbon species appear to be homogeneously distributed over the catalyst particles. The small differences in the XANES spectra are attributed to saturation and concentration effects. However, the sample obtained after ten dehydrogenation cycles is an exception, as the purple and green spectra appear to be different from the other regions of the particle. This will be discussed in more detail later on.

As the Pt-Ga catalyst is being cycled, the performance drops. This may be related with changes in the coke formed on the catalyst, while at the same time TGA has revealed more coke is deposited during the third and tenth dehydrogenation cycle. By carefully comparing the XANES spectra obtained of each of the catalyst materials, as shown in Figure 3.9, it can be observed that the peak at 285 eV becomes progressively more intense relative to the peak at 288.9 eV, meaning that more C=C species are

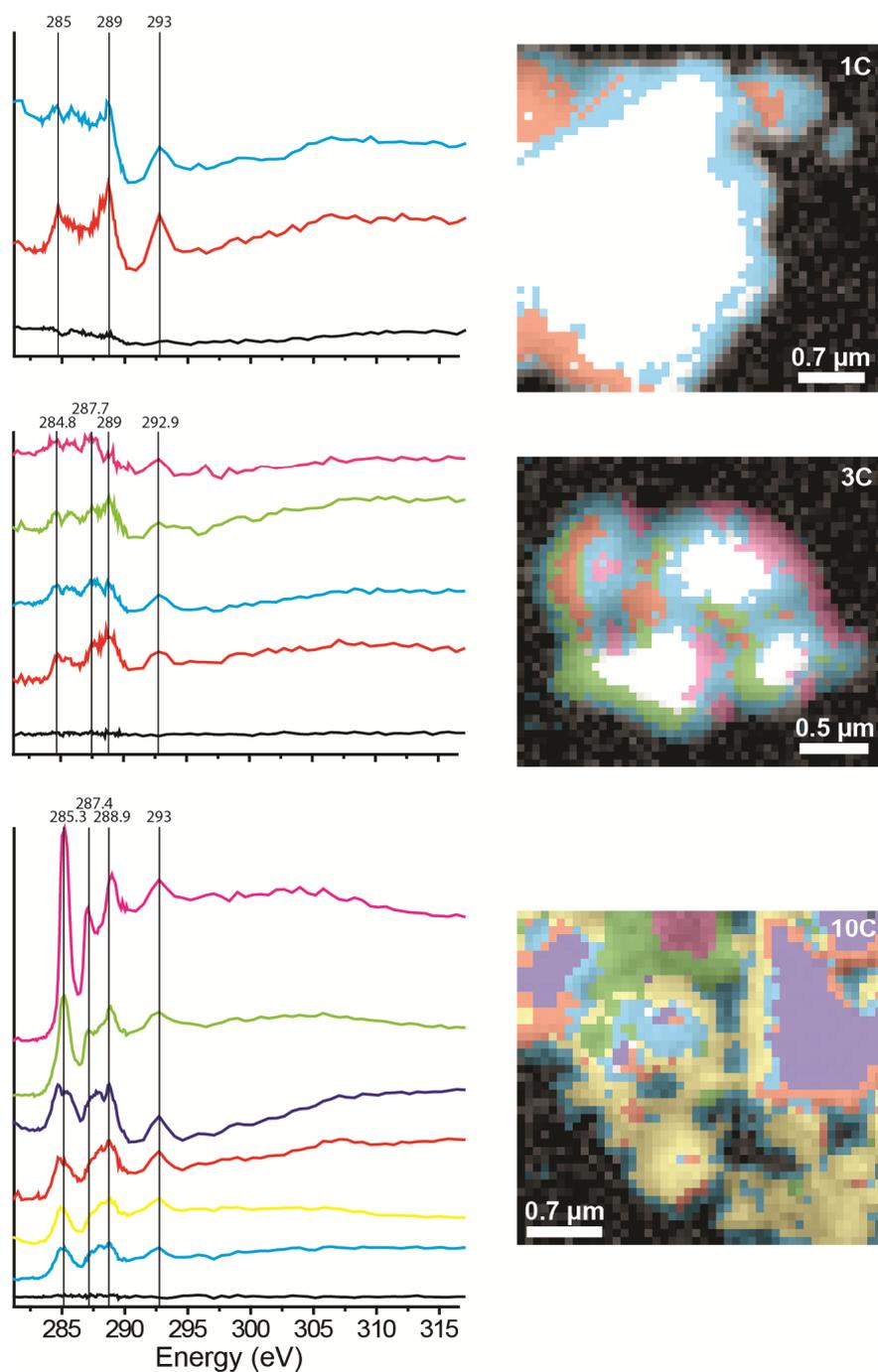


**Figure 3.8.** Carbon K-edge X-ray absorption spectra of coke deposits on the Pt-Ga/Al<sub>2</sub>O<sub>3</sub> catalysts collected from the propane dehydrogenation reactor, and after the first, third and tenth dehydrogenation cycle are shown at the left side of the Figure. The corresponding X-ray microscopy images are shown to the right; the spectra correspond with the region in the microscopy image with the same color. White areas in the STXM image where too thick to obtain a meaningful XANES spectrum and are therefore excluded from analysis.

formed at the expense of C-C moieties. The intensity of other bands does not change, suggesting that the coke is slowly becoming more graphitic, although the obtained  $D_1/G$  ratios extracted from the operando Raman spectra do not support this observation. Also the band at 287.5 eV is more prominent in the spectra obtained after 3 and 10 cycles.

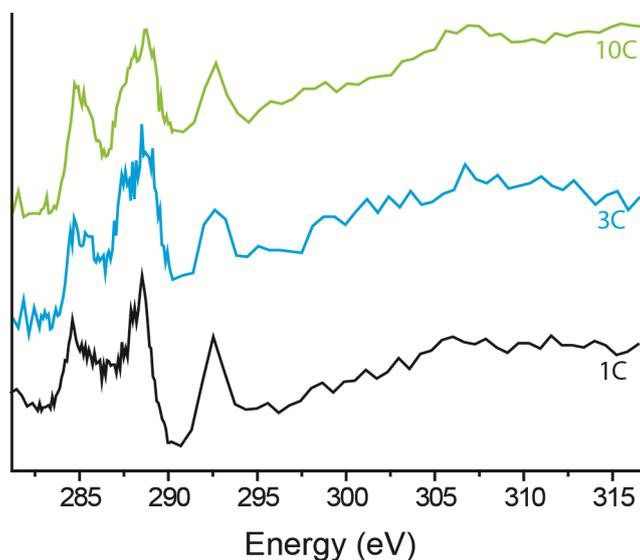


**Figure 3.9.** X-ray absorption spectra of Pt-Ga catalysts collected from the propane dehydrogenation reactor after the first, third and tenth dehydrogenation cycle. The XANES spectra are normalized relatively to the pre-edge and the peak at 289 eV. The peak at 285 eV becomes progressively stronger as the catalyst is cycled for longer times.

In Figure 3.10 the coke deposits formed on the four catalysts collected from the propane dehydrogenation reactor at the end of the 10<sup>th</sup> dehydrogenation cycle are compared. The same three XANES peaks as before are present in the spectra, and occasionally an additional shoulder is observed around 287.5 eV. Again, the intensities of the three main peaks are compared: the ratio of the peaks at 285 and 289 eV is different for the four catalyst materials. After 10 dehydrogenation cycles, the peak at 285 eV is relatively weaker for the catalysts containing Pt and Pt-Sn and is strong for the catalyst containing only Ga. This implies that the coke formed on the Ga/Al<sub>2</sub>O<sub>3</sub> catalyst is relatively ordered while those formed on the Pt/Al<sub>2</sub>O<sub>3</sub> catalyst are more disordered.

As was mentioned before, the heterogeneities in the coke deposits formed are observed in some of the STXM images, which are shown in Figure 3.11. When comparing the XANES spectra of the different regions in the images at the top of the Figure, it is clear that the purple and green spectra appear different from the other areas of this image: the peaks are more narrow and intense, and the edge jump is more pronounced. This suggests that the coke species are more graphitic and ordered than the carbon species present on other regions of the catalyst particle. Next to the graphs, the image in black and white corresponds with the X-ray absorption map at the oxygen K-edge (537.8 eV). More X-ray absorption means that more oxygen is present, which is directly related to the thickness of the catalyst particle. This means there is a relatively low amount of catalyst present at the area corresponding with the green and purple spectra. As the amount of coke at this location is very high, this suggests that the coke deposits are (at least partially) present outside the catalyst. Similar heterogeneities are observed in Figure 3.11 for the Pt/Al<sub>2</sub>O<sub>3</sub> catalyst collected

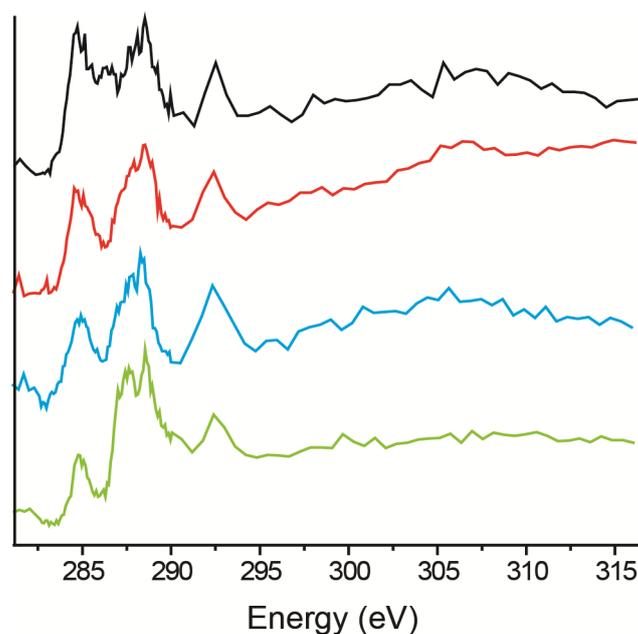


**Figure 3.10.** X-ray absorption spectra of deactivated Pt (green), Pt-Sn (blue), Pt-Ga (red) and Ga (black) catalysts collected from the propane dehydrogenation reactor after 10 cycles. The intensity of the spectra is normalized in respect to the band at 289 eV and the pre-edge. The relative intensity of the peak at 285 eV is markedly different for the four catalyst materials.

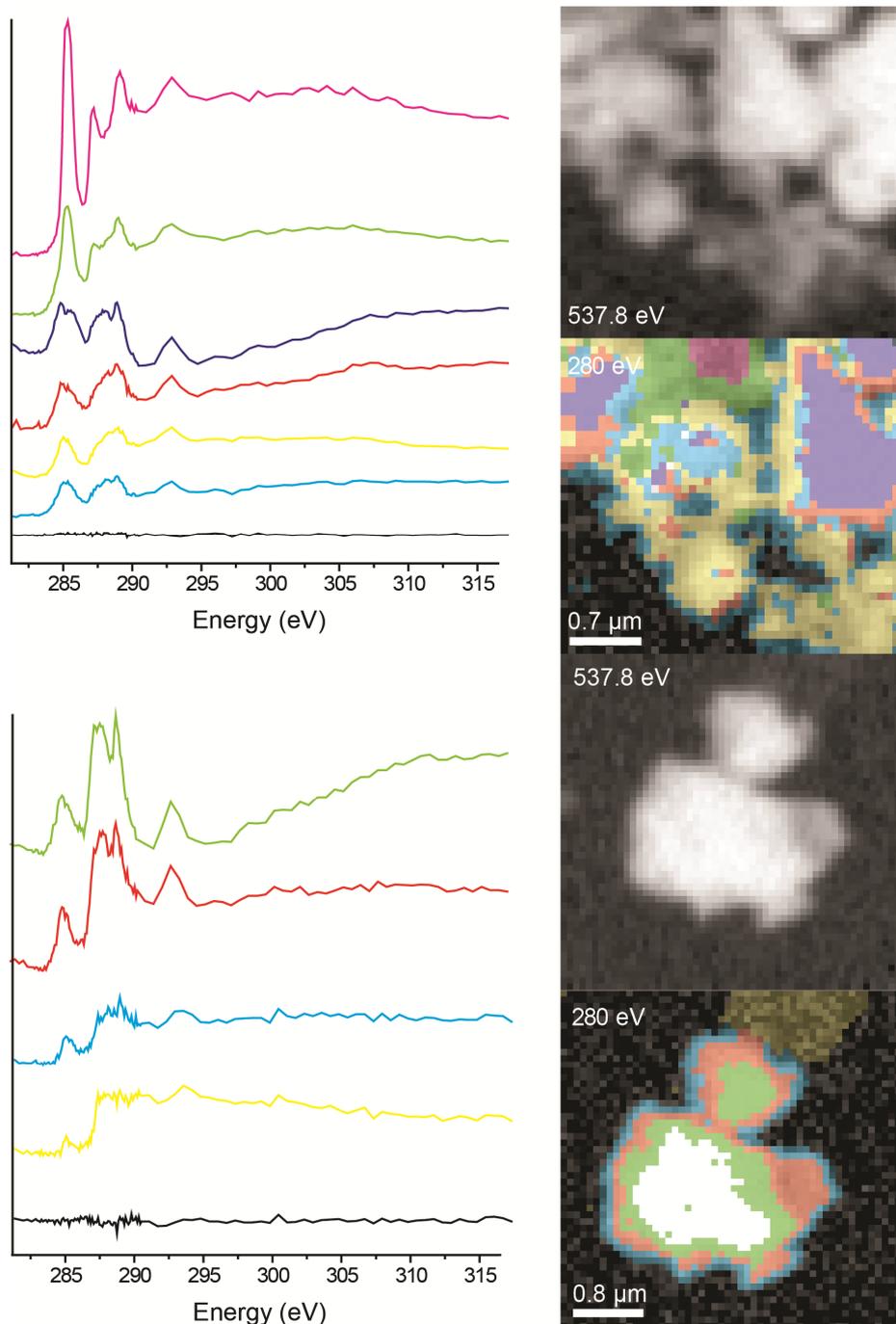


**Figure 3.11.** Carbon K-edge X-ray absorption spectra of the Pt-Ga/Al<sub>2</sub>O<sub>3</sub> (top) and Pt/Al<sub>2</sub>O<sub>3</sub> catalyst (bottom), collected from the PDH reactor after 10 successive dehydrogenation cycles. The colors of the spectra correspond with the colors in the STXM image obtained at 280 eV. In addition a STXM image obtained at 537.8 eV, which is the absorption edge of oxygen, is shown. Areas where very little or no oxygen is present (green purple at the top image, and yellow at the bottom) contain a high amount of carbon, which is present outside the catalyst particle. Note that the position of the particles has shifted between the two images.

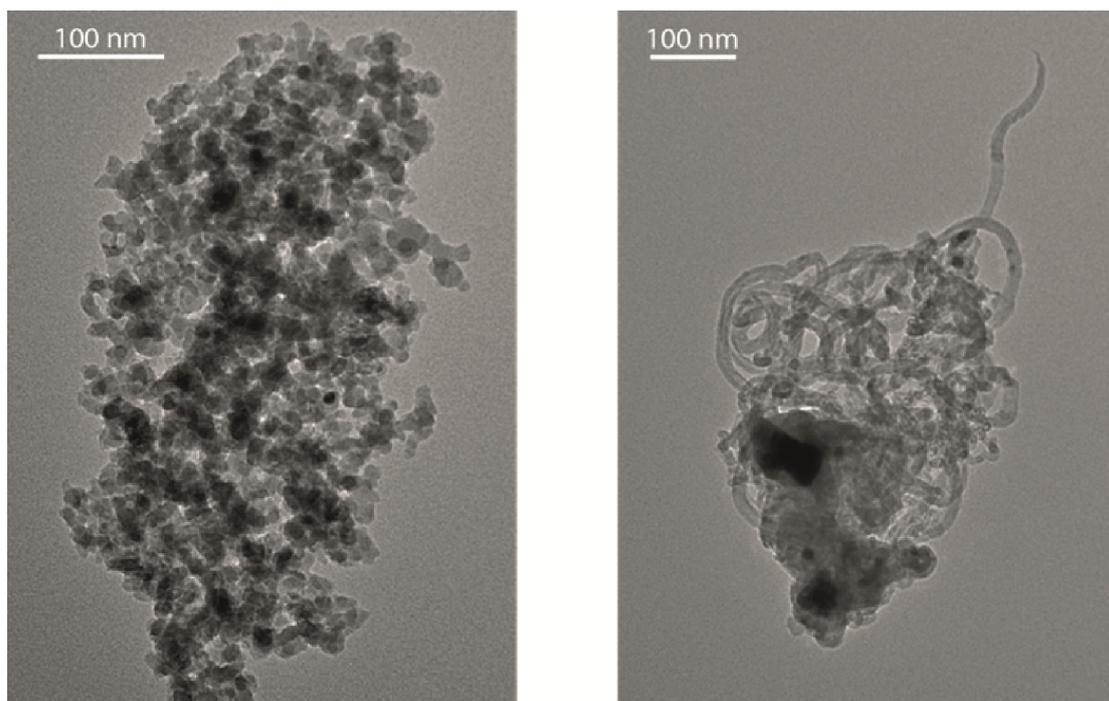


**Figure 3.12.** TEM images of the fresh Pt/Al<sub>2</sub>O<sub>3</sub> catalyst (left) and after ten propane dehydrogenation-regeneration cycles. On the outside of the deactivated catalyst (top part of the particle), fiber-like structures have formed, which is believed to be the same type of coke species on the exterior of the catalyst particle, as was observed by STXM.

from the reactor after 10 propane dehydrogenation cycles. The spectrum corresponding with the yellow region in the image is again different from the bulk of the catalyst particle. In this instance, the features of the spectra are very weak while the edge jump is very pronounced. The carbon deposits are clearly not located on the catalyst material, as no X-ray absorption is measured at the oxygen K-edge. These observations are confirmed by TEM experiments on the deactivated catalyst materials, in which carbon filaments were observed to have grown out of the catalyst particles. This is shown in Figure 3.12, where bright field images of a fresh and deactivated Pt/Al<sub>2</sub>O<sub>3</sub> particle are shown. These carbon filaments were observed for each of the catalyst materials, independent of the time exposed to propane. However, it is important to stress here that the carbon filaments are only observed on a minority of the catalyst particles. These filaments explain the areas in Figure 3.11, which have a high concentration of carbon while they are outside of the catalyst particles.

Summarizing, STXM provides information on the nature of the coke deposits within individual catalyst particles. However, the interpretation of the data is not straightforward, as different functionalities have been connected with the observed peaks in literature. Nevertheless, some trends are observed. First of all, the relative intensity of the peak at 285 eV, corresponding with the  $\pi^*$  transition of C=C bonds in aromatics, becomes more dominant after the catalyst performs the dehydrogenation reaction for longer times, which implies the carbon deposits contain more aromatic species. This is not in agreement with observations made by Raman spectroscopy, since the  $D_1/G$  ratio of coke deposits formed on the Pt-Ga catalyst at the end of the first, third and tenth cycle was found to be very similar. At the same time, these catalyst materials lose their activity, which may be related to the intensity increase of this STXM peak. When the relative intensity of the peak at 285 eV is compared for the different catalysts under study, it was found that this peak is strong for the Ga and Pt-Ga catalysts, and relatively weak for the Pt and Pt-Sn catalysts. This is in agreement with operando Raman spectroscopy, as coke formed after ten dehydrogenation cycles on the Ga and Pt-Ga catalysts is markedly more graphitic in nature than coke deposits formed on the Pt and Pt-Sn catalysts. For the latter two catalysts, a slightly higher  $D_1/G$  ratio is also observed.

During the first cycles, the Pt-Ga catalyst displays similar catalytic activity as the Pt/ $\text{Al}_2\text{O}_3$  catalyst, while at the final cycles the conversion is very similar to the Ga/ $\text{Al}_2\text{O}_3$  catalyst. The XANES peak at 285 eV is relatively strong after 10 dehydrogenation cycles for the Pt-Ga and Ga/ $\text{Al}_2\text{O}_3$  catalysts compared to the Pt and Pt-Sn/ $\text{Al}_2\text{O}_3$  catalyst. This indicates that the coke formed on Ga has a more disordered chemical nature from coke formed on Pt-based catalysts. An explanation for this would be that Pt, unlike  $\text{GaO}_x$ , is able to further dehydrogenate coke deposits already formed, creating more graphitic species. This effect can also explain differences in the chemical nature of coke located on the outside of the catalyst particle compared to coke formed on the inside of the particle. Furthermore, inside the catalyst particle, the coke species are confined by the pore structure of the catalyst particle, which obviously constricts the growth and chemical nature of the carbon deposits.

### 3.4 Conclusions

Four catalyst materials, Pt, Ga, Pt-Ga and Pt-Sn supported on  $\text{Al}_2\text{O}_3$ , were prepared and tested for the catalytic dehydrogenation of propane. Catalyst deactivation by coke deposition was of specific interest, and for this reason the deactivated catalyst materials were studied by operando Raman spectroscopy, TEM, TGA and STXM. The different techniques provide complementary information regarding the coke formed after ten propane dehydrogenation cycles. Trends in the Raman spectra as a function of the amount of coke were observed, implying that the nature of the coke deposits partially depend on the amount of coke formed. For Pt-Ga and Ga catalysts we observe the highest amount of coke as observed with TGA, the lowest  $D_1/G$  ratio as observed with operando Raman and the highest X-ray absorption peak corresponding with C=C bonds (285 eV). The reverse is the case for the Pt and Pt-Sn catalysts, meaning that the coke formed on these two catalyst materials is relatively more disordered compared to the coke deposits formed on the Ga and Pt-Ga catalysts. In addition, STXM analysis shows that the coke deposits formed on the catalyst material are not homogeneous, as coke filaments are formed on the catalyst's exterior, which have a different chemical nature as the coke formed inside the catalyst particle. In addition, sintering of the Pt nanoparticles was observed by TEM. This means that STXM will afford additional information to bulk characterization techniques on the coke type and amount formed on the catalyst material.

### 3.5 Acknowledgements

Marjan Versluijs (Utrecht University) is kindly acknowledged for performing the TGA experiments. Jörg Raabe (Swiss Light Source), Inés González-Jimenez and Christoph Sprung (Utrecht University) are thanked for their assistance in performing the STXM experiments. The Pollux beamline (Swiss Light Source, Paul Scherrer Institute, Villigen, Switzerland) is acknowledged for providing the opportunity to perform the STXM experiments. Florian Meirer (Utrecht University) is thanked for

his assistance in with the analysis of the STXM data. Hien Pham and Datye Abhaya (University of New Mexico) are thanked for the dark field TEM measurements.

### 3.6 References

- (1) Sahoo, S. K.; Rao, P. V. C.; Rajeshwer, D.; Krishnamurthy, K. R.; Singh, I. D. *Appl. Catal. A-Gen.* **2003**, *244*, 311.
- (2) Airaksinen, S. M. K.; Banares, M. A.; Krause, A. O. I. *J. Catal.* **2005**, *230*, 507.
- (3) McGregor, J.; Huang, Z.; Parrott, E. P. J.; Zeitler, J. A.; Nguyen, K. L.; Rawson, J. M.; Carley, A.; Hansen, T. W.; Tessonier, J.-P.; Su, D. S.; Teschner, D.; Vass, E. M.; Knop-Gericke, A.; Schlögl, R.; Gladden, L. F. *J. Catal.* **2010**, *269*, 329.
- (4) Iglesias-Juez, A.; Beale, A. M.; Maaijen, K.; Weng, T. C.; Glatzel, P.; Weckhuysen, B. M. *J. Catal.* **2010**, *276*, 268.
- (5) Sattler, J. J. H. B.; Beale, A. M.; Weckhuysen, B. M. *Phys. Chem. Chem. Phys.* **2013**, *15*, 12085.
- (6) Guisnet, M.; Magnoux, P. *Appl. Catal. A-Gen.* **2001**, *212*, 83.
- (7) Niemantsverdriet, J. W.; van Langeveld, A. D. *Fuel* **1986**, *65*, 1396.
- (8) Albers, P.; Seibold, K.; Prescher, G.; Muller, H. *Appl. Catal. A-Gen.* **1999**, *176*, 135.
- (9) Virnovskaia, A.; Jørgensen, S.; Hafizovic, J.; Prytz, Ø.; Kleimenov, E.; Hävecker, M.; Bluhm, H.; Knop-Gericke, A.; Schlögl, R.; Olsbye, U. *Surf. Sci.* **2007**, *601*, 30.
- (10) Van Donk, S.; de Groot, F. M. F.; Stéphan, O.; Bitter, J. H.; de Jong, K. P. *Chem. Eur. J.* **2003**, *9*, 3106.
- (11) Schoonheydt, R. A. *Chem. Soc. Rev.* **2010**, *39*, 5051.
- (12) Hofmann, J. P.; Mores, D.; Aramburo, L. R.; Teketel, S.; Rohnke, M.; Janek, J.; Olsbye, U.; Weckhuysen, B. M. *Chem. Eur. J.* **2013**, *19*, 8533.
- (13) De Jesus, L. R.; Dennis, R. V.; Depner, S. W.; Jaye, C.; Fischer, D. A.; Banerjee, S. *J. Phys. Chem. Lett.* **2013**, *4*, 3144.

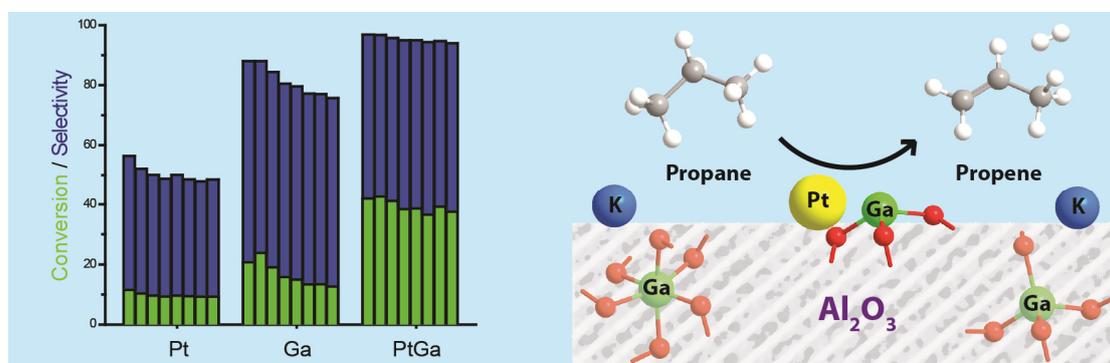
- (14) De Smit, E.; Swart, I.; Creemer, J. F.; Hoveling, G. H.; Gilles, M. K.; Tylicszak, T.; Kooyman, P. J.; Zandbergen, H. W.; Moring, C.; Weckhuysen, B. M.; de Groot, F. M. F. *Nature* **2008**, *456*, 222.
- (15) Aramburo, L. R.; de Smit, E.; Arstad, B.; van Schooneveld, M. M.; Sommer, L.; Juhin, A.; Yokosawa, T.; Zandbergen, H. W.; Olsbye, U.; de Groot, F. M. F.; Weckhuysen, B. M. *Angew. Chem. Int. Ed.* **2012**, *51*, 3616.
- (16) Aramburo, L. R.; Ruiz-Martínez, J.; Sommer, L.; Arstad, B.; Buitrago-Sierra, R.; Sepúlveda-Escribano, A.; Zandbergen, H. W.; Olsbye, U.; de Groot, F. M. F.; Weckhuysen, B. M. *Chem. Cat. Chem.* **2013**, *5*, 1386.
- (17) Aramburo, L. R.; Teketel, S.; Svelle, S.; Bare, S. R.; Arstad, B.; Zandbergen, H. W.; Olsbye, U.; de Groot, F. M. F.; Weckhuysen, B. M. *J. Catal.* **2013**, *307*, 185.
- (18) Nijhuis, T. A.; Tinnemans, S. J.; Visser, T.; Weckhuysen, B. M. *Phys. Chem. Chem. Phys.* **2003**, *5*, 4361.
- (19) Bhasin, M. M.; McCain, J. H.; Vora, B. V.; Imai, T.; Pujadó, P. R. *Appl. Catal. A-Gen.* **2001**, *221*, 397.
- (20) Niwa, M.; Katada, N. *Chem. Rec.* **2013**, *13*, 432.
- (21) Nesterenko, N. S.; Ponomoreva, O. A.; Yuschenko, V. V.; Ivanova, I. I.; Testa, F.; Di Renzo, F.; Fajula, F. *Appl. Catal. A-Gen.* **2003**, *254*, 261.
- (22) Zheng, B.; Hua, W.; Yue, Y.; Gao, Z. *J. Catal.* **2005**, *232*, 143.
- (23) Tuinstra, F.; Koenig, J. L. *J. Chem. Phys.* **1970**, *53*, 1126.
- (24) Sadezky, A.; Muckenhuber, H.; Grothe, H.; Niessner, R.; Poschl, U. *Carbon*, **2005**, *43*, 1731.
- (25) Bernard, S.; Beyssac, O.; Benzerara, K.; Findling, N.; Tzvetkov, G.; Brown Jr., G. E. *Carbon N. Y.* **2010**, *48*, 2506.
- (26) Stagg, S. M.; Querini, C. A.; Alvarez, W. E.; Resasco, D. E. *J. Catal.* **1997**, *168*, 75.
- (27) Bai, L.; Zhou, Y.; Zhang, Y.; Liu, H.; Sheng, X. *Ind. Eng. Chem. Res.* **2009**, *48*, 9885.
- (28) Li, Q.; Sui, Z.; Zhou, X.; Zhu, Y.; Zhou, J.; Chen, D. *Top. Catal.* **2011**, *54*, 888.
- (29) Lerotic, M.; Jacobsen, C.; Schäfer, T.; Vogt, S. *Ultramicroscopy* **2004**, *100*, 35.
- (30) Atamny, F.; Blocker, J.; Henschke, B.; Schlogl, R.; Keil, M.; Bradshaw, A. M. *J. Phys. Chem* **1992**, *96*, 4522.

- (31) Yoon, T. H.; Benzerara, K.; Ahn, S.; Luthy, R. G.; Tyliczszak, T.; Brown, G. E. *Environ. Sci. Technol.* **2006**, *40*, 5923.
- (32) Brandes, J.; Cody, G.; Rumble, D.; Haberstroh, P.; Wirick, S.; Gelinas, Y. *Carbon N. Y.* **2008**, *46*, 1424.
- (33) Buijnsters, J. G.; Gago, R.; Jiménez, I.; Camero, M.; Agulló-Rueda, F.; Gómez-Aleixandre, C. *J. Appl. Phys.* **2009**, *105*, 093510.
- (34) Aramburo Corrales, L. R. Spatiotemporal Spectroscopy of Molecular Sieves: Interplay between Hydrothermal Treatments and the Methanol-To-Hydrocarbons Reaction, PhD Thesis, Utrecht University, 2012.
- (35) Fischer, D. A.; Wentzcovitch, R. M.; Carr, R. G.; Continenza, A.; Freeman, A. *J. Phys. Rev. B.* **1991**, *44*, 1427.



## Chapter 4

# Pt-Ga/Al<sub>2</sub>O<sub>3</sub> as a Highly Active, Selective and Stable Catalyst for the Dehydrogenation of Propane



A novel catalyst material, based on 1000 ppm Pt, 1.5-3 wt% of Ga and 0.25 wt% of K supported on alumina, was tested for the dehydrogenation of propane. A synergy between Pt and Ga is observed that resulted in a very active and stable catalyst, that is highly resistant to coking. The catalyst material was investigated with a wide range of characterization techniques and it is proposed that coordinately unsaturated Ga<sup>3+</sup> sites of the catalyst are responsible for the C-H activation of propane, while dispersed Pt assists in the formation and desorption of hydrogen.

This Chapter is based on the manuscript: J.J.H.B. Sattler, I.D. Gonzalez-Jimenez, L. Luo, B.A. Stears, A Malek, D.G. Barton, B.A. Kilos, M.P. Kaminsky, T.W.G.M. Verhoeven, E.J. Koers, M. Baldus, B.M. Weckhuysen, Pt promoted Ga/Al<sub>2</sub>O<sub>3</sub> as a Highly Active, Selective and Stable Catalyst for the Dehydrogenation of Propane, *Angew. Chem. Int. Ed.* **53** (2014) 9251-9256.

## 4.1 Introduction

As was discussed in Chapter 1,  $\text{GaO}_x$  is known to be an active catalyst material for the dehydrogenation of propane, albeit one that is considerably less active compared to Pt-based catalyst formulations. Only a few authors have explored the merits of combining Pt and Ga in a propane dehydrogenation (PDH) catalysts, and they found that for these systems, Ga is a promoter element, while Pt is responsible for the alkane dehydrogenation activity.<sup>1-4</sup> Within this context, a comparison with the promoting effect of Sn on Pt PDH catalysts has been made, as the electronic and geometric effects were used to explain the positive promoter contribution of Ga.

These reports are in strong contrast with the Pt-Ga catalysts discussed in this Chapter, where minute amounts of Pt are combined with Ga to obtain a highly active selective and stable propane dehydrogenation catalyst. A series of catalyst materials, consisting of combinations of 1000 ppm Pt, 1.5 - 3 wt% of Ga and 0.25 wt% K was prepared. Catalytic tests were performed on these catalyst materials in a reactor setup, during which on-line operando UV-Vis and Raman spectroscopic data was collected. The catalytic data obtained suggests that Ga is the active dehydrogenation element, while Pt is considered to promote the activity of the catalyst.

In order to understand what makes the developed catalyst materials so effective in the propane dehydrogenation reaction, a wide range of characterization techniques, including X-ray photoelectron spectroscopy (XPS), temperature programmed reduction (TPR), transmission electron microscopy (TEM), <sup>71</sup>Ga magic-angle spinning nuclear magnetic resonance (MAS NMR), N<sub>2</sub> physisorption, transmission electron microscopy (TEM) and CO chemisorption, was used to investigate the chemical and physical properties of Ga and Pt.

## 4.2 Experimental

### 4.2.1 Catalyst Preparation

The catalyst materials were prepared by the incipient wetness impregnation method by impregnating an alumina support with an aqueous solution containing

Pt(NH<sub>3</sub>)<sub>4</sub>(NO<sub>3</sub>)<sub>2</sub> (Aldrich, 99.995%), Ga(NO<sub>3</sub>)<sub>3</sub> (Aldrich, 99.9%) and KNO<sub>3</sub> (Aldrich, > 99%). In total, nine catalysts were prepared, containing either 1.5 or 3 wt% of Ga (Ga or 3Ga), optionally promoted with 1000 ppm Pt (Pt), 0.25 wt% K (K) or both. Combinations of the abbreviations shown between brackets are used henceforth for the identification of the catalyst materials and are summarized in Table 4.1. For comparison, a catalyst only containing 1000 ppm Pt is included. After impregnation, the catalyst materials are calcined in air at 750 °C.

**Table 4.1.** The composition of the catalyst materials prepared by the incipient wetness impregnation method and the corresponding sample codes. Furthermore, a Pt-Sn and a commercial-like CrO<sub>x</sub>/Al<sub>2</sub>O<sub>3</sub> reference catalysts are included.

Catalyst material (supported on alumina)	Sample code
1000 ppm Pt, 1.5 wt% Ga, 0.25 wt% K	PtGaK
1000 ppm Pt, 3 wt% Ga, 0.25 wt% K	Pt3GaK
1000 ppm Pt, 1.5 wt% Ga	PtGa
1000 ppm Pt, 3 wt% Ga	Pt3Ga
1.5 wt% Ga, 0.25% K	GaK
3 wt% Ga, 0.25% K	3GaK
1.5 wt% Ga	Ga
3 wt% Ga	3Ga
1000 ppm Pt	Pt
Bare alumina	Al <sub>2</sub> O <sub>3</sub>
13 wt% CrO <sub>x</sub> , 0.25% Na	CrO <sub>x</sub>
0.5 wt% Pt, 1.5 wt% Sn	Pt-Sn

#### 4.2.2 Catalyst Characterization

Bright field TEM analysis was performed on a Tecnai 20 apparatus equipped with a field emission gun at 200 keV. For N<sub>2</sub> physisorption, a TriStar 3000 V6.08 A has been used at -196 °C after drying the samples overnight. Aberration corrected STEM was performed on a JEOL JEM-ARMS200CF (200kV) apparatus, which was equipped with an Oxford Energy Dispersive Spectroscopy system and a wide area detector for atomic resolution elemental analysis.

$^{71}\text{Ga}$  magic-angle spinning nuclear magnetic resonance (MAS NMR) were performed a 9.4 T Bruker Avance III NMR system using an MAS rate of 16 kHz is used. In order to minimize baseline distortions, a windowless spin-echo pulse sequence was used, with an echo delay of 2  $\mu\text{s}$  and a dead time of 5  $\mu\text{s}$ .<sup>5</sup> The radio frequency field strength was set to 83 kHz and experiments conducted lasted for 12 days. X-ray photoelectron spectroscopy (XPS) experiments were performed on a Thermo Scientific K-Alpha apparatus, equipped with an Al ( $K\alpha$ ) anode. The catalyst powder was deposited on a carbon sticky tape in order to minimize charging effects. In addition, quasi in-situ XPS was performed on the Pt<sub>3</sub>GaK catalyst material, which was reduced in a reactor for 1 h under a H<sub>2</sub> flow. The reduced catalyst was transferred under an inert atmosphere to a Kratos AXIS Ultra spectrometer equipped with a monochromatic X-ray source and a delay-line detector. Spectra were obtained using an Al ( $K\alpha$ ) anode operating at 150 W and with a background pressure of  $2 \times 10^{-9}$  bar. The CasaXPS program is used to analyze the obtained XPS spectra.

Temperature programmed reduction (TPR) experiments were performed a Micromeritics Autochem II flow system, equipped with a TCD detector. Approximately 0.25 g of catalyst is placed in a quartz tube and after a drying step at 150 °C under an inert atmosphere, the material is heated to 700 °C at a rate of 5 °C/min under a flow of 5% H<sub>2</sub> in He. A Micromeritics ASAP 2020 apparatus was used to determine the Pt dispersion of the PtGaK catalyst using CO adsorption. For this purpose, 1.8 g of sample was loaded in a quartz sample tube. The catalyst was subject to different treatments: a pretreatment by flushing N<sub>2</sub> for 10 min at 35 °C, an oxidation step (10% O<sub>2</sub> in He) at different temperatures (550-650 °C) for 240 min, a reduction step in H<sub>2</sub> at different temperatures (550-650 °C) for 240 min and an evacuation step (7 mbar) for 60 min. Two consecutive CO adsorption isotherm were collected at 35 °C with 15 pressure points between 33 and 867 mbar. Finally, the metal dispersion was calculated based on the difference between these isotherms, assuming a unitary ratio of CO to surface Pt.

#### 4.2.3 Catalytic Testing and Study of Coke Deposition

The materials were tested for the dehydrogenation of propane on a reactor setup which allows for the use of operando Raman and UV-Vis spectroscopy, combined with on-line GC analysis.<sup>6</sup> A quartz reactor, including two optical grade windows, was loaded with 0.15 g of catalyst material on a bed of quartz wool. In total eight

dehydrogenation-regeneration cycles have been performed. The dehydrogenation reaction step was run at 620 °C with a flow of 9 ml of propane per min for a total of 15 min (WHSV = 6.5 h<sup>-1</sup>), after which the catalyst was regenerated by flowing a mixture of O<sub>2</sub> (6%) in He over the catalyst material at 750 °C. In between these reaction steps the reactor is flushed with He. Compared to the reaction conditions used in Chapter 2 and 3, the temperature of the reaction and regeneration step are higher (both 600 °C) and the space velocity is twice as high (WHSV = 3.2 h<sup>-1</sup>). The composition of the reaction stream was continuously analyzed by an on-line GC, equipped with a FID (Porabond-Q column) and TCD (Carboxan column) detector. The long-term stability test was performed at identical conditions. Operando Raman and UV-Vis spectra are collected by respectively a Kaiser Optical Systems Raman spectrometer (7 accumulations and 5 s exposure time) and an Avantes 2048 UV-Vis spectrometer equipped with a high temperature probe (50 accumulations and 70 ms exposure time). After the 8<sup>th</sup> dehydrogenation step, instead of regenerating the catalyst, the reactor is cooled to ambient under a He flow, and the catalyst material collected from the reactor for TGA-MS analysis. Between 10 and 25 mg of the catalyst material was loaded in a Perkin-Elmer Pyris 1 TGA instrument. The sample was dried at 150 °C under an Ar flow, and consecutively heated from 30 to 900 °C under air at a ramp of 10 °C/min, while changes in weight of the sample were measured. The gas flow exiting the TGA apparatus was measured with a Omnistar mass spectrometer from Pfeiffer Vacuum.

## 4.3 Results and Discussion

### 4.3.1 Catalytic Testing

The catalyst materials were tested in a reactor for eight successive dehydrogenation-regeneration cycles, each consisting of a 15 min propane dehydrogenation step at 620 °C, followed by a treatment in air at 750 °C for 30 min. A summary of the catalytic data obtained for the ten materials studied is given in Table 4.2 for the first, second and eighth cycles. In addition, Figure 4.1 shows the selectivity and activity during each cycle on the bare support, the Pt, 3Ga, Pt3Ga and Pt3GaK catalysts.

From Figure 4.1 and the Table 4.2, large differences between the catalytic performances of the catalyst materials are observed. In case of the catalyst materials that contain both Pt and Ga, a relatively high conversion is observed, which is close to the chemical equilibrium for the first dehydrogenation cycle, i.e. ~ 55% at 620 °C and 1 atm pressure. When Pt is absent, the conversion of propane is roughly halved, while the absence of Ga results in an even larger drop in catalyst activity. The selectivity is high for all catalyst materials that contain both Pt and Ga, but again drops when either element is absent. These effects imply a synergy between Pt and Ga that results in a highly active and selective catalyst. Alkali dopants, such as K, are known to increase the propylene selectivity and decrease coke deposition by poisoning Brønsted acid sites present on the catalyst material.<sup>7</sup> Indeed, a slight increase in propylene selectivity after K addition is observed to the Ga and PtGa catalysts. Two reference catalysts, namely CrO<sub>x</sub> and Pt-Sn supported on Al<sub>2</sub>O<sub>3</sub>, were tested under identical conditions (the Pt-Sn/Al<sub>2</sub>O<sub>3</sub> catalyst was used as well in Chapter 3, while the CrO<sub>x</sub>/Al<sub>2</sub>O<sub>3</sub> catalyst material is the same as described in an article by Bennici et al.<sup>8</sup>). The Pt-Ga catalysts under investigation have a similar excellent performance as the commercial-like CrO<sub>x</sub> and Pt-Sn/Al<sub>2</sub>O<sub>3</sub> during the first cycle. Finally, the bare support displayed a very low conversion and selectivity and is therefore considered to be inactive.

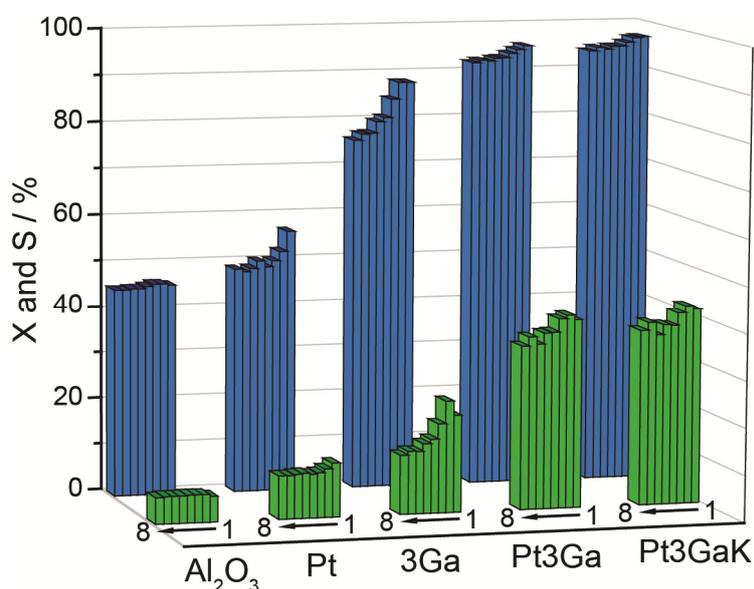


**Figure 4.1.** Conversion of propane (X, green) and selectivity towards propylene (S, blue) during eight successive propane dehydrogenation (PDH) cycles on the Al<sub>2</sub>O<sub>3</sub> support, Pt, 3Ga, Pt3Ga and Pt3GaK catalysts. Both Pt and Ga are required in order to obtain a very active PDH catalyst.

**Table 4.2.** The conversion (X) and selectivity (S) of the 12 catalyst materials measured halfway the first, second and eighth cycles. The initial activity was slightly higher, and dropped slowly during the propane dehydrogenation step.

Catalyst	First cycle		Second cycle		Eighth cycle	
	X (%)	S (%)	X (%)	S (%)	X (%)	S (%)
PtGaK	42.0	96.7	41.9	96.1	35.3	93.5
Pt3GaK	41.9	96.9	42.6	96.7	37.5	94.0
PtGa	42.0	96.7	42.6	96.8	32.3	92.8
Pt3Ga	40.3	95.4	41.3	94.6	35.0	91.9
GaK	14.7	88.9	24.0	86.5	15.7	78.2
3GaK	21.8	89.0	21.8	85.4	10.4	64.8
Ga	15.8	81.3	20.4	84.8	15.3	77.4
3Ga	20.7	88.0	23.8	88.0	12.6	75.7
Pt	11.5	56.4	10.3	52.1	9.2	48.5
Al <sub>2</sub> O <sub>3</sub>	5.5	45.5	5.9	45.8	5.6	44.7
CrO <sub>x</sub>	40.3	92.4	41.9	91.6	39.7	91.8
Pt-Sn	39.6	96.1	6.5	64.0	5.6	50.5

During the second PDH cycle the catalysts did not deactivate significantly. In fact, for the GaK, Ga and 3Ga catalysts, the propane conversion even increases. This implies that these catalysts require an activation period, related to exposure to oxygen at 750 °C. Indeed, by treating the GaK catalyst with oxygen at 750 °C prior to the first propane dehydrogenation cycle, the conversion is increased from 14.7 to 20.5%. Treating the catalyst at 620°C under air prior to reaction has less of a beneficial effect, as the conversion is only 18.5% for the first propane dehydrogenation cycle. Apparently, a high temperature during the regeneration is required for the Ga to remain active for the PDH process.

For the eighth cycle the values of propane conversion and propylene selectivity have dropped for all catalysts. The deactivation of these materials is the least severe for the catalysts containing both Pt and Ga. It is known that Pt-based dehydrogenation catalysts deactivate due to sintering of the metal nanoparticles, an effect provoked by the harsh conditions of the dehydrogenation reaction, which is exactly what is

observed for the Pt-Sn reference material.<sup>9-11</sup> Therefore it is surprising that even though the dehydrogenation and oxidation are performed at relatively high temperatures, no such deactivation is observed for the Pt-Ga catalysts: the synergy between the two elements remains as these materials continue to outperform their analogues that contain only Ga.

In addition to the aforementioned catalytic tests, a long-term stability test was performed on the Pt<sub>3</sub>GaK catalyst, which displayed the highest performance in the PDH reaction. The experiment consisted of about 150 cycles over a 14 day period, and is shown in Figure 4.2. It was found that the PDH activity drops during the first two days of testing, after which the catalyst performance remained stable during a twelve day evaluation period, resulting in a propane conversion of 31% and a selectivity towards propylene of 93%.

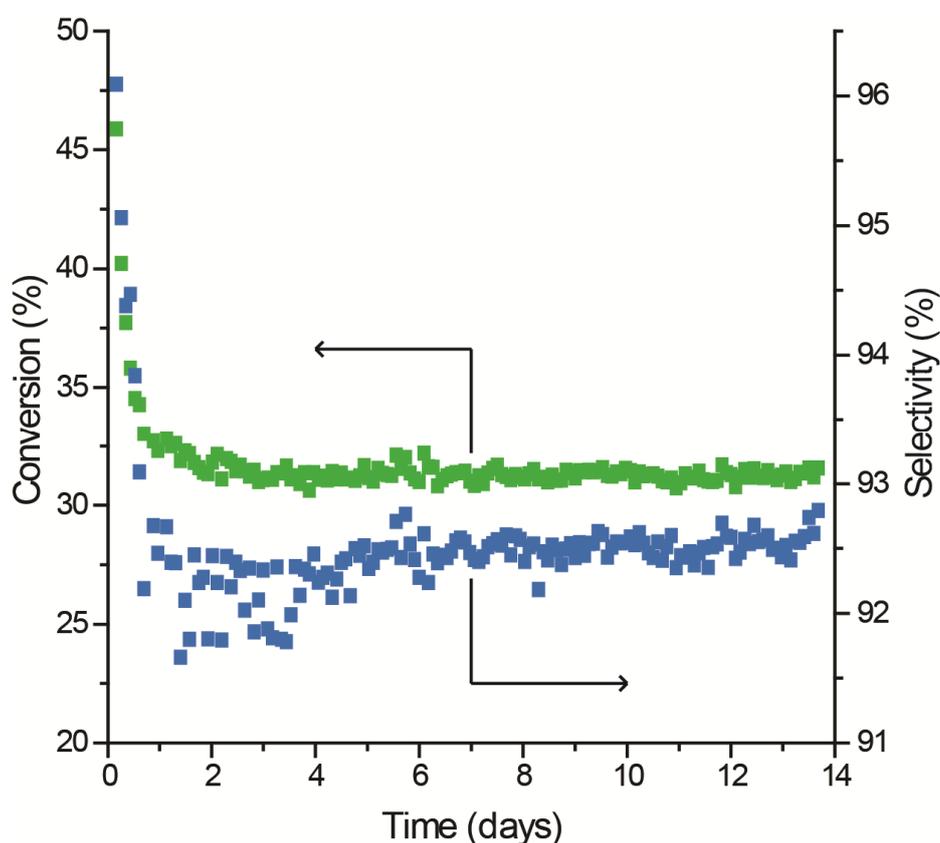


**Figure 4.2.** Long term stability test of the Pt<sub>3</sub>GaK catalyst, which was cycled for approximately 150 times over a 14 day period. During the first two days, both the conversion and selectivity drop, after which the catalyst performance remains stable for 12 days-on-stream.

### 4.3.2 Analysis of the Coke Deposits

Operando UV-Vis spectra were collected in a continuous fashion on the different catalyst materials during the PDH and regeneration steps, making use of the reactor setup described in more detail in Chapter 2. In Figure 4.3, the operando UV-Vis spectra obtained during the eighth dehydrogenation cycle for the PtGa and PtGaK catalysts are presented. At the start, the spectrum of the catalyst is almost featureless, which is due to the white color of the material. Over time, as carbon is deposited on the catalyst, the absorbance of the material increases. This darkening is a slow and continuous process for the PtGa catalyst, but at the end of the 15 min cycle the catalyst has become black. With the addition of K to the catalyst material, a little darkening is observed during the initial stages of the reaction, after which the spectrum does not change anymore. It appears that the presence of K inhibits further coke deposition, which is confirmed by the white-grey coloration of the material. These effects of the presence (or absence) of K are observed for all materials. Notable exceptions are the bare support and the catalyst containing only Pt, as the darkening is relatively low for these materials.

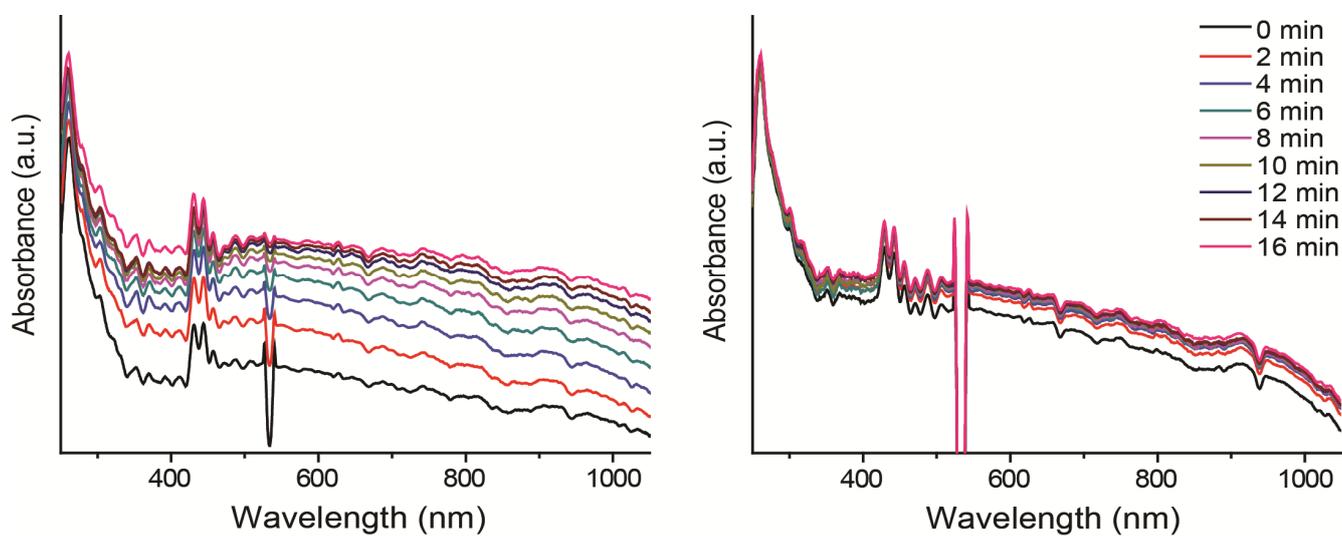


**Figure 4.3.** Operando UV-Vis spectra obtained during the eighth dehydrogenation cycle on the PtGa (left) and PtGaK (right) catalysts. The feature at 532 nm in the spectrum originates from diffusely scattered light from the Raman laser source.

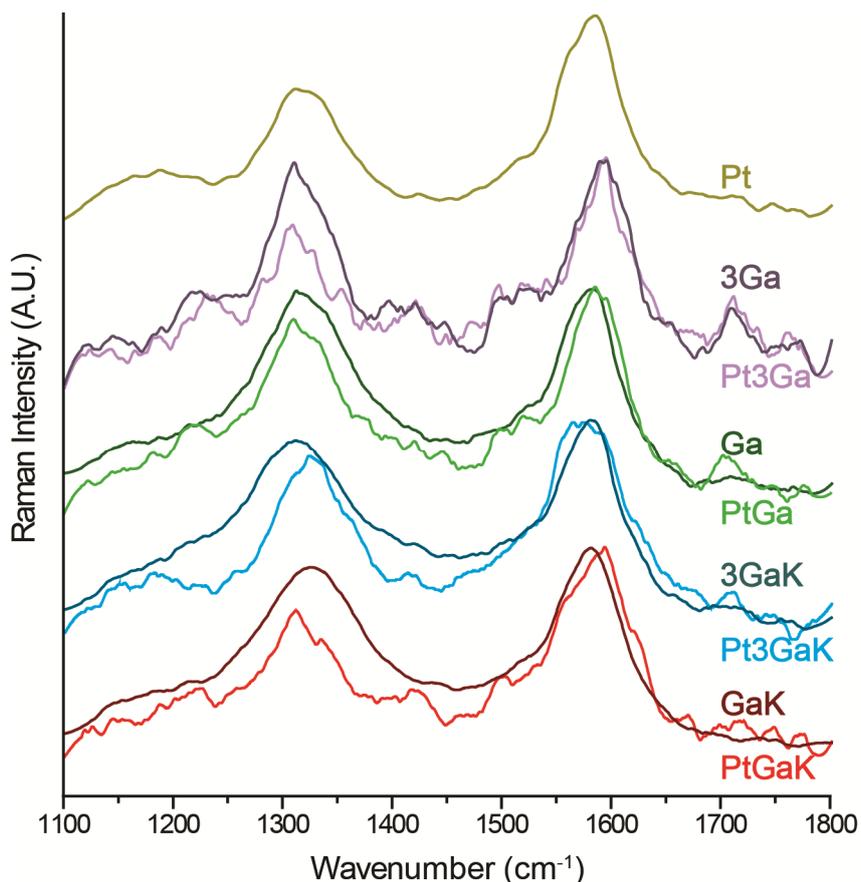


**Figure 4.4.** Operando Raman spectra of the coke species formed of each of the catalysts under investigation during the eighth dehydrogenation cycle. The spectra are normalized with respect to the G band at 1590 cm<sup>-1</sup>. The lighter colored Raman spectra are of Pt-containing catalysts, while the darker catalysts are of their non Pt-containing counterparts.

Operando Raman spectra are collected simultaneously with the operando UV-Vis spectra, so trends observed by both characterization techniques can be correlated. In Figure 4.4, the Raman spectra of each of the catalyst materials obtained at the end of the eighth cycle are compared. Four separate bands can be distinguished in the spectra, corresponding with the quartz reactor window (at 1040 and 1166 cm<sup>-1</sup>) and carbon deposits (1320 and 1590 cm<sup>-1</sup>). The first band corresponding with coke is the so-called G or graphite band, corresponding with a perfect graphitic lattice. The second band is the D<sub>1</sub> or disordered coke band at 1320 cm<sup>-1</sup>, which corresponds with graphite sheet edges and defects within the graphene layer, as was discussed more extensively in Chapter 2.<sup>12,13</sup> The ratio of these bands provides specific information on the nature of the coke deposits, such as the level of graphitization of the coke on the

catalysts.<sup>14</sup> As the operando Raman spectra are quite noisy, Lorentzian line shapes are used to fit the bands and therefore determining the intensity of the band accurately.

Interestingly, a distinct effect of Pt promotion on the nature of the coke species is observed, as the relative intensity of the D<sub>1</sub> band decreases. The catalyst materials that contain Pt and Ga have a D<sub>1</sub>/G ratio of approximately 0.75, while catalysts that do not contain any Pt have an average D<sub>1</sub>/G ratio of 0.97. A possible explanation of this phenomenon is that Pt may further dehydrogenate the carbon deposits, resulting in a higher chemical nature of the coke deposits. Of note, however, is the fact that coke deposited on the bare support has a D<sub>1</sub>/G ratio of 0.78, similar to the value obtained on the Pt-promoted catalysts. Note that these values for the D<sub>1</sub>/G ratio are very different from those reported in Chapter 3, which may be related to the amount of coke formed, differences in the catalyst materials or to differences in the reaction conditions. As the cycles only last 15 min, only a few Raman spectra are collected. For this reason, a detailed analysis of the Raman spectra similar to Chapter 2 and 3, where the average values for the width and position of the Raman bands of 10 consecutive spectra at steady state conditions was determined, was not possible.

After the eighth cycle, the catalyst materials are not regenerated, but instead collected from the reactor and analyzed by thermogravimetric analysis (TGA) combined with on-line mass spectrometry (MS). The deposits are burned by heating the material from ambient to 900 °C under an oxygen flow. This is a powerful combination for determining the amount and nature of coke deposits on the deactivated catalysts, as the TGA measures the decrease in mass corresponding with the combustion of coke, which is confirmed by following the formation of CO<sub>2</sub> by MS. This is shown in Figure 4.5, where the changes of weight per temperature interval and the CO<sub>2</sub> concentration profiles as a function of temperature are shown for the ten materials under study. The CO<sub>2</sub> profiles show that the combustion of the coke deposits take place between 300 and 650 °C. All catalyst materials continuously lose weight, and the weight loss corresponding to this temperature range is between 0.2 and 0.5 wt%. The weight loss and amount of CO<sub>2</sub> detected is the smallest for the catalyst containing only Pt, the bare support and the catalysts containing K, which are coincidentally the materials showing the least darkening by operando UV-Vis spectroscopy. On the contrary, the absence of K and presence of Ga results in significant amounts of coke on the catalyst surface as the feature corresponding with the loss of weight due to the combustion of coke can be clearly distinguished, while it is difficult to observe for the

other samples. In addition, the amount of CO<sub>2</sub> measured by MS is markedly higher for these samples. As Brønsted acidity is often associated with the deposition of coke, the presence of GaO<sub>x</sub> may introduce acidity on the catalyst surface, resulting in this increase in coke deposition. Doping the catalyst with potassium would immediately poison these sites. This would also imply the bare support has a very low acidity to start with.

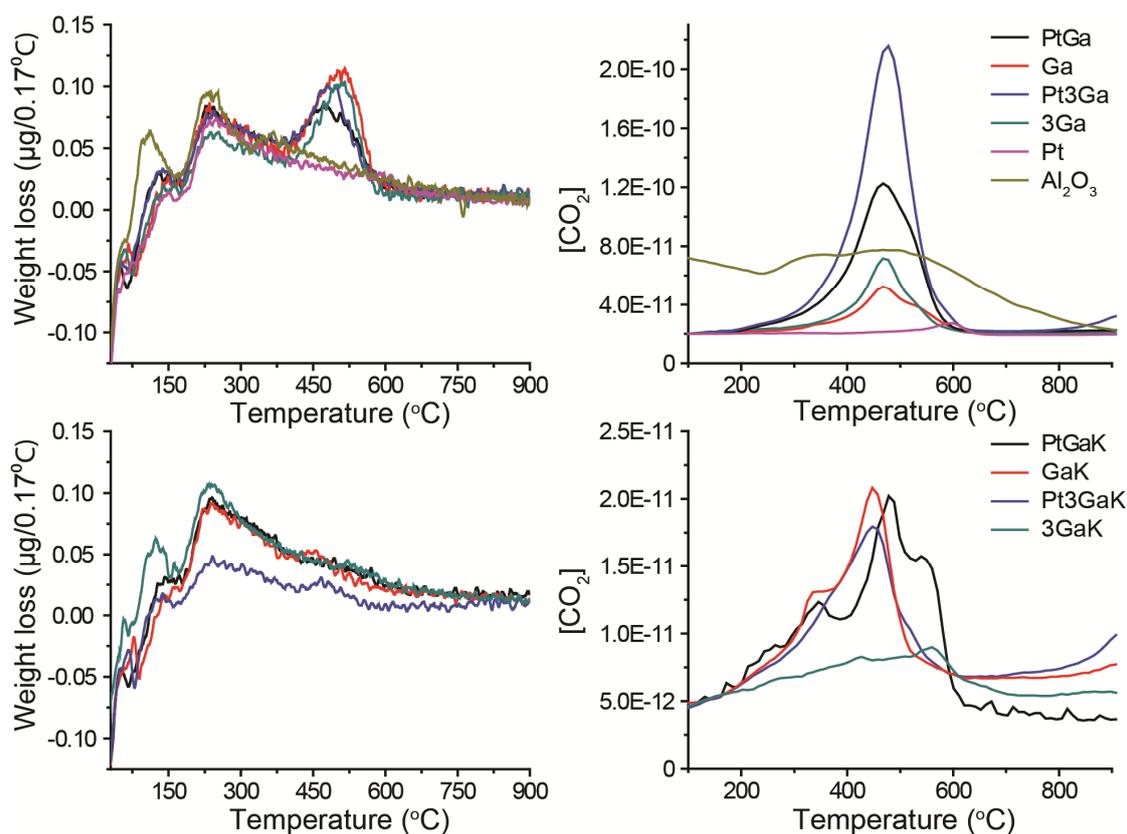


**Figure 4.5.** To the right, the weight loss of the catalysts per 0.17 °C interval for the K containing catalysts (bottom) and non K containing catalysts (top) as measured by thermogravimetical analysis (TGA). Around 500 °C a bump is visible in the graph, which corresponds with the combustion of coke. To the left the CO<sub>2</sub> concentration profiles are shown, which were collected simultaneously by mass spectrometry (MS). Note that these CO<sub>2</sub> concentration profiles are not quantitative.

The temperature where combustion occurs is related to the chemical nature of the coke and the relative position of species in respect to the catalytic centers: on one hand, if the coke deposits are more graphitic, they require higher temperatures to be combusted, while on the other hand proximity to catalytically active centers can

catalyze combustion.<sup>15,16</sup> From operando Raman spectroscopy it was determined that the presence of Pt results in more graphitic species formed on the catalyst. However, this cannot account for the higher combustion temperature of the coke formed on the 1000 ppm Pt catalyst, as for example no clear difference is observed between the TGA-MS data of the PtGa and Ga catalysts. Possibly, the presence of Ga is important to catalyze the combustion of coke for this catalyst system. On the other hand, Pt may be completely covered by coke and therefore cannot assist in the combustion of the carbon deposits.

**Table 4.3.** Summary of the analysis of the coke species formed on the catalysts. In addition to the quantity of coke measured by TGA and the D<sub>1</sub>/G ratio obtained by Raman spectroscopy, the temperature at which the coke is combusted, as measured as well by TGA and MS, are shown. The weight loss / CO<sub>2</sub> signal is strongest at the given temperatures. Finally, in the CO<sub>2</sub> profiles, shoulders that are present are mentioned between brackets.

Catalyst	Quantity of Coke (wt%)	D <sub>1</sub> /G	T <sub>comb</sub> (TGA)	T <sub>comb</sub> (MS)
PtGaK	0.33	0.74	490	480 (340, 545)
Pt3GaK	0.24	0.80	475	450 (520)
PtGa	0.55	0.84	475	470
Pt3Ga	0.52	0.73	485	480
GaK	0.23	0.96	455	450 (330)
3GaK	0.43	0.94	525	560 (420)
Ga	0.34	0.98	510	470 (540)
3Ga	0.33	1.00	510	470 (530)
Pt	0.44	0.64	(-)	590
Al <sub>2</sub> O <sub>3</sub>	0.46	0.78	(-)	480 (320)

Table 4.3 summarizes the information collected on the coke species formed on the prepared Pt-Ga catalysts by TGA-MS and operando Raman spectroscopy. As mentioned before, the presence of K results in lower amounts of coke on the catalyst, while the presence of Pt results in more graphitic coke deposits.

### 4.3.3 Catalyst Characterization and Identification of the Active Site

The freshly prepared catalyst materials were first characterized by N<sub>2</sub>-physisorption and TEM-EDX. The pore volume and surface area of the catalyst materials were compared by N<sub>2</sub> physisorption, the results of which have been summarized in Table 4.4. It is clear that the impregnation of the metals does not result in significant changes to the surface area or pore volume of the catalyst material. In Figure 4.6, a TEM image of a PtGaK catalyst particle of about 200 nm in diameter is shown. After analyzing multiple particles (~20), no evidence was observed for the presence of large Pt or Ga<sub>2</sub>O<sub>3</sub> crystallites, indicating a high dispersion and small particle size of these metals. This was confirmed by EDX linescans, also shown in the Figure, which reveals a homogeneous dispersion of the Ga and Pt over the catalyst particle.

In order to identify the specific Ga surface species present, <sup>71</sup>Ga MAS NMR and XPS were employed for studying the Pt3Ga and 3Ga catalysts. The NMR spectra of these two (fresh) catalysts are shown in Figure 4.7. Two peaks with chemical shifts of 151 and 15 ppm are observed (the chemical shift is relative to Ga(NO<sub>3</sub>)<sub>3</sub>), that were attributed to tetrahedral (IV) and octahedral (VI) Ga, respectively.<sup>17</sup> The spectra have a strong resemblance to <sup>71</sup>Ga MAS NMR spectra of a ternary oxide composed of Ga, Al and O, as has been reported by Chen et al.<sup>18</sup> Such a mixed oxide is likely formed during the high temperatures (750 °C) of the calcination step after the impregnation. Chen et al. proposed that a spinel structure is formed, in which Ga<sup>3+</sup> is preferentially located in a tetrahedral coordination. Such a tetrahedral preference of Ga<sup>3+</sup> has been reported for several mixed oxides containing Ga and is explained by a covalent contribution to the metal oxygen bond caused by the so-called d-block contraction. As

**Table 4.4.** Pore volume and surface area measured by N<sub>2</sub> physisorption for the PtGaK and Pt3GaK catalyst materials and the bare support.

Catalyst	Pore Volume (ml/g)	BET surface area (m <sup>2</sup> /g)
Alumina	0.24	73.8
PtGaK	0.23	71.2
Pt3GaK	0.24	74.8

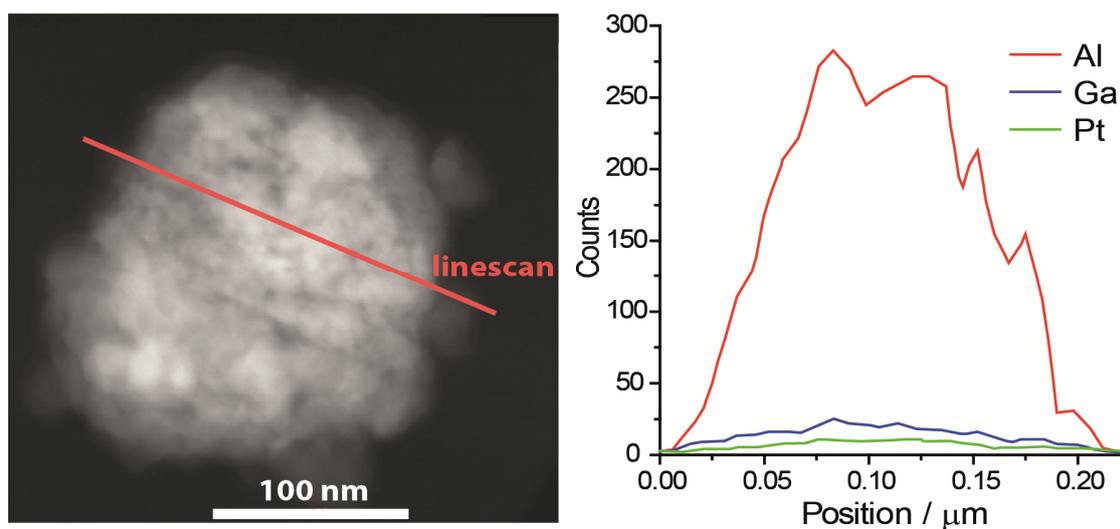


**Figure 4.6.** TEM image of a PtGaK catalyst particle (left) along with an EDX linescan (right) that corresponds with the red line in the TEM image.

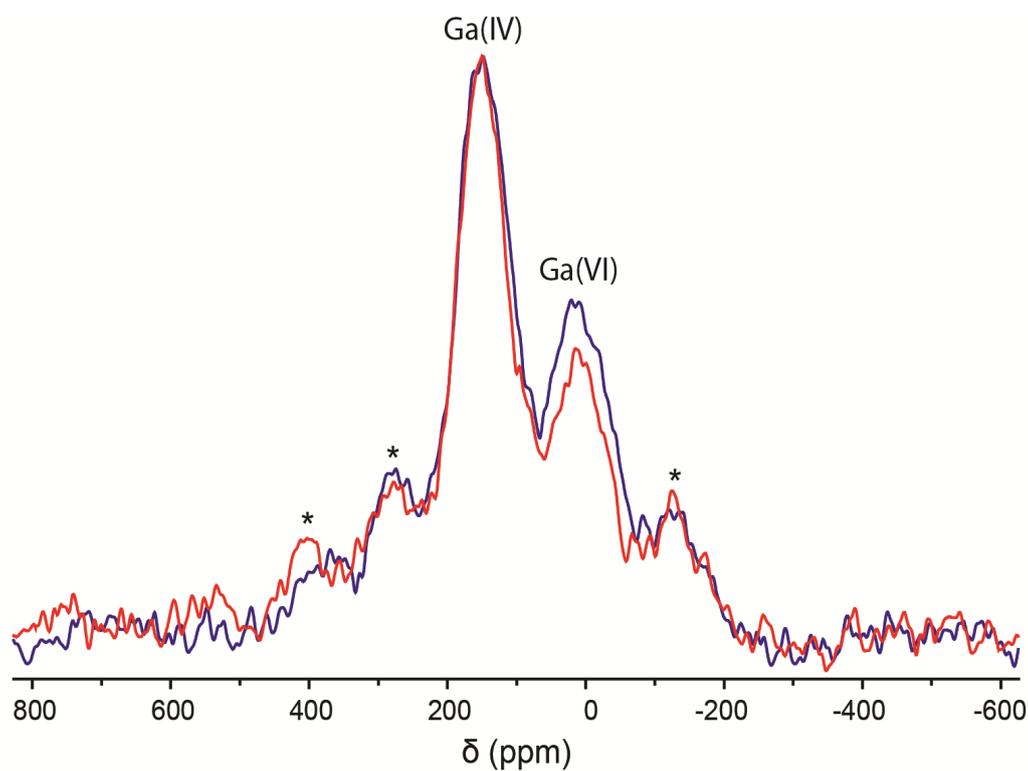


**Figure 4.7.**  $^{71}\text{Ga}$  MAS NMR spectra of fresh Pt<sub>3</sub>Ga (red) and 3Ga (blue) catalyst materials. The spectra have been normalized in respect to the peak corresponding with tetragonal Ga (151 ppm). The asterisks denote the spinning sidebands.

the d-orbital comes completely filled, it ineffectively shields the nuclear charge, resulting in a higher polarization power.

XPS measurements were performed on the 3Ga and Pt3Ga catalysts, in order to obtain information on the surface species of the catalyst material. The most relevant spectra obtained are depicted in Figure 4.8. The deconvolution operation of the Al 2p, Ga 3d and Ga 2p core levels was done as the following: First of all, the bare Al<sub>2</sub>O<sub>3</sub> support was measured (not shown) and the parameters obtained were used to fit the oxygen and aluminum species of the two catalysts. As the signal of the Al 2p edge has almost the same energy as the Pt 4f, the known ratio between the Al 2s and Al 2p peaks is used to fit the Al 2p signal, while the remainder is used to fit the Pt 4f signal. Again, the known ratio between Pt 4f 5/2 and Pt 4f 7/2 is used to obtain this fit. The Pt signal obtained corresponds with metallic Pt (70,8 and 74.0 eV). However the presence of minute amounts of oxidic Pt cannot be excluded (PtO 4f 7/2 = 72.9 eV, PtO<sub>2</sub> 4f 7/2 = 74.5 eV).

Both the Ga 3d (20.6 eV) and Ga 2p (1119.0 eV) edges correspond with Ga<sup>3+</sup>; no evidence of Ga<sup>+</sup> (19.1 eV; (-)) or metallic Ga (18.5 eV; 1115,6 eV) is observed.<sup>19,20</sup> For fitting the Ga 3d signal, a similar procedure as for the Al 2p edge is used. From the XPS data presented in Figure 4.8, the surface composition can be calculated and compared to the composition of the catalyst as a whole, as is summarized in Table 4.5. The concentration of Ga on the surface is surprisingly similar to the composition of the catalyst as a whole (4.11 wt% vs 3 wt%). This is an indication that a significant amount of the Ga is incorporated in the bulk of the support, which in agreement with the observation made by NMR that a mixed Ga<sub>2</sub>O<sub>3</sub>-Al<sub>2</sub>O<sub>3</sub> oxide is formed. On the

**Table 4.5.** Chemical composition of the surface of the 3Ga and Pt3Ga catalysts as measured by XPS. The concentrations of the elements present at the surface have been expressed in wt%, which allows for a more clear comparison between the surface composition and the catalyst composition as a whole.

Catalyst	Al (wt%)	O (wt%)	Ga (wt%)	Pt (wt%)
3Ga	54.6	41.3	4.1	0
Pt3Ga	54.2	39.8	4.7	1.3

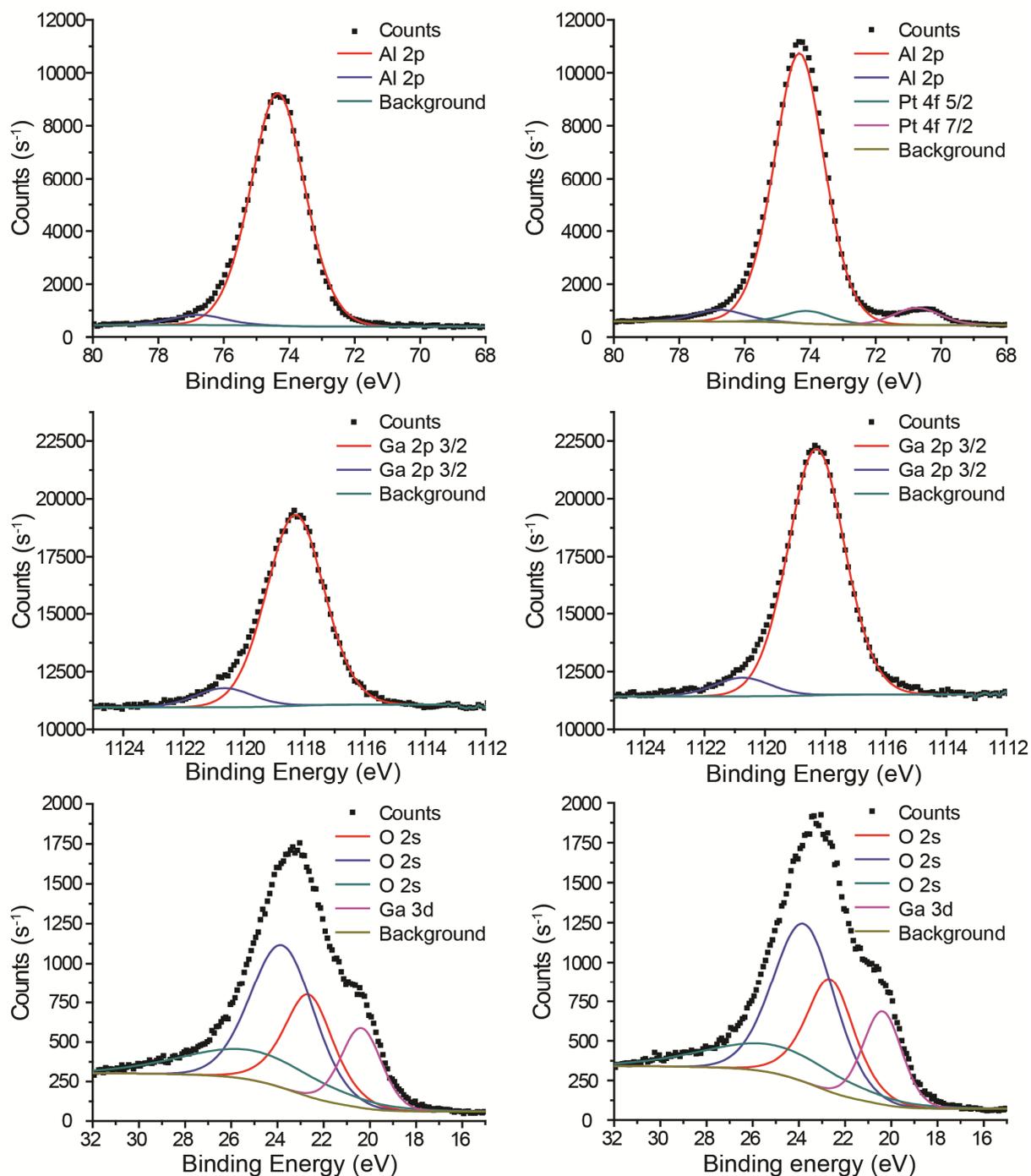


**Figure 4.8.** XPS spectra of the fresh 3Ga (left) and Pt3Ga (right) catalyst. On the top the Al 2p edge (including Pt 4f), in the middle the Ga 2p and at the bottom the O 2s (and the Ga 3d) edges are shown.

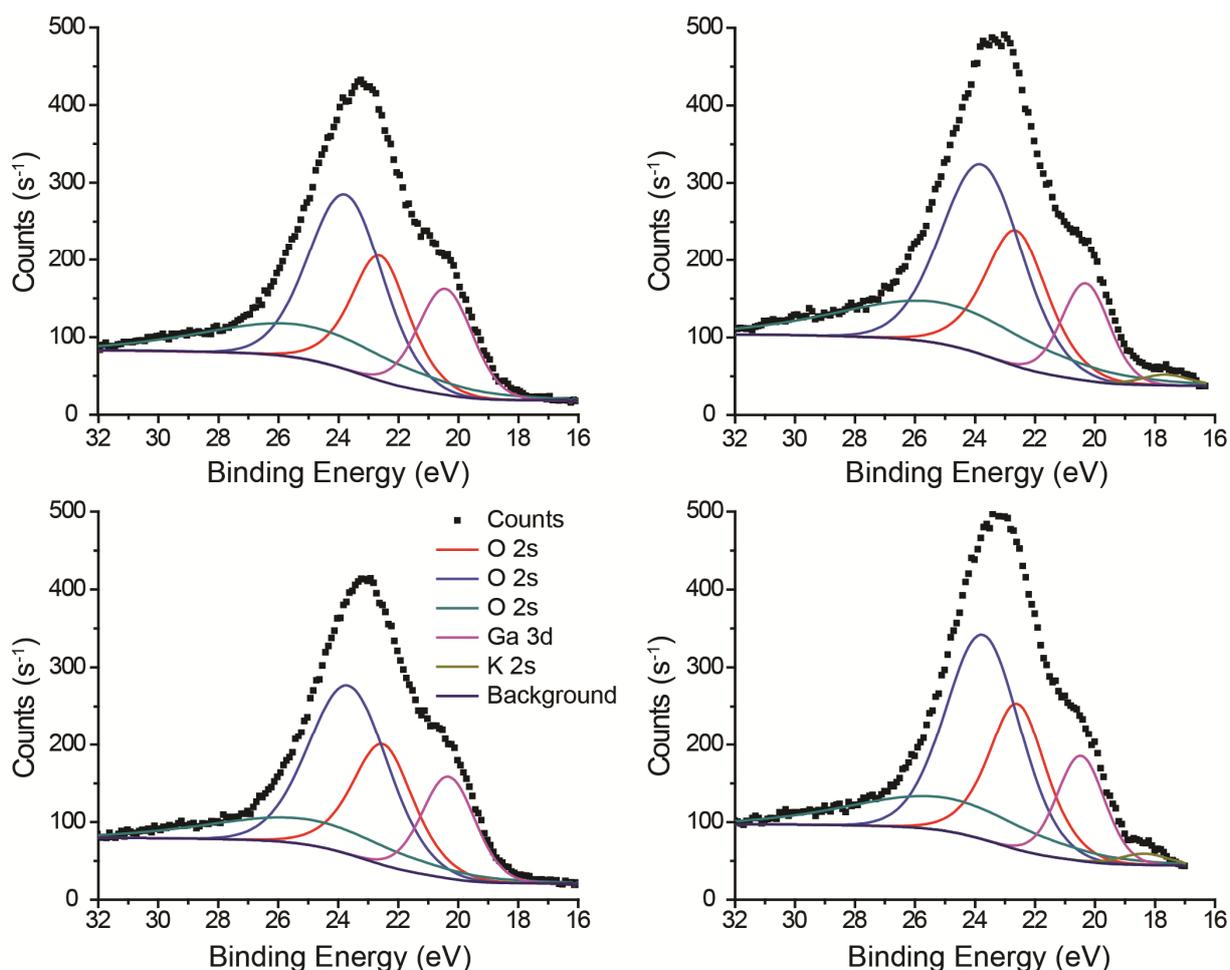


**Figure 4.9.** XPS spectra of 3Ga (left and Pt3GaK (right) catalysts before (top) and after (bottom) being treated in hydrogen at 620 °C for 30 min. No evidence of Ga reduction was observed.

contrary, the apparent concentration of Pt is high on the surface (1.3 wt% observed vs. 1000 ppm in the catalyst's composition, suggesting Pt is well dispersed on the catalyst surface. In addition, the presence of Pt has a small effect on the distribution of the Ga species: The concentration of Ga on the catalyst surface is higher for the Pt3Ga catalyst compared to the 3Ga catalyst (4.67 vs. 4.11 wt%). Secondly, from the  $^{71}\text{Ga}$  MAS NMR spectra of these two catalysts (Figure 4.7), it is observed that relatively a larger amount of tetrahedrally coordinated  $\text{Ga}^{3+}$  is present for the Pt3Ga compared to the 3Ga catalyst. This implies that the presence of Pt, results in more surface tetrahedral  $\text{Ga}^{3+}$  species, which (when coordinately unsaturated) serve as active sites for the dehydrogenation reaction.

Because metallic Ga is liquid at ambient conditions and  $\text{Ga}_2\text{O}$  a volatile compound, it is important to consider the reducibility of  $\text{Ga}^{3+}$ , especially since the dehydrogenation reaction is performed at high temperatures in a reducing atmosphere. Alternatively, a Pt-Ga alloy may be formed by hydrogen spill-over from the Pt, reducing  $\text{Ga}^{3+}$  to  $\text{Ga}^0$  which is then incorporated in the Pt nanoparticle.<sup>2,21-23</sup> For this reason, quasi in-situ XPS measurements were performed, where the Pt3Ga and 3Ga catalyst materials were heated under a hydrogen atmosphere at 620 °C in a separate reactor for 30 min. After this treatment, the material was loaded in the XPS apparatus, without being exposed to air. Again, as is shown in Figure 4.9, no reduced Ga species were detected in the Ga 3d and Ga 2p edges for either catalyst.

These findings were confirmed by temperature programmed reduction experiments that were performed to measure the reducibility of these 3Ga and Pt3Ga catalysts. Figure 4.10 shows that the concentration of hydrogen in a helium flow as a function of temperature remains constant from ambient to 700 °C, which means no hydrogen is consumed as no species on the catalyst are being reduced. Seemingly, the mixed Ga-Al oxide is too stable to be reduced at these conditions, even in the presence of Pt.

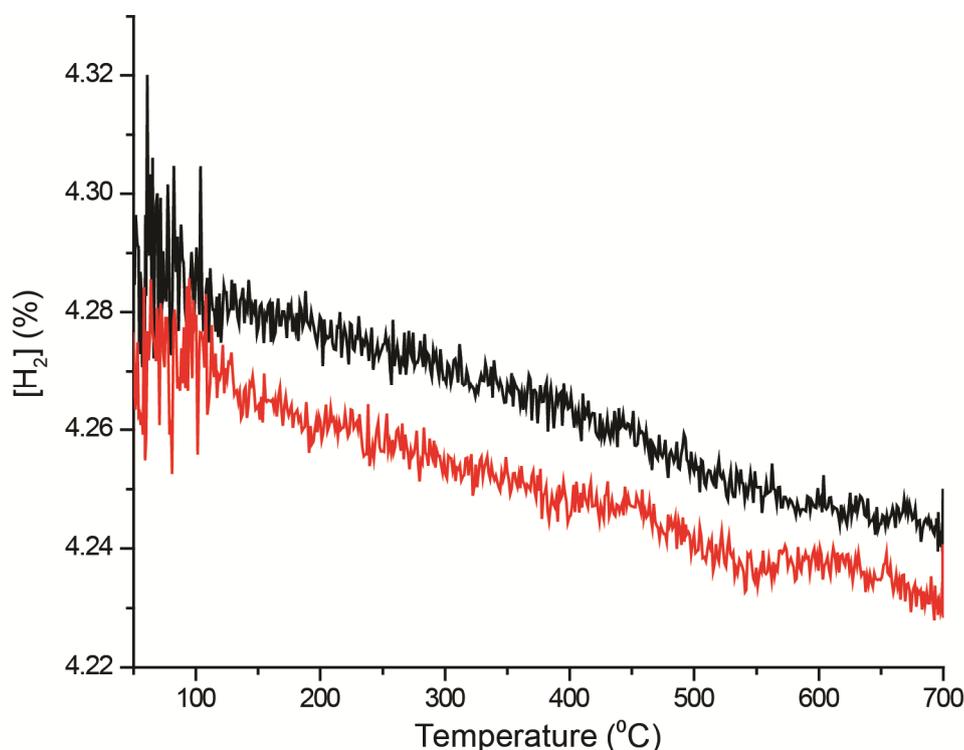


**Figure 4.10.**  $\text{H}_2$  concentration (in He) versus temperature during the TPR experiment for the 3Ga (black) and Pt3Ga (red) catalysts. The lack of features in the graph indicates no reduction is taking place.

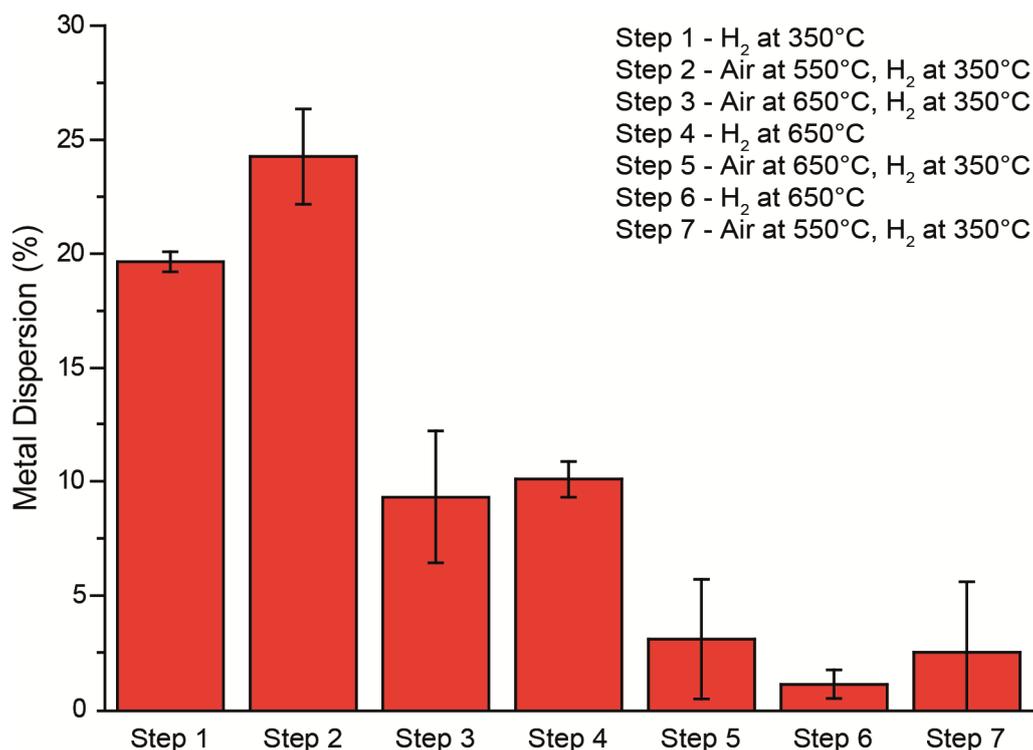


**Figure 4.11.** Pt dispersion of the PtGaK catalyst after the material is thermally treated under air and hydrogen at elevated temperatures. The Pt dispersion drops after step 3 and 5, wherein the material is treated under air at 650 °C. Treating the material under air at 550 °C, or under hydrogen at 650 °C has no negative effect on the Pt dispersion.

Finally, CO chemisorption was used to study the effect of elevated temperatures on the dispersion of the Pt in both oxidizing and reducing atmospheres. The PtGaK catalyst was stepwise heated and treated under either hydrogen or air at 350, 550 and 650 °C, without removing it from the chemisorption unit. In total, seven steps were performed, which are explained in Figure 4.11. Following each step, the catalyst is cooled to ambient temperatures and the Pt dispersion measured by CO chemisorption. The material is treated in hydrogen at 350 °C following each time the catalyst is exposed to air, in order to reduce any PtO<sub>x</sub> species that may have formed. During the second step, which is treating the catalyst for 30 min in air at 550 °C, a small increase of Pt dispersion is observed. However, when the catalyst is treated at 650 °C under air (steps 3 and 5) the dispersion drops dramatically, in accordance to what has been reported in literature on the sintering of Pt nanoparticles dispersed on an alumina support.<sup>24-26</sup> On the contrary, no negative effect is observed by treating the catalyst under a hydrogen atmosphere at otherwise identical conditions (steps 4 and 6). A final

treatment under air at 550 °C does not improve the Pt dispersion, so the sintering appears to be irreversible.

During the cycling operation, the catalysts are regenerated at 750 °C under air, considerably harsher conditions and should therefore have similar or more severe negative effects on the Pt dispersion. Hence, there is no direct correlation between the Pt surface area and the activity of the catalyst material, which means Pt is not the species mainly responsible for the PDH activity of the catalyst.

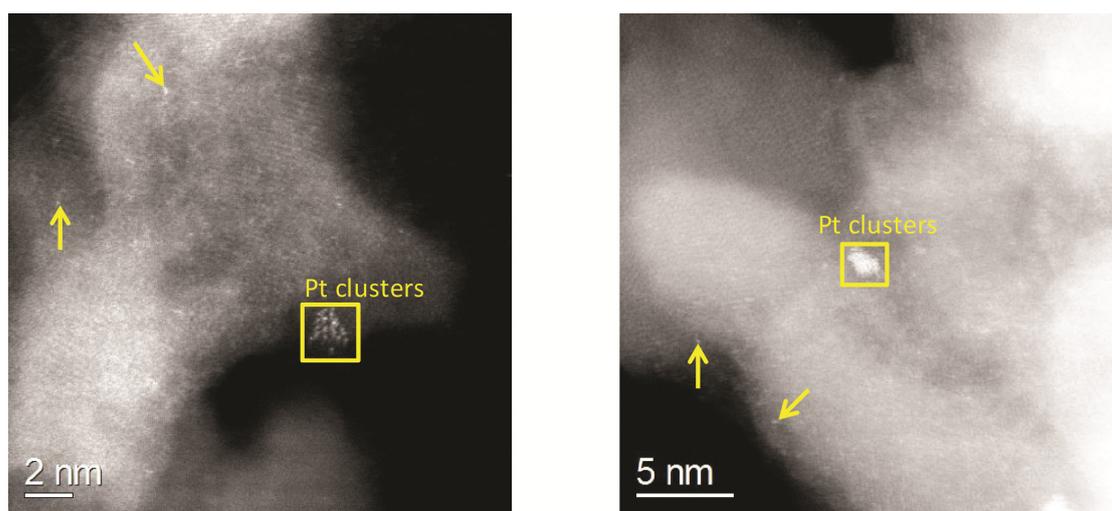


**Figure 4.12.** Aberration corrected STEM images of a fresh (left) and spent (right) PtGaK catalyst, in which small Pt clusters and single atoms are observed. By energy dispersive spectroscopy (EDS), an uniform distribution of Ga was observed on the catalyst surface.

In addition, aberration corrected STEM images of a fresh and spent (after 8 dehydrogenation cycles) sample of the PtGaK catalyst were collected, and are shown in Figure 4.12. In both images, small Pt clusters and individual Pt atoms (indicated by the yellow arrows) are observed.

As the single Pt atoms are difficult to see, and only a few Pt clusters were detected, it was not possible to determine how much the total Pt dispersion decreased during the dehydrogenation reaction. Nevertheless, it is clear that single Pt atoms are still present after several dehydrogenation cycles.

From Figure 3.4 it is clear that Pt nanoparticles supported on a Pt/Al<sub>2</sub>O<sub>3</sub> catalyst readily sinter during reaction. For the PtGaK catalyst however, the average particle size has hardly increased, and Pt single atoms are still observed. This significantly

higher stability of the supported Pt is either caused by the significant lower Pt loading, or by the fact that a surface of a mixed Ga-Al oxide provides a relatively strong interaction with the Pt nanoparticles.

Combining the trends observed with  $^{71}\text{Ga}$ -NMR and XPS, the presence of Pt results in a higher concentration of surface tetrahedral  $\text{Ga}^{3+}$  species. Nevertheless, such a relatively small increase of active sites cannot account for the high activity observed for the Pt3Ga catalyst, compared to 3Ga. As the catalyst containing only Pt is nearly inactive towards dehydrogenation, and the Pt dispersion drops severely after treatment under air at elevated temperatures (while the catalyst performance remains stable), it is assumed that not Pt but coordinately unsaturated  $\text{Ga}^{3+}$  species are responsible for the C-H bond activation.<sup>27-29</sup> Proposed reaction mechanisms for paraffin dehydrogenation on  $\text{Ga}_2\text{O}_3$  are discussed in a review by Copéret, where the dissociative adsorption of propane results in the formation of a surface hydroxyl and either a Ga-alkyl or Ga-alkoxy species.<sup>30,31</sup> After the elimination of the  $\beta$ -hydrogen by the formation of a Ga-hydride or a second surface hydroxyl group, propylene desorbs. However, as Pidko et al. have pointed out, the subsequent regeneration of the active sites by the formation of hydrogen has a very high energy barrier, and the reduction of the  $\text{Ga}^{3+}$  forming  $\text{Ga}^+$  and  $\text{H}_2\text{O}$  is energetically more favourable.<sup>32</sup> In this case, the catalyst system is too stable to be reduced in such a manner, meaning that the H-Ga-OH species need to be regenerated by a different route. Therefore we postulate that the promoting function of the Pt consists of the assistance in the regeneration of these sites, i.e. it facilitates the recombination of hydrogen atoms to hydrogen and subsequently freeing the active  $\text{Ga}^{3+}$  sites for the next dehydrogenation cycle.

## 4.4 Conclusions

A porous alumina support loaded with 1000 ppm Pt and 1.5-3 wt% of Ga results in a highly active and selective formulation for the catalytic dehydrogenation of propane. This catalyst formulation can compete with industrially relevant catalyst systems, such as Pt-Sn/ $\text{Al}_2\text{O}_3$  and  $\text{CrO}_x/\text{Al}_2\text{O}_3$ . The developed catalyst is highly resistant to coking and remains active for prolonged reaction times. A combination of structural, morphological and surface characterization points towards a synergistic and bi-

functional character originating from the supported Ga and Pt moieties. It is proposed that Ga is providing the active sites for propane dehydrogenation, while Pt possesses unique promoting characteristics and is mainly present as single atoms.

## 4.5 Acknowledgements

Marjan Versluijs (Utrecht University) is thanked for performing the TGA-MS experiments. Lin Luo, Brien Stears, Andrzej Malek, David Barton, Beata Kilos and Mark Kaminsky (The Dow Chemical Company) are acknowledged for performing the CO chemisorption, the two-week long dehydrogenation experiment and for helpful discussions. Eline Koers and Marc Baldus (Utrecht University) are thanked for performing the  $^{71}\text{Ga}$  MAS NMR experiment. Tiny Verhoeven and Hans Niemantsverdriet (Eindhoven University of Technology) are acknowledged for performing the XPS experiments and related data processing. Alan Nicholls (University of Illinois-Chicago), Hien Pham and Datye Abhaya (University of New Mexico) are thanked for the aberration corrected STEM measurements.

## 4.6 References

- (1) Jablonski, E. L.; Castro, A. A.; Scelza, O. A.; de Miguel, S. R. *Appl. Catal. A-Gen.* **1999**, *183*, 189.
- (2) Siddiqi, G.; Sun, P.; Galvita, V.; Bell, A. T. *J. Catal.* **2010**, *274*, 200.
- (3) Sun, P.; Siddiqi, G.; Vining, W. C.; Chi, M.; Bell, A. T. *J. Catal.* **2011**, *282*, 165.
- (4) Chao, K. J.; Wei, A. C.; Wu, H. C.; Lee, J. F. *Micropor. Mesopor. Mat.* **2000**, *35-36*, 413.
- (5) Ma, C.; Li, P.; Chen, Q.; Zhang, S. *J. Magn. Reson.* **2013**, *233*, 87.
- (6) Nijhuis, T. A.; Tinnemans, S. J.; Visser, T.; Weckhuysen, B. M. *Phys. Chem. Chem. Phys.* **2003**, *5*, 4361.
- (7) Michorczyk, P.; Ogonowski, J. *Appl. Catal. A-Gen.* **2003**, *251*, 425.

- (8) Bennici, S. M.; Vogelaar, B. M.; Nijhuis, T. A.; Weckhuysen, B. M. *Angew. Chem. Int. Ed.* **2007**, *46*, 5412.
- (9) Bartholomew, C. H. *Appl. Catal. A-Gen.* **2001**, *212*, 17.
- (10) Nagai, Y.; Hirabayashi, T.; Dohmae, K.; Takagi, N.; Minami, T.; Shinjoh, H.; Matsumoto, S. *J. Catal.* **2006**, *242*, 103.
- (11) Nagai, Y.; Dohmae, K.; Ikeda, Y.; Takagi, N.; Tanabe, T.; Hara, N.; Guilera, G.; Pascarelli, S.; Newton, M. A.; Kuno, O.; Jiang, H.; Shinjoh, H.; Matsumoto, S. *Angew. Chem. Int. Ed.* **2008**, *47*, 9303.
- (12) Sadezky, A.; Muckenhuber, H.; Grothe, H.; Niessner, R.; Poschl, U. *Carbon*, **2005**, *43*, 1731.
- (13) Pimenta, M. A.; Dresselhaus, G.; Dresselhaus, M. S.; Cançado, L. G.; Jorio, A.; Saito, R. *Phys. Chem. Chem. Phys.* **2007**, *9*, 1276.
- (14) Sattler, J. J. H. B.; Beale, A. M.; Weckhuysen, B. M. *Phys. Chem. Chem. Phys.* **2013**, *15*, 12085.
- (15) Vu, B. K.; Shin, E. W. *Catal. Lett.* **2011**, *141*, 699.
- (16) Vu, B. K.; Song, M. B.; Ahn, I. Y.; Suh, Y.-W.; Suh, D. J.; Kim, W.-I.; Koh, H.-L.; Choi, Y. G.; Shin, E. W. *Appl. Catal. A-Gen.* **2011**, *400*, 25.
- (17) Areán, C. O.; Delgado, M. R.; Montouillout, V.; Massiot, D. *Z. Angw. Allg. Chem.* **2005**, *631*, 2121.
- (18) Chen, M.; Xu, J.; Su, F.; Liu, Y.; Cao, Y.; He, H.; Fan, K. *J. Catal.* **2008**, *256*, 293.
- (19) Carli, R.; Bianchi, C. L. *Appl. Surf. Sci.* **1994**, *74*, 99.
- (20) Priyantha, W.; Radhakrishnan, G.; Droopad, R.; Passlack, M. *J. Cryst. Growth* **2011**, *323*, 103.
- (21) Sun, P.; Siddiqi, G.; Chi, M.; Bell, A. T. *J. Catal.* **2010**, *274*, 192.
- (22) Iwasa, N.; Mayanagi, T.; Ogawa, N.; Sakata, K.; Takezawa, N. *Catal. Lett.* **1998**, *54*, 119.
- (23) Dominguez, F.; Sanchez, J.; Arteaga, G.; Choren, E. *J. Mol. Catal. A-Chem.* **2005**, *228*.
- (24) Adler, S. F.; Keavney, J. J. *J. Phys. Chem.* **1960**, *64*, 208.
- (25) Lee, T. J.; Kim, Y. G. *J. Catal.* **1984**, *90*, 279.

- (26) Bradley, S. A.; Sinkler, W.; Brown, D. A.; Bigelow, W.; Voyles, P. M.; Allard, L. F. *Catal. Lett.* **2012**, *142*, 176.
- (27) Lavalley, J. C.; Daturi, M.; Montouillout, V.; Clet, G.; Otero Areán, C.; Rodríguez Delgado, M.; Sahibed-dine, A. *Phys. Chem. Chem. Phys.* **2003**, *5*, 1301.
- (28) Zheng, B.; Hua, W.; Yue, Y.; Gao, Z. *J. Catal.* **2005**, *232*, 143.
- (29) Takahashi, M.; Nakatani, T.; Iwamoto, S.; Watanabe, T.; Inoue, M. *Ind. Eng. Chem. Res.* **2006**, *45*, 3678.
- (30) Liu, Y.; Li, Z. H.; Lu, J.; Fan, K. *J. Phys. Chem. C* **2008**, *112*, 20382.
- (31) Copéret, C. *Chem. Rev.* **2010**, *110*, 656.
- (32) Pidko, E. A.; Hensen, E. J. M.; van Santen, R. A. *J. Phys. Chem. C* **2007**, *111*, 13068.

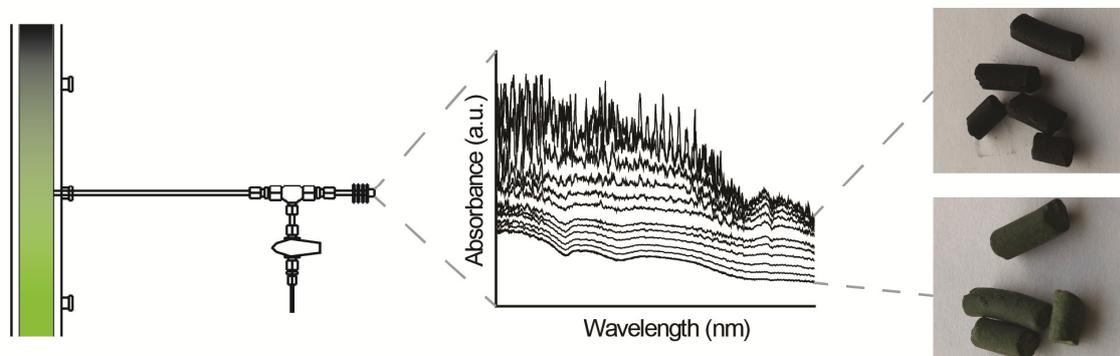


## **Part 2**



## Chapter 5

# Operando UV-Vis Spectroscopy of a $\text{CrO}_x/\text{Al}_2\text{O}_3$ Propane Dehydrogenation Catalyst in a Pilot-Scale Reactor



A novel operando UV-Vis spectroscopic setup has been designed, constructed and tested for the investigation of catalyst bodies loaded in a pilot-scale reactor under relevant reaction conditions. Spatiotemporal insight in the formation and burning of coke deposits on an industrial  $\text{CrO}_x/\text{Al}_2\text{O}_3$  catalyst during propane dehydrogenation has been obtained. Coke deposition is faster at the top of the reactor compared to the bottom, and the combustion of the coke deposits takes place as a front travelling down the length of the reactor.

This Chapter is based on the manuscript: J.J.H.B. Sattler, I.D. Gonzalez-Jimenez, A. M. Mens, M. Arias, T. Visser, B.M. Weckhuysen, Operando UV-Vis spectroscopy of a catalytic solid in a pilot-scale reactor: Deactivation of a  $\text{CrO}_x/\text{Al}_2\text{O}_3$  propane dehydrogenation catalyst, *Chem. Commun.* **49** (2013) 1518-1520.

## 5.1 Introduction

CrO<sub>x</sub>-based propane dehydrogenation (PDH) catalysts, such as those used for the Catofin<sup>®</sup> and Linde-BASF processes, deactivate over time due to coke deposition. On one hand, the deposition of coke is essential, as the combustion of the carbon deposits provides the heat required to run the endothermic dehydrogenation reaction. On the other hand, when excessive amounts of coke are formed, local hotspots formed during the regeneration step lead to the sintering of the alumina support. As was discussed in Chapter 1, these hotspots may lead to the incorporation of Cr ions in the bulk of the support oxide and therefore result in irreversible catalyst deactivation.<sup>1,2</sup> Hence, the regeneration needs to be started at the appropriate time, which is currently done by analyzing the product stream of a reactor. In potential, a better approach would be to observe the rate of coke deposition directly by an operando spectroscopic technique, and as was shown in Chapter 2 and 4, operando UV-Vis spectroscopy is a powerful tool to monitor the rate of coke deposition on catalyst materials during propane dehydrogenation.

This research approach was pioneered in our group in 2003 by Nijhuis, Tinnemans and co-workers, who designed a novel setup where on-line MS was combined with operando Raman and UV-Vis spectroscopy. This setup, almost identical to the one used in Chapters 2-4, was used to study the deactivation of CrO<sub>x</sub>-based dehydrogenation catalysts.<sup>3</sup> For this purpose a small quartz reactor was inserted in an oven, in which two holes were present at opposite sides. A UV-Vis probe was inserted in one hole, while the Raman light source was focused on the sample through the other hole. The combination of these two techniques is powerful, as the darkening measured by UV-Vis spectroscopy can be used to correct the loss in intensity of the coke bands in the Raman spectra due to catalyst darkening. Hence, Raman spectroscopy becomes a semi-quantitative technique to determine on-line the amount of coke deposited on the catalyst material.<sup>4</sup> In a follow-up study, the possibility to obtain spatiotemporal information of the catalyst bed was explored by modifying the setup to include multiple UV-Vis probes.<sup>5</sup> It was shown that the rate of coke deposition depended on the relative height of the catalyst bed, which was corroborated by operando Raman spectroscopy. Later on, Bennici, Nijhuis et al. took this method of catalyst diagnostics to the next level by designing an expert-control algorithm for

the propane dehydrogenation reactor, that used operando Raman spectroscopy to continuously monitor the deposition of coke.<sup>6</sup> When the intensity of the Raman bands reached a set value, the regeneration step was started automatically, and when the bands corresponding with coke have disappeared, the next propane dehydrogenation step is begun.

The next logical step is to scale up this promising methodology from the small quartz reactor tube to a more industrially relevant setting, which means the design and construction of a pilot scale reactor in which special probes for UV-Vis and Raman spectroscopy can be inserted.

In this Chapter, we present the design, construction and testing of this novel pilot-scale reactor, in which specially developed operando UV-Vis probes are inserted to characterize catalyst materials under realistic reaction conditions. To the best of our knowledge, this is the first time a spectroscopic technique is used to characterize a catalytic solid directly inside a pilot-scale reactor. This is done by taking the dehydrogenation of propane into propylene over an industrial  $\text{CrO}_x/\text{Al}_2\text{O}_3$  catalyst, shaped in the form of 3 mm-sized catalyst bodies, as a showcase. The results presented in this Chapter illustrate the potential to implement these spectroscopic devices in an industrial environment for e.g. catalyst diagnostics.

## 5.2 Experimental

### 5.2.1 Design of the Pilot-Scale Reactor

Figure 5.1 shows the detailed scheme and photograph of the pilot-scale reactor designed and constructed. The 90 cm tall fixed bed (internal diameter of 3 cm) reactor is made from the stainless steel T316 alloy and has a volume of 0.65 L and a maximum operating pressure of 15 bar. The reactor is placed inside a three-staged oven consisting of 6 heating elements of 500 W each. The temperature is controlled by three thermocouples placed in a thermo-well inside the reactor. Four slots have been made along the length of the reactor, in which operando UV-Vis probes could be mounted. As the temperature at the reactor's extremities is lower compared to the rest of the catalyst bed, the outer 14 cm have been filled with stainless steel balls with a diameter of 6 mm.

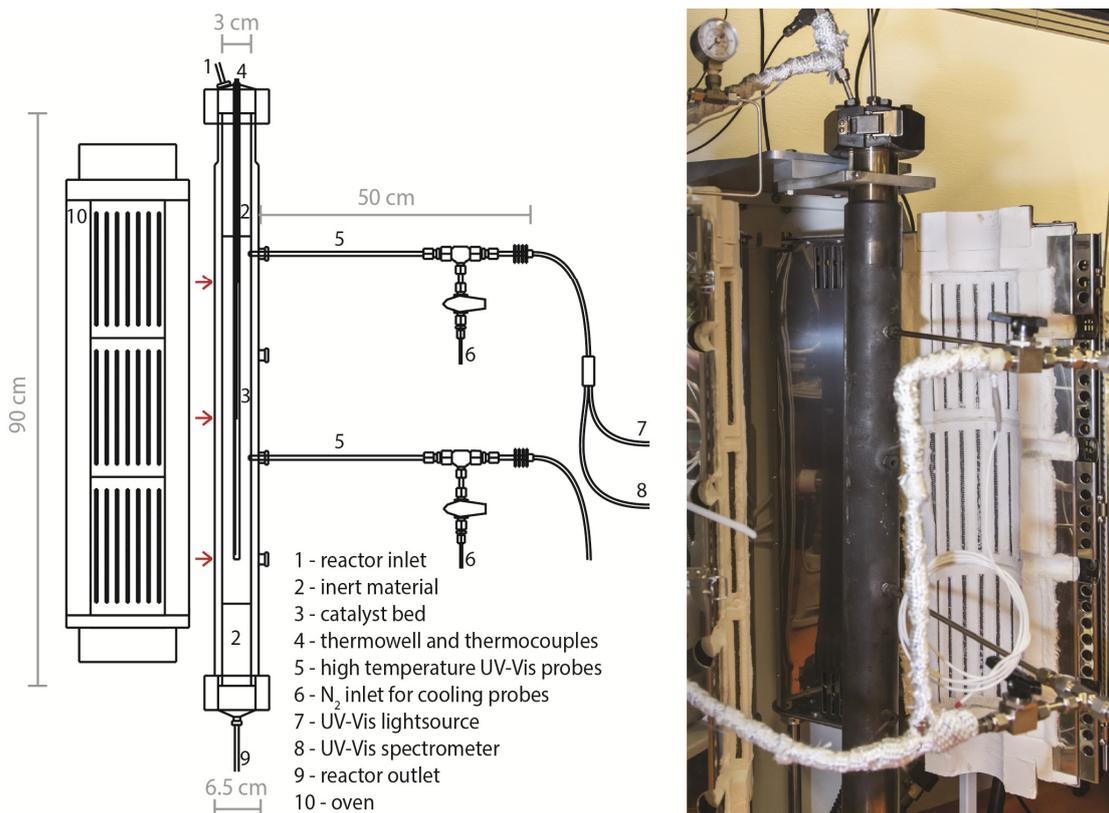


**Figure 5.1.** Detailed scheme and picture of the pilot-scale setup for studying catalyst bodies under reaction conditions. Key to this setup are the specially designed UV-Vis probes, which can be inserted at different heights of the reactor tube. The red arrows indicate the height of the catalyst bed where the thermocouples measure the temperature.

### 5.2.2 Design and Testing of the Operando UV-Vis Probes

Two custom designed operando UV-Vis probes, shown in Figure 5.2, are inserted in the reactor; the first probe is placed approximately at the same height as the first thermocouple, while the second probe is positioned between the second and third thermocouple. The UV-Vis probe consists of six excitation and one collection optical fiber, which are connected to a Deuterium-Halogen light source and an Avaspec 2048 UV-Vis spectroscope. The optical fibers are glued together and encapsulated in a ceramic shell. The probes are designed to operate under the high temperatures of the propane dehydrogenation reaction. They are installed inside a stainless steel tube, making it possible to flow N<sub>2</sub> along its length, which provides cooling and prevents fouling of the tip. Spectra are saved every 2 min, with 50 accumulations of 40 ms

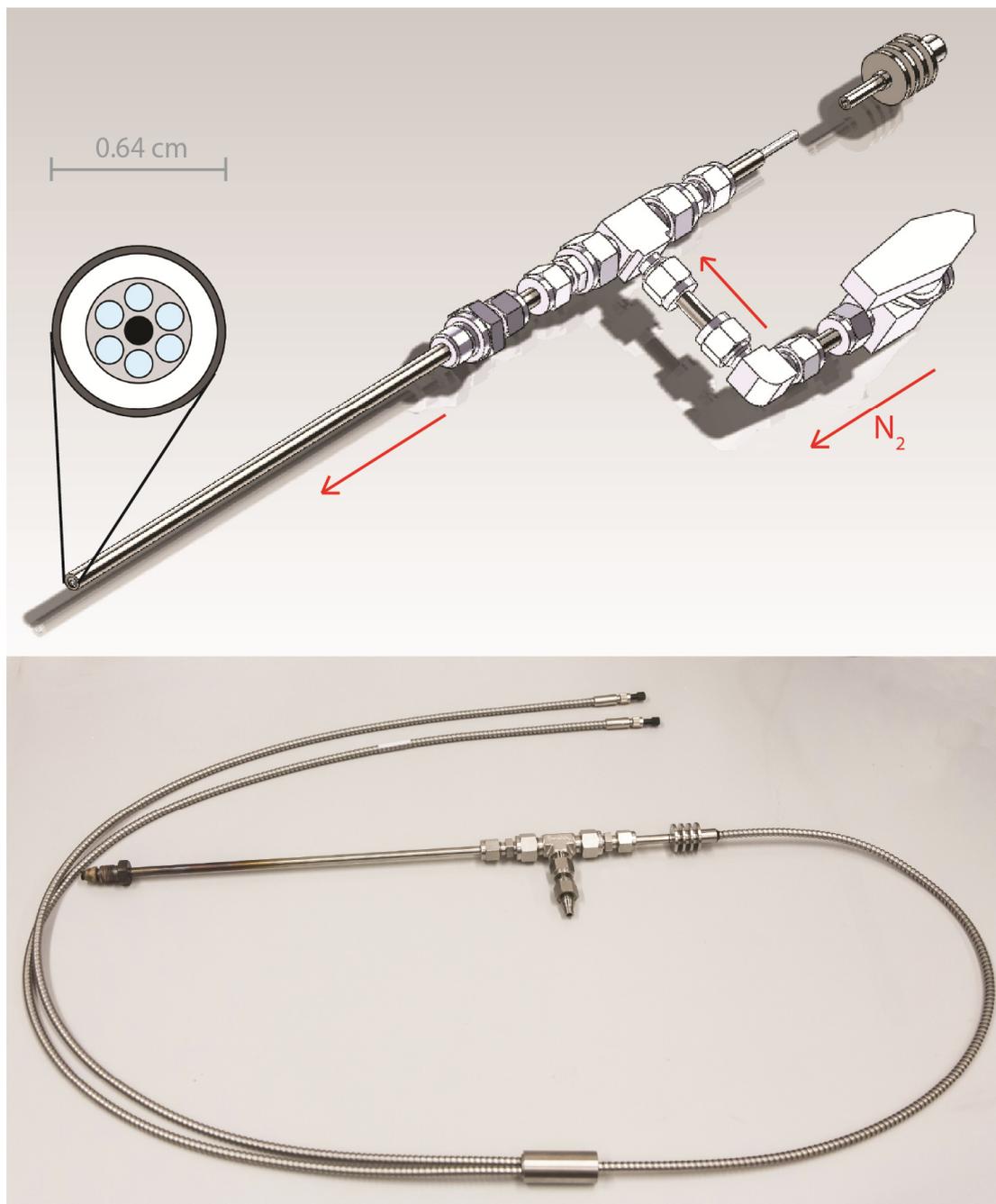


**Figure 5.2.** Scheme (top) and picture (bottom) of the custom designed operando UV-Vis probe, which was used to gather UV-Vis spectra in the pilot-scale setup. The red arrows indicate the flow direction of the  $N_2$ .

exposure time each. Operando UV-Vis spectroscopy has frequently been used to study chromia/alumina catalysts under alkane dehydrogenation conditions on the lab-scale.<sup>4,8-11</sup> D-d transitions of chromium oxide species can be observed as broad bands in the UV-Vis spectra;  $Cr^{6+}$  species present bands at around 275 and 365 nm, while

$\text{Cr}^{3+}$  species typically display absorption bands around 300, 450, 590 and 615 nm.<sup>12-14</sup> In Chapter 1, it was proposed that  $\text{Cr}^{3+}$  species are the active sites for the dehydrogenation reaction, while  $\text{Cr}^{6+}$  is considered to be inactive.<sup>3,15</sup> Secondly, catalyst darkening due to coke deposition can be visualized by this approach.<sup>16,17</sup>

### 5.2.3 Dehydrogenation of Propane

The potential of the developed pilot-scale reactor setup was explored by studying the catalytic dehydrogenation of propane over an industrial catalyst. For this reason, the reactor was filled with approximately 500 g of  $\text{CrO}_x/\text{Al}_2\text{O}_3$  extrudates, with inert material (which were stainless steel balls with a diameter of 6 mm) at the extremities of the reactor. The catalyst consists of 20 wt% Cr (mixture of  $\text{Cr}^{3+}$  and  $\text{Cr}^{6+}$ ) and 1 wt% Na on an alumina support. The reaction is performed at approximately 550 °C with a flow of 4500 ml/min of  $\text{N}_2$  and 500 ml/min of propane over a 6 h period. These flows correspond with a weight hourly space velocity (WHSV) of 0.1  $\text{h}^{-1}$ . The outlet of the reactor setup is connected to a GC equipped with a FID (Porabond-Q column) and TCD (Carboxan column) detector to analyze the reaction products. After the dehydrogenation step, the catalyst is regenerated by flowing 150 ml/min oxygen in 2200 ml/min nitrogen to the point where no more  $\text{CO}_x$  was detected in the gas chromatographs. During the reaction, the temperature is continuously monitored by three thermocouples located at different heights of the catalyst bed, as is shown in Figure 5.1. The reaction equilibrium is very sensitive to the temperature: when the reaction temperature is increased, conversion of propane is increased at the expense of selectivity towards propylene, as the cracking of reaction products becomes more prevalent.

## 5.3 Results and Discussion

The conversion of propane and selectivity towards propylene are shown in the top section of Figure 5.3. Initially, a high conversion of propane is observed, that gradually drops over time from 47% to 37%. At the same time the selectivity towards propylene increases from 80% to 88%. Such values for the conversion and selectivity are typical for this catalyst material under the applied conditions. Apart of the general

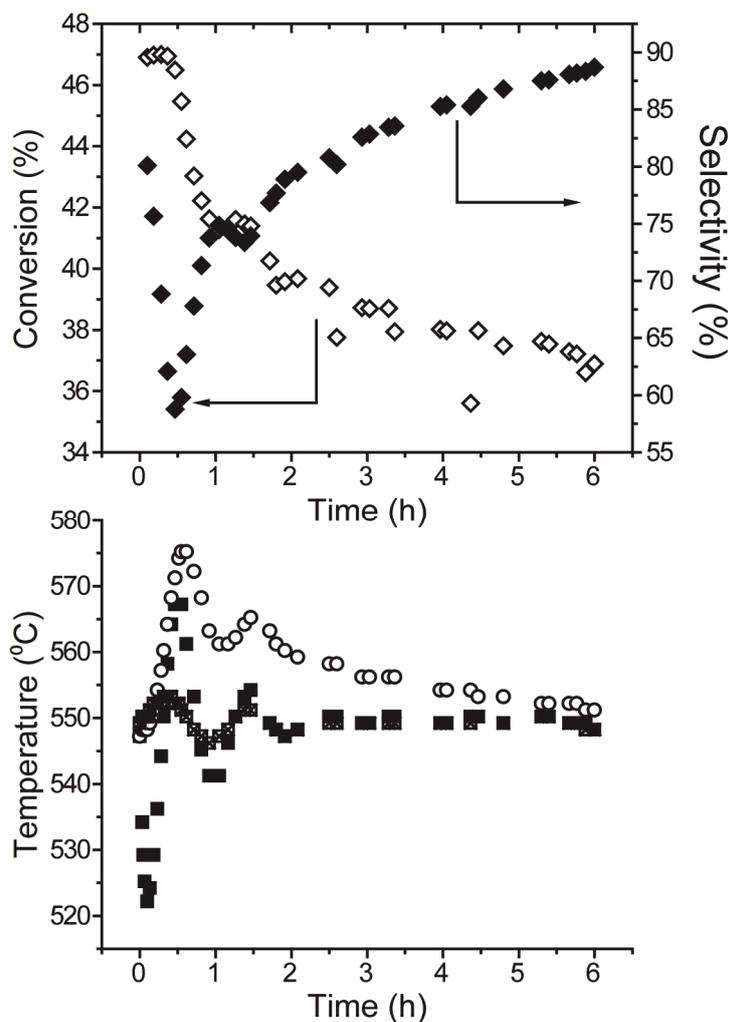


**Figure 5.3.** At the top, the conversion ( $\square$ ) and selectivity ( $\blacksquare$ ) obtained during the dehydrogenation experiment are shown, while at the bottom the temperature as a function of time on stream as measured by the three thermocouples is shown ( $\circ$  for top,  $\blacksquare$  for middle and  $\times$  for the bottom).

trend in the conversion and selectivity, some fluctuations can be observed, which are attributed to changes in the temperature of the reactor. At the bottom of Figure 5.3, the temperature of the catalyst bed during the propane dehydrogenation, as measured by the thermocouples inside the thermowell is plotted. By comparing the two graphs, we can correlate the changes of selectivity and conversion with temperature fluctuations within the reactor; an increase in temperature from 550 to 575 °C coincides with a drop in selectivity from 80 to 60%. These fluctuations occur as the heating system attempts to correct for the loss of heat due to the endothermicity of the

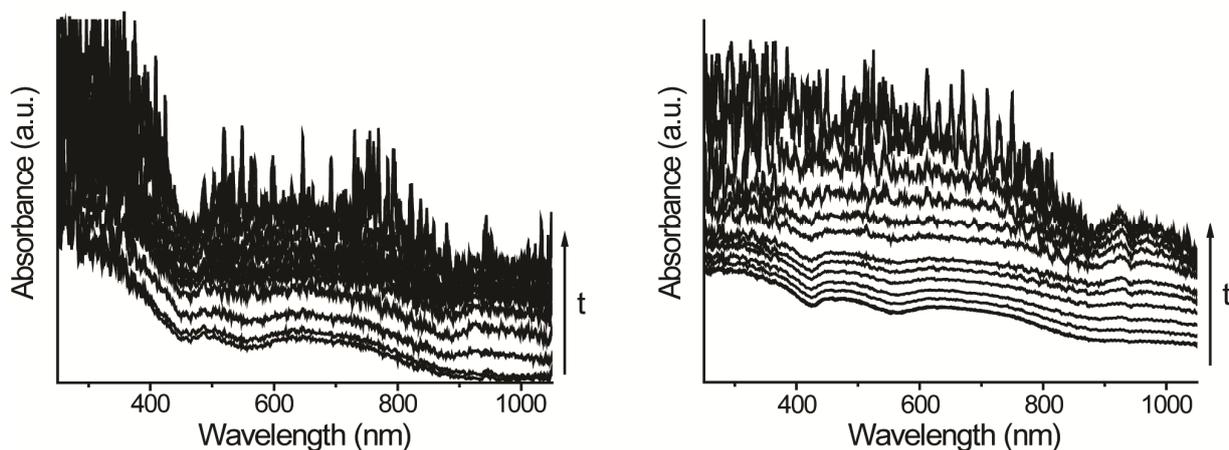


**Figure 5.4.** Operando UV-Vis spectra obtained with the top (left) and bottom (right) probes during the propane dehydrogenation reaction. The absorption bands corresponding with the chromium d-d transitions slowly become obfuscated as carbon deposits are formed.

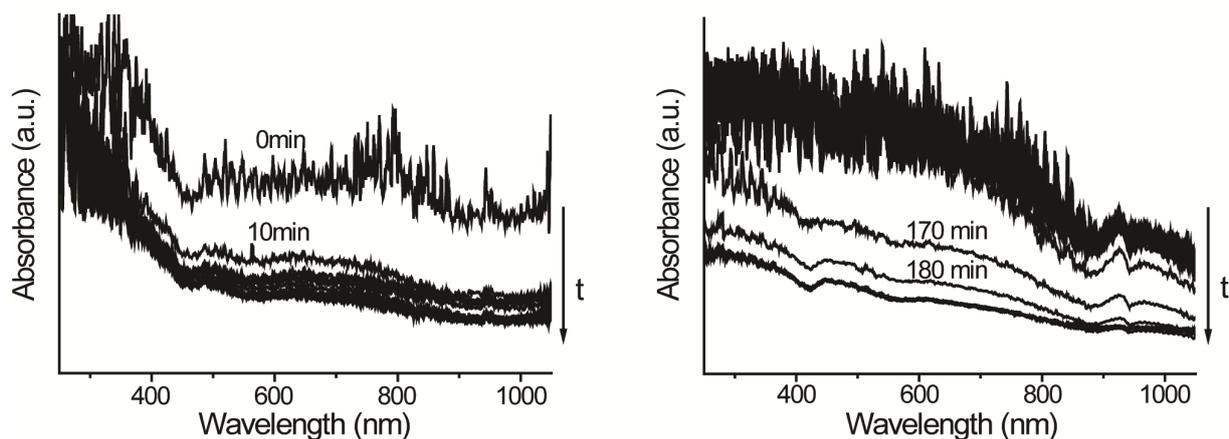


**Figure 5.5.** Operando UV-Vis spectra obtained with the top (left) and bottom (right) probes during the regeneration of the catalyst material. Absorption bands corresponding to the chromium d-d transitions, become visible again as the carbon deposits are combusted.

reaction. Due to the size of the reactor, it takes a considerable amount of time for the temperature to stabilize.

Operando UV-Vis spectra of the catalyst are collected continuously during the propane dehydrogenation reaction in order to monitor the deposition of coke, and are shown in Figure 5.4. At the start,  $\text{Cr}^{3+}$ -species, characterized by UV-Vis bands at

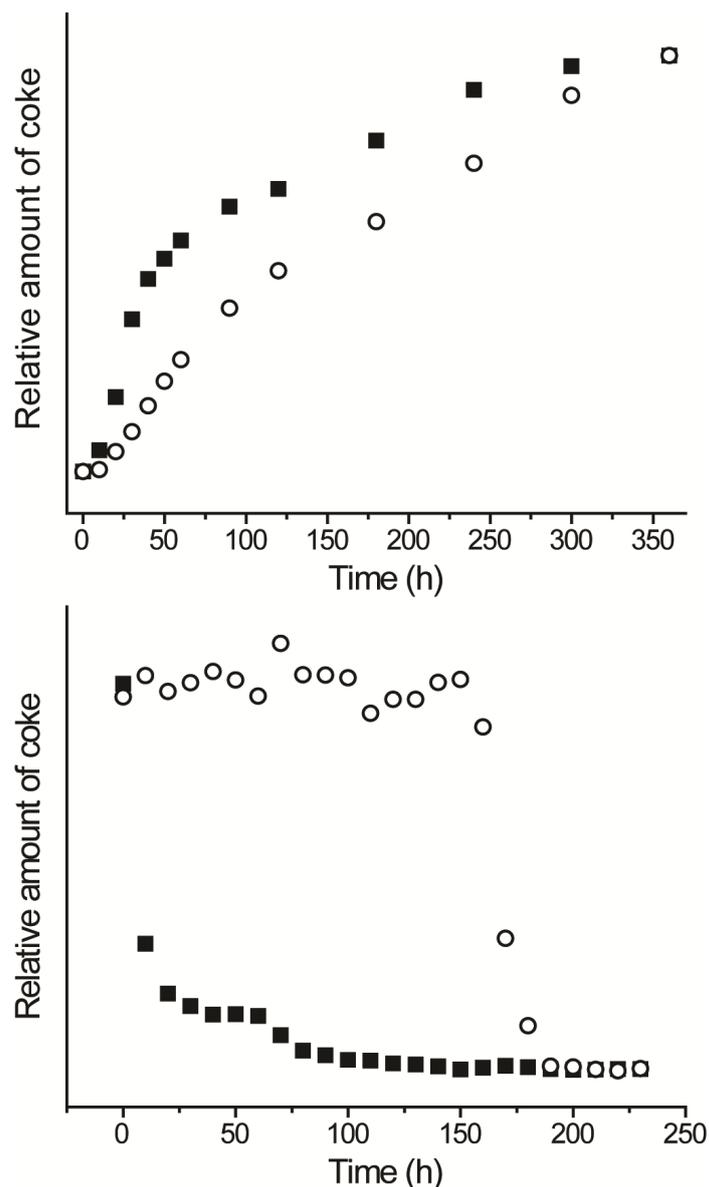


**Figure 5.6.** Normalized average absorption in the region between 600 and 700 nm of the operando UV-Vis spectra during the dehydrogenation reaction (top) and regeneration steps (bottom) as measured by the UV-Vis probes at the top (○) and the bottom (■).

around 300, 450 and 620 nm are identified. With time on stream, coke is deposited on the catalyst surface and the absorption increases over the entire range of wavelengths. After 2 h, the spectral features of the  $\text{Cr}^{3+}$ -species are difficult to identify as the catalyst material darkens due to the deposition of coke. This process becomes more prevalent during the rest of the cycle, eventually resulting in featureless and noisy UV-Vis spectra. In Figure 5.5, operando UV-Vis spectra collected with the two

probes during the subsequent oxidation-regeneration step are shown. For the top probe at the right side of the Figure, a drop in absorbance is observed after only 10 min into the regeneration step, resulting in the original spectrum of the fresh catalyst. For the bottom probe, no changes are observed in the spectra for the first 2.5 h, but within the next 30 min, the coke is combusted and the spectrum looks identical to that obtained at the start of the propane dehydrogenation experiment.

In order to study the coke deposition and combustion rate over time at different heights of the catalyst bed, a value for the absorption is obtained by averaging all data points of the UV-Vis spectra between 600-700 nm. The operando UV-Vis spectra obtained by both probes are compared by normalizing these values, as is shown in Figure 5.6. From the top part of the Figure, it can be observed that the formation of coke deposits at the top of the reactor is initially fast, after which it slows down. This is in strong contrast what occurs at the bottom of the reactor, where coke deposition is clearly a more gradual process. A similar analysis has been performed on the UV-Vis spectra during the oxidation-regeneration step and the results are presented in the graph at the bottom of Figure 5.6. At the top of the reactor the coke deposits are

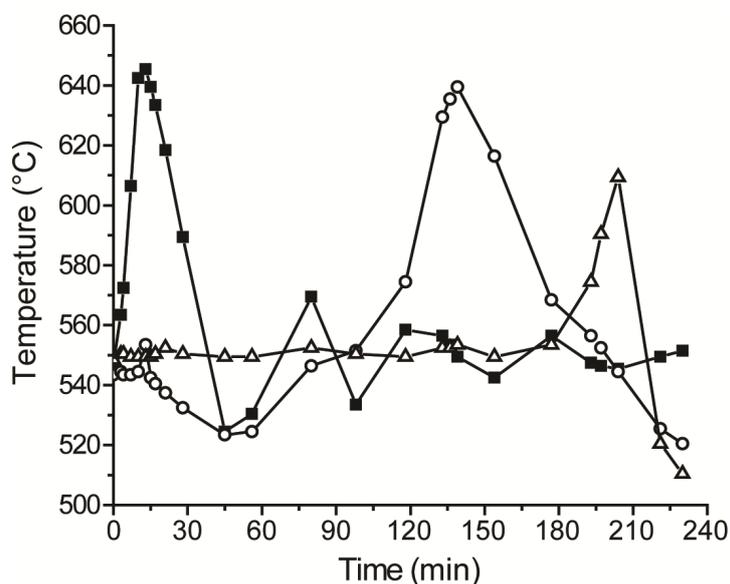


**Figure 5.7.** Temperature read-out of the top (■), middle (○) and bottom (Δ) thermocouples inside the pilot-scale reactor setup during the regeneration step. The oxidation provides extra heat to the system, which can be measured. This effect is visible at different times for the different thermocouples, first for the top, followed by the middle and bottom thermocouples.

readily combusted within 30 min, while this process requires about 3 h for the bottom part of the reactor. In both cases, the overall drop in UV-Vis absorption is rapid, which suggests that coke combustion is fast and that it takes place as a front, travelling through the reactor bed from top to bottom. This finding is corroborated by the heat released during combustion as measured over time by the three thermocouples which are located at distinct positions in the reactor. These results are shown in Figure 5.7.

To distinguish whether the darkening observed in the operando UV-Vis spectra is truly due to coke deposition on the catalyst extrudates, and not on the UV-Vis probe itself, a second experiment was performed where the reaction was halted after one hour to examine the individual  $\text{CrO}_x/\text{Al}_2\text{O}_3$  extrudates. As is shown in Figure 5.8, indeed the tip of the UV-Vis probe has remained free of coke deposits. In addition, the few extrudates located directly behind the probe, that were measured by the UV-Vis probe during the reaction, have become dark. Furthermore, the flow of nitrogen along the length of the probe did not interfere with the darkening of the catalyst extrudates measured, as the darkening of these particles was found to be representative for the

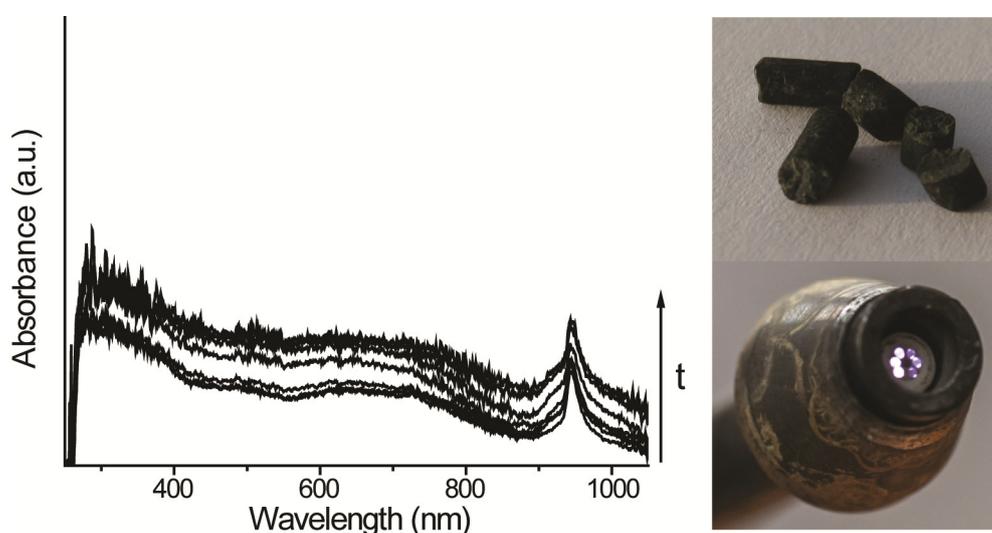


**Figure 5.8.** To investigate the effect of flowing  $\text{N}_2$  through the probes, the dehydrogenation experiment was halted after 1 h, after which the probe is removed and the extrudates behind the probe were investigated. These extrudates, shown in the picture, have significantly darkened during the experiment and are representative for other particles at that height of the reactor. At the same time the probe's tip had remained clear of coke.

catalyst bodies at that height of the pilot-scale reactor. Finally, it was apparent that the catalyst particles had a different color, depending on the height of the reactor bed. This is in agreement with the observations made with operando UV-Vis spectroscopy.

## 5.4 Conclusions

A novel pilot-scale reactor, in which operando UV-Vis spectroscopic probes can be inserted at specific places along the reactor bed, has been designed, constructed and tested for the catalytic dehydrogenation of propane. In addition, operando UV-Vis probes were designed and constructed that were able to withstand the harsh conditions of the propane dehydrogenation reaction. This new design allows for the on-line monitoring of the formation and combustion of coke deposits by on-line monitoring the UV-Vis absorption intensity. Moreover, by using multiple probes located along the length of the catalyst bed, it is possible to observe spatiotemporal differences in the rate of carbon deposition and the consecutive combustion of the formed coke deposits. Coke deposition is more rapid at the top compared to the bottom part of the reactor bed, and coke combustion takes place as a front, which travels down the length of the catalyst bed. The results presented illustrate the potential of using operando spectroscopic probes to study industrially relevant catalyst extrudates by UV-Vis spectroscopy under realistic reaction conditions in a pilot-scale reactor setup.

## 5.5 Acknowledgements

Ad Mens, Maria Arias and Tom Visser (Utrecht University) are thanked for their contributions in the design and construction of the pilot-scale reactor. Rene Teunissen and Marcel Scherrenburg (Avantes) are kindly acknowledged for their work in the design and construction of the probes. Finally, Robert Terorde and Peter Berben (BASF) are thanked for providing the  $\text{CrO}_x/\text{Al}_2\text{O}_3$  propane dehydrogenation catalyst.

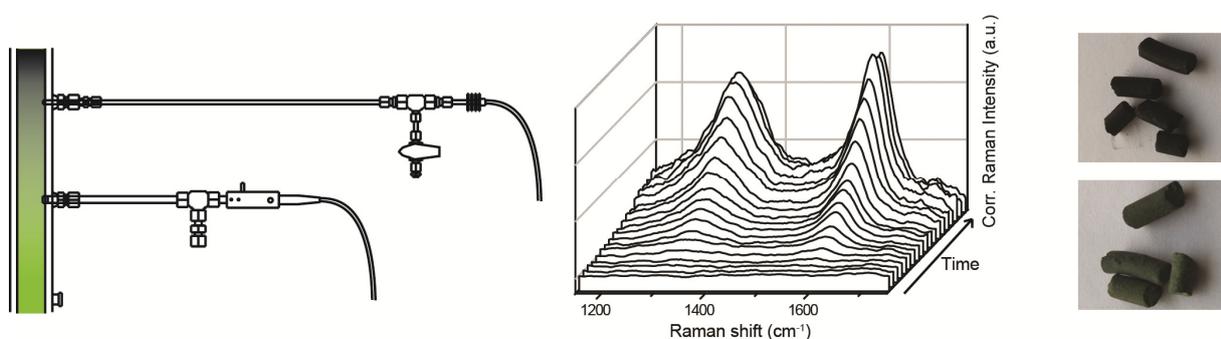
## 5.6 References

- (1) Puurunen, R. L.; Beheydt, B. G.; Weckhuysen, B. M. *J. Catal.* **2001**, *204*, 253.
- (2) Puurunen, R. L.; Weckhuysen, B. M. *J. Catal.* **2002**, *210*, 418.
- (3) Nijhuis, T. A.; Tinnemans, S. J.; Visser, T.; Weckhuysen, B. M. *Phys. Chem. Chem. Phys.* **2003**, *5*, 4361.
- (4) Tinnemans, S. J.; Kox, M. H. F.; Nijhuis, T. A.; Visser, T.; Weckhuysen, B. M. *Phys. Chem. Chem. Phys.* **2005**, *7*, 211.
- (5) Nijhuis, T. A.; Tinnemans, S. J.; Visser, T.; Weckhuysen, B. M. *Chem. Eng. Sci.* **2004**, *59*, 5487.
- (6) Bennici, S. M.; Vogelaar, B. M.; Nijhuis, T. A.; Weckhuysen, B. M. *Angew. Chem. Int. Ed.* **2007**, *46*, 5412.
- (7) Weckhuysen, B. M.; Schoonheydt, R. A. *Catal. Today* **1999**, *51*, 223.
- (8) Malleswara Rao, T. V.; Deo, G.; Jehng, J.-M.; Wachs, I. E. *Langmuir* **2004**, *20*, 7159.
- (9) Weckhuysen, B. M.; de Ridder, L. M.; Schoonheydt, R. A. *J. Phys. Chem* **1993**, *97*, 4756.
- (10) Weckhuysen, B. M.; Bensalem, A.; Schoonheydt, R. A. *J. Chem. Soc. Faraday Trans.* **1998**, *94*, 2011.
- (11) Weckhuysen, B. M.; Verberckmoes, A. A.; Debaere, J.; Ooms, K.; Langhans, I.; Schoonheydt, R. A. *J. Mol. Catal. A-Chem.* **2000**, *151*, 115.
- (12) Shee, D.; Sayari, A. *Appl. Catal. A-Gen.* **2010**, *389*, 155.
- (13) Sokolov, S.; Stoyanova, M.; Rodemerck, U.; Linke, D.; Kondratenko, E. V. *J. Catal.* **2012**, *293*, 67.
- (14) Michorczyk, P.; Pietrzyk, P.; Ogonowski, J. *Micropor. Mesopor. Mat.* **2012**, *161*, 56.
- (15) De Rossi, S.; Ferraris, G.; Fremoiotti, S.; Garrone, E.; Ghiotti, G.; Campa, M. C.; Indovina, V. *J. Catal.* **1994**, *148*, 36.
- (16) Praserthdam, P.; Mongkhonsi, T.; Kunatippapong, S.; Jaikaew, B.; Lim, N. *Stud. Surf. Sci. Catal.* **1997**, *111*, 153.
- (17) Iglesias-Juez, A.; Beale, A. M.; Maaijen, K.; Weng, T. C.; Glatzel, P.; Weckhuysen, B. M. *J. Catal.* **2010**, *276*, 268.



## Chapter 6

# Real-Time Quantitative Operando Raman Spectroscopy on a $\text{CrO}_x/\text{Al}_2\text{O}_3$ Propane Dehydrogenation Catalyst in a Pilot-Scale Reactor



Combined operando UV-Vis/Raman spectroscopy has been used to study the deactivation of  $\text{CrO}_x/\text{Al}_2\text{O}_3$  catalyst extrudates in a pilot scale propane dehydrogenation reactor. For this purpose, a specially designed Raman probe has been constructed and tested. The light absorption measured by operando UV-Vis spectroscopy was used to correct for the effect of catalyst darkening, effectively making operando Raman spectroscopy a quantitative technique to on-line determine the amount of coke deposits during the first hour of propane dehydrogenation. Differences in the rate of coke deposition were observed between the top and bottom of the pilot-scale reactor, which were related to the local temperature of the catalyst bed.

This Chapter is based on the manuscript: J.J.H.B. Sattler, A.M. Mens, B.M. Weckhuysen, *ChemCatChem* (2014) DOI: 10.1002/cctc.201402649. .

## 6.1 Introduction

As was shown in Chapters 2-4, operando Raman spectroscopy is an excellent tool for studying the type and amount of carbon deposits formed during the dehydrogenation of propane over a wide range of catalyst materials.<sup>1-4</sup> This characterization method provides non-invasive method for obtaining detailed information on the type of coke deposits formed at reaction conditions. Raman spectroscopy is a quantitative technique, as the intensity of the scattered Raman light is directly proportional to the amount of scattering molecules. However, part of the scattered Raman light will be absorbed by the catalytic solid, which is directly related to the degree of coloration of the catalytic solid. This means that, as the catalyst deactivates by e.g. coke deposition, the self-absorption of the Raman signal becomes more prevalent as the catalytic solid becomes increasingly black. This results in an overall decrease of the Raman intensity collected, making quantitative use of the technique difficult if not simply impossible.<sup>5-7</sup>

Fortunately, as was shown by Tinnemans et al., changes in the value of the diffuse reflectance  $R_\infty$  of a catalytic solid (as measured by operando UV-Vis spectroscopy) can be directly used to correct for the self-absorption of the Raman signal.<sup>5,6,8</sup> Indeed, the relationship between the diffuse reflectance and the observed Raman intensity can be written as follows:

$$\Psi_\infty = \frac{\rho I_0}{s} \cdot G(R_\infty) \quad 6.1$$

$$G(R_\infty) = \frac{R_\infty(1 + R_\infty)}{(1 - R_\infty)} \quad 6.2$$

where  $\Psi_\infty$  = observed Raman intensity for a powdered sample of infinite thickness,  $I_0$  the intensity of the laser light source,  $\rho$  the coefficient of Raman generation and  $s$  the scattering coefficient. For Equation 6.1 to be valid, the scattering coefficient  $s$  should remain constant during the experiment. Furthermore, as this formula is derived from the Kubelka-Munk equation, the correlation between absorption and the concentration

of light absorbing species breaks down at very high values for light absorption, which means at very low values for  $R_{\infty}$ .<sup>9</sup>

By using this quantitative Raman approach, Tinnemans et al. have measured the diffuse reflectance  $R_{\infty}$  of the catalytic solid in a lab-scale reactor, similar to the one used in Chapters 2-4, with operando UV-Vis spectroscopy, while collecting operando Raman spectroscopic data simultaneously.<sup>5,6,8</sup> By using the obtained value for  $R_{\infty}$  and the aforementioned Equations 6.1 and 6.2, it was then possible to calculate the true Raman spectral intensity, which correlates with the amount of coke deposits present. In a follow-up study, Bennici et al. have used this approach to develop an expert catalytic reactor control system in a lab-scale reactor, where the regeneration of the catalyst bed is started automatically, when a certain amount of coke on the catalyst material is measured by combined operando Raman/UV-Vis spectroscopy.<sup>10</sup>

Inspired by these promising results, we opted to bring this operando Raman/UV-Vis approach to the next level by building a pilot scale reactor in which holes were introduced to insert optical fiber probes for studying the catalyst bed. The first results of these efforts have been described in Chapter 5 where operando UV-Vis probes have been used for the on-line monitoring of the coke formation on a commercial  $\text{CrO}_x/\text{Al}_2\text{O}_3$  catalyst, shaped in the form of mm-sized extrudates, during the propane dehydrogenation reaction.<sup>11</sup> In this Chapter the developed approach is taken one step further as a special operando Raman probe was designed, constructed and tested for its use in the pilot scale reactor. It is important to mention here that the design of this operando Raman probe is significantly more complex than the UV-Vis probes, described in Chapter 5.

Indeed, as photons come in contact with the catalyst material, they can be either scattered elastically (Rayleigh scattering) or inelastically (Raman scattering). Inelastic scattering means that the photons lose or gain energy, as (vibrational) energy is transferred from or to the sample. As Raman scattered light is only a small fraction of the total scattered light, a high flux of photons on a single spot is required to get a strong enough Raman signal. Therefore, a lens is used to focus a bundle of laser light on the sample and collect the backscattered Raman signal. This means the probe has to be constructed in such a way that it can focus a laser beam on the catalyst sample. While the operando UV-Vis probe consists of optical fibers that are directly connected to the light source and the spectrometer, optics are present inside the Raman probe that filter and transfer the Raman scattered light from the outer lens to

the fibers that connect the probe with the spectrometer and light source. It turned out that these optics are very sensitive for heat fluctuations and require continuous cooling, hence the design of the probes had to be adjusted for this purpose.

In this Chapter we show the design, construction and testing of a Raman probe in the pilot-scale reactor. Raman spectroscopy proved to be an excellent method for visualizing the deposition and burning of the coke species on the  $\text{CrO}_x/\text{Al}_2\text{O}_3$  extrudates during the dehydrogenation of propane during two successive dehydrogenation-regeneration cycles. The dehydrogenation experiment was performed twice under identical conditions, with the exception of the relative position of the operando UV-Vis and Raman probes along the reactor bed.  $R_{\infty}$  was obtained from the operando UV-Vis spectra from one experiment, where it was used to correct the intensity of the operando Raman spectra obtained during the other experiment. In this way, quantitative information, in addition to chemical information on the type of coke via the  $D_1/G$  ratio, was directly obtained by analyzing the operando Raman spectra measured during propane dehydrogenation and catalyst regeneration at different locations of the catalyst bed.

## 6.2 Experimental

### 6.2.1 Design of the Raman Probes

Figure 6.1 shows a schematic drawing and photograph of the pilot scale reactor used, including two operando UV-Vis probes and a single operando Raman probe. The two UV-Vis probes described in Chapter 5, have been replaced with two others, which have a longer metal casing, but are otherwise identical. In Figure 6.2, a more detailed schematic and photograph of the newly designed Raman probe is shown. Crucial to the design is that the actual Raman probe is inserted into a metal casing, which is fixed to the reactor. The seal between the probe and the casing consists of a Teflon ferrule, allowing some flexibility in the relative position of the probe inside the casing. In this way the probe can be moved closer or further with respect to the catalyst bed, providing a means for focusing the Raman light source onto the catalyst material. The Raman probe has a larger diameter (3/8" vs. 1/4") compared to the UV-Vis probes, which is why the sockets in the reactor were adjusted to fit both the

probes. Some spacing is present between the probe and the casing, along which N<sub>2</sub> is flowed to prevent fouling of the probe tip. As an additional measure to prevent fouling, a sapphire window is present at the end of the metal casing, serving as a barrier to prevent reactants from entering. The flow of N<sub>2</sub> can exit the casing via small holes drilled at the edge of the sapphire window.

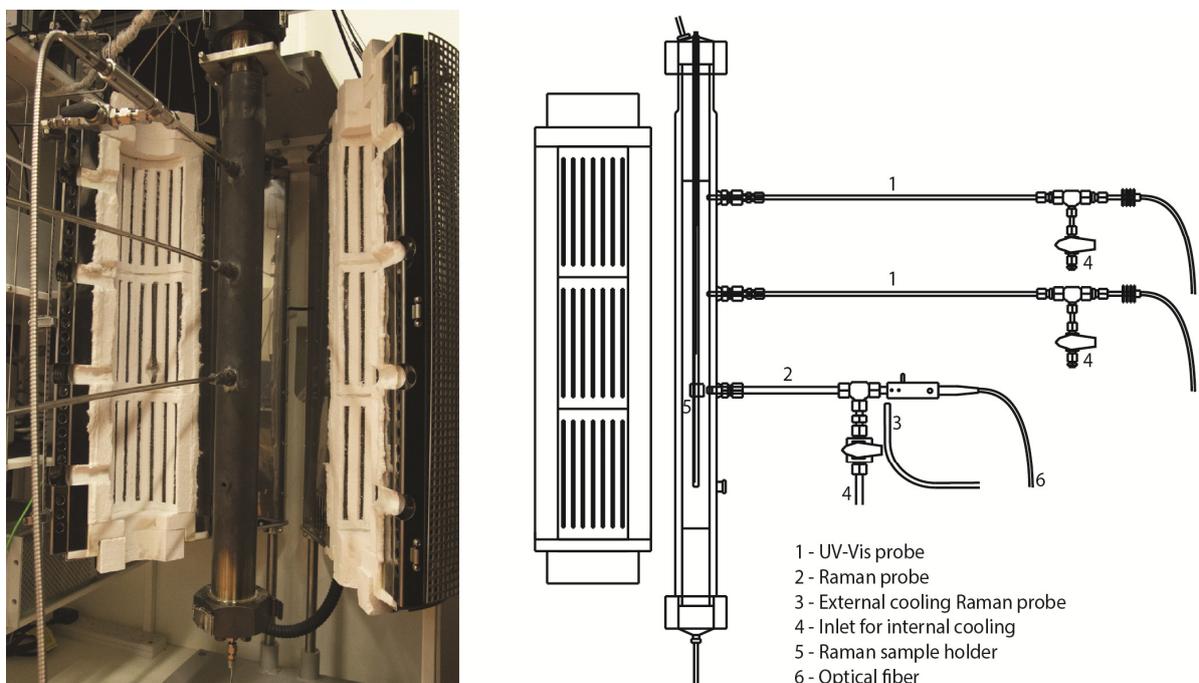


**Figure 6.1.** Detailed scheme and photograph of the pilot scale reactor used to study the deactivation of CrO<sub>x</sub>/Al<sub>2</sub>O<sub>3</sub> extrudates during propane dehydrogenation. The reactor has been slightly modified to allow both operando UV-Vis and Raman probes to be used to study the catalyst bed; the differences compared to Figure 5.1 are shown in the legend of the Figure.

A schematic of the optics inside of the Raman probe is shown in the inset of Figure 6.2. The probe is connected by an optical fiber to the laser light source. When exiting the fiber, light is converted to a parallel beam by a lens and travels through a band-pass filter, which blocks the Raman signal of the Si-O vibrations of the optical fiber, only transmitting light with a wavelength of 532 nm. The light will then travel along the length of the probe through the dichroic filter and is focused on the catalyst particle by a second lens. Backscattered light is then collected and converted to a parallel beam by the same lens. From this direction, the dichroic filter effectively functions as a mirror for the incident light. Through another mirror the light passes

through a long-pass filter assembly, which only allows the Stokes shifted light through. A third lens focusses the parallel beam on a second optical fiber, which is connected to the Raman spectrometer. As the positioning of the lenses, mirrors and filters is very precise, the temperature of this part of the probe should not exceed 200 °C.<sup>12</sup> The probe is mostly made of steel, which can conduct heat from the reactor to the optics of the probe. To alleviate this, a jet of air is used to cool this exterior of the Raman probe.

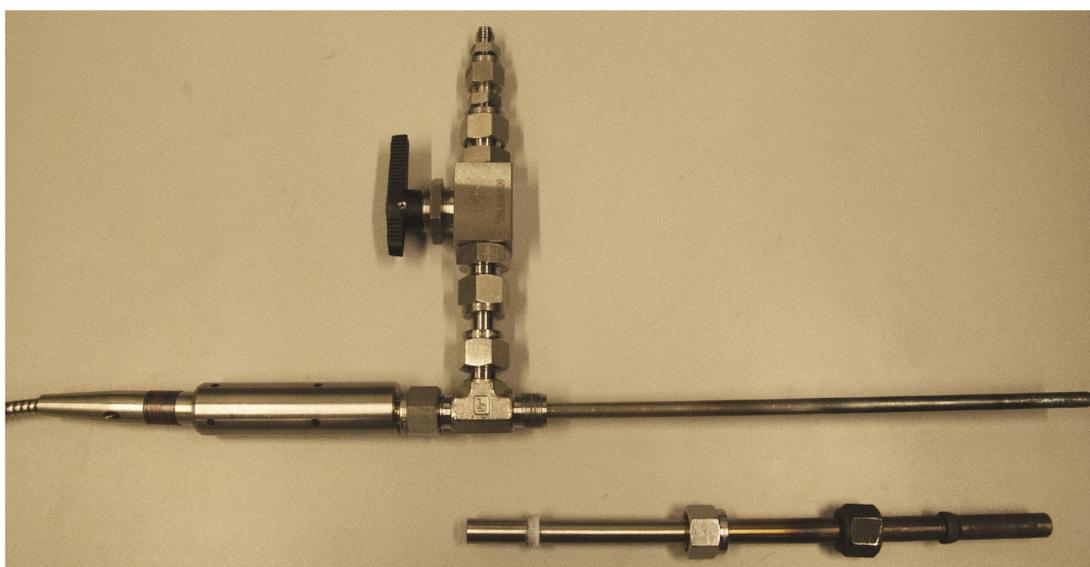
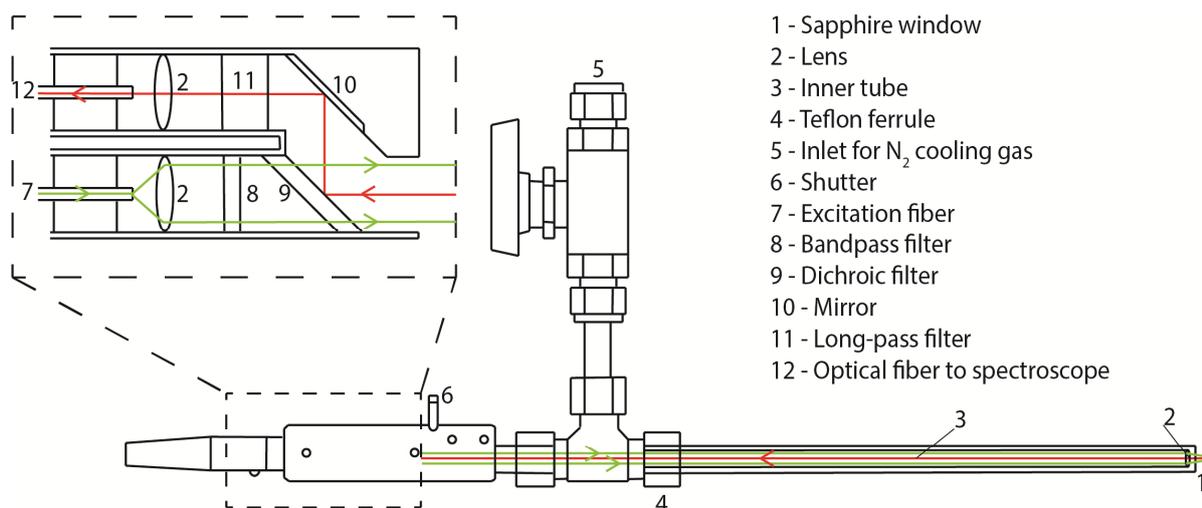


**Figure 6.2.** Scheme and photograph of the operando Raman probe used during the catalytic dehydrogenation of propane.<sup>12</sup> In the Scheme's inset, a zoomed in display of the optics inside the probe are shown. The green arrows show the pathway of the incident laser light, while the red arrows show the pathway of the collected Raman signal through the operando Raman probe. In the photograph, the actual Raman probe and the metal casing are shown separately.

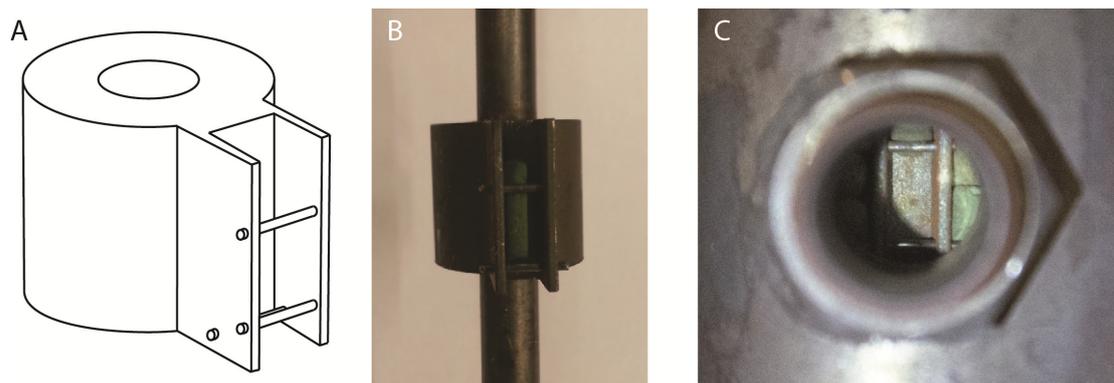


**Figure 6.3.** Scheme (A) of the sample holder, which has been attached to the thermowell inside the reactor. The first picture (B) shows this sample holder attached to the thermowell, and the second (C) the sample holder as seen through the socket in the reactor, after packing the reactor. The  $\text{CrO}_x/\text{Al}_2\text{O}_3$  catalyst extrudate is kept in place by three small metal wires with a diameter of 0.5 mm.

As mentioned before, the lens located at the tip of the Raman probe focusses the laser beam on the sample. As the catalyst bed sets as it is heated, individual catalyst extrudates change position due to e.g. thermal expansion. Since only a small section of a single catalyst extrudate is studied, the movement of the catalyst bed can result in a loss of focus, making the collection of the Raman signal impossible. To avoid this problem, a sample holder, in which a single catalyst particle can be fixated, was attached to the thermo-well inside the reactor. In this way, the probe would be focused on the same spot of a specific extrudate during the complete dehydrogenation cycle. The sample holder is designed as such, that it makes minimal contact with the catalyst extrudate which is placed inside. A schematic display and pictures of this sample holder are shown in Figure 6.3.

### 6.2.2 Dehydrogenation of Propane

The pilot plant reactor, described in Chapter 5.2.1, and outlined in Figure 6.1, was filled with approximately 500 g of  $\text{CrO}_x/\text{Al}_2\text{O}_3$  extrudates, with 14 cm of inert stainless steel balls (diameter of 6 mm) at the reactor's extremities. The catalyst extrudates have a diameter of about 3 mm and a length of 3-8 mm. They consist of 20 wt% of Cr (mixture of  $\text{Cr}^{3+}$  and  $\text{Cr}^{6+}$ ) and 1 wt% of Na on an alumina support. The Raman and UV-Vis probes are alternately located at the bottom, middle and top

sockets respectively. The Raman probe is connected to an Ava-Raman-532TEC spectrometer, which is equipped with a 532 nm laser light source. Spectra are collected with 10 s acquisition time and 10 accumulations. The two UV-Vis probes are both connected to a deuterium-halogen light source and an Avaspec 2048 UV-Vis spectroscope, and spectra are collected every 100 s, with an acquisition time of 50 ms and 100 accumulations.

The dehydrogenation reaction is performed at approximately 550 °C at a pressure of approximately 1.5 bar. A flow of 5000 ml/min, consisting of 10 vol% of propane in N<sub>2</sub> (WHSV = 0.1 h<sup>-1</sup>), is flown over the catalyst bed over a period of 6 h. The outlet of the reactor is connected with a GC equipped with a FID (Porabond-Q column) and a TCD (Carboxan column) detector for analyzing the composition of the resultant gas flow. After the dehydrogenation step, the coke formed on the catalyst is burnt off by flowing a mixture of O<sub>2</sub> (140 ml/min) and nitrogen (2200 ml/min) at the same temperature. The regeneration is stopped when no more CO<sub>x</sub> is detected by GC analysis. The reactor is then flushed with nitrogen and a second dehydrogenation cycle is started. The temperature of the top, middle and bottom of the catalyst bed is continuously monitored by three thermocouples inserted in the thermo-well.

## 6.3 Results and Discussion

### 6.3.1 Dehydrogenation Experiment with the Raman Probe located at the Bottom of the Reactor

In a first experiment, two subsequent propane dehydrogenation-regeneration cycles were performed with the developed pilot-scale reactor setup. The two operando UV-Vis probes were positioned in the upper two reactor opening slots and the operando Raman probe was placed in the third opening slot, at the bottom of the catalyst bed. The conversion and selectivity results, as well as the temperature as measured by the three thermocouples, are summarized in Figure 6.4. At the start of the first PDH cycle, the catalyst material displays a conversion of propane of ~50%, which drops to 40% over the following 6 h. The selectivity to propylene is initially 80%, quickly dropping to 50% after which it slowly increases to 90%, similar to the values reported in Figure 5.3. This erratic behavior of the selectivity is caused by fluctuations in the temperature

of the catalyst bed. The heating system of the reactor overcompensates for the loss of heat due to the endothermicity of the dehydrogenation reaction, which makes side reactions such as cracking more prevalent. During the first minute of the second dehydrogenation cycle, an additional effect is observed. The temperature of the catalyst bed increases to 580 °C, after which it quickly drops again to 550 °C. This increase is most probably caused by the reduction of  $\text{Cr}^{6+}$  species that were formed during the oxidation step, as this reduction process results in the (partial) oxidation or

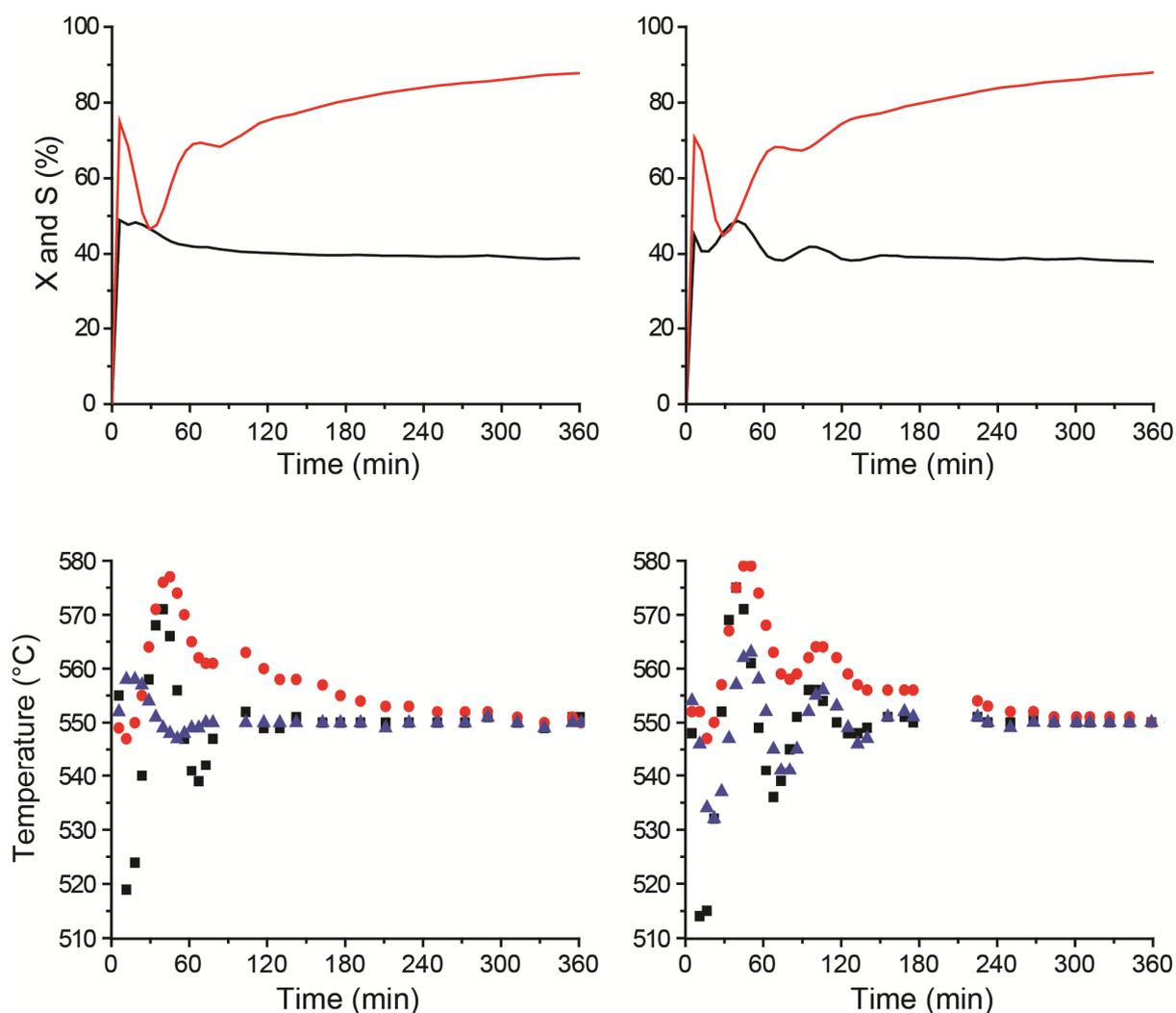


**Figure 6.4.** The top two graphs show the conversion (black) and selectivity (red) measured during the first and second dehydrogenation cycle during the first experiment on industrial-like  $\text{CrO}_x/\text{Al}_2\text{O}_3$  catalysts. The second set of graphs show the temperature profiles at the top (black), middle (red) and bottom (blue) of the catalyst bed, as measured by the three thermocouples inserted in the thermowell.

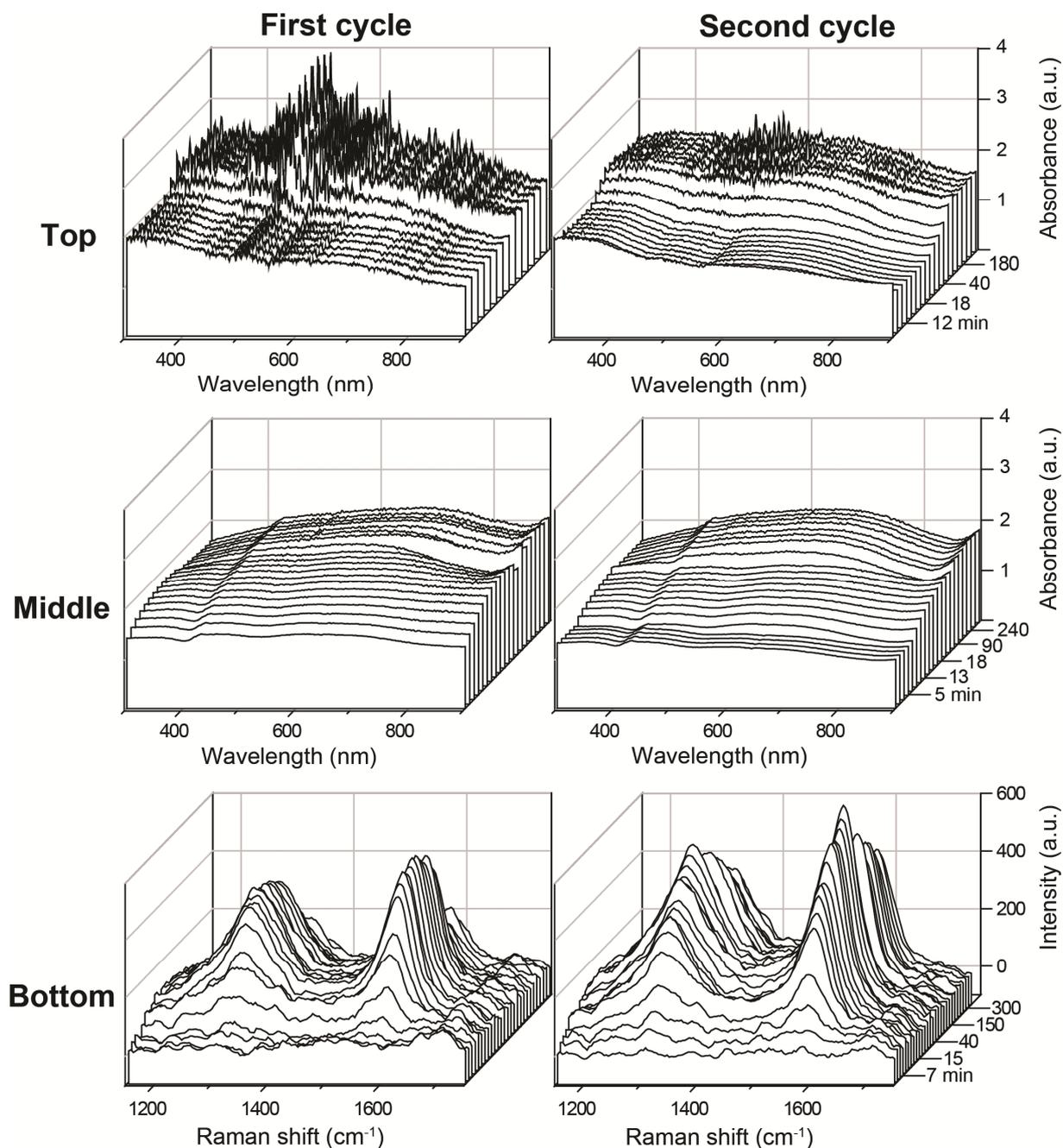


**Figure 6.5.** Operando UV-Vis spectra of industrial-like  $\text{CrO}_x/\text{Al}_2\text{O}_3$  catalyst extrudates, collected during the dehydrogenation of propane at  $550\text{ }^\circ\text{C}$  with the probe at the top (top graphs) and middle (second set of graphs), as well as operando Raman spectra obtained with the bottom probe (third row of graphs). The data obtained during the first cycle are shown to the left, and data obtained during the second cycle are shown to the right.

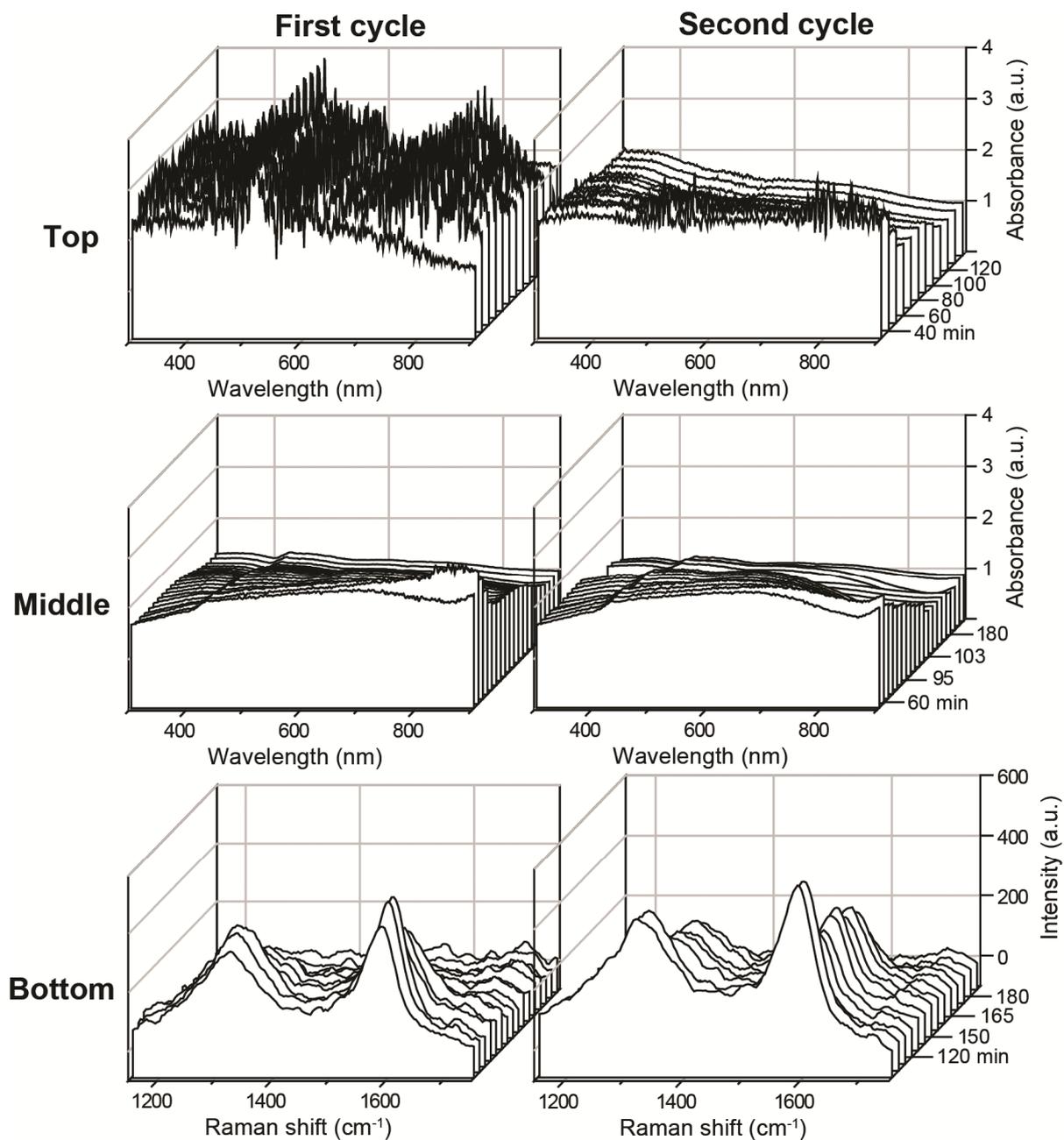


**Figure 6.6.** Operando UV-Vis spectra of industrial-like  $\text{CrO}_x/\text{Al}_2\text{O}_3$  catalyst extrudates, obtained with the probe at the top (top graphs) and middle (second set of graphs), as well as operando Raman spectra obtained with the bottom probe during the combustion of the coke deposits formed during the dehydrogenation reaction. The first oxidation step is shown at the left, and second oxidation step to the right.

combustion of propane. The values of conversion and selectivity obtained during the second cycle, as well as the temperature profile of the catalyst bed closely resemble the first cycle.

In Figure 6.5, the operando UV-Vis and Raman spectra obtained during the two dehydrogenation steps of the first experiment are shown. With the two operando UV-Vis probes installed, the absorption bands corresponding with the d-d transitions of  $\text{Cr}^{3+}$  (300, 450 and 620 nm) are observed at the start of the dehydrogenation step. Over the course of the propane dehydrogenation cycle, the absorption increases gradually as the bands of the  $\text{Cr}^{3+}$  species become obscured by coke species. This darkening takes place rapidly during the first hour of reaction, after which no additional darkening was observed, possibly because the catalyst is already completely black at this point. This process of darkening starts with a delay of 20 min at the top of the catalyst bed, but otherwise takes place similar to the middle of the reactor. During these first 20 min, the temperature at the top of the reactor has dropped below 550 °C, while remaining at 550 °C at the middle. Possibly coke is not formed, or at least at a much lower rate, below 550 °C. Operando Raman spectra were obtained of the bottom of the catalyst bed. Two bands corresponding with coke at 1320 ( $\text{D}_1$ ) and 1590  $\text{cm}^{-1}$  (G) start forming a few minutes into the dehydrogenation cycle. The intensity of the two bands increases during the first 20 min of reaction, after which their intensity starts dropping due to catalyst darkening.

The spectra collected during the two regeneration steps, which were applied after running the propane dehydrogenation steps, are shown in Figure 6.6. The catalyst darkening, as measured by UV-Vis spectroscopy, as well as the coke bands in the Raman spectra disappear rapidly as the coke is combusted during the regeneration step. The time where coke is combusted is dependent on the height of the catalyst bed. Indeed, the spectral features corresponding with coke deposits disappear after 80 min at the top, 120 min in the middle and 180 min at the bottom of the catalyst bed. In other words, coke combustion gradually travels as a front from the top to the bottom of the reactor bed.

### 6.3.2 Dehydrogenation Experiment with the Raman probe located at the Top of the Reactor

A second experiment was performed with exactly the same experimental settings, with the exception that the operando Raman probe is now inserted in the top slot of the pilot-scale setup, while the two operando UV-Vis probes are inserted at the second and third slot. In Figure 6.7, the conversion, selectivity and temperature profiles are

shown. As can be expected, the same fluctuations in the propane conversion, propylene selectivity and local temperature of the catalyst bed are observed as during the first dehydrogenation experiment, which is shown in Figure 6.4.

In Figure 6.8, the operando Raman spectra obtained of the top of the catalyst bed and the operando UV-Vis obtained of the in the middle and bottom of the catalyst bed are shown. By operando Raman spectroscopy it was observed, that coke deposition started after 20 min at the top of the reactor bed. Indeed, the two characteristic

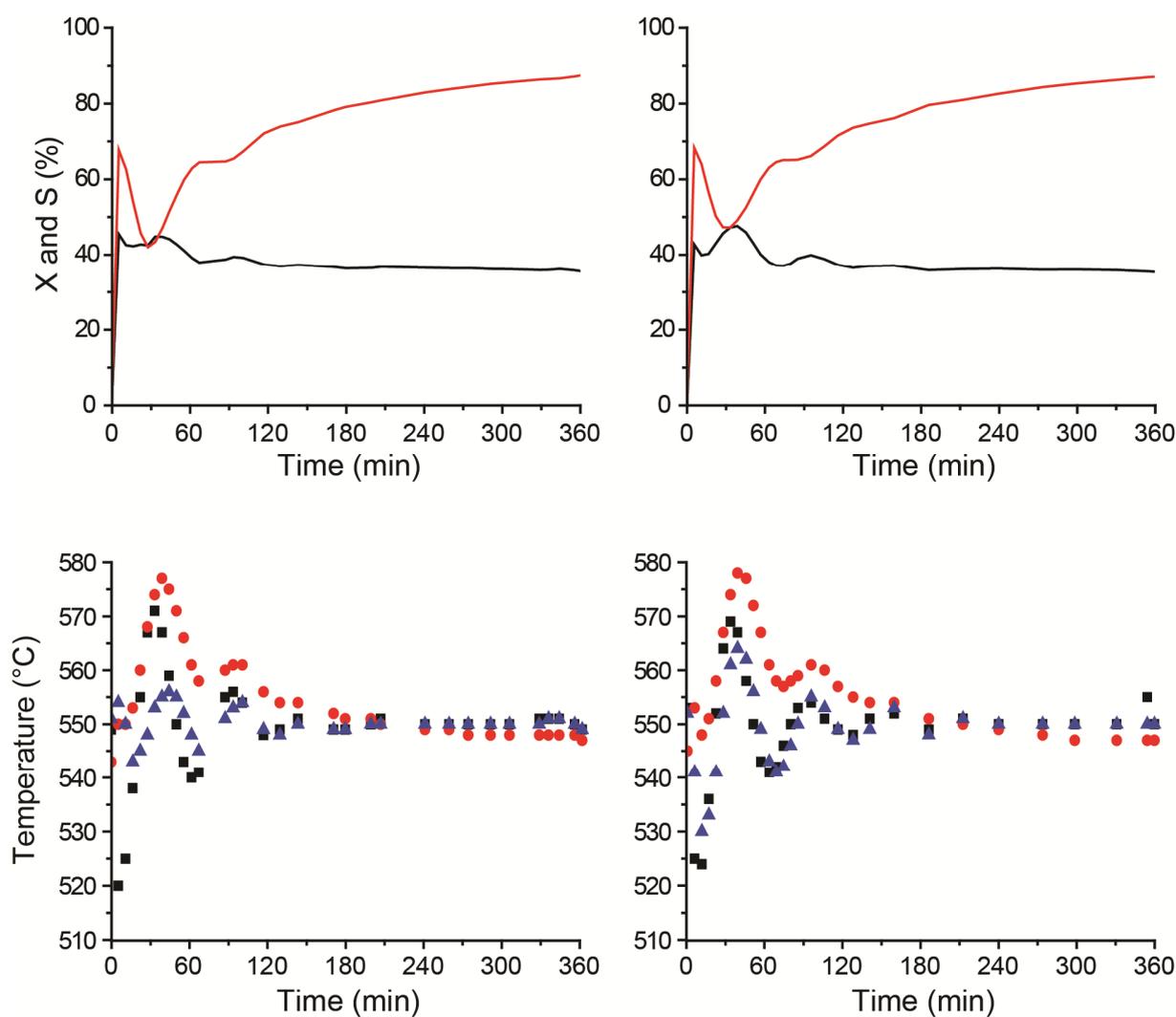


**Figure 6.7.** The top two graphs show the conversion (black) and selectivity (red) measured during the first and second dehydrogenation cycle during the second experiment of industrial-like  $\text{CrO}_x/\text{Al}_2\text{O}_3$  catalyst extrudates. The second set of graphs show the temperature profiles at the top (black), middle (red) and bottom (blue) of the catalyst bed, as measured by the three thermocouples inserted in the thermowell.

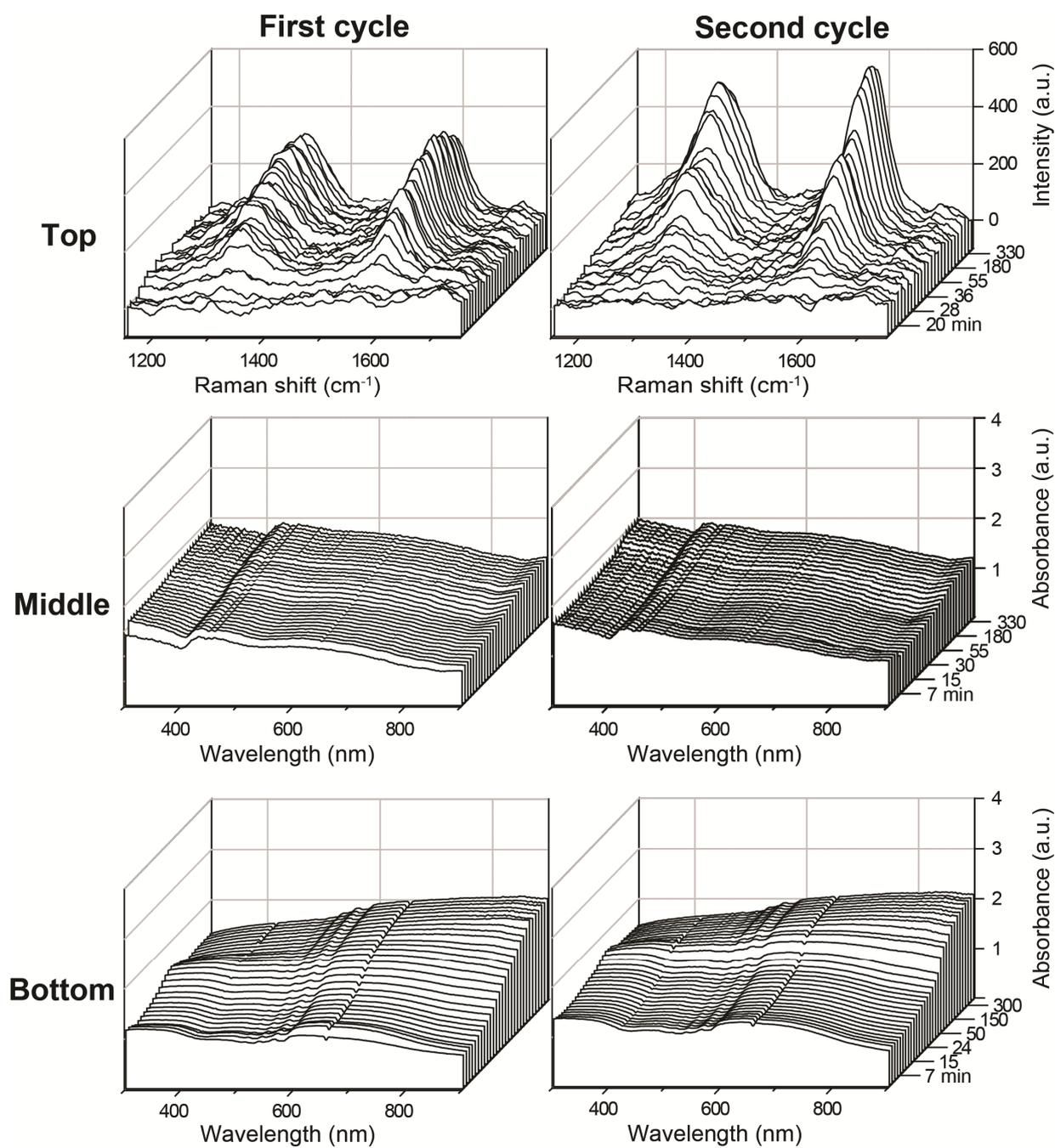


**Figure 6.8.** Operando Raman and UV-Vis spectra of industrial-like  $\text{CrO}_x/\text{Al}_2\text{O}_3$  catalyst extrudates collected at  $550\text{ }^\circ\text{C}$  during the second propane dehydrogenation experiment at the top, middle and bottom of the catalyst bed. In each graph, the formation of coke deposits is clearly visible. The data obtained during the first cycle are shown to the left, and data obtained during the second cycle are shown to the right.

Raman bands corresponding with coke at 1320 ( $D_1$ ) and 1590  $\text{cm}^{-1}$  (G), appear after 20 min on steam, and then gradually increase while reacting a maximum approximately 60 min into the dehydrogenation step. The operando UV-Vis probes inserted at the middle and bottom socket of the pilot-scale reactor revealed that catalyst darkening took place during the first hour of the dehydrogenation steps, after which the overall UV-Vis spectral intensities remained the same. These trends are identical to those shown in Figure 6.5 for the first dehydrogenation experiment. Similarly, the regeneration of the coke deposits (not shown) after the first and second propane dehydrogenation step shows the same trends as those shown in Figure 6.6.

### 6.3.3 Quantitative Coke Analysis

As the trends observed during the two experiments are so similar, the absorbance measured by operando UV-Vis spectroscopy in one experiment can be used to correct the operando Raman spectra collected in the other experiment. In other words, as both operando UV-Vis and Raman spectroscopic data are collected at the top and bottom of the reactor, the deposition of coke can be analyzed quantitatively at these two positions of the catalyst bed. This analysis was performed by determining the average absorption between 566.5 and 586.6 nm, which is the energy range of the Raman scattered photons of the carbon deposits (the laser has a wavelength of 532 nm, which equals 18800  $\text{cm}^{-1}$ ; the Raman bands of coke are located between 1150 and 1750  $\text{cm}^{-1}$ , which is 17650 and 17050  $\text{cm}^{-1}$ , or 566.5 and 586.6 nm, respectively). The average value for absorption in this region of the operando UV-Vis spectra is determined and converted into reflectance, which is used to calculate  $G(R_\infty)$  using Equation 6.2. The averaged absorption is used to minimize effects due to noise in the spectra.

The values of  $G(R_\infty)$  are shown in the top graphs of Figure 6.9 for both propane dehydrogenation cycles at the top and bottom of the catalyst bed.  $G(R_\infty)$  drops rapidly during the first 30-40 min of the dehydrogenation reaction to reach a stable value close to 0, meaning that after 40 min almost no light is reflected back from the catalyst sample and that additional darkening is not measured any more. At this point, the catalyst has become very dark and no further coke deposition can be measured by operando UV-Vis spectroscopy. Therefore, the correction of the operando Raman spectra for catalyst darkening by making use of Equation 6.1, is only valid during the

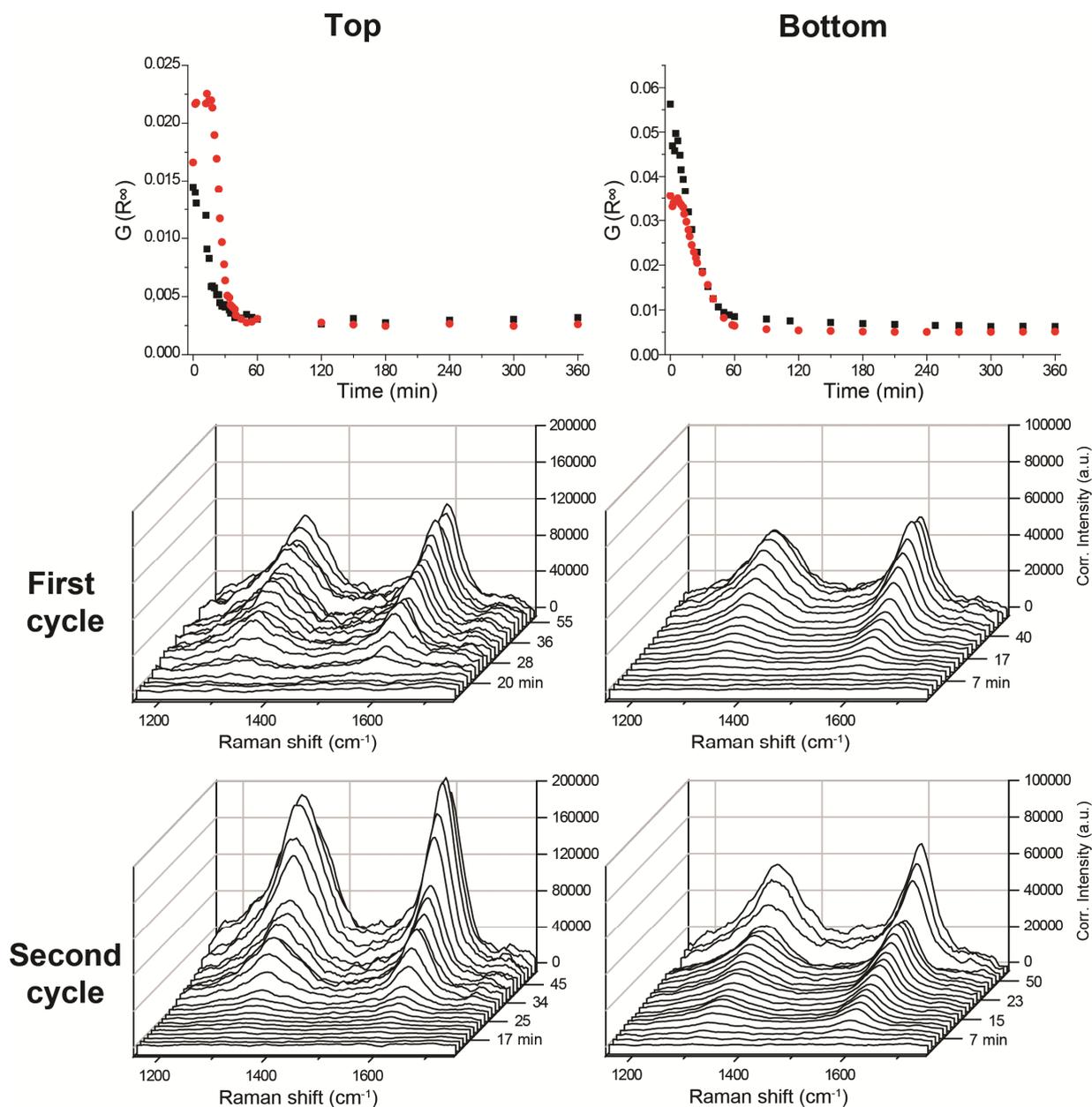


**Figure 6.9.** In the top two graphs, the  $G(R_{\infty})$  is plotted as a function of time for the first (black) and second dehydrogenation cycle (red). The second row of graphs shows the corrected operando Raman spectra for the first hour of the first propane dehydrogenation cycle, and the bottom two graphs shows the intensity corrected operando Raman spectra for the first hour of the second propane dehydrogenation cycle. The data acquired at the top of the reactor is shown at the left, while the data obtained when the Raman probe was located at the bottom slot is shown to the right.

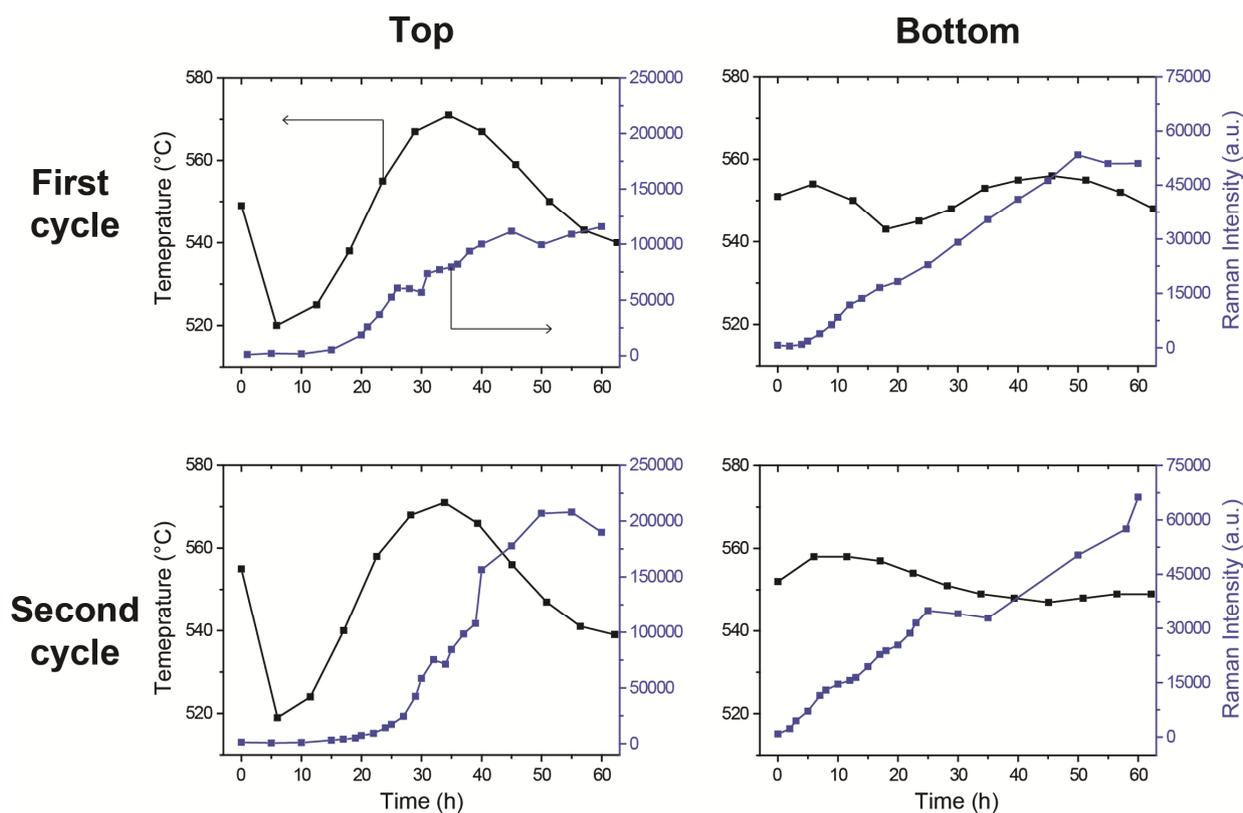


**Figure 6.10.** In the graphs the (corrected) intensity of the G band (blue) and the temperature of the catalyst bed (black) are plotted versus time for the first hour for the top and bottom of catalyst bed, for both cycles.

first hour of the propane dehydrogenation reaction. The results of this spectral correction approach are summarized in Figure 6.9 for the first and second dehydrogenation cycle at the top and bottom of the catalyst bed.

For the top probe (graphs to the left) the D<sub>1</sub> and G band start appearing 20 min into the dehydrogenation reaction, which rapidly increase in intensity during the following 30 min. For the bottom probe (graphs to the left) the intensity of the Raman bands starts to increase almost immediately and gradually continue to do so for the following 55 min. It is important to mention here that this quantitative analysis could not be used to study the combustion of coke deposits, since the darkening cannot be determined accurately at the start of the regeneration step. Furthermore, the combustion of coke is a relatively rapid process, taking place in a few minutes, during which only a few operando Raman spectra are collected.

In Figure 6.10 the corrected intensity of the G Raman band measured at the top and bottom of the catalyst bed as function of time is shown for both dehydrogenation

cycles. The actual values of the intensity of the Raman band cannot be compared directly. For each experiment, the probe will be positioned somewhat differently relative to the catalyst extrudate, which results in differences in the quality of the spectra, including the intensity of the Raman bands. However, the relative rate at which the intensity of the G Raman band increases during the different experiments can be compared. In Figure 6.10 it is shown that the rate of coke deposition is different for the top and bottom of the pilot-scale reactor. For the top no coke is deposited during the first 20 min, after which the amount of coke rapidly increases; at the bottom of the reactor the intensity of the G Raman band increases almost linearly in time during the first 50 min. The temperature of the catalyst bed as measured by the thermocouples at the top and bottom of the catalyst bed are shown. During the first 20 min, the temperature of the catalyst bed is significantly lower at the top of the reactor compared to the bottom and at the same time the coke deposition is faster at the bottom. Between 20 and 40 min into the dehydrogenation reaction, the temperature at the top of the catalyst bed is higher compared to the bottom; now the coke deposition is faster at the top of the catalyst bed. In addition, at the bottom both the temperature

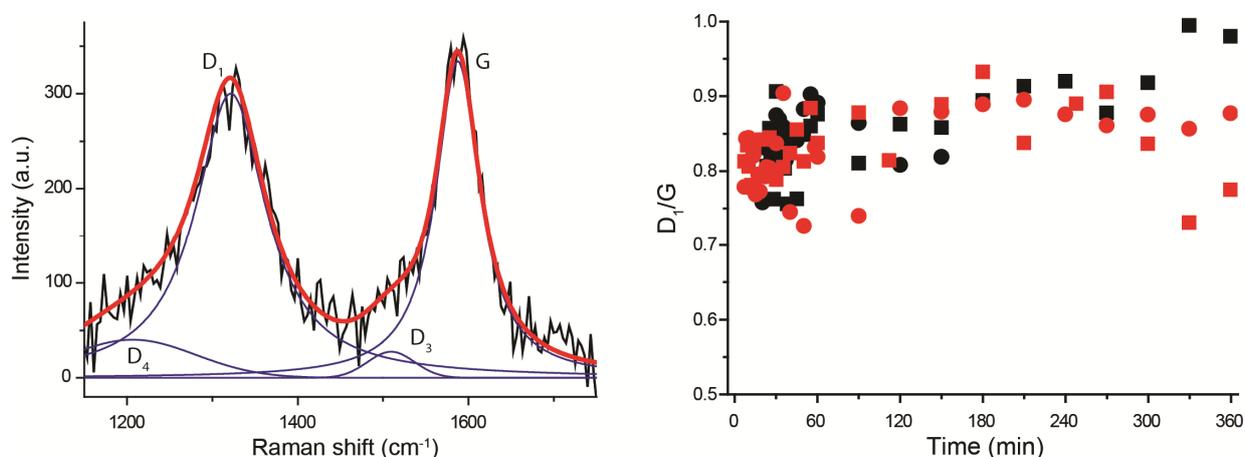


**Figure 6.11.** To the left, a deconvoluted Raman spectrum showing four coke bands, similarly to those reported in Chapter 2 and by Sadezky et al. is shown.<sup>13</sup> This deconvolution was used to determine the ratio between the D<sub>1</sub> and G Raman bands, which is a measure of the chemical nature of the coke deposits. These D<sub>1</sub>/G ratios are shown for all the operando Raman spectra collected, both at the top (black) and bottom (red) of the catalyst bed and both for the first (square) and second (circle) dehydrogenation cycle. This analysis has been performed on the uncorrected Raman spectra.

and the rate of coke deposition remain stable throughout the experiment. This clearly suggests a link between the temperature of the catalyst bed and the rate of coke deposition.

Finally, the ratio of the intensity of the D<sub>1</sub> and G bands of the Raman spectra shown in Figure 6.5 are determined by deconvoluting the Raman spectra in the same fashion as discussed in Chapter 2, taking the approach developed by Sadezky and co-workers.<sup>13</sup> The results are shown in Figure 6.11. Here, it is clear that the absolute D<sub>1</sub>/G values vary a lot in the consecutively measured operando Raman spectra, both at the top and bottom of the reactor. As a consequence, there is no clear difference in the chemical nature of the coke deposits formed at the top and bottom of the catalyst bed. On average, the D<sub>1</sub>/G ratio is 0.84. This means that the chemical nature of the coke deposits formed on an industrial-like CrO<sub>x</sub>/Al<sub>2</sub>O<sub>3</sub> catalyst extrudate is independent on its location of the catalyst bed, or the time it is exposed to propane.

## 6.4 Conclusions

In this Chapter we have described the design, construction and testing of an operando Raman probe, which could be inserted in a pilot-scale reactor to study the process of coke deposition on a CrO<sub>x</sub>/Al<sub>2</sub>O<sub>3</sub> extrudate during the dehydrogenation of propane. The probe is designed as such, that a flow of N<sub>2</sub> can be used to cool the probe and keep the tip clear of coke deposits. Furthermore, the probe can be moved with respect to the catalyst bed for focusing purposes. In addition to the Raman probe, two operando UV-Vis probes were used to study the catalyst bed during two consecutive propane dehydrogenation-regeneration cycles. By combining the information gathered from the operando Raman and UV-Vis spectra from the two cycles it was possible to determine the type and amount of coke deposits formed along the reactor bed during the first hour of propane dehydrogenation. Differences in the rate of coke deposition were observed as a function of catalyst bed height, which are related to differences in the local catalyst bed temperature. A higher reaction temperature would result in faster coke deposition, while the chemical nature of the coke deposits, as expressed as the D<sub>1</sub>/G ratio, is independent of catalyst bed height and time-on-stream. In addition, the combustion of the coke deposits could be visualized by the operando

spectroscopic probes, and it took place as a reacting front, travelling down the length of the catalyst bed.

## 6.5 Acknowledgements

Maria Arias, Tom Visser and Ad Mens (Utrecht University) are acknowledged for their work in the design and construction of, and adaptations to the pilot scale reactor. Willem Jan Mulder, Albert Borreman and Rene Teunissen (Avantes) are acknowledged for their work in the design and construction of the operando UV-Vis and Raman probes.

## 6.6 References

- (1) Iglesias-Juez, A.; Beale, A. M.; Maaijen, K.; Weng, T. C.; Glatzel, P.; Weckhuysen, B. M. *J. Catal.* **2010**, *276*, 268.
- (2) Wu, Z.; Stair, P. *J. Catal.* **2006**, *237*, 220.
- (3) Airaksinen, S. M. K.; Banares, M. A.; Krause, A. O. I. *J. Catal.* **2005**, *230*, 507.
- (4) Li, Q.; Sui, Z.; Zhou, X.; Zhu, Y.; Zhou, J.; Chen, D. *Top. Catal.* **2011**, *54*, 888.
- (5) Kuba, S.; Knoezinger, H. *J. Raman Spectrosc.* **2002**, *33*, 325.
- (6) Tinnemans, S. J.; Kox, M. H. F.; Nijhuis, T. A.; Visser, T.; Weckhuysen, B. M. *Phys. Chem. Chem. Phys.* **2005**, *7*, 211.
- (7) Hof, F.; Bosch, S.; Englert, J. M.; Hauke, F.; Hirsch, A. *Angew. Chem. Int. Ed.* **2012**, *51*, 1.
- (8) Waters, D. N. *Spectrosc. Acta, Part A Mol. Biomol. Spectrosc.* **1994**, *50*, 1833.
- (9) Kubelka, P.; Munk, F. *Z. Tech. Phys. A* **1931**, *11*, 593.
- (10) Bennici, S. M.; Vogelaar, B. M.; Nijhuis, T. A.; Weckhuysen, B. M. *Angew. Chem. Int. Ed.* **2007**, *46*, 5412.
- (11) Sattler, J. J. H. B.; González-Jiménez, I. D.; Mens, A. M.; Arias, M.; Visser, T.; Weckhuysen, B. M. *Chem. Commun.* **2013**, *49*, 1518.

- (12) Zhang, J. Miniature spectrometers working with cellular phones and other portable electronic devices. US Patent 5122127, 2009.
- (13) Sadezky, A.; Muckenhuber, H.; Grothe, H.; Niessner, R.; Poschl, U. *Carbon*, **2005**, *43*, 1731.



## Chapter 7

# Summary, Concluding Remarks and Future Prospects

In this Chapter, a summary of the PhD work will be given. Furthermore, a more distant view on the results obtained leads to new insights into the differences in propane dehydrogenation performance and coke formation of metal and metal oxide catalysts. In the future prospects part, the commercial potential of the highly active stable and selective Pt-Ga propane dehydrogenation system developed, and of the operando spectroscopic probes for on-line analysis of coke deposition will be discussed. Finally, new avenues for studying these catalyst systems will be proposed.

## 7.1 Summary

In this PhD thesis, we have studied the catalytic performance and deactivation of different metal and metal oxide catalysts for the selective dehydrogenation of propane. With the current market situation, the catalytic dehydrogenation of propane is becoming of increasing importance for the petrochemical industry to meet the worldwide demand of propylene.

In **Chapter 1**, a critical assessment is made of the three main systems for the dehydrogenation of propane that have been reported in literature, namely supported  $\text{GaO}_x$ ,  $\text{CrO}_x$  and Pt-Sn catalysts. By comparing the typical values for the initial yield versus the deactivation rate and space velocity, it was concluded that Pt-Sn provides the most active and stable catalyst. The mechanism of coke deposition on these catalysts is also discussed in this Chapter, and the deep dehydrogenation and polymerization of strongly adsorbed reaction intermediates is believed to be of key importance in this process.

As we have shown in **Chapter 2**, the chemical nature and amount of the coke deposits formed on Pt and Pt-Sn/ $\text{Al}_2\text{O}_3$  catalyst materials is strongly dependent on the partial pressures of propane, propylene and hydrogen in the feed. By operando Raman spectroscopy, trends in the position, width and intensity of the Raman bands were observed. These trends indicated that the increase in hydrogen partial pressure resulted in the formation of less coke, which had a more graphitic nature. At the same time, the addition of hydrogen increases the activity and stability of the catalyst material. The positive effect of hydrogen is attributed to the competitive adsorption of hydrogen on the surface of the Pt catalyst, lowering the concentration of adsorbed hydrocarbon species and therefore decreasing the likelihood that these species polymerize into coke.

In addition to the feed composition, the type of metal used for the dehydrogenation catalyst has a profound influence on the chemical nature of the coke species formed. This is discussed in **Chapter 3**, where scanning transmission X-ray microscopy (STXM), thermogravimetric analysis (TGA) and Raman spectroscopy are used to study the coke deposits formed not only on the Pt and Pt-Sn/ $\text{Al}_2\text{O}_3$ , but also on Pt-Ga and Ga/ $\text{Al}_2\text{O}_3$  propane dehydrogenation catalysts. Relatively more coke is formed on

the latter two materials, as revealed by TGA, which additionally has a more graphitic nature, as was revealed by STXM and Raman spectroscopy. As STXM is a microscopy technique, it allows for the investigation of individual catalyst particles. Although coke was uniformly distributed on the catalyst particle, and no differences in the chemical nature of coke deposits could be observed, the XANES spectra of coke formed on the outside of the catalyst material was clearly different from coke formed in the interior of the catalyst particle. This highlights that next to bulk characterization techniques, single catalyst particle analysis is also necessary to gain a full understanding of the physicochemical processes taking place.

In **Chapter 4**, a novel catalyst system for the dehydrogenation of propane, based on 1000 ppm Pt and 1.5-3 wt% of GaO<sub>x</sub> on an alumina support, is discussed. The combination of these two metals results in a highly active, selective and stable formulation for the catalytic dehydrogenation of propane, which can rival commercially applied systems, such as CrO<sub>x</sub>/Al<sub>2</sub>O<sub>3</sub> and Pt-Sn/Al<sub>2</sub>O<sub>3</sub>. A clear synergistic effect is observed between both metals, and a combination of structural, morphological and surface characterization techniques was utilized to understand this synergy. Lewis acid Ga<sup>3+</sup> species were believed to be the active sites responsible for C-H bond activation, mainly because CO chemisorption revealed that there was no correlation between Pt dispersion and catalyst activity, and that a catalyst containing solely Pt was inactive. Pt is believed to have a promoting function, possibly assisting in the rate limiting step of propane dehydrogenation on GaO<sub>x</sub> catalysts, which is the recombination of hydrogen adatoms.

In the Chapters discussed above, operando Raman and UV-Vis spectroscopy was used to study the formation of coke deposits on propane dehydrogenation catalysts. By this method, information on the rate of coke deposition and the type of coke formed can be obtained during continuous cycling operations. Furthermore, as was discussed before in the work of Tinnemans, Nijhuis and Bennici,<sup>1-3</sup> quantitative analysis of coke deposition is possible by using the absorption measured by UV-Vis spectroscopy to correct for the effect of self-absorption of the Raman signal by the catalyst material. In an industrial dehydrogenation reactor, such an approach is highly desirable, as careful control of the coke deposition is required to prevent irreversible catalyst deactivation during the regeneration step. For this reason, **Chapter 5** describes the design, construction and testing of a pilot scale reactor in which specially designed UV-Vis probes could be inserted at different heights, relative to the catalyst bed. The

UV-Vis probes are designed and constructed to be able to withstand the harsh conditions of the propane dehydrogenation reaction. The reactor was filled with 0.5 kg of commercial  $\text{CrO}_x/\text{Al}_2\text{O}_3$  extrudates, and by measuring the darkening of these extrudates at different heights of the catalyst bed, it was observed that coke deposition was more rapid at the top of the reactor, compared to the bottom. Combustion of the formed coke deposits takes place as a front, which travels down the length of the reactor. The next step was to design, construct and test an operando Raman probe, which is described in **Chapter 6**. Here, by combining the operando spectroscopic data obtained by operando UV-Vis and Raman spectroscopy, the formation of coke deposits could be followed quantitatively in time. Differences in the rate of coke deposition were again observed, and were attributed to fluctuations in temperature of the catalyst bed. The process of coke deposition was faster when the temperature of the catalyst bed was higher.

## 7.2 Concluding Remarks

In this PhD Thesis, the dehydrogenation of propane on Pt,  $\text{GaO}_x$  and  $\text{CrO}_x$  catalysts was investigated, with the deactivation by coke deposition on these materials being of special interest. In **Chapter 1**, the mechanisms behind these processes are discussed, based on findings reported in literature. By combining the experimental results described in this PhD with these general literature trends, the coking process on metal and metal oxide-based dehydrogenation catalysts can be compared.

Secondly, in **Chapter 4** we have reported a new catalytic system based on a Pt-promoted  $\text{Ga}/\text{Al}_2\text{O}_3$  catalyst, whose performance could rival commercial dehydrogenation catalysts. Therefore, we will discuss the opportunities to apply this catalyst system commercially. Finally, novel approaches on the characterization of coke deposits formed on propane dehydrogenation catalysts are reported. Scanning Transmission X-ray microscopy proved to be an excellent technique to study the chemical nature of individual catalyst particles. In addition, the design, construction and testing of operando UV-Vis and Raman probes, and using these to quantitatively follow the deposition of coke species on  $\text{CrO}_x/\text{Al}_2\text{O}_3$  extrudates, clearly proves that such spectroscopic techniques may be applied in an industrial setting.

### 7.2.1 Coke Deposition on Metals and Metal Oxides

In **Chapter 1**, the proposed reaction mechanisms including potential energy plots are shown for Pt-, CrO<sub>x</sub>- and GaO<sub>x</sub>-based dehydrogenation catalysts (Figure 1.22 – 1.24 and Scheme 1.2 – 1.4). Although the energy barriers reported in these Figures can explain the differences in the specific activity reported in literature very well, the results are based on DFT calculations on either very small clusters (CrO<sub>x</sub>), or ideal crystal planes (GaO<sub>x</sub> and Pt), which do not closely resemble actual dehydrogenation catalysts.<sup>4-7</sup> In addition, the model and methods used to calculate the reaction intermediates are different for each metal. In case of the CrO<sub>x</sub> catalyst systems, a larger cluster where the interaction with more neighboring Cr or support atoms is taken into account, should be used. In the case of supported GaO<sub>x</sub> dehydrogenation catalysts, the presence of highly ordered GaO<sub>x</sub> crystal planes are highly unlikely. As was shown in **Chapter 4**, a mixed Ga-Al oxide support is formed instead, so performing calculations on clusters that resemble this ternary oxide are more realistic. Although the trends reported in the literature support the conclusions of **Chapter 1**, an elaborate study, where the same method is used to study the dehydrogenation of propane on more realistic models of each of these catalyst materials, is highly desirable.

In the experimental data presented in this PhD thesis, several trends are observed which affect the process of coke deposition on propane dehydrogenation catalysts. First of all, in **Chapter 2** we have clearly shown that the composition of the feed has a profound influence on the chemical nature of the coke deposits formed on Pt and Pt-Sn/Al<sub>2</sub>O<sub>3</sub>. With the addition of H<sub>2</sub>, the catalysts performance would increase and a lower amount of coke which had a more graphitic nature was formed on the catalyst. These trends were explained by the competitive adsorption of hydrogen on the active sites of the catalyst material, which would make the polymerization of adsorbed hydrocarbons less likely, hampering the rapid formation of coke deposits. On the contrary, increasing the partial pressure of propylene significantly increased the amount of coke deposited.

In **Chapter 5 and 6**, while studying CrO<sub>x</sub>/Al<sub>2</sub>O<sub>3</sub> extrudates in a pilot scale reactor, it was observed that the actual dehydrogenation reaction takes place, at least initially, at the top of the catalyst bed of the pilot-scale reactor. After all, a drop in temperature due to the endothermic nature of the dehydrogenation reaction is clearly observed

during the first minutes of the reaction at this location of the reactor bed, which is not observed for the middle and bottom of the catalyst bed. This implies that the composition of the gas flow is distinctly different at the top of the catalyst bed (100% propane) from the bottom of the bed (mixture of hydrogen, propane, propylene and cracking products). Nevertheless, as was observed with operando Raman spectroscopy, the coke species formed at the top are very similar to those formed at the bottom of the reactor bed. This suggests that on Pt-based dehydrogenation catalysts, the effects of feed composition are different compared to CrO<sub>x</sub>-based dehydrogenation catalysts. Note however, that a more complete study, similar as described in **Chapter 2**, is required to fully understand the effects of feed composition on the coke deposition on CrO<sub>x</sub> propane dehydrogenation catalysts.

Another instance where differences were observed in the process of coke formation on metals and metal oxide propane dehydrogenation catalysts are reported in **Chapter 3**. Here, Raman spectroscopy, TGA and STXM were used to study the coke formation on Pt, Pt-Sn, Pt-Ga and Ga/Al<sub>2</sub>O<sub>3</sub> propane dehydrogenation catalysts. On the first two catalysts, the coke deposits were somewhat more disordered than coke formed on the latter two materials. Significant amounts of coke were deposited on these catalyst materials (~5 wt% for Pt and Pt-Sn and ~9 wt% on Ga and Pt-Ga). A connection was found between the nature of the coke deposits, as measured by Raman spectroscopy, and the amount of coke formed, determined by TGA. With increasing amounts of coke, the D<sub>1</sub>/G ratio increased and the G band became more narrow, and shifted to higher wavenumbers. These trends indicate the formation smaller, more ordered graphitic crystals, when the total amount of coke is increased.

These trends are in strong contrast with the operando Raman spectra reported in Figure 4.4 on coke species formed on Pt-Ga catalysts and their Ga analogs, since these spectra reveal that coke formed on the Pt-containing catalysts was markedly more graphitic. In addition, very low amounts of coke are deposited on these catalyst materials (0.2-0.5 wt%).

It is not straightforward to rationalize why coke formation is different on Pt-based catalysts on one hand and GaO<sub>x</sub> and CrO<sub>x</sub> propane dehydrogenation catalysts on the other hand. A problematic factor is that the process of coke formation during propane dehydrogenation, as is described in **Chapter 1**, has been researched almost exclusively on Pt surfaces. Therefore, much less information is available on the type of coke precursors and intermediates that are formed on metal oxides. This means we

are limited to educated guesses why the process of coke deposition is different on these materials.

First we have to consider that the active sites of Pt- are distinctly different from CrO<sub>x</sub>-based propane dehydrogenation catalysts. Propane can be dehydrogenated by any surface Pt atom, and the adsorbed hydrocarbon species can migrate over the surface of the nanoparticle. Hydrogen can also adsorb, dissociate and migrate over the Pt surface. As was shown in Scheme 1.4, the adsorbed propane and propylene can be further dehydrogenated, forming strongly adsorbed species which can merge into larger hydrocarbons and eventually coke. Many of the intermediates shown in Scheme 1.4 have multiple interactions with the catalyst, which will likely require several Pt atoms. These larger hydrocarbons continue to be dehydrogenated when in proximity of a Pt nanoparticle, eventually resulting in the formation of highly graphitic coke species. The exact orientation of the adsorbed hydrocarbon in respect to the Pt surface is not crucial for deep dehydrogenation to occur, since several active sites are directly adjacent to each other.

On the contrary, during the dehydrogenation of propane on metal oxides, the aforementioned mechanisms cannot be used to describe the process of coke formation. The active sites of the metal oxides consists of coordinately unsaturated Lewis acid sites, where also the neighboring oxygen atoms play an important role in the dehydrogenation mechanism. It is reasonable to assume that instead of being clustered into nanoparticles like the Pt-based dehydrogenation catalysts, the active sites are spread homogeneously over the catalyst surface. Since the active sites are not in direct proximity of each other, and the fact that the migration of the adsorbed hydrocarbons over the surface of the metal oxide catalyst likely more problematic compared to migration over a Pt surface, the formation of coke precursors by the merger of adsorbed hydrocarbon species is relatively more difficult on metal oxide catalysts compared to the Pt nanoparticles. Furthermore, it is difficult to envision how the adsorbed propane species form multiple bonds with these Lewis acid sites required for deep dehydrogenation to occur. Finally, when larger hydrocarbons are formed, it is more unlikely for these molecules to orient in a way where the relatively isolated Lewis acid sites can dehydrogenate the molecule further. This means, that the process of coke deposition will likely follow a different mechanism on the metal oxide catalysts, compared to Pt-based materials.

As was observed by operando Raman spectroscopy in Chapter 4, coke formed on Pt-Ga had a more graphitic nature compared to their Ga analogs. This can be explained by the fact that further dehydrogenation of larger hydrocarbon molecules is more facile on Pt-based catalysts compared to the metal oxide catalysts. The reason why this effect is not observed for the catalyst materials discussed in Chapter 3, is that such large amounts of coke are formed, that the vast majority of the coke will not be present in the proximity of the active species, making the further dehydrogenation of the coke deposits very difficult.

The feed composition, especially the presence of hydrogen, has a more profound influence on the process of coke deposition on the Pt catalysts, compared to the metal oxide catalysts. Hydrogen can competitively adsorb on the Pt nanoparticles, decreasing the surface coverage of the adsorbed propane species. This makes the process where these precursors merge into larger hydrocarbons less likely. The agglomeration of adsorbed propane species to form coke is already less likely on metal oxide catalysts, as the active sites are much more isolated, and the migration of such adsorbed hydrocarbons over the surface of the catalyst is arguably more difficult. Furthermore, considering the high energy barrier for the recombination of hydrogen on the metal oxide catalysts, the competitive of hydrogen on the active sites on these metal oxide catalysts is energetically unfavorable. Hence, hydrogen may merely act as a spectator species during the dehydrogenation reaction over metal oxide catalysts, not affecting the process of coke deposition. A summary of the experimental results on coke deposition, and their interpretation is given in Table 7.1.

#### 7.1.1 Industrial Application of the Pt-Ga Propane Dehydrogenation Catalyst

In **Chapter 4**, a novel catalyst for the dehydrogenation of propane is presented, based on a Ga/Al<sub>2</sub>O<sub>3</sub> material promoted with 1000 ppm of Pt. The material was tested for relative short dehydrogenation cycles of 15 min, during which the material exhibited an excellent and stable performance. After each cycle, the material was regenerated in air at 750 °C, which was necessary for the material to remain highly active. In addition, the minute amounts of coke that have formed during the dehydrogenation step are combusted. In Figure 7.1, the excellent performance of the Pt<sub>3</sub>GaK catalyst is highlighted, when the material is compared with propane dehydrogenation catalysts reported in the open literature.

**Table 7.1.** Summary of the trends in coke deposition obtained by experiments reported in this PhD thesis. Effects of the feed, the type of catalyst and the amount of coke formed are explained. For this comparison only the experimental data from Chapters 2-4 have been used, as the same reactor was used and the reaction condition were similar.

	Chapter 2 Effect feed	Chapter 4 Effect catalyst material	Chapter 3 Effect amount of coke
Observation	<p>1 - In the presence of hydrogen, less coke is deposited, the <math>D_1/G</math> ratio is increased and Raman bands become more narrow and change position.</p> <p>2 - Increased partial pressures of propylene result in more coke being deposited.</p> <p>3 - The addition of steam results in less coke being formed, which has a lower <math>D_1/G</math> ratio.</p>	<p>Coke formed on Pt-Ga catalysts was found to be more graphitic in nature compared to coke formed on catalysts that contain only Ga. In these cases, relatively low amounts of coke were formed (&lt; 1 wt%).</p>	<p>It is observed that the <math>D_1/G</math> ratio increases, the G band shifts to higher wavenumbers and becomes more narrow as more coke is formed on the catalyst material.</p>
Explanation	<p>1 - Smaller, more ordered graphite crystallites are formed.</p> <p>2 - Propylene is more reactive than propane, and readily polymerizes to form coke.</p> <p>3 - Steam inhibits the formation of coke.</p>	<p>Deep dehydrogenation of coke deposits is more likely on Pt-based catalysts, which is highlighted by the higher graphicity of the coke, compared to their Ga-based dehydrogenation catalysts.</p>	<p>As excessive amounts of coke are formed, the effect of the catalyst becomes less as most of the coke is not in proximity of the active phase. More coke therefore, results in the formation of smaller, more ordered graphite crystallites.</p>

Currently, two commercial processes for the dehydrogenation of propane are available, namely Catofin<sup>®</sup> and Oleflex<sup>™</sup> processes, which were discussed in **Chapter 1.2**. In the experiments discussed in **Chapter 4**, a fixed bed reactor was used, just as is the case for the Catofin<sup>®</sup> process. The Catofin<sup>®</sup> process uses a series of parallel fixed bed reactors, in which alternatively short dehydrogenation and regeneration steps are performed. The heat required to run the dehydrogenation reaction is provided by the combustion of coke deposits formed on the CrO<sub>x</sub>/Al<sub>2</sub>O<sub>3</sub> catalyst. Since so little coke is formed on the Pt-Ga catalyst, the combustion would only provide a fraction of the heat required to run the dehydrogenation reaction, meaning that an alternate source of heat will be required. Secondly, when starting the regeneration, the catalyst bed needs to be heated from 620 to 750 °C and consecutively needs to be cooled again for the next dehydrogenation step. This would take a significant amount of time and energy, making a fixed bed system an unattractive option for the commercial application of this catalyst system.

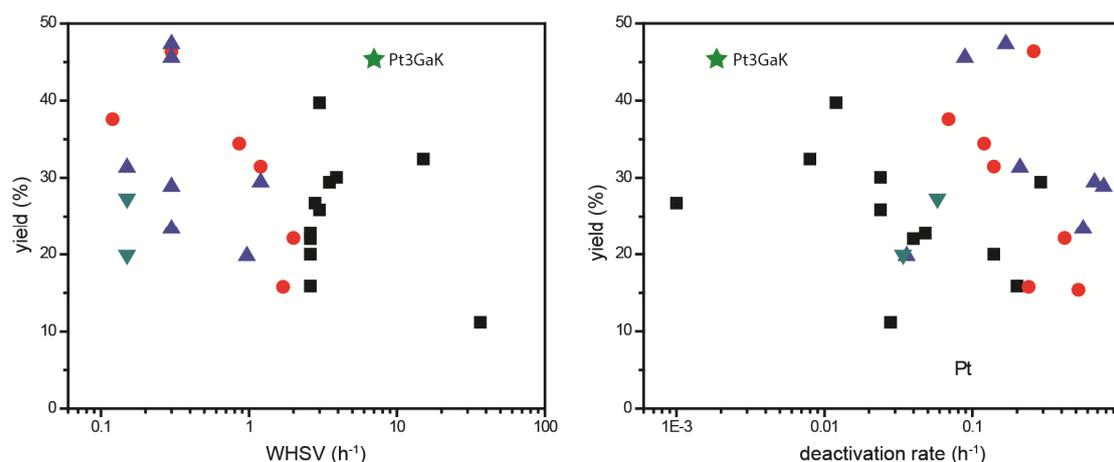


**Figure 7.1.** To the left, the yield of propylene is plotted versus the weight hourly space velocity (WHSV) and to the right the yield is plotted versus the deactivation rate. The graphs are identical to those shown in Figures 1.25 and 1.26, with the addition of the Pt3GaK catalyst. Black squares are used for the Pt-based catalysts and blue triangles for Ga-based catalysts reported in literature.

When comparing the Pt-Ga catalyst with the Pt-Sn/Al<sub>2</sub>O<sub>3</sub> system used for the Oleflex<sup>™</sup> process, some similarities can be observed. The Oleflex<sup>™</sup> process utilizes a series of fluidized bed reactors and a catalyst regeneration unit to perform the

dehydrogenation reaction. The heat required to run the endothermic dehydrogenation process is provided by heating the gas flow, instead of the combustion of the coke deposits. The catalyst material moves through the reactors and regeneration unit, completing a cycle every 5 to 10 days. For the regeneration of the Pt-Sn/Al<sub>2</sub>O<sub>3</sub> catalyst, a chlorine-air mixture is used to redisperse the Pt nanoparticles. The dehydrogenation of propane on the novel Pt-Ga catalyst can be performed on a similar process, with the exception that the cycles need to be significantly shorter. In the 14-day dehydrogenation experiment, shown in Figure 4.2, the high conversion of 46% drops over a 2-day period to ~32%. The reason for this deactivation is not known, but could be related to either the sintering of the Pt, sintering of the alumina support or leaching of the Ga species by to the formation of volatile Ga species. Since it is not known at this time which of these processes are responsible for this deactivation, it is questionable if the Pt-Ga would retain its high initial activity when chlorine is added during the regeneration step. Since the dehydrogenation reaction (620 °C) takes place at a different temperature than the regeneration (750 °C), it is advantageous to have separate sections for both processes which is the case for the fluidized catalyst bed system. For these reasons, an adapted version of the Oleflex™ process seems the most promising option for the commercial application of this novel Pt-Ga propane dehydrogenation system.

#### 7.1.2 Novel methodologies for the study of coke deposits

In **Chapter 3**, the coke deposits formed on Pt, Pt-Sn, Ga and Pt-Ga catalysts are investigated by scanning transmission X-ray microscopy (STXM). To the best of our knowledge, this was the first time this technique was used to study deactivated propane dehydrogenation catalysts. By this method, valuable insights on the process of coke deposition on individual catalyst particles is obtained. This analysis can be taken a step further, for example by investigating the X-ray absorption edges of the metals present on the catalyst. Some limitations apply however, as the technique requires a significant amount of the element under study in order to obtain X-ray absorption spectra of a good quality. STXM has also been used to study catalyst systems at reaction conditions. As an example, in-situ STXM was used to study phase changes of a Fe-based Fischer-Tropsch catalyst at reaction conditions, while the formation of coke species could also be followed over time.<sup>8</sup> Clearly, it would be very interesting to study the deposition of coke on propane dehydrogenation catalysts at

reaction conditions. However, since the dehydrogenation of propane takes place at considerably different reaction conditions, the reactor cells used by de Smit et al. will need to be adjusted. Summarizing, gaining in-situ chemical information on individual catalyst particles during the dehydrogenation of propane would provide valuable insights on the process of coke deposition on these type of materials.

The use of operando spectroscopy in a pilot-scale reactor was highlighted in **Chapter 5 and 6**. By combining operando UV-Vis and Raman spectroscopy, the amount of coke can be determined quantitatively during the dehydrogenation of propane. An expert reactor control system can use the spectral information obtained by both operando probes to automatically regulate the regeneration of the catalyst bed. However, the operando spectroscopic probes will need to be improved further before they can be used in a real industrial dehydrogenation reactor. First of all, separate UV-Vis and Raman probes are needed in order to acquire quantitative information on the coke deposition. This is not ideal, as each separate probe may collect information from a slightly different section of the catalyst bed. As will be discussed in further in this Chapter, both spectroscopic techniques can potentially be combined a single probe, averting that issue.

As described in **Chapter 6**, using the current method of using a lens to focus a bundle of laser light on a single catalyst extrudate, is not the perfect way to collect Raman spectra. Movement of the extrudate may result in a loss of focus, making the collection of spectral data impossible. Another method however, would be to use a parallel beam instead of a focused beam to illuminate the sample, which is basically measuring the sample without focusing the laser beam. In this way a significant part of the laser light is wasted as it does not hit the sample, which means much less Raman photons are generated. This downside can be overcome by using a much stronger laser source. Although this method would prove more costly, it probes a larger area of the catalyst bed and therefore does not just rely on a single, fixated extrudate.

It is also important to consider the shortcomings of this procedure of combining Raman and UV-Vis spectroscopy. This approach, first reported by Kuba and Knözinger, is based on the Kubelka-Munk theory to which some limitations apply.<sup>9</sup> At high values for absorption, the assumption that the scattering coefficient  $s$  is independent of the absorption coefficient ( $R_\infty$ ) breaks down. This implies that this approach would work better on (yellow, white) Pt-Sn or GaO<sub>x</sub> catalyst compared to

(green)  $\text{CrO}_x$  catalysts. Furthermore, as was shown in Chapter 6, this approach loses validity when the catalyst turns very dark due to very high amounts of coke.

## 7.2 Outlook

Several promising avenues have not been investigated during this PhD research, but deserve to be mentioned. First of all, in **Chapter 4** a synergy effect was observed between highly dispersed Pt and Lewis acid  $\text{GaO}_x$  species, resulting in a highly active propane dehydrogenation catalyst. The results reported in the Chapter imply that Lewis acid  $\text{Ga}^{3+}$  species were providing the dehydrogenation activity of the catalyst, while Pt acted as a promoter. We hypothesized, that the role of the Pt was to assist with the recombination of the hydrogen adatoms, since theoretical calculations show this is the rate limiting step of propane dehydrogenation on  $\text{GaO}_x$ -based dehydrogenation catalysts. It would be very interesting to perform additional quantum-chemical calculations on this system to investigate whether the recombination of hydrogen is really energetically more favorable on Pt. Furthermore, the hydrogen adatoms will need to diffuse from the  $\text{Ga}^{3+}$  active sites to the Pt atoms for this recombination to occur, and it would be worthwhile to investigate how facile this diffusion is. In a similar fashion, the diffusion of adsorbed hydrocarbons on metal oxide-based propane dehydrogenation catalysts can be investigated.

Secondly, as was mentioned before, it would be desirable to integrate operando UV-Vis and Raman spectroscopy in a single probe. This can be done in multiple ways. First of all, the optics of both techniques can be placed next to each other in a single probe. The Raman and UV-Vis spectra should be collected alternately, since otherwise the scattered Raman light would interfere with the collection of the UV-Vis spectra. Since the collection of a UV-Vis spectrum only takes a few seconds this is not problematic.

A second method would be to use a probe in which the optics are made as such that you can alternate between both techniques. For example, as was described previously, a parallel beam of laser light is used to generate Raman scattered photons. By adding a switch and a system of mirrors inside the probe, one could alternate between the Raman and UV-Vis light source to illuminate the catalyst sample, while the

backscattered light would alternately be collected by a Raman and UV-Vis spectroscope.

A third option would be to use the Raleigh scattered light to correct the operando Raman spectra for the effect of darkening. By adjusting the long-pass filter to allow a fixed amount of Raleigh light to pass through, the decrease in intensity of this signal can be used instead of the UV-Vis spectra for correcting the Raman spectra. A downside of using this method however is that the absorption of light is not uniform over the entire Raman spectra, which means an error is made when using the Raleigh scattered light is used for the quantification of coke deposition.

Finally, the Raman probe discussed in **Chapter 6** can only measure coke deposits formed on the outer microns of the  $\text{CrO}_x/\text{Al}_2\text{O}_3$  extrudates. As was shown in **Chapter 3** by STXM analysis, even in micron-sized catalyst bodies, coke deposits on the exterior and interior of the catalyst particles were different. Therefore, it is important to investigate how homogeneously coke is deposited on these  $\text{CrO}_x/\text{Al}_2\text{O}_3$  extrudates, specifically in the interior of these particles. Surface offset Raman spectroscopy (SORS) is a technique, where Raman spectroscopic data can be collected from the bulk of the material in addition to the surface.<sup>10-12</sup> Two Raman spectra are collected simultaneously with this technique; one of the surface where the incident light hits the sample and one at an offset position which is located a few millimeters away. The incident light scatters throughout the interior of the sample, before it is collected at the offset position. Some of this light collected by the second probe will be scattered inelastically during this process and therefore will contain chemical information of the bulk. By continuously collecting spectra, while adjusting the relative position of the sample and the offset where these spectra are collected, a 3-dimensional map consisting of Raman spectra can be obtained by performing a PCA analysis. This method has been used to study catalyst extrudates, for example the spatial distribution of molybdenum oxide species in an alumina extrudate.<sup>13</sup> Such an approach could also be used to study the chemical nature and distribution of coke deposits in  $\text{CrO}_x/\text{Al}_2\text{O}_3$  extrudates.

### 7.3 Nederlandse Samenvatting

Olefines, zoals ethyleen en propyleen, zijn de meest gebruikte platform moleculen in de petrochemische industrie. De belangrijkste manier om deze moleculen te produceren, is via het kraken van olie en nafta, maar door de steeds stijgende vraag naar olefines gecombineerd met de hoge olie prijzen, heeft ertoe geleid dat de petrochemische industrie naar alternatieve bronnen zoekt, zoals schaliegas en biomassa, om deze olefines te produceren. In schaliegas bronnen zit niet alleen methaan, maar ook ethaan en propaan, welke via de dehydrogenatie reactie omgezet kunnen worden naar olefines. Voor de omzetting van propaan naar propyleen bijvoorbeeld, zijn hoge temperaturen (600 °C) en een katalysator nodig.

Een katalysator is een materiaal die een chemische reactie versnelt, zonder zelf verbruikt te worden. In het geval van propaan dehydrogenatie, biedt de katalysator een oppervlak waar de propaan moleculen op kunnen adsorberen. De vorming van bepaalde reactie intermediaren die nodig zijn om propyleen te vormen (zoals degene getoond in Schema 1.2 en 1.3), wordt zo gefaciliteerd. Verschillende metalen vertonen katalytische activiteit voor dehydrogenatie, waarvan platinum, chroom-oxide en gallium-oxide de belangrijkste zijn. Om een katalysator zo efficiënt mogelijk te maken, moet deze een zo'n groot mogelijk oppervlak hebben. Door het actieve metaal als nanodeeltjes af te zetten op een drager materiaal, wordt dit doel bereikt.

In Hoofdstuk 1 worden de drie belangrijkste katalysatoren voor de dehydrogenatie van propaan, namelijk Pt, CrO<sub>x</sub> en GaO<sub>x</sub>, vergeleken op basis van wat gepubliceerd is in de literatuur. Specifiek wordt de initiale opbrengst en de snelheid van de deactivatie vergeleken ten opzichte van de zgn. space velocity (wat een maat is voor de hoeveelheid reactant ten opzichte van de hoeveelheid katalysator is). Hieruit blijkt dat de platinum katalysatoren een stuk actiever en stabiel zijn dan de gallium en chroom oxide katalysatoren. Verder wordt het dehydrogenatie reactie mechanisme en deactivatie van deze materialen besproken.

De deactivatie kan plaats vinden op verschillende manieren. Ten eerste kunnen de katalytische nanodeeltjes onstabiel zijn tijdens de reactie, waardoor ze samenklonteren (zgn. sinteren). Hierdoor neemt het metaal oppervlak af wat de katalysator minder efficiënt maakt. Een tweede deactivatie mechanisme is de zgn. coke formatie, wat min of meer neerkomt op de polymerisatie van geadsorbeerde

koolstofmoleculen. Op deze manier wordt er grafeen-achtig materiaal gevormd op het oppervlak van de katalysator. Doordat het oppervlak bedekt is, kan de katalysator zijn werk niet meer doen. Hierom wordt de katalysator in de industrie regelmatig behandeld met zuurstof bij hoge temperatuur, om deze koolstof (coke) afzetting weg te branden.

In Hoofdstuk 2 wordt dit proces op een Pt katalysator bestudeerd met in-situ Raman spectroscopie, wat betekent dat er spectroscopische informatie verzameld wordt van de coke deposities tijdens de dehydrogenatie reactie. Hiermee wordt de formatie van de koolstof afzetting gevolgd over tijd, zoals te zien is in Figuren 2.5 en 2.6. Kleine veranderingen in de spectra, zoals de positie de breedte van, en de ratio tussen de pieken, onthullen chemische informatie over de grafeen-achtige species. Als voorbeeld, wanneer waterstofgas wordt toegevoegd tijdens de propaan dehydrogenatie reactie, worden de pieken in het Raman spectrum nauwer en veranderen van positie. Dit betekent dat er kleinere en meer geordende coke deeltjes gevormd worden. Tegelijkertijd neemt de activiteit en de stabiliteit van de katalysator toe. Dit positieve effect van waterstofgas wordt veroorzaakt door de competitieve adsorptie van het waterstof op de katalysator, waardoor de vorming van de coke deeltjes wordt gehinderd.

In Hoofdstuk 3 worden de coke afzettingen op verschillende soorten propaan dehydrogenatie katalysatoren vergeleken door middel van Scanning Transmission X-ray Microscopy (STXM). Dit is een microscopie techniek, waar gebruik gemaakt wordt van Röntgen staling om plaatjes van individuele katalysator deeltjes te maken, waar elke pixel een X-ray absorptie spectrum bevat. Uit deze analyse bleek dat coke uniform gevormd wordt op het oppervlak van de katalysator, maar dat coke buiten het deeltje anders is. Ook bleek dat coke gevormd op gallium dehydrogenatie katalysatoren meer geordend was dan coke gevormd op platinum katalysatoren.

Een nieuwe katalysator voor de dehydrogenatie van propaan, gebaseerd op platinum en galliumoxide afgezet op een aluminum drager wordt besproken in Hoofdstuk 4. Het gedrag van deze katalysator is uniek, vanwege de hoge activiteit, selectiviteit en stabiliteit, welke gelijk is aan industriële dehydrogenatie katalysatoren, terwijl de samenstelling heel anders is. De concentratie van platinum op de katalysator is zeer laag is (0.1 gewichtsprocent), maar toch zijn beide metalen nodig om propaan effectief om te zetten. Het unieke karakter van deze katalysatoren is onderzocht met verschillende technieken, waaruit bleek dat het platinum functioneert als een

promotor, terwijl het gallium oxide de dehydrogenatie verzorgt. Het platinum is (gedeeltelijk) aanwezig als individuele atomen, en is belangrijk om de energetisch meest ongunstige reactiestap op het gallium oxide te versnellen.

Twee belangrijke technieken om de vorming van de coke afzetting te volgen tijdens de dehydrogenatie reactie zijn UV-Vis en Raman spectroscopie. Deze technieken zijn tot dusver alleen in een lab gebruikt om dit proces te bestuderen. Daarbij is het mogelijk om de spectroscopische informatie verzameld met deze twee technieken te combineren, om zo exact te bepalen hoeveel koolstof er is afgezet op de katalysator. Deze methode kan ook toegepast worden in industriële reactoren, om precies te bepalen wanneer de katalysator geregenereerd moeten worden. Om deze reden wordt in Hoofdstuk 5 en 6 het design en de constructie van een zgn. pilot scale reactor besproken, waarin 0.5 kg katalysator past. Verder worden nieuwe UV-Vis en Raman probes getest, die in deze reactor gestoken kunnen worden om de katalysator te bestuderen bij reactie condities. Meerdere probes worden geplaatst in de reactor, waardoor spectroscopische informatie wordt verzameld op verschillende locaties in het katalysator bed. De snelheid waar coke formatie plaatsvindt, bleek afhankelijk van de temperatuur van de katalysator, waar een hogere temperatuur leidt tot snellere coke formatie. Inderdaad bleek het mogelijk om in situ de hoeveelheid koolstof afzetting te kunnen bepalen, wat de industriële potentie van deze benadering aantoonde.

## 7.4 References

- (1) Nijhuis, T. A.; Tinnemans, S. J.; Visser, T.; Weckhuysen, B. M. *Chem. Eng. Sci.* **2004**, *59*, 5487.
- (2) Tinnemans, S. J.; Kox, M. H. F.; Nijhuis, T. A.; Visser, T.; Weckhuysen, B. M. *Phys. Chem. Chem. Phys.* **2005**, *7*, 211.
- (3) Bennici, S. M.; Vogelaar, B. M.; Nijhuis, T. A.; Weckhuysen, B. M. *Angew. Chem. Int. Ed.* **2007**, *46*, 5412.
- (4) Lillehaug, S.; Børve, K. J.; Sierka, M.; Sauer, J. *J. Phys. Org. Chem.* **2004**, *17*, 990.
- (5) Lillehaug, S.; Jensen, V. R.; Børve, K. J. *J. Phys. Org. Chem.* **2006**, *19*, 25.
- (6) Yang, M.; Zhu, Y.; Zhou, X.; Sui, Z.; Chen, D. *ACS Catal.* **2012**, *2*, 1247.
- (7) Liu, Y.; Li, Z. H.; Lu, J.; Fan, K. *J. Phys. Chem. C* **2008**, *112*, 20382.

- (8) De Smit, E.; Swart, I.; Creemer, J. F.; Hoveling, G. H.; Gilles, M. K.; Tyliczak, T.; Kooyman, P. J.; Zandbergen, H. W.; Moring, C.; Weckhuysen, B. M.; de Groot, F. M. F. *Nature* **2008**, *456*, 222.
- (9) Kuba, S.; Knoezinger, H. *J. Raman Spectrosc.* **2002**, *33*, 325.
- (10) Matousek, P.; Clark, I. P.; Draper, E. R. C.; Morris, M. D.; Goodship, A. E.; Everall, N.; Towrie, M.; Finney, W. F.; Parker, A. W. *Appl. Spectrosc.* **2005**, *59*, 393.
- (11) Matousek, P.; Morris, M. D.; Everall, N.; Clark, I. P.; Towrie, M.; Draper, E.; Goodship, A. E.; Parker, A. W. *Appl. Spectrosc.* **2006**, *59*, 1485.
- (12) Schulmerich, M. V.; Dooley, K. A.; Vanasse, T. M.; Goldstein, S. A.; Morris, M. D. *Appl. Spectrosc.* **2007**, *61*, 671.
- (13) Zandbergen, M. W.; Jacques, S. D. M.; Weckhuysen, B. M.; Beale, A. M. *Angew. Chem. Int. Ed.* **2012**, *51*, 957.

## **Appendices**



**Table S1.1.** Summary of the catalytic data of the Pt-based dehydrogenation catalysts reported in literature. Values of conversion and selectivity of the end and start of each catalytic run are shown. From the articles considered, only the best performing catalyst is included.

Catalyst	Reaction temperature (°C)	Space velocity (h <sup>-1</sup> )	Feed composition	Conversion (%) <sup>a</sup>	Selectivity (%) <sup>a</sup>	Specific activity (s <sup>-1</sup> ) <sup>b</sup>	k <sub>d</sub> (h <sup>-1</sup> )	Catalyst life <sup>c</sup> (h)	Reference
1) 0.1 wt% Pt-Na-[Fe] / ZSM-5	520	WHSV = 15.1; WHSV = 18.1	C <sub>3</sub> H <sub>8</sub> = 25, He = 75; iC <sub>4</sub> = 33, H <sub>2</sub> = 7, He = 60	33-13 20-10	98.3-99.8 96.5-98.6	1.51; 1.08	0.0080; 0.0041	166	<sup>1</sup>
2) 2 wt% Pt – 1wt% Sn / CeO <sub>2</sub> / C	520	WHSV = 24.8	iC <sub>4</sub> = 33, H <sub>2</sub> = 7, He = 60	37-20	90-100	1.27*10 <sup>-1</sup>	0.0051	140	<sup>2</sup>
3) 0.35 wt% Pt – 1.26 wt% Sn / Al <sub>2</sub> O <sub>3</sub>	519	WHSV = 3.5	C <sub>3</sub> H <sub>8</sub> = 30 kPa, N <sub>2</sub> = 70	31-20	95-98	1.09*10 <sup>-1</sup>	0.29	5	<sup>3</sup>
4) 0.5 wt% Pt – 0.6 wt% Sn / MgAl <sub>2</sub> O <sub>4</sub>	550	WHSV = 36.6	C <sub>3</sub> H <sub>8</sub> = 50, H <sub>2</sub> = 50	12-11	92-95	4.97*10 <sup>-1</sup>	0.028	3.5	<sup>4</sup>
5) 0.6 wt% Pt – 5 wt% Ga / MgAl <sub>2</sub> O <sub>4</sub>	605	WHSV = 3.9	C <sub>3</sub> H <sub>8</sub> = 73; H <sub>2</sub> = 27	31-30	97-98	1.76*10 <sup>-1</sup>	0.024	2	<sup>5</sup>
6) 0.5 wt% Pt / Zn / Silicalite	555	WHSV = 2.8	C <sub>3</sub> H <sub>8</sub> = 95; C <sub>2</sub> H <sub>6</sub> = 4.5, iC <sub>4</sub> H <sub>8</sub> = 0.5	27-25	99-100	1.75*10 <sup>-1</sup>	0.0010	100	<sup>6</sup>
7) 0.58 wt% Pt-Sn / K-L	600	WHSV = 13.2	iC <sub>4</sub> = 33, H <sub>2</sub> = 67	61-46	92-99.8	3.94*10 <sup>-1</sup>	0.0048	126	<sup>7</sup>

8) 1.0 wt% Pt-Sn / SiO <sub>2</sub>	500	WHSV = 248	iC <sub>4</sub> = 50, H <sub>2</sub> = 50	19-15	95-96	2.090	0.14	2	8
9) 0.5 wt% Pt / Zn-Beta	555	WHSV = 2.6	C <sub>3</sub> H <sub>8</sub> = 100	40-29	55-90	1.41*10 <sup>-1</sup>	0.04	12	9
10) 0.5 wt% Pt-Na / Sn-ZSM-5	590	WHSV = 3	C <sub>3</sub> H <sub>8</sub> = 75, H <sub>2</sub> = 25	41.7-39.1	95.3-98	2.20*10 <sup>-1</sup>	0.012	9	10
11) 0.5 wt% Pt-Zn / Na-Y	555	WHSV = 2.6	C <sub>3</sub> H <sub>8</sub> = 100	24.8-15.7	91.6-90.6	1.45*10 <sup>-1</sup>	0.048	12	9
12) 0.5 wt% Pt-Sn-Na / Al-SBA-15	590	WHSV = 3.0	C <sub>3</sub> H <sub>8</sub> = 75, H <sub>2</sub> = 25	27.5-12.6	~ 94	1.43*10 <sup>-1</sup>	0.024	40	11
13) 0.9 wt% Pt / Mg(Ga)(Al)O	600	WHSV = 2.6	C <sub>3</sub> H <sub>8</sub> = 20, H <sub>2</sub> = 25, He = 55	16-11.4	99.2	1.13*10 <sup>-2</sup>	0.20	2	12
14) 0.7 wt% Pt / Mg(In)(Al)O	600	WHSV = 2.6	C <sub>3</sub> H <sub>8</sub> = 20, H <sub>2</sub> = 25, He = 55	20.4-16.3	98	1.83*10 <sup>-2</sup>	0.14	2	13

a: First value is obtained at the start of the cycle, second at the end.

b: Specific activity is defined as  $\frac{\text{mol olefin formed}}{\text{mol Pt} \cdot \text{t(s)}}$ .

c: Catalyst life = total time single cycle/experiment

## References

- (1) Waku, T.; Biscardi, J. A.; Iglesia, E. *Chem. Commun.* **2003**, 9, 1764.
- (2) Serrano-Ruiz, J. C.; Sepúlveda-Escribano, A.; Rodríguez-Reinoso, F. *J. Catal.* **2007**, 246, 158.
- (3) Barias, O. A.; Holmen, A.; Blekkan, E. A. *J. Catal.* **1996**, 158, 1.

- (4) Salmones, J.; Wang, J.-A.; Galicia, J. A.; Aguilar-Rios, G. *J. Mol. Catal. A-Chem.* **2002**, *184*, 203.
- (5) Zhou, Y.; Davis, M. D. U.S. Patent 5214227. 5214227, 1993.
- (6) Barri, S. A. I.; Tahir, R. U.S. Patent 5126502. 5126502, 1992.
- (7) Cortright, R. D.; Hill, J. M.; Dumesic, J. A. *Catal. Today* **2000**, *55*, 213.
- (8) Stagg, S. M.; Querini, C. A.; Alvarez, W. E.; Resasco, D. E. *J. Catal.* **1997**, *168*, 75.
- (9) De Cola, P. L.; Gläser, R.; Weitkamp, J. *Appl. Catal. A-Gen.* **2006**, *306*, 85.
- (10) Zhang, Y.; Zhou, Y.; Huang, L.; Xue, M.; Zhang, S. *Ind. Eng. Chem. Res.* **2011**, *50*, 7896.
- (11) Duan, Y.; Zhou, Y.; Zhang, Y.; Sheng, X.; Xue, M. *Catal. Lett.* **2011**, *141*, 120.
- (12) Siddiqi, G.; Sun, P.; Galvita, V.; Bell, A. T. *J. Catal.* **2010**, *274*, 200.
- (13) Sun, P.; Siddiqi, G.; Vining, W. C.; Chi, M.; Bell, A. T. *J. Catal.* **2011**, *282*, 165.

**Table S1.2.** Summary of the catalytic data of the CrO<sub>x</sub>-based dehydrogenation catalysts reported in literature. Values of conversion and selectivity of the end and start of each catalytic run are shown. From the articles considered, only the best performing catalyst is included.

Catalyst	Reaction temperature (°C)	Space velocity (h <sup>-1</sup> )	Feed composition	Conversion (%) <sup>a</sup>	Selectivity (%) <sup>a</sup>	Specific activity (s <sup>-1</sup> ) <sup>b</sup>	k <sub>d</sub> (h <sup>-1</sup> )	Catalyst life <sup>c</sup> (h)	Reference
1) Mesoporous 9wt% CrO <sub>x</sub> / Al <sub>2</sub> O <sub>3</sub>	580	(-)	C <sub>3</sub> H <sub>8</sub> = 5, He = 95	15.7-10.0	98	(-)	0.52	1	<sup>1</sup>
2) Mixed oxide 40% Cr <sub>2</sub> O <sub>3</sub> / 60% Al <sub>2</sub> O <sub>3</sub>	588+/-2	WHSV = 3.3	iC <sub>4</sub> H <sub>10</sub> = 100	~23-14	99.4	6.87*10 <sup>-4</sup>	0.48	1.25	<sup>2</sup>
3) 73 wt% Cr <sub>2</sub> O <sub>3</sub> -pillared α-ZrP	550	WHSV = 1.7	C <sub>3</sub> H <sub>8</sub> = 7, He = 93	18.1-6.3	87.1	1.23*10 <sup>-5</sup>	0.24	5	<sup>3</sup>

4) Ga-Cr mixed oxide on $\alpha$ -ZrP (20.1 wt% Cr, 9.3 wt% Ga)	550	WHSV = 2	$C_3H_8 = 7$ , He = 93	27.6-4.4	80	$5.05 \cdot 10^{-5}$	0.42	5	4
5) 14-16 wt% $CrO_x / Al_2O_3$	540	WHSV = 46.6	$iC_4H_{10} = 10$ , $N_2 = 90$	16 (start 1 <sup>st</sup> cycle) 8 (30 <sup>th</sup> cycle)	98 +/- 1	$1.21 \cdot 10^{-3}$	0.026	30	5
6) 5 wt% $CrO_x / SBA-1$	550	WHSV = 1.2	$C_3H_8 = 6.67$ , $CO_2 = 33.3$ , He = 60	37-26	85-92	$1.66 \cdot 10^{-4}$	0.14	3.75	6
7) 4 wt% $CrO_x / ZrO_2$	550	WHSV = 0.3	$C_3H_8 = 2.5$ , $N_2 = 97.5$	60.9-24.3	76.2-87.0	$2.86 \cdot 10^{-5}$	0.26	6	7
8) (1% wt% Cr) Cr-Si-Zr Xerogel	450	WHSV = 0.86	$C_3H_8 = 1.9$ , $N_2 = 0.2$ , He = 97.1	37.8-22.7 (35m and 400m)	91.1-94.7	$1.85 \cdot 10^{-4}$	0.12	6.08	8
9) Cr(2)Mg(12) Al(4)O <sub>x</sub> (mixed metal oxide)	700	WHSV = 3.2	$C_2H_6 = 28.6$ , $N_2 = 71.4$	29.6	71	$6.54 \cdot 10^{-4}$	(-)	1	9
10) 5 wt% Cr, 10 wt% Ce / SBA-15	700	GHSV = 3600	$C_2H_6 = 25$ , $CO_2 = 75$	55-46	96-97	(-)	0.059	5	10
11) 20wt% Cr 1wt% Na / $Al_2O_3$	550	WHSV = 0.12	$C_3H_8 = 10$ , $N_2 = 90$	47-37	80-89	$7.41 \cdot 10^{-6}$	0.069	6	11

a: First value is obtained at the start of the cycle, second at the end.

b: Specific activity is defined as  $\frac{mol\ olefin\ formed}{mol\ Cr \cdot t(s)}$

c: Catalyst life = total time single cycle/experiment

## References

- (1) Shee, D.; Sayari, A. *Appl. Catal. A-Gen.* **2010**, 389, 155.
- (2) Marcilly, C.; Delmon, B. *J. Catal.* **1972**, 24, 336.
- (3) Pérez-Reina, F. J.; Rodríguez-Castellón, E.; Jiménez-López, A. *Langmuir* **1999**, 15, 8421.
- (4) Alcántara-Rodríguez, M.; Rodríguez-Castellón, E.; Jiménez-López, A. *Langmuir* **1999**, 15, 1115.
- (5) Hakuli, A.; Kytökiivi, A.; Krause, A. O. I. *Appl. Catal. A-Gen.* **2000**, 190, 219.
- (6) Michorczyk, P.; Pietrzyk, P.; Ogonowski, J. *Micropor. Mesopor. Mat.* **2012**, 161, 56.
- (7) Zhang, X.; Yue, Y.; Gao, Z. *Catal. Lett.* **2002**, 83, 19.
- (8) Furdala, K.; Tilly, T. D. *J. Catal.* **2003**, 218, 123.
- (9) Tsyganok, A.; Green, R. G.; Giorgi, J. B.; Sayari, A. *Catal. Commun.* **2007**, 8, 2186.
- (10) Shi, X.; Ji, S.; Wang, K. *Catal. Lett.* **2008**, 125, 331.
- (11) Sattler, J. J. H. B.; González-Jiménez, I. D.; Mens, A. M.; Arias, M.; Visser, T.; Weckhuysen, B. M. *Chem. Commun.* **2013**, 49, 1518.

**Table S1.3.** Summary of the catalytic data of the GaO<sub>x</sub>-based dehydrogenation catalysts reported in literature. Values of conversion and selectivity of the end and start of each catalytic run are shown. From the articles considered, only the best performing catalyst is included.

Catalyst	Reaction temperature (°C)	Space velocity (h <sup>-1</sup> )	Feed composition	Conversion (%) <sup>a</sup>	Selectivity (%) <sup>a</sup>	Specific activity (s <sup>-1</sup> ) <sup>b</sup>	k <sub>d</sub> (h <sup>-1</sup> )	Catalyst life <sup>c</sup> (h)	Reference
1) 1.7 wt% Ga <sub>2</sub> O <sub>3</sub> / SiO <sub>2</sub>	550	WHSV = 0.97 h <sup>-1</sup>	C <sub>3</sub> H <sub>8</sub> = 10 Ar = 90	23-20	86-80	4.97*10 <sup>-4</sup>	0.036	5	1
2) Ga <sub>2</sub> O <sub>3</sub> / MTS	550	WHSV = 0.33	<i>i</i> -C <sub>4</sub> H <sub>10</sub> = 10,	46-40	58.3 to	5.52*10 <sup>-5</sup>	0.092	2.67	2

(mesoporous silica) Ratio Ga/Si = 0.05		$h^{-1}$	He = 90		<i>i</i> -C <sub>4</sub> H <sub>8</sub>				
3) $\beta$ -Ga <sub>2</sub> O <sub>3</sub>	500	WHSV = 0.15 $h^{-1}$	C <sub>3</sub> H <sub>8</sub> = 2.5, N <sub>2</sub> = 97.5	33-12	95-95	$6.95 \cdot 10^{-7}$	0.21	6	<sup>3</sup>
4) Ga <sub>2</sub> O <sub>3</sub>	600	WHSV = 1.2 $h^{-1}$	C <sub>3</sub> H <sub>8</sub> = 17, CO <sub>2</sub> = 83	31-3	95-82	$3.55 \cdot 10^{-5}$	0.67	4	<sup>4</sup>
5) 5 wt% Ga <sub>2</sub> O <sub>3</sub> / ZrO <sub>2</sub> ; 6) 5 wt% Ga <sub>2</sub> O <sub>3</sub> / TiO <sub>2</sub>	600	WHSV = 0.3 $h^{-1}$	C <sub>3</sub> H <sub>8</sub> = 2.5, N <sub>2</sub> = 97.5; C <sub>3</sub> H <sub>8</sub> = 2.5, CO <sub>2</sub> = 5, N <sub>2</sub> = 92.5	39-6; 32-8	74; 73	$1.90 \cdot 10^{-5}$ ; $1.54 \cdot 10^{-5}$	0.77 0.56	3	<sup>5</sup>
7) Ga <sub>8</sub> Al <sub>2</sub> O <sub>15</sub>	500	WHSV = 0.3 $h^{-1}$	a) C <sub>3</sub> H <sub>8</sub> = 2.5, N <sub>2</sub> = 97.5; b) C <sub>3</sub> H <sub>8</sub> = 2.5, CO <sub>2</sub> = 5, N <sub>2</sub> = 92.5	51.7-22.5; 49.7-33.1 <sup>d</sup>	91.6-98.2; 91.7-98.0 <sup>d</sup>	$2.39 \cdot 10^{-6}$ ; $2.30 \cdot 10^{-6}$	0.168; 0.089	8	<sup>6</sup>
9) 5 wt% Ga <sub>2</sub> O <sub>3</sub> / H-ZSM-5 (w Si / Al=97)	650	WHSV = 0.36 $h^{-1}$	C <sub>2</sub> H <sub>6</sub> = 3, CO <sub>2</sub> = 15, Ar = 82	23.7-14.5	85.9-93.7	$2.84 \cdot 10^{-5}$	0.0086	70	<sup>7</sup>
10) 0.001 wt% Pt, 1.2 wt% Ga / Al <sub>2</sub> O <sub>3</sub>	590	GHSV = 400 $h^{-1}$	C <sub>3</sub> H <sub>8</sub> = 100	39	86	(-)	(-)	0.25	<sup>8</sup>

a: First value is obtained at the start of the cycle, second at the end.

b: Specific activity is defined as  $\frac{\text{mol olefin formed}}{\text{mol Ga} \cdot t(s)}$

c: Catalyst life = total time single cycle/experiment

## References

- (1) Saito, M.; Watanabe, S.; Takahara, I.; Inaba, M.; Murata, K. *Catal. Lett.* **2003**, *89*, 213.
- (2) Nesterenko, N. S.; Ponomoreva, O. A.; Yuschenko, V. V.; Ivanova, I. I.; Testa, F.; Di Renzo, F.; Fajula, F. *Appl. Catal. A-Gen.* **2003**, *254*, 261.
- (3) Zheng, B.; Hua, W.; Yue, Y.; Gao, Z. *J. Catal.* **2005**, *232*, 143.
- (4) Michorczyk, P.; Ogonowski, J. *Appl. Catal. A-Gen.* **2003**, *251*, 425.
- (5) Xu, B.; Zheng, B.; Hua, W.; Yue, Y.; Gao, Z. *J. Catal.* **2006**, *239*, 470.
- (6) Chen, M.; Xu, J.; Su, F.; Liu, Y.; Cao, Y.; He, H.; Fan, K. *J. Catal.* **2008**, *256*, 293.
- (7) Shen, Z.; Liu, J.; Xu, H.; Yue, Y.; Hua, W.; Shen, W. *Appl. Catal. A-Gen.* **2009**, *356*, 148.
- (8) Iezzi, R.; Bartolini, A.; Buonomo, F. U.S. Patent 0198428, 2002.



## List of Abbreviations

avg.	average
BET surface area	Brunauer-Emmett-Teller surface area
CCR	continuous catalyst regeneration
CVD	chemical vapor deposition
DRIFTS	diffuse reflectance infrared Fourier transform spectroscopy
DFT	density functional theory
DH	dehydrogenation
EELS	electron energy loss spectroscopy
FBD	fluidized bed dehydrogenation
FID	flame ionization detector
FTO	Fischer-Tropsch to olefins
HERFD-XANES	high energy resolution fluorescence detection x-ray absorption near edge structure
HWHM	half width half maximum
GC	gas chromatography
GHSV	gas hourly space velocity
IR	infrared
LDH	layered double hydroxide
MTBE	methyl tertiary butyl ether
MTO	methanol to olefins
MTH	methanol to hydrocarbons
NGL	natural gas liquids
NMR	nuclear magnetic resonance
ODH	oxidative dehydrogenation
PCA	principle component analysis
PDH	propane dehydrogenation
regen.	regeneration
RWGS	reverse water gas shift
SFGIR	sum frequency generation infra-red

SHC	selective hydrogen combustion
SIMS	secondary ion mass spectrometry
SORS	Surface offset Raman spectroscopy
STAR	steam active reforming
STXM	scanning transmission X-ray microscopy
STEM	scanning transmission electron microscopy
TCD	thermal conductivity detector
TEM	transmission electron microscopy
TEOM	tapered element oscillating microbalance
TGA	thermal gravimetric analysis
TOF	turn-over frequency
TOS	time-on-stream
TPR	temperature programmed reduction
TPD	temperature programmed desorption
UPS	ultraviolet photoelectron spectroscopy
UV-Vis	ultra violet and visible
WGS	water gas shift
WHSV	weight hourly space velocity
wt%	weight percent
XAS	X-ray absorption spectroscopy
XANES	X-ray absorption near edge structure
XPS	X-ray photoelectron spectroscopy
XRD	X-ray diffraction

## List of Publications and Presentations

### Publications

J.J.H.B. Sattler, I.D. Gonzalez-Jimenez, A. M. Mens, M. Arias, T. Visser, B.M. Weckhuysen, Operando UV-Vis spectroscopy of a catalytic solid in a pilot-scale reactor: Deactivation of a CrO<sub>x</sub>/Al<sub>2</sub>O<sub>3</sub> propane dehydrogenation catalyst, *Chem. Commun.* **49** (2013) 1518-1520.

J.J.H.B. Sattler, A.M. Beale, B.M. Weckhuysen, Operando Raman spectroscopic study on the deactivation of Pt and Pt-Sn/Al<sub>2</sub>O<sub>3</sub> propane dehydrogenation catalysts, *Phys. Chem. Chem. Phys.* **15** (2013) 12095-12103.

J.J.H.B. Sattler, I.D. Gonzalez-Jimenez, L. Luo, B.A. Stears, A. Malek, D.G. Barton, B.A. Kilos, M.P. Kaminsky, T.W.G.M. Verhoeven, E.J. Koers, M. Baldus, B.M. Weckhuysen, Pt promoted Ga/Al<sub>2</sub>O<sub>3</sub> as a Highly Active, Selective and Stable Catalyst for the Dehydrogenation of Propane, *Angew. Chem. Int. Ed.* **53** (2014) 9251-9256.

J.J.H.B. Sattler, J. Ruiz-Martinez, E. Santillan-Jimenez, B.M. Weckhuysen, Catalytic Dehydrogenation of Light Alkanes on Metals and Metal Oxides, *Chem. Rev.* (2014) Published online, DOI: 10.1021/cr50002436

J.J.H.B. Sattler, A.M. Mens, B.M. Weckhuysen, Real-Time Quantitative Operando Raman Spectroscopy of a CrO<sub>x</sub>/Al<sub>2</sub>O<sub>3</sub> Propane Dehydrogenation Catalyst in a Pilot-Scale Reactor, *ChemCatChem* (2014) accepted, DOI: 10.1002/cctc.201402649. .

J.J.H.B. Sattler, I.D. Gonzalez Jimenez, B.M. Weckhuysen, Nano-Scale Chemical Imaging of Individual Catalyst Particles for Studying the Coke Formed During Propane Dehydrogenation, *in preparation*.

D.R. Stellwaagen, J.J.H.B. Sattler, K.P. de Jong, J.H. Bitter, Support effects in molybdenum oxide catalyzed transesterification, *in preparation*.

## Oral Presentations

Deactivation of Pt based Dehydrogenation Catalysts: A Combined in-situ Spectroscopy Study, J.J.H.B. Sattler, A. Iglesias-Juez, A.M. Beale, B.M. Weckhuysen, Europacat X, Glasgow, United Kingdom, September 1<sup>st</sup>, 2011.

Operando UV-Vis Spectroscopy of a Catalytic Solid in a Pilot-Scale Reactor: Deactivation of a CrO<sub>x</sub>/Al<sub>2</sub>O<sub>3</sub> Propane Dehydrogenation Catalyst, J.J.H.B. Sattler, I.D. Gonzalez Jimenez, B.M. Weckhuysen, NCCC XIV, Noordwijkerhout, the Netherlands, March 12<sup>th</sup>, 2013.

Operando UV-Vis Spectroscopy of a Catalytic Solid in a Pilot-Scale Reactor, J.J.H.B. Sattler, I.D. Gonzalez Jimenez, B.M. Weckhuysen, EMRS-Spring meeting, Strasbourg, France, May 28<sup>th</sup>, 2013.

Operando UV-Vis and Raman spectroscopy in a pilot-scale reactor: CrO<sub>x</sub> deactivation during dehydrogenation of propane as a showcase, J.J.H.B. Sattler, I.D. Gonzalez Jimenez, B.M. Weckhuysen, NAM 23, Louisville, Kentucky, the United States, June 5, 2013.

Operando UV-Vis Spectroscopy in a Pilot-Scale Reactor; Deactivation of a CrO<sub>x</sub>/Al<sub>2</sub>O<sub>3</sub> Propane Dehydrogenation Catalyst, J.J.H.B. Sattler, I.D. Gonzalez Jimenez, B.M. Weckhuysen, Europacat XI, Lyon, France, September 4<sup>th</sup>, 2013.

Pt-Ga/Al<sub>2</sub>O<sub>3</sub> as a Highly Active, Selective and Stable Catalyst for the Dehydrogenation of Propane, J.J.H.B. Sattler, I.D. Gonzalez Jimenez, B.M. Weckhuysen, NCCC XV, Noordwijkerhout, the Netherlands, March 11<sup>th</sup>, 2014.

## Acknowledgements

In de afgelopen 4 jaar, zijn er verschillende mensen geweest die een bijdrage hebben geleverd aan de totstandkoming van dit proefschrift. Hierbij wil ik in het algemeen iedereen bedanken. More specific acknowledgements can be found at the end of the individual Chapters.

Ten eerste wil ik mijn promotor en dagelijkse begeleider, prof. Weckhuysen bedanken. Beste Bert, bedankt voor het vertrouwen dat je in mij gesteld hebt 4 jaar geleden. Ik heb onze samenwerking altijd als plezierig ervaren. Je gaf me de ruimte en mogelijkheden om nieuwe dingen te proberen en was altijd aanspreekbaar als ik advies nodig had. Jouw aanstekelijke drive om het onderzoek steeds een stapje verder te brengen zijn belangrijk geweest om dit proefschrift op het punt te krijgen waar het nu is. Verder wil ik dr. Andrew Beale, prof. Frank de Groot en prof. Krijn de Jong bedanken voor de wetenschappelijke discussies die we hebben gevoerd.

Inés, I want to thank you for the two years we have worked closely together on much of the work described in this thesis. Not only was it great to work with you as a colleague and friend, but I have also learned a lot from you during this time. I also want to thank Javi. For four and a half years we have worked together on our review, and I think we can be proud of the result. Jens Schoenmakers wil ik bedanken voor zijn inzet tijdens zijn bachelors thesis.

Verder wil ik het secretariaat, en dan specifiek Dymph en Monique, bedanken voor hun hulp met allerlei administratieve zaken. Ad M, ik ben je veel dank verschuldigd voor het werk dat je gestoken hebt in het herbouwen van de pilot reactor. Ook wil ik de andere technici, Ad E, Fouad, Marjan, Oscar en Vincent bedanken voor hun hulp.

Dear colleagues, I want to thank all of you for the fun times we had during lab-uitjes, borrels and congresses. Furthermore, I want to thank all the officemates I had over the years; Javi, Arjen, Yuen, Hendrik, Sophie, Peter M and Mustafa. I would like to thank Christoff, Bojan, Mustafa, Ines, Hendrik, Korneel, Matti, Tamara and Luis for their company during the several beamtrips. It was also a pleasure to work with you in the lab; Upakul, Ramon, Inés L, Joris, Hendrik and Elena. I also want to acknowledge my friends in the Futsal team over the years; Rob, Rene, Gonzalo, Javi, Philip, Wouter, Tomas, Thomas, Carlo, Zoran, Roy, Sam, Joe and Gareth. For the

several trips I joined, visiting Aken, Oktoberfest, Istanbul and skiing at Winterberg, I especially want to thank the organizers Thomas, Zafer and Roy for the good memories. Finally I also want to mention Ana, Daniel, Davide, Elena, Fiona, Gang, Inge, Ilona, Jeroen, Jinbao, Jovana, JX, Peter B, Piter, Qingyun, Raphael, Rosa, Wenhao; Thank you for the good times.

Arjen, Bram en Sjoerd, bedankt voor de vriendschap over de jaren. Tenslotte wil ik mijn familie bedanken. Papa, Mama, Ivana, Sharon en Nicolai, bedankt voor jullie onvoorwaardelijke steun en liefde.

## **About the Author**

Jesper Sattler was born on the 10<sup>th</sup> of March, 1986 in Veenendaal, the Netherlands. After graduating from the Christian Lyceum Veenendaal, he was admitted at Utrecht University in 2004. He received a bachelor of science (BSc) degree in 2007, with the thesis entitled 'Electrochemistry of Silicon Carbide in Fluoride Solutions', at the group of Condensed Matter and Interfaces, under the supervision of prof. dr. John J. Kelly. In the same year, he started a master study majoring in Chemistry and Physics at Utrecht University. He joined the group of Inorganic Chemistry and Catalysis, under the supervision of prof. dr. ir. Bert M. Weckhuysen. In 2010 he received his master of science (MSc) degree with the thesis entitled 'Thiophene Oligomerisation Inside H-ZSM-5 Crystals: Non-Uniform Catalytic Behaviour of Zeolite Crystals as Revealed by In-Situ Microspectroscopy'. After a 6 month internship at Albemarle he rejoined the group of Inorganic Chemistry and Catalysis as a PhD student, researching the deactivation of propane dehydrogenation catalysts under the supervision of prof. dr. ir. Bert M. Weckhuysen. His research was funded by the National Research School Combination-Catalysis (NRSC-C) and ACTS-Aspect. The results obtained during this period are described in this thesis and were presented as posters or oral presentations at different international conferences.

